LBNL-40585
UC-414

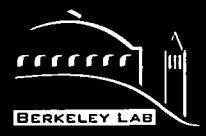

ERNEST ORLANDO LAWRENCE
BERKELEY NATIONAL LABORATORY

A Search for Charmless Dihadron Decays of Neutral *b*-Hadrons

Shigeki Misawa

Physics Division

March 1997

Ph.D. Thesis

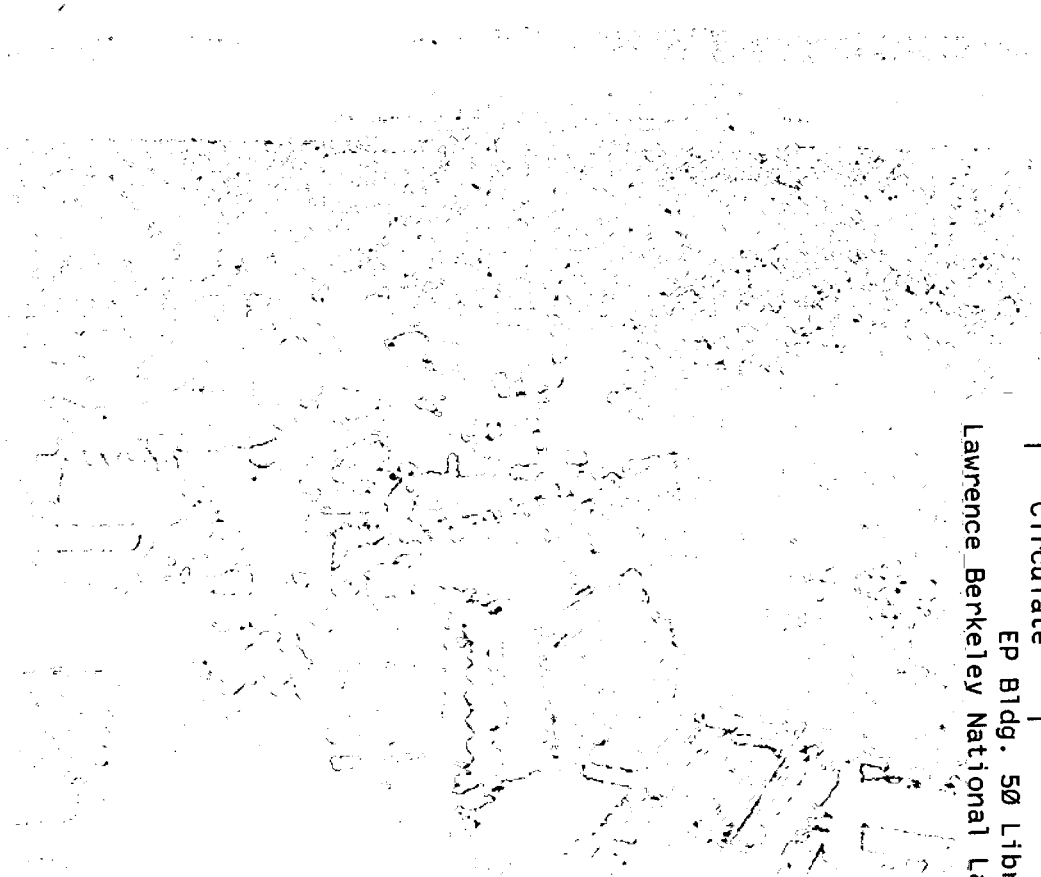

DISCLAIMER

LBNL-40585
UC-414

A Search for Charmless Dihadron Decays of Neutral *b*-Hadrons

Shigeki Misawa
Ph.D. Thesis

Department of Physics
University of California, Berkeley

and

Physics Division
Ernest Orlando Lawrence Berkeley National Laboratory
University of California
Berkeley, CA 94720

March 1997

This work was supported by the Office of Energy Research of the U.S. Department of Energy under Contract No. DE-AC03-76SF00098.

A Search for Charmless Dihadron Decays of Neutral b-Hadrons

by

Shigeki Misawa

S.B. (Massachusetts Institute of Technology) 1985
S.B. (Massachusetts Institute of Technology) 1985
S.M. (Massachusetts Institute of Technology) 1985

A dissertation submitted in partial satisfaction of the

requirements for the degree of

Doctor of Philosophy

in

Physics

in the

GRADUATE DIVISION

of the

UNIVERSITY OF CALIFORNIA, BERKELEY

Committee in charge:

Professor Kam-Biu Luk, Chair
Professor Robert Jacobsen
Professor Stephen Derenzo

March 17, 1997

A Search for Charmless Dihadron Decays of Neutral *b*-Hadrons

by

Shigeki Misawa

Abstract

A Search for Charmless Dihadron Decays of Neutral b-Hadrons

by

Shigeki Misawa

Doctor of Philosophy in Physics

University of California, Berkeley

Professor Kam-Biu Luk, Chair

A search for charmless dihadron decays of neutral b-hadrons was performed using data obtained from 800 GeV/c proton-gold interactions. The following upper limits on the b-hadron branching ratios (including charge conjugates) were obtained at the 90% confidence limit:

$$\mathrm{Br}(B_s \to K^+K^-) + r_s \times \mathrm{Br}(B_d \to \pi^+\pi^-) < 2.0 \times 10^{-3}$$

$$\mathrm{Br}(B_d \to K^+K^-) < 9.5 \times 10^{-4}, \quad \mathrm{Br}(B_s \to \pi^+\pi^-) < 2.0 \times 10^{-3}$$

$$\mathrm{Br}(B_d \to K^+\pi^-) < 1.9 \times 10^{-3}, \quad \mathrm{Br}(B_s \to K^-\pi^+) < 2.2 \times 10^{-3}$$

$$\mathrm{Br}(B_d \to p\bar{p}) < 1.6 \times 10^{-3}, \quad \mathrm{Br}(B_s \to p\bar{p}) < 9.0 \times 10^{-3}$$

$$\mathrm{Br}(\Lambda_b \to K^+p^-) < 6.1 \times 10^{-3}, \quad \mathrm{Br}(\Lambda_b \to \pi^+p^-) < 9.7 \times 10^{-3}$$

where r_s was determined to be 2.9 ± 0.8. These limits assume that $B_d/B_s/\Lambda_b$ hadrons are produced in proton on nucleon interactions in the ratio $(38 \pm 5.7) : (13 \pm 3.2) : (9.6 \pm 1.7)$ and that the branching ratio for the cascade decay b-hadron $\to J/\psi + X \to \mu^+\mu^- + X$ is $(6.97 \pm .64) \times 10^{-4}$.

Contents

List of Figures

List of Tables

Acknowledgment

The completion of this thesis would not have been possible without the support, assistance and encouragement of a number of individuals. In recognition of their assistance, I would like to thank the following individuals:

- My parents for providing financial support and for never questioning the length of time it took me to complete this thesis.
- My sister and brother-in-law for accepting my "gifts" of used computer equipment and for making life out at Fermilab more enjoyable.
- Stuart Gitlow, MD, for providing the much needed reality checks.
- The late Professor Harry Bingham, for supporting my adventures into the application of C++ and object oriented programming to high energy physics data analysis. Craig Ballagh for providing much appreciated Fortran support and for hearing my rants about the evils of Fortran.
- Professor Kam-Biu Luk for being there to pick up the pieces after the train wreck and guiding me through the analysis process. Fellow E789 graduate student Dave Pripstein for helping me get up to speed with the E789 analysis code.
- Professor Bob Jacobsen, thesis committee member, for reading the drafts and keeping me abreast of the developments in software engineering.
- Matthew Sohn for pushing C++ and object oriented programming on me in the beginning. Dr. Matthew Austern of Silicon Graphics for providing a sounding board during our joint forays into object oriented programming and for answering my questions about theoretical physics. Dr. Paul Kunz of SLAC for providing encouragement during my adventures into object oriented data analysis.

- Chuck Lawrence and Andrei Cogan, system administrators for the LBL Mechanical Engineering HP cluster, for allowing me unlimited access to their machines. Art Ferruzzi, physics department system administrator, for providing Unix support. Rusty Wright and Michele Tomkin of U.C. Workstation Support for providing help in keep my SPARCstation running.

- Finally, Anne Takizawa and Donna Sakima of the physics department for moral support.

Chapter 1

Introduction

1.1 Standard Model

The Standard Model is the theory currently used to explain most of the structure of the physical world. The model contains a group of spin 1/2 particles called *fermions* and three fundamental interactions, the electromagnetic, weak and strong interactions, that act on these fermions. Each force is carried by one or more spin 1 particles called *bosons*. The carrier of the electromagnetic force is the *photon*, a massless, electrically neutral particle. There are three massive carriers of the weak force, the electrically charged W^+ and W^- and the electrically neutral Z. Finally, there are eight massless, electrically neutral quanta of the strong interactions called *gluons*. The one interaction that is not explained by the Standard Model is gravitation.

1.1.1 Fermions

The fundamental fermions in the Standard Model can be separated into two groups, those particles that are subject to the strong interaction and those particles that are not. The former are called *quarks*, the latter *leptons*.

Leptons

There are currently six leptons in the Standard Model, the *electron*, *muon*, and *tau* and their respective *neutrinos*. Each lepton is mirrored by an anti-particle with opposite charge and helicity. The leptons can be logically grouped into three pairs or *generations* of

particles:

$$\begin{pmatrix} \nu_e \\ e^- \end{pmatrix}, \begin{pmatrix} \nu_\mu \\ \mu^- \end{pmatrix}, \begin{pmatrix} \nu_\tau \\ \tau^- \end{pmatrix} \tag{1.1}$$

The lower member of each pair has a non-zero mass and an electric charge of $-e$, where e is the magnitude of the charge of the electron. The charged leptons can interact electromagnetically through the emission or absorption of a photon. They can also interact weakly through the emission or absorption of $W^\pm$ and Z bosons. The upper members of each pair, the neutrinos, are believed to be massless and are electrically neutral. Being electrically neutral, the neutrinos can interact only weakly.

The charged weak interactions couple the neutrino and the charged lepton in a generation through the emission or absorption of a $W^\pm$. More accurately, the *left-handed* leptons are grouped into *weak isospin doublets*, while the *right-handed* leptons are grouped into *weak isospin singlets*:

$$\begin{pmatrix} \nu_e \\ e^- \end{pmatrix}_L, \begin{pmatrix} \nu_\mu \\ \mu^- \end{pmatrix}_L, \begin{pmatrix} \nu_\tau \\ \tau^- \end{pmatrix}_L \tag{1.2}$$

$$e_R^-,\ \mu_R^-,\ \tau_R^- \tag{1.3}$$

Charged weak interactions couple the upper and lower components of the left-handed doublet but do not couple members of different generations. They also do not interact with the leptons in the weak isospin singlets. The generations differ only in the mass of the charged lepton in each generation.

Quarks

The second group of fermions in the Standard Model are the quarks. There are currently 6 types or *flavors* of quarks in the Standard Model: *up*, *down*, *charm*, *strange*, *top*, and *bottom*. Each quark is mirrored by an anti-quark with opposite charge and helicity. (Each quarks may also be in one of three color charge states. Color charge is discussed in the section describing the strong force.) Like the leptons, the quarks can be grouped into generations:

$$\begin{pmatrix} u \\ d \end{pmatrix}_L, \begin{pmatrix} c \\ s \end{pmatrix}_L, \begin{pmatrix} t \\ b \end{pmatrix}_L. \tag{1.4}$$

$$u_R,\ d_R,\ c_R,\ s_R,\ t_R,\ b_R \tag{1.5}$$

As with the leptons, the quarks are grouped into left-handed weak isospin doublets which couple to the charged weak current and right-handed weak isospin singlets which do not. Unlike the leptons, all quarks possess non-zero mass and an electrical charge. The upper member of each generation possess an electric charge of $+\frac{2}{3}e$ and the lower member possess a charge of $-\frac{1}{3}e$. Finally, unlike the leptons, the quarks also interact strongly, i.e., exchange gluons. One additional unique feature of the quarks is that they are not seen in isolation. For reasons that are not completely understood, quarks are isolated into *mesons* which are quark – anti-quark pairs and *baryons* which are bound states of three quarks.

1.1.2 Fundamental Interactions

The three interactions in the Standard Model are described by the exchange of bosons. These bosons, referred to as *gauge bosons*, are the quanta associated with a special class of quantum fields called *gauge fields*, which are invariant with respect to a class of transformations called *local gauge transformations*. This class of transformations is important because fields that are invariant under these transformations are *renormalizable*. This means that infinities that arise in the calculation of physical quantities can be removed through the suitable redefinition of a finite set of parameters.

The three interactions in the Standard Model are explained by two essentially separate theories. The first, *quantum chromodynamics* (QCD), covers strong interactions. The second, the *electro-weak* theory, describes weak and electromagnetic interactions. QCD is the simpler of the two theories because it describes a field that is invariant with respect to a local gauge transformation. In contrast, the electro-weak theory involves two separate fields whose local gauge invariances have been "spontaneously broken".

Quantum Chromodynamics

Quantum chromodynamics is the gauge theory that describes the strong interactions, the force that is thought to bind quarks together to form the mesons and baryons. Residual inter-quark strong forces are what is believed to bind protons and neutrons, both baryons, together to form the nuclei of atoms. This residual interaction acts in much the same way as the Van der Waal forces, which are the residuals of the electromagnetic interaction between electrons and nuclei in an atom, binding atoms together into molecules.

QCD specifies that all quarks carry a strong charge referred to as *color* [1].

$$\begin{pmatrix} q_{red} \\ q_{green} \\ q_{blue} \end{pmatrix} \tag{1.6}$$

This charge is called color because there are three fundamental types of strong charges, *red*, *green*, *blue*, just as in the theory of human vision where three fundamental colors can be used to describe the response of the human eye to visible light. The existence of three strong color charges should be contrasted with electromagnetism where there are only two types of charges, positive and negative.

As was stated previously, it is believed that all quarks are isolated in mesons or baryons, free quarks having not been observed. Although unproven, it is believed that QCD can explain this phenomena. The belief is that all matter that is constructed of quarks must exist in or be confined to color *singlet* states. The mesons are considered to be color singlet states of a quark and an anti-quark, where the anti-quark carries a color charge that is the anti-color of the color charge carried by the quark. The baryons are considered to be bound states of three quarks of different color, i.e., one red quark, one green quark and one blue quark. In addition to providing a possible explanation for the presence of mesons and baryons, the concept of color in QCD also "fixes" some problems in the renormalizability of the electro-weak theory called *anomalies.*

The gluons, the quanta of the QCD field, each carry a color and an anti-color charge. Of the 9 possible combinations of a color charge and an anti-color charge, one combination, $(1/\sqrt{3})(r\bar{r} + g\bar{g} + b\bar{b})$, is a color singlet (i.e., *colorless*) and is not assigned to a gluon. The remaining 8 combinations form a color *octet* and are considered to be the physical gluons. In QCD, these 8 gluons are the quanta of a quantum field that are invariant under a local $SU(3)$ gauge transformation.

The singlet designation of hadrons and the octet designation of the 8 gluons is directly related to this local $SU(3)$ gauge transformation. The three colors charges, r, g, and b, form a three-dimensional (color triplet) representation of $SU(3)$. The colorless $q\bar{q}$ mesons are those combinations (direct products) of q and $\bar{q}$ that form a one-dimensional or color singlet representation of $SU(3)$. The colorless qqq baryons are those combinations of three quarks that form a one-dimensional (color singlet) representation of $SU(3)$. Finally, the 8 gluons are those combinations of color and anti-color charges that form an 8-dimensional

(color octet) representation of $SU(3)$.

One fundamental problem with QCD is that it is a "strong" interaction, that is the coupling constant in the strong interaction is greater than one. As a result, perturbative techniques, where equations are written in terms of powers of an expansion parameter (in this case α_s), cannot be easily applied to QCD to make theoretical predictions of physical processes. However, there are a few situations where perturbation theory can be applied. These situations are beneficiaries of the fact that gluons carry color charge. (Unlike photons in electromagnetism which do not carry an electrical charge.) Since gluons carry color charge, the QCD coupling constant *runs* or varies in a manner that makes it smaller at higher energy. Calculations show that the QCD coupling constant α_s varies with Q^2, the characteristic energy of a given process:

$$\alpha_s(Q^2) = \frac{\alpha_s(\mu^2)}{1 + \frac{\alpha_s(\mu^2)}{12\pi}(33 - 2n_f)log(Q^2/\mu^2)} \tag{1.7}$$

In this expression, μ is the energy at which α_s has been measured and n_f is the number of quark flavors. As long as the number of quark flavors is less than 16, the QCD coupling constant decreases with Q^2 for the interaction. This energy behavior characterizes QCD as being *asymptotically free.*

Electro-Weak Theory

The electro-weak theory, developed principally by Glashow, Weinberg and Salam, describes the electromagnetic and weak interactions [2, 3, 4]. Like QCD, it is based on quantum fields that are invariant under local gauge transformations. However, unlike QCD, these symmetries are *spontaneously broken.*

In the electro-weak theory there are two vector fields, one invariant under a local $SU(2)$ gauge transformation, the other invariant under a local $U(1)$ gauge transformation. The $SU(2)$ field consists of three separate vector fields (designated for this discussion as $\vec{b}^1$, $\vec{b}^2$ and $\vec{b}^3$). There are three massless gauge bosons associated with the $SU(2)$ field, one for each vector field. These gauge bosons only interact with the left-handed lepton doublets and quark doublets, which are massless at this level of the theory. Since the $SU(2)$ gauge bosons interact with only the left-handed doublets the $SU(2)$ field is typically referred to as an $SU(2)_L$ field. The left-handed lepton and quark doublets for the first generation are

shown in equation 1.8:

$$\begin{pmatrix} u \\ d' \end{pmatrix}_L, \begin{pmatrix} \nu_e \\ e \end{pmatrix}_L \tag{1.8}$$

The $\vec{b}^1$ and $\vec{b}^2$ vector fields couple the upper member of the doublet to the lower member of the doublet.

A massless boson is associated with the $U(1)$ vector field (for the sake of this discussion the field is designated $\vec{a}$). Unlike the $SU(2)$ field, the $U(1)$ field couples to both left-handed and right-handed quarks and leptons. However, the strength of the coupling is dependent on the *weak-hypercharge* of the particle to which it couples.

Already more complex than QCD, this is not the end of the complexities associated with the electro-weak theory. First, the $SU(2)_L$ symmetry is spontaneously broken. The simplest way that this is accomplished in the Standard Model is through the presence of an $SU(2)$ doublet of scalar (spin zero) fields that has a finite vacuum expectation value. The addition of the scalar doublet results in the $\vec{b}^i$ and $\vec{a}$ fields acquiring a finite mass. It is a linear combination of the now massive $\vec{b}^1$ and $\vec{b}^2$ fields that make up the fields associated with the physical massive W^+ and W^- bosons of the weak interactions. The remaining $\vec{b}^3$ and $\vec{a}$ fields mix in a manner that results in one massive vector field and one massless vector field. The quanta associated with the massive field is the physical Z neutral vector boson of the weak interaction. The quantum of the massless field is the physical photon.

The next complication in the electro-weak theory is that the quark states in the hadronic weak isospin doublets are not eigenstates of the mass matrix. In the Standard Model, the leptons and hadrons acquire a mass as a result of the Yukawa couplings between the scalar doublet and the fermions. In the case of the quarks, the eigenstates of the mass matrix are linear combinations of the quark states in the weak isospin doublets. The standard method of representing this *mixing* is through the Cabibbo-Kobayashi-Maskawa (CKM) matrix[5, 6]:

$$\begin{pmatrix} d' \\ s' \\ b' \end{pmatrix} = \begin{pmatrix} V_{ud} & V_{us} & V_{ub} \\ V_{cd} & V_{cs} & V_{cb} \\ V_{td} & V_{ts} & V_{tb} \end{pmatrix} \begin{pmatrix} d \\ s \\ b \end{pmatrix} \tag{1.9}$$

This matrix expresses the lower members of the hadronic weak isospin doublet as a linear combination of the mass eigenstates. The primed states in equation 1.9 are weak quark states, the unprimed states are the mass eigenstates. The result is that weak interactions (or more specifically, charged weak interactions) can cause a change in generation (in hadrons)

in addition to causing a change in flavor when the hadron doublets are written with mass eigenstates.

Finally, the electro-weak theory predicts that the remnants of the scalar doublet will be manifest as an electrically neutral scalar boson, called the Higgs, that couples to all the massive fermions and the $W^{\pm}$ and Z bosons. Despite its prediction of a currently unseen massive scalar boson, the mechanism of spontaneous symmetry breaking does have benefits. First, it provides a mechanism through which the weak interaction gauge bosons can acquire mass. Second, it provides a mechanism by which the fermions can acquire a mass, namely through a Yukawa coupling to the scalar doublet.

1.2 CKM Matrix

One fundamental problem with the Standard Model is that it does not specify the magnitude of the generation mixing in weak interactions. Although the Standard Model places some constraints on the CKM matrix, (e.g., unitarity), it does not completely determine the CKM matrix. The constraints placed on the CKM matrix by the Standard Model reduce the number of free parameters in the matrix to 3 rotation angles (θ_{12}, θ_{13}, θ_{23}) and 1 phase (δ_{13}):

$$\begin{pmatrix} c_{12}c_{13} & s_{12}c_{13} & s_{13}e^{-i\delta_{13}} \\ -s_{12}c_{23} - c_{12}s_{23}s_{13}e^{i\delta_{13}} & c_{12}c_{23} - s_{12}s_{23}s_{13}e^{i\delta_{13}} & s_{23}c_{13} \\ s_{12}s_{23} - c_{12}c_{23}s_{13}e^{i\delta_{13}} & -c_{12}s_{23} - s_{12}c_{23}s_{13}e^{i\delta_{13}} & c_{23}c_{13} \end{pmatrix} \tag{1.10}$$

where

$$c_{ij} = cos\ \theta_{ij}$$
$$s_{ij} = sin\ \theta_{ij}.$$

However, it is up to experiments to determine the values of the rotation angles and the phase. One of the goals in experimental particle physics has therefore been to place constraints on the elements of the CKM matrix and to verify aspects of the Standard Model that are tied to the CKM matrix. For example, verification of the various unitarity constraints on the CKM matrix would place limits on the number of generations in the Standard Model. Another example is the confirmation or refutation of δ_{13} as the sole source of charge – parity (CP) violation, which was first observed in K_L decays [7].

Empirically, the elements of the CKM matrix follows the pattern shown in equation 1.11, where $\lambda \equiv sin\theta_c \simeq 0.221$ is the expansion parameter [8]. (θ_c is the Cabibbo angle [6].)

$$\begin{pmatrix} 1-\frac{1}{2}\lambda^2 & \lambda & A\lambda^3(\rho-i\eta) \\ -\lambda & 1-\frac{1}{2}\lambda^2-iA^2\lambda^4\eta & A\lambda^2 \\ A\lambda^3(1-\rho-i\eta) & -A\lambda^2 & 1 \end{pmatrix} + O(\lambda^4) \qquad (1.11)$$

Precise determinations of the CKM elements V_{ud}, V_{us} and V_{cd} and slightly less precise measurements of V_{cs} have been made in experiments with mesons and baryons that contain the u, d, c, and s quarks [9, 10]. In theory, V_{td} and V_{ts} can be obtained from charged weak current decays of hadrons containing top quarks; however, the large mass ($\approx$ 180 GeV) of the top [11, 12] and the fact that $V_{tb} \simeq 1$ make this unlikely [13]. Extracting these two matrix elements from processes involving virtual top quarks and no bottom quarks, such as in flavor changing neutral current (FCNC) processes, is also problematic because they are suppressed by small CKM couplings.

Given the problems of determining V_{td} and V_{ts} in non b-quark processes and top decays, the logical solution is to look at the decays of hadrons containing b-quarks. Decay processes involving the decay of a b-quark via a virtual t-quark such as $b \rightarrow s\gamma$ are a natural place to obtain a measurement of V_{td} and V_{ts}. In addition, experiments with b-quarks are natural places to measure V_{cb} and V_{ub}.

1.3 B Physics

Theoretically, the CKM matrix elements V_{cb}, V_{ub}, V_{tb}, V_{ts}, and V_{td} can be determined from looking at different b-hadron processes. These include measuring b-hadron lifetimes, semi-leptonic and hadronic branching ratios, $B^0\overline{B^0}$ mixing, and b-hadron penguin decays [13, 14, 15]. More specifically, V_{cb} has been determined from the b-hadron lifetime [16], V_{cb} and V_{ub} have been obtained from the inclusive lepton spectrum from semi-leptonic B decays [17], and V_{ts} and V_{td} can be extracted from $B^0\overline{B^0}$ mixing measurements [18].

The desire to look at b decays is not limited to determining the elements of the CKM matrix. In relating the experimental observables to elements of the CKM matrix, understanding the QCD effects is usually required. Hence, the study of b decays can also be

used to test QCD models. For example, the extraction of V_{cb} from exclusive semileptonic B decays involving $b \to c$ transitions requires the determination of a hadronic form factor which can be determined from the Heavy Quark Effective theory (HQET) [13]. Connecting measured parameters from $B^0\overline{B^0}$ mixing to the CKM matrix elements requires constants that can be calculated using Lattice QCD [13]. A final example, applicable to the analysis in this thesis, involves tests of *factorization.* A fundamental assumption made in the calculations of two body hadronic B decays is that the hadronization of the u or c from the decay of the b is independent of the hadronization of the emitted W^- [15, 19]. By comparing two body hadronic and semi-leptonic b decays, the validity of factorization can be tested [14].

1.3.1 Charmless b decays

The major goal of this analysis was the measurement of the branching ratios of neutral b-hadrons to two charged, charmless hadrons. More specifically, the goals were to measure the branching ratios of the decays given in equation 1.12, 1.13 and 1.14.

$$\begin{aligned} B_d^0(\overline{B_d^0}) &\to \pi^+\pi^- \\ &\to K^+\pi^-(\pi^+K^-) \\ &\to K^+K^- \\ &\to p\bar{p} \end{aligned} \tag{1.12}$$

$$\begin{aligned} B_s^0(\overline{B_s^0}) &\to K^+K^- \\ &\to \pi^+K^-(K^+\pi^-) \\ &\to \pi^+\pi^- \\ &\to p\bar{p} \end{aligned} \tag{1.13}$$

$$\begin{aligned} \Lambda_b^0(\overline{\Lambda_b^0}) &\to p\pi^-(\bar{p}\pi^+) \\ &\to pK^-(\bar{p}K^+) \end{aligned} \tag{1.14}$$

Assuming only weak interactions, i.e. ignoring QCD and electromagnetic effects, the charmless decays of b-hadrons proceeds through $b \to u$ transition, with the emission/absorption of a virtual W (see Figure 1.1). At this level, b-hadron decays with charmless final states are suppressed relative to decays with charm since charmless decay amplitudes are proportional to $V_{ub} \propto \lambda^3$ (see equation 1.11) whereas amplitudes for decays to final states with charm are proportional to $V_{cb} \propto \lambda^2$. Within the group of charmless decays,

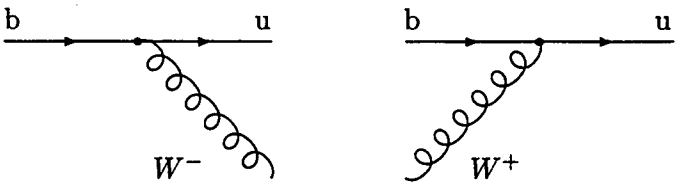

Figure 1.1: W emission/absorption diagrams.

those containing strange quarks in the final state (with no strange in the initial state) are further suppressed relative to those processes containing down quarks in the final state. (The former contains a $V_{us} \propto \lambda$ factor in the decay amplitude, the latter contains a $V_{ud} \propto 1$ factor.)

When QCD effects are taken into account, the charmless decays are modified by the addition of new diagrams, most notably the penguin diagrams. These new diagrams in some cases dominate over the tree–level diagrams, in particular those containing $u \to s$ transitions. The next to leading order (NLO) effective Hamiltonian (with QCD and electroweak effects) that describes charmless two body decays of b-hadrons is [20]:

$$H_{\Delta B=1} = \frac{G_F}{\sqrt{2}} \left[V_{ub}V_{uq}^* \left(c_1 O_1^u + c_2 O_2^u\right) - V_{tb}V_{tq}^* \sum_{i=3}^{10} c_i O_i \right] + H.C. \tag{1.15}$$

The $V_{qq'}$ factors are the complex CKM matrix elements, the c_i's are the Wilson coefficients, the O_i's are local operators generated by QCD and electro-weak interactions, and G_F is the Fermi coupling constant. The Wilson coefficients characterize short distance effects whereas the local operators characterize long distance effects [21]. The first two O_i terms correspond to the tree–level diagrams, the other eight terms correspond to strong and electroweak penguins [20]. The quark diagrams for B decays to two mesons and two baryons that can be derived from the effective Hamiltonian are shown in Figures 1.2 and 1.3 [22]. Among the B to two meson diagrams, the annihilation, W exchange and vertical W loop graphs have been argued to be helicity or form-factor suppressed [22, 23]. All the B to two baryon diagrams are color suppressed [22].

The diagrams in Figures 1.2 and 1.3 include charged and uncharged initial and final state mesons. A smaller set of diagrams describe the case of neutral B mesons to two charged hadrons. In particular, the relevant diagrams are shown in Figure 1.4 for decays to two charmless charged mesons and Figure 1.5 for decays to two protons. Since the annihilation,

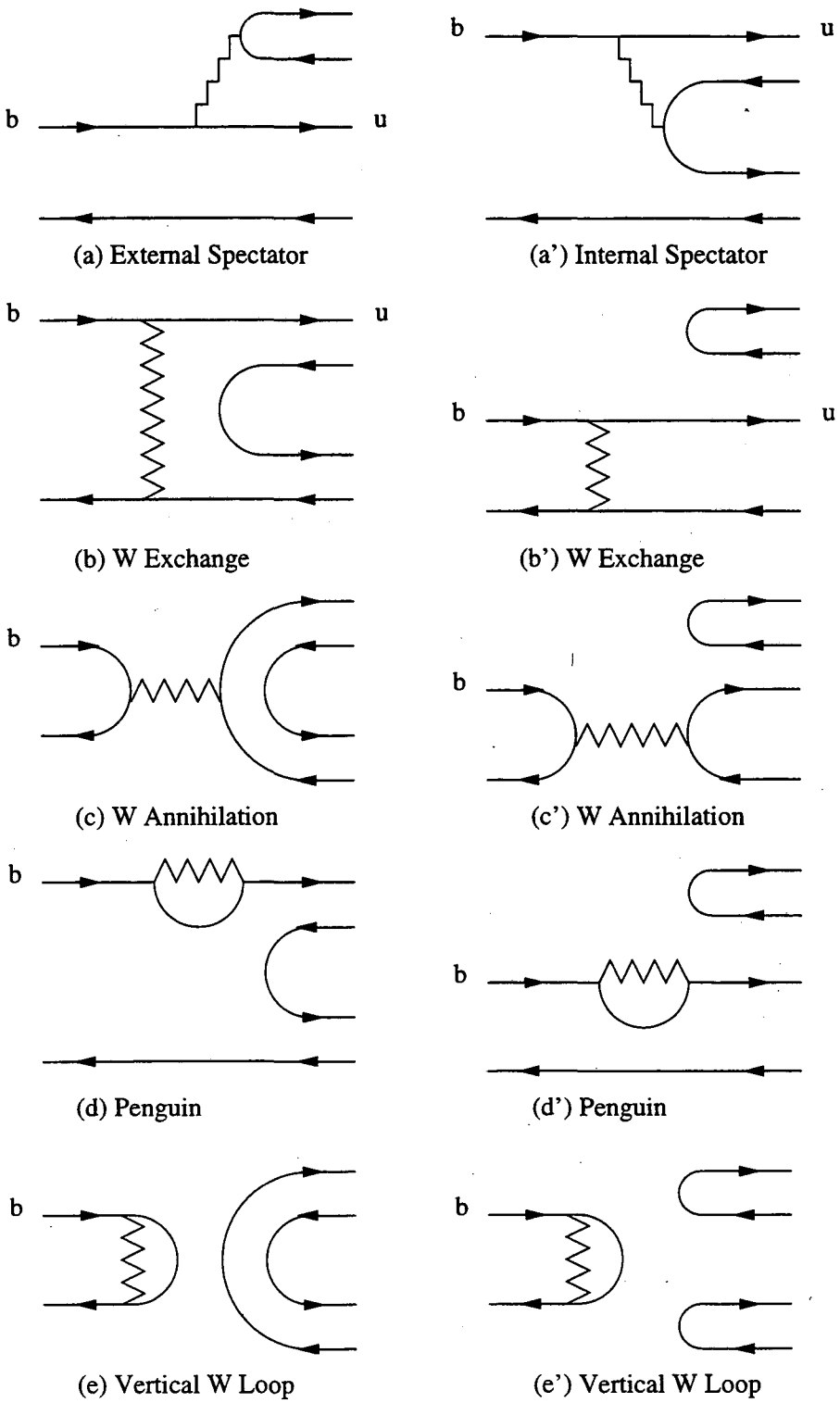

Figure 1.2: Quark diagrams for B decays to two mesons.

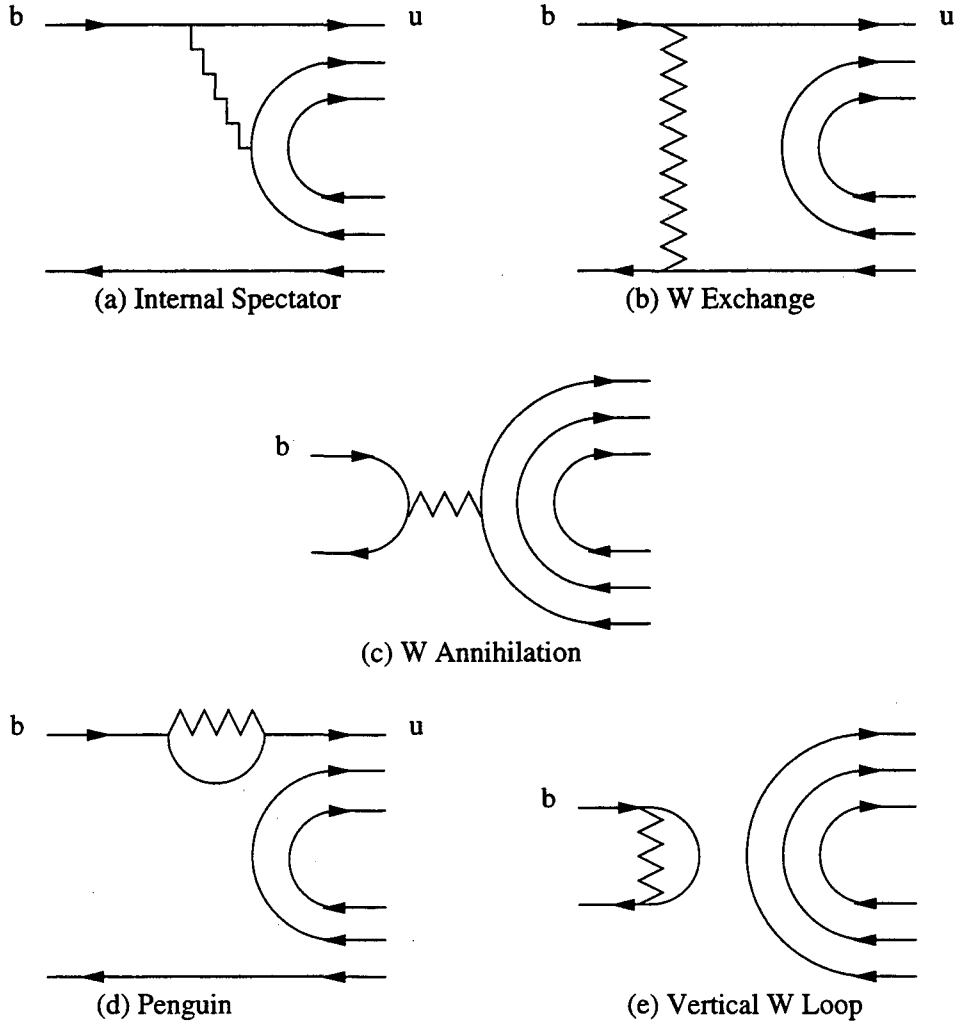

Figure 1.3: Quark diagrams for B decays to two baryons.

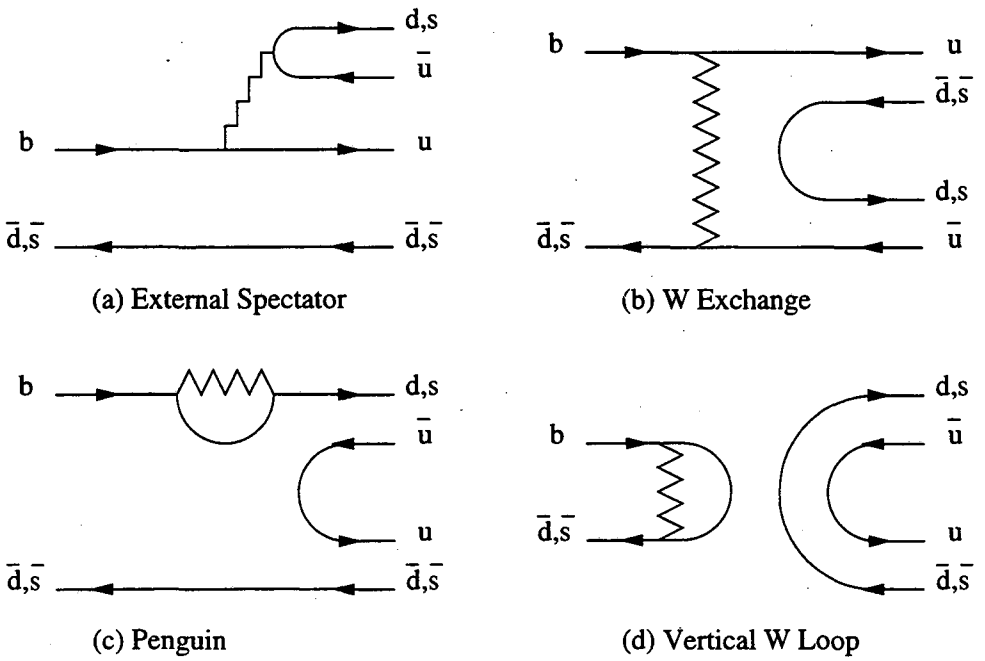

Figure 1.4: Quark diagrams for neutral B decays to two charged mesons.

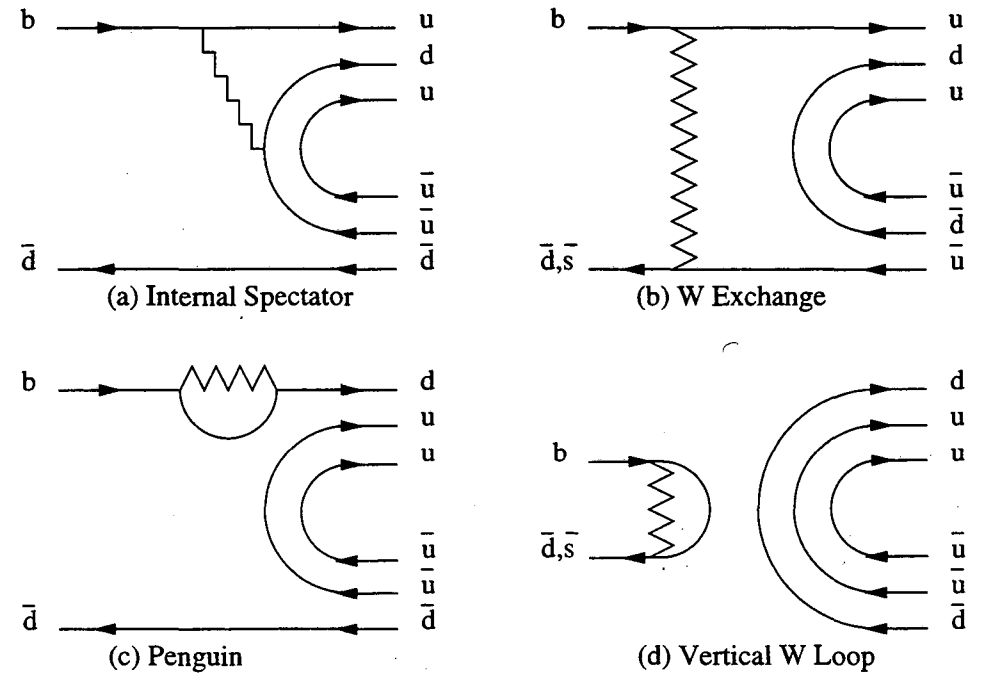

Figure 1.5: Quark diagrams for neutral B decays to two protons.

Transition Type	Decay Mode	Diagram			
		(a)	(b)	(d)	(e)
$\Delta C = 0$	$B_d^0 \to \pi^+\pi^-$	-1	-1	-1	-1
and	$B_d^0 \to K^+K^-$	0	-1	0	-1
$\Delta S = 0$	$B_s^0 \to \pi^+K^-$	-1	0	-1	0
$\Delta C = 0$	$B_d^0 \to K^+\pi^-$	-1	0	-1	0
and	$B_s^0 \to \pi^+\pi^-$	0	-1	0	-1
$\Delta S = 1$	$B_s^0 \to K^+K^-$	-1	-1	-1	-1

Table 1.1: Relative contributions of the various quark diagram to the B meson decay rate for selected modes.

W exchange and vertical W loop diagrams are suppressed, $\Gamma(B_d \to K^+K^-)$ and $\Gamma(B_s \to \pi^+\pi^-)$ are effectively zero when compared to the rates of the other processes [24].

The weighting factors multiplying the different diagrams in the amplitude for different neutral B to two charged meson processes are shown in Table 1.1 [24]. Note the separation into strangeness conserving ($\Delta S = 0$) and strangeness changing ($\Delta S = 1$) processes. Since processes within each group share common diagrams, the amplitudes for the processes can be related to each other. For example, the amplitude for $B_d \to \pi^+\pi^-$ should equal the sum of the amplitudes for $B_s \to K^+K^-$ and $B_s \to \pi^+K^-$. Similar relationships hold between the decays of the neutral B meson and the charged B meson [24]. By measuring the complete set of B decays to $\pi\pi$, πK and KK, it may be possible to determine the angles α and β in the CKM unitarity triangle shown in Figure 1.6 [24]. These angles, in turn, can be related to the CP violating phase, δ_{13} [13].

1.3.2 Theoretical Limits

There have been several theoretical calculations of the branching ratio of the B meson to two mesons [25, 23, 26, 19], all assume factorization holds. Several researchers have also looked into the branching ratio of B mesons to two baryons [27, 28, 29]. Table 1.2 lists a range of theoretical predictions for a selected set of B meson decay *channels* (or modes).

Sources of uncertainty in these theoretical calculations include uncertainty in the form-factors for the hadronic two body matrix elements, uncertainty in the effects of annihilation and penguin diagrams, effects of final state interactions, and renormalization group

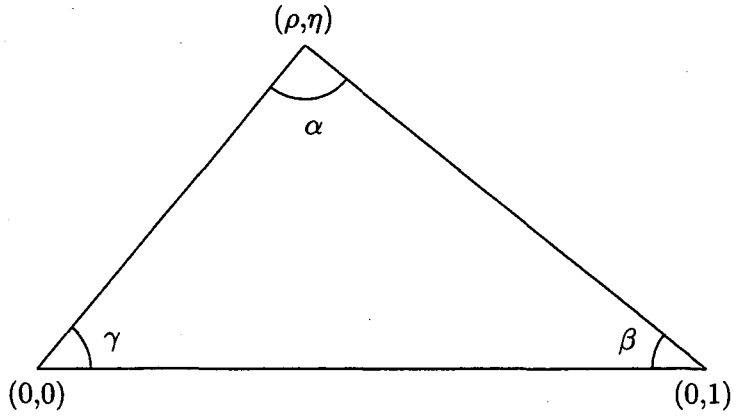

Figure 1.6: CKM unitarity triangle. ρ and η are the Wolfenstein parameters in the CKM matrix. (See equation 1.11.)

Decay Mode	BR $\times 10^{-5}$
$B_d^0 \to \pi^+\pi^-$	1.8 ± 0.8
$B_d^0 \to K^+\pi^-$	.65 – 2.4
$B_d^0 \to p\bar{p}$	0.74
$B_s^0 \to K^+K^-$	.57 – 2.1
$B_s^0 \to \pi^+K^-$	1.8 ± 0.8

Table 1.2: Theoretical limits on selected branching ratios.

effects on penguin diagrams [23]. From the measurement of the branching ratios, it should be possible to determine the importance of the penguins in the different decay channels, which is not well understood [23]. In addition, it may be possible to verify the correctness of the factorization procedure [26].

1.3.3 Current Experimental Limits

Several experiments have searched for charmless hadronic B decays in the channels of interest in this thesis. Some of the earliest measurements were made by ARGUS at DORIS II and by CLEO at CESR, the most recent results come from CLEO II at CESR and OPAL and DELPHI at LEP.

ARGUS

In 1990, the ARGUS collaboration at the DORIS II e^+e^- storage ring at DESY set an upper limit of $\mathrm{BR}(B^0_d \to \pi^+\pi^-) < 1.3 \times 10^{-4}$ [30]. The limit was obtained from the analysis of 214 pb^{-1} of data taken at the $\Upsilon(4s)$ resonance. The techniques used to isolate B events were very similar to the ones used by CLEO outlined below.

CLEO

The most conclusive searches for rare hadronic B decays in the channels studied in this thesis were made at the Cornell Electron Storage Ring (CESR) by the CLEO collaboration [31, 32]. In analyzing data from 2.6 million $B\overline{B}$ pairs produced at the $\Upsilon(4s)$ resonance, a branching fraction of $(1.8^{+0.6+0.2}_{-0.5-0.3} \pm 0.2) \times 10^{-5}$ for the sum of $B^0_d \to \pi^+\pi^-$ and $B^0_d \to K^+\pi^-$ was measured. Table 1.3 contains the upper limits at the 90% confidence level (CL) obtained by CLEO for the processes investigated in this thesis. The techniques used to isolate rare b decay events include the following: First, an energy-constrained identification of B mesons was made. In other words, the sum of the energies of the two daughters was required to equal the energy of the B meson, which in turn, was equal to the beam energy of 5.3 GeV. Second, a calculation of the beam-constrained mass was made to determine the invariant mass of the candidate B meson. Third, b events were isolated from background by utilizing differences in their respective event shapes. B decay products are distributed spherically in the lab frame, since the B is produced almost at rest and is spin zero. Also, candidate B's are produced uniformly in $\cos(\theta)$, where θ is the angle between the B candi-

Decay Mode	BR $\times 10^{-5}$
$B_d^0 \to \pi^+\pi^-$	< 2.0
$B_d^0 \to K^+\pi^-$	< 1.7
$B_d^0 \to K^+K^-$	< 0.4
$B_d^0 \to p\bar{p}$	< 3.4

Table 1.3: Experimental upper bounds for selected B meson decay modes from CLEO (90%CL).

date thrust axis and that of the remaining particles in the event. In contrast, non B events are peaked at $\cos(\theta) \approx \pm 1$. Finally, particle identification was obtained through dE/dx measurements.

OPAL

Operating at a different experimental environment from CLEO, the OPAL collaboration at LEP has also published upper limits for B_d to $\pi^+\pi^-$ and π^-K^+[33]. The use of Z decays as a source of B mesons also allowed the OPAL collaboration to set upper limits on the branching ratios for B_s to K^+K^- and π^+K^-. (The decay of the $\Upsilon(4s)$ to a B_s pair is not kinematically allowed.) A total of 1.92 million Z's, produced from the collision of e^+e^- at the Z resonance, were used in the analysis. In the analysis, four characteristics were used to isolate B events from background events. First, the momentum of the produced B hadrons was a substantial fraction of the beam momentum. That is, the fragmentation of b-quarks into B hadrons was *hard*. Second, decay products of the B meson were distributed isotropically in the rest frame of the B. In contrast, the combinatorial background was peaked in the forward and backward regions with respect to the hypothesized parent particle. Third, the opening angle between the two daughter hadrons of the B was smaller relative to the background. Finally, the long lifetime of the B meant that a detached decay vertex could be used to isolate B events from the background. Additional background reduction was achieved through the use of partial particle identification from dE/dx information. After the application of these cuts, no events were present above the expected background. The resulting 90% confidence level upper limits on the four branching ratios obtained at OPAL are shown in Table 1.4. Note that the results assume a $\Gamma(\mathrm{Z} \to b\bar{b})/\Gamma(\mathrm{Z} \to hadrons)$ decay

Decay Mode	BR $\times 10^{-5}$
$B_d^0 \to \pi^+\pi^-$	< 4.7
$B_d^0 \to K^+\pi^-$	< 8.1
$B_s^0 \to K^-\pi^+$	< 26
$B_s^0 \to K^+K^-$	< 14

Table 1.4: Experimental upper bounds for selected B meson decay modes from OPAL (90% CL).

Decay Mode	BR $\times 10^{-5}$
$B_d^0 \to \pi^+\pi^-$	< 5.5
$B_{d,s}^0 \to K^+\pi^-$	< 9
$B_{d,s}^0 \to K^+K^-$	< 12
$B_d^0 \to p\bar{p}$	< 35

Table 1.5: Experimental upper bounds for selected B meson decay modes from DELPHI (90% CL).

width ratio of 0.217 and a fragmentation ratio of b-quarks to B_d and B_s of 39.5% and 12% respectively.

DELPHI

Also operating at LEP, the DELPHI collaboration has looked for two body decays of the B meson [34] as well. An analysis of 1.7 million Z decays resulted in a single candidate event in the $B_{d,s}^0 \to K\pi$ channel with an estimated background of 0.29 ± 0.09 events. Upper limits at the 90% confidence level for other channels investigated by the DELPHI collaboration are shown in Table 1.5. In obtaining these upper limits, the DELPHI collaboration utilized techniques that were similar to those employed by the OPAL collaboration. This is no surprise given the similarities in experimental environments at the two experiments. In particular, DELPHI utilized detached secondary vertex, particle identification, and hard fragmentation cuts. In addition, a b-tagging algorithm and impact parameter cuts were used.

Source	$\sigma_{b\bar{b}}$ (nb)	$< b\bar{b}\ pairs >$ (per sec)	$\sigma_{b\bar{b}}/\sigma_T$
Υ(4s)	1.15	0.146	0.25
Z^0	7.0	0.0162	0.215
$p\bar{p}$	60000	694	8×10^{-4}
pN	5.7	10	4.5×10^{-7}

Table 1.6: Parameters for different B production environments.

1.4 B Production

The small branching ratios for rare hadronic b decays means that experiments searching for rare b decays must be carried out in an environment where a large number of b's are produced. There are currently four environments where b physics is carried out. In addition to the e^+e^- colliders at the $\Upsilon(4S)$ resonance (CLEO) and at the Z resonance (LEP) mentioned above, there are $p\bar{p}$ colliders (CDF and DØ), and fixed-target experiments (E771 and E789). The relevant figures of merit for these four environments are shown in Table 1.6. In order to produce a large number of b mesons, a large b production cross section, $\sigma_{b\bar{b}}$, is required as well as high luminosity. Table 1.6 shows the cross section at the various environments and the net $b\bar{b}$ production rate assuming typical luminosities seen at CLEO, LEP, DØ and E789. However, a high production rate is not a sufficient condition for a b experiment. If the total cross section, σ_T, is large relative to the b production cross section, then extracting the b events from the other non-b events may be difficult.

A significant fraction of the current knowledge of b physics has come from CLEO at CESR where the e^+e^- center of mass energy is at the mass of the $\Upsilon(4S)$. At this energy, an e^+e^- pair combines to form a virtual photon that can decay into a $b\bar{b}$ pair. The $b\bar{b}$ pair can then combine to form an $\Upsilon(4S)$ meson, a $b\bar{b}$ bound state. Being just above the threshold for decay into a B meson and its charge conjugate, the $\Upsilon(4S)$ is assumed to decay predominantly into two B mesons. As can be seen from the $\sigma_{b\bar{b}}/\sigma_T$ ratio in Table 1.6, CLEO benefits from an extremely clean experimental environment. However, b physics at CESR suffers from the following drawbacks:

- Small production rate due to low luminosity.
- No B_s and Λ_b production.

- Very short b-hadron decay length due to the low momentum of the b-hadron.

At the Z resonance some of the problems associated with b production at the $\Upsilon(4S)$ can be eliminated. However, it does have its own set of drawbacks. The majority of b physics results at the e^+e^- colliders at the Z come from experiments at LEP, most notably ALEPH, DELPHI and OPAL. At the Z resonance, an e^+e^- pair combines to form a Z that can subsequently decay into a $b\bar{b}$ quark pair, which then fragments into b-hadrons. The conditions at the Z resonance are similar to the conditions at the $\Upsilon(4S)$ resonance in that the signal to noise ratio (S/N) is large. (See Table 1.6.) An additional benefit at the Z resonance is that the b-hadrons are produced with a significant boost, resulting in an average decay length of 2.7 mm. This is in contrast to a 27 μm decay length at the $\Upsilon(4S)$ [35]. The long decay length allows the use of a detached vertex (i.e., a decay vertex spatially separate from the production vertex) to isolate b decay events from other events. Another benefit at the Z is that B_s and Λ_b hadrons can also be produced. Despite its advantages, the present generation of e^+e^- colliders at the Z suffer from the same low production rate that are characteristic of e^+e^- colliders at the $\Upsilon(4S)$ resonance.

If the production rate of $b\bar{b}$ was the sole criterion for choosing an environment for conducting b physics, $p\bar{p}$ colliders would be the overwhelming choice. At the Tevatron, where the center of mass energy is 1.8 TeV, the $b\bar{b}$ production rate is enormous (See Table 1.6). However, the signal to noise ratio is dismal in comparison to e^+e^- colliders. Thus hadron collider experiments, like CDF and DØ, need trigger systems that can isolate $b\bar{b}$ events from other *minimum bias* events. In addition to the poor S/N ratio, a large fraction of b-quarks are produced at small angles with respect to the beam line and thus either escape the detector or are difficult to extract from the beam remnants.

The final environment for doing b physics is at a fixed target experiment, which is where the data used in this analysis was collected. As can be seen from Table 1.6, the cross section for b production is fairly low. However, the high effective luminosity, the result of using high density targets, translates to high b production rates. The major problem with b physics in a fixed target environment is the extremely poor S/N ratio.

1.4.1 Hadronic b-Hadron Production

Theoretically, the production of b-hadrons in hadron collisions is believed to be *factorizable* into a *hard* QCD parton scattering process and *soft* QCD initial and final state

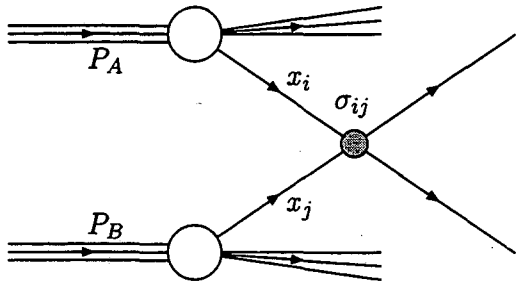

Figure 1.7: Hadro - production of b-quarks.

processes [36]. The hard QCD process involves short distance (high energy) interactions between the gluon and quark (anti-quark) constituents of the colliding hadrons that result in the production of a $b\bar{b}$ quark pair, as shown in Figure 1.7. Since this process involves short distances, perturbative QCD can be used. The soft QCD processes are the long distance (low energy) interactions that control the hadronization of the $b\bar{b}$ pair created from the hard process into b-hadrons.

Mathematically, the production cross section for $b\bar{b}$ pairs in hadron collisions can be written in the following form:

$$\sigma(s) = \sum_{i,j} \int dx_1 dx_2 \hat{\sigma}_{ij}(x_1 P_A, x_2 P_B, m^2, \mu^2) F_i^A(x_1, \mu) F_j^B(x_2, \mu) \tag{1.16}$$

where x_1 and x_2 are, respectively, the fraction of the parent hadron momentum carried by parton i and j, $\hat{\sigma}_{ij}$ is the cross section of the hard scattering between parton i and j, F_i^A and F_j^B are the number densities of partons i and j in hadron A and B, m is the mass of the b-quark, and μ (of the order of m) is the renormalization and factorization scale of the interaction [36].

Parton Subprocesses

The leading order (LO) Feynman diagrams for the parton process involve quark–anti-quark interactions and gluon–gluon (or gluon fusion) interactions. These processes are shown in Figures 1.8 and 1.9 respectively. Current theoretical calculations of the cross section for hadroproduction of b-quarks include next-to-leading order (NLO) interactions involving gluon "bremstrehlung" [36]. Figure 1.10 and 1.11 are examples of the NLO diagrams.

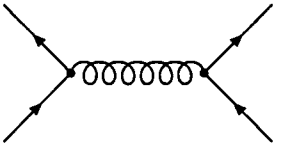

Figure 1.8: Quark – anti-quark diagram.

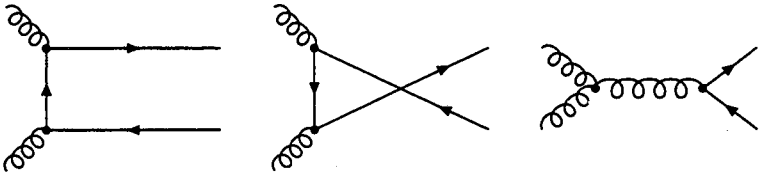

Figure 1.9: Gluon – gluon fusion diagrams.

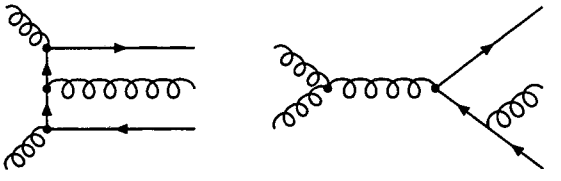

Figure 1.10: NLO diagrams with a real gluon.

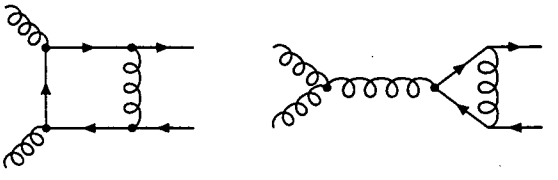

Figure 1.11: NLO diagrams with a virtual gluon.

B Production Characteristics

From the NLO calculations, it is possible to get an understanding of the kinematics of B mesons that are produced at a fixed target environment. Shown in Figures 1.12, 1.13, and 1.14 are, respectively, the distributions of the transverse momentum in the laboratory frame (P_t), the distribution of the Feynman X (X_F), and the energy distribution of the b hadrons generated from the interaction of a stationary proton with an 800 GeV/c proton. In the center of mass system with energy $\sqrt{S}$, X_F is defined as $P_{\|}/P_{MAX}$, where $P_{MAX} \approx \sqrt{S}/2$ and is the maximum possible momentum of the b-hadron and $P_{\|}$ is the momentum of the b-hadron parallel to the direction of the incident proton beam. At E789, where the proton beam energy is 800 GeV, $P_{MAX} = 19.37$ GeV/c.

The high energy of the b-hadron results in a long decay length for the b-hadron. For a lifetime of 1.57 ps [37], the current world average, the average longitudinal and transverse decay lengths are approximately 1.22 cm and 0.0258 cm at E789. Figures 1.15 and 1.16 show the longitudinal and transverse position of the decay vertex respectively. The distribution of the transverse position vs. longitudinal (Z) position of the decay vertex is shown in Figure 1.17. Note that these distributions were generated with the assumption of production at a point.

In the following chapters, the search for charmless dihadron decays of b-hadrons at E789 is discussed in detail. Chapter 2 discusses the E789 spectrometer and provides some information about the running conditions. Chapter 3 contains a detailed discussion of the steps taken to extract the information needed to place an upper limits on the branching ratios. It documents the event reconstruction algorithm, Monte Carlo simulation of the experiment, the event selection criteria, the procedure for determining the event acceptance and efficiency, and the procedure for determining the systematic errors. Finally, Chapter 4 consolidates the results of the analysis, presents the procedure for determining the upper limits on the branching ratios and gives the upper limits at the 90% confidence limit that were obtained for the various decay modes.

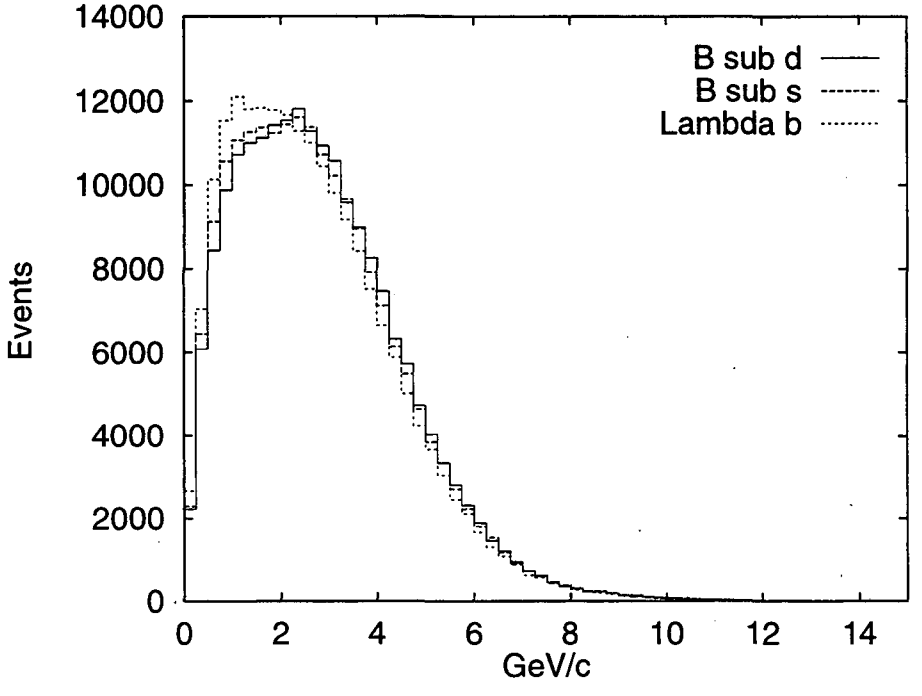

Figure 1.12: Center-of-mass P_t spectrum for B_d, B_s, and Λ_b hadrons produced in the interaction of 800 GeV protons with a fixed target (Monte Carlo).

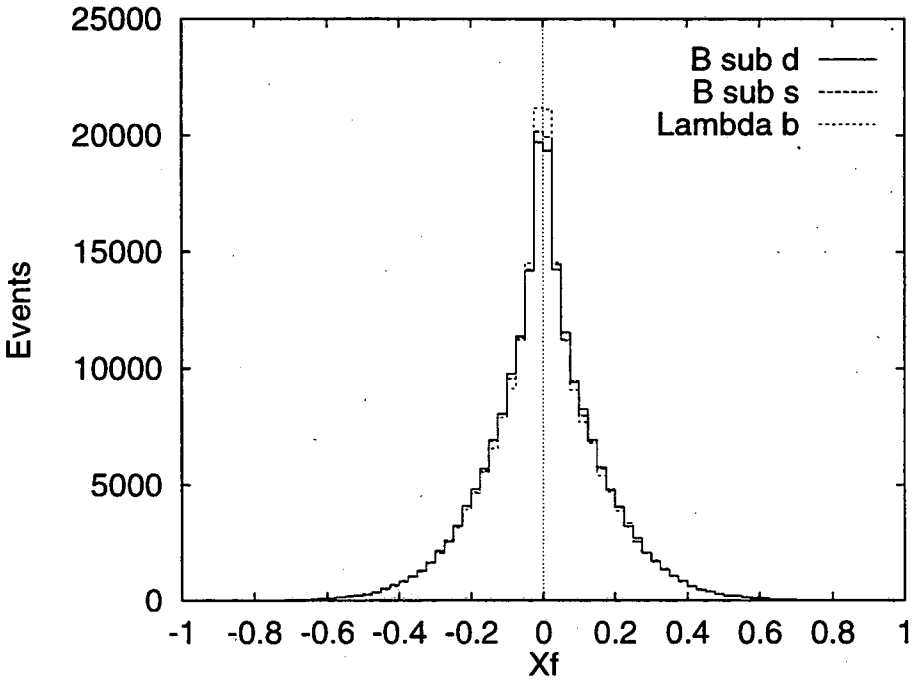

Figure 1.13: Center-of-mass X_F spectrum for B_d, B_s, and Λ_b hadrons produced in the interaction of 800 GeV protons with a fixed target (Monte Carlo).

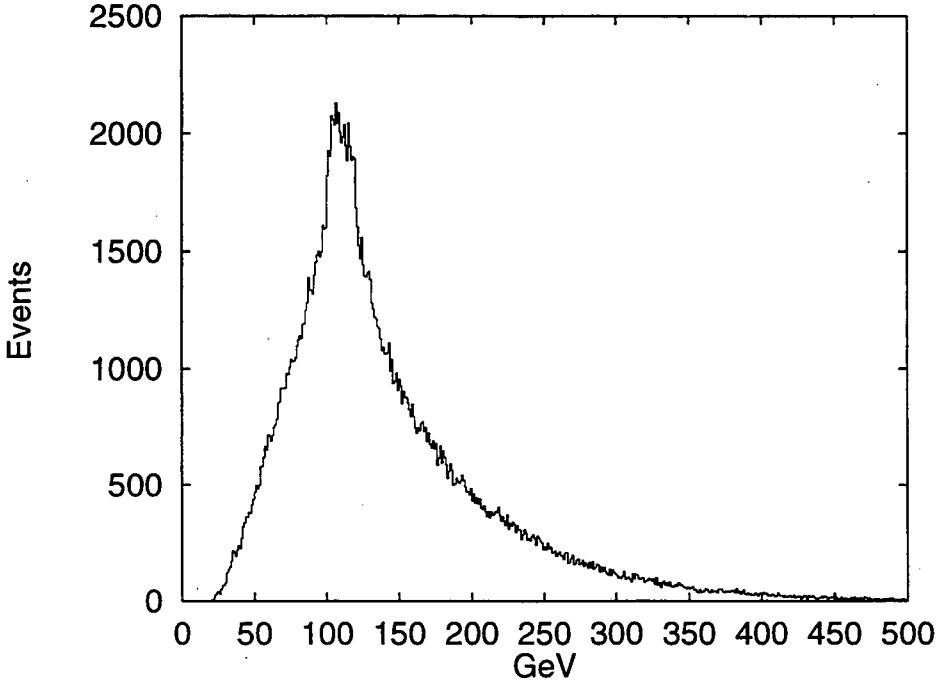

Figure 1.14: Laboratory frame energy spectrum of B_d mesons produced in the interaction of 800 GeV protons with a fixed target (Monte Carlo).

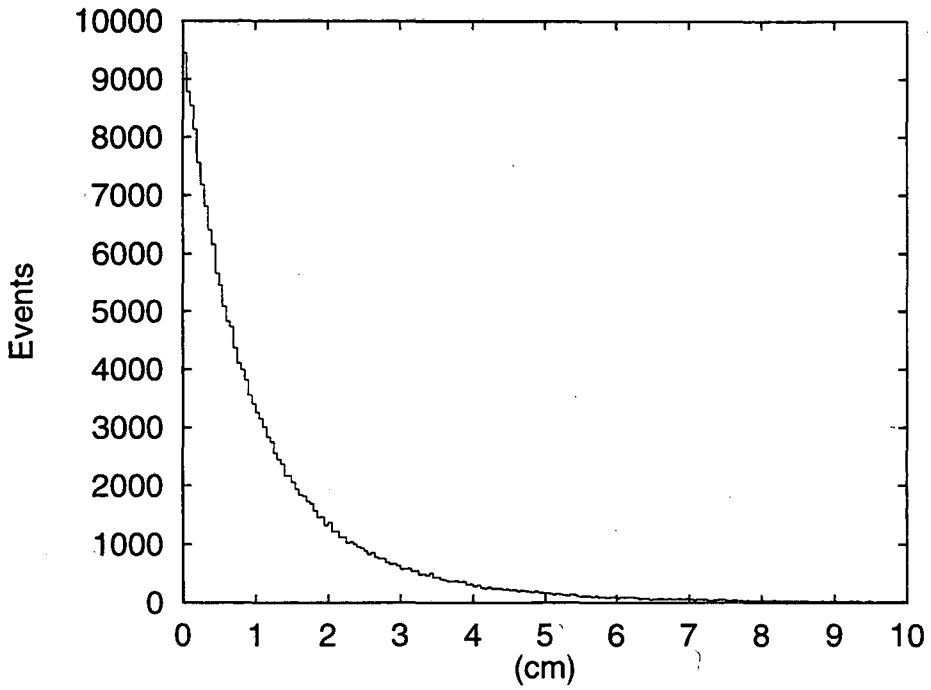

Figure 1.15: Z position of the decay vertex of B_d mesons produced in the interaction of 800 GeV protons with a fixed target (Monte Carlo).

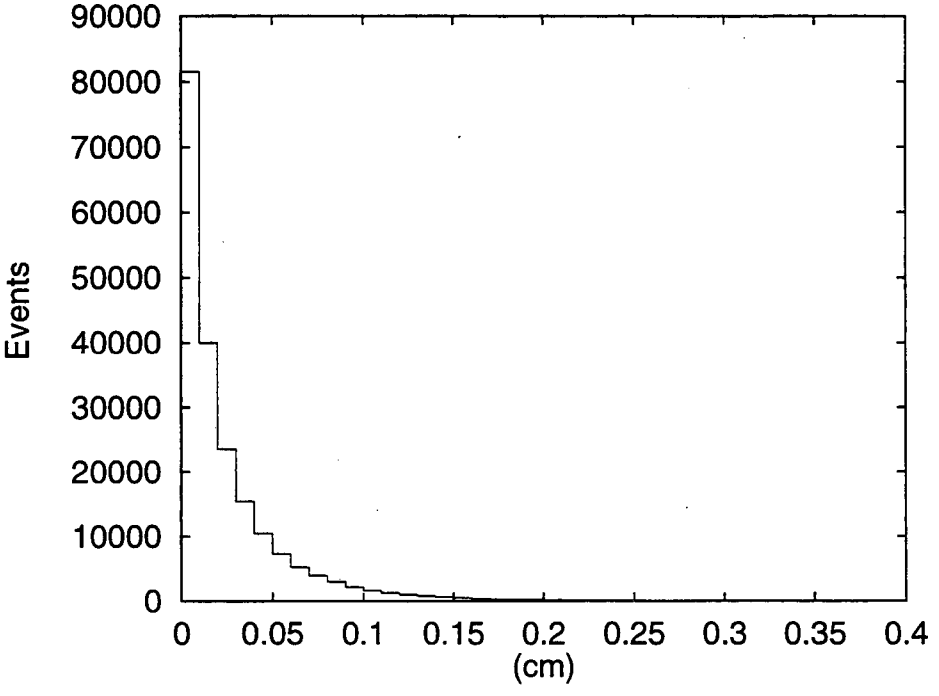

Figure 1.16: Transverse position of the decay vertex of B_d mesons produced in the interaction of 800 GeV protons with a fixed target (Monte Carlo).

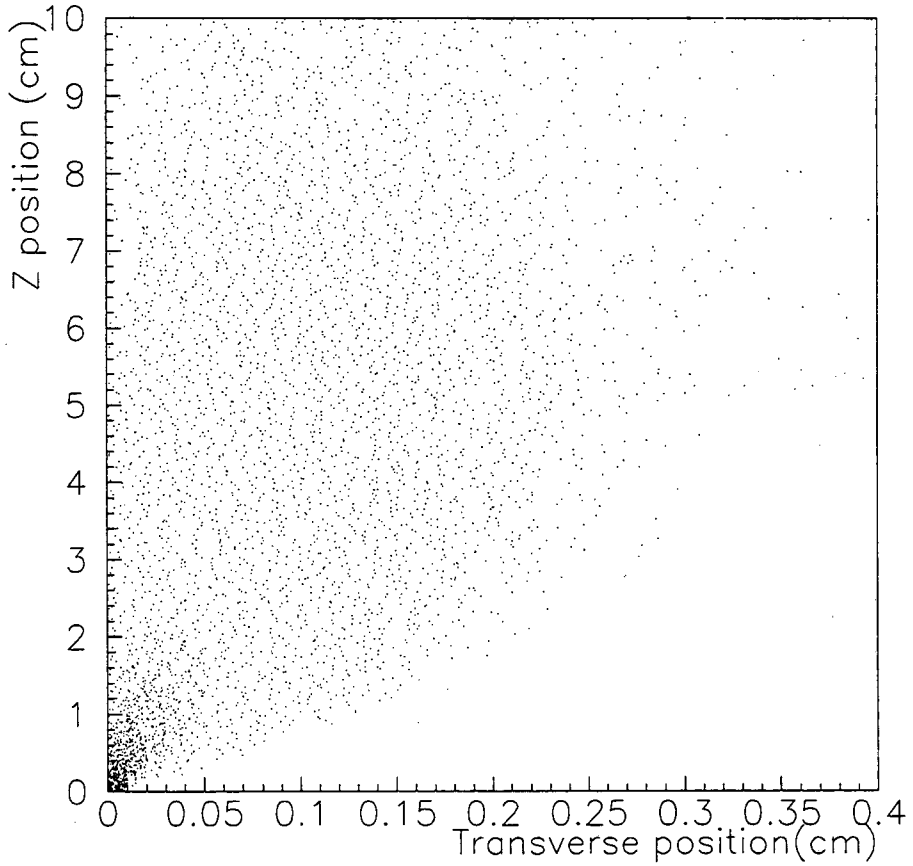

Figure 1.17: Z position versus transverse position of the decay vertex of B_d mesons produced in the interaction of 800 GeV protons with a fixed target (Monte Carlo).

Chapter 2

Experiment

2.1 Overview

The data used in this analysis was collected at the E789 fixed target experiment at Fermilab. In the experiment, b-hadrons were produced in the interaction of an 800 GeV/c proton beam with a gold (Au) target. The decay products of the produced b-hadrons were then tracked by detector planes in the E789 spectrometer. In order to describe the spectrometer, it is necessary to define a reference coordinate system so that the position and orientation of the different components of the spectrometer can be discussed. The standard E789 coordinate system consists of a right-handed coordinate system centered at the nominal location where the incident proton beam intersects the plane defined by the front face of the first spectrometer magnet (SM12) (See section 2.4.4). The Z axis is in the direction of the incident proton beam and the Y axis is defined to point vertically upward. Finally, the X axis is defined to point horizontally, completing the right-handed coordinate system.

2.2 Proton Source

The 800 GeV/c protons used in the experiment were provided by the Tevatron accelerator at Fermilab. The accelerator delivered these high energy protons in 1 ns long bunches called *buckets* that, at E789, contained on the order of 20 protons. The arrival time between buckets was $\sim$ 19 ns, which corresponds to the 53.1 MHz RF frequency of the accelerator. The stream of proton buckets provided by the accelerator was not

continuous; instead, it was broken up into spills that arrived approximately every 60 seconds (corresponding to the time required to accelerate the protons up to 800 GeV/c and the spill duration). The duration of each spill was approximately 23 seconds. When combined with the average occupancy per bucket and the inter-bucket period, approximately 2×10^{10} protons per spill were delivered to the experiment during the b-physics run.

2.3 Target Structure

The target used in the b-run was a gold strip 3 mm long (ΔZ), 200 μm high (ΔY) and 5 cm wide (ΔX). This meant that the interaction vertices were highly localized in Z (along the beam direction) and Y (transverse to the beam direction) position. Since the height of the target was smaller than the width (in Y) of the beam, the alignment of the beam was constantly monitored. (See section 2.4.1.) The alignment procedure is outlined in reference [38].

The target was located at $Z = -331.8$ cm and was contained in a vacuum box that extended 28 cm downstream of the target. This allowed the association of any downstream vertices with particle decays as opposed to particle interactions. A 3 mil thick titanium window separated the vacuum in the box from the rest of the spectrometer.

2.4 Spectrometer

The E789 spectrometer is a spectrometer that was designed primarily to study two body decays. Its most unique feature was its adjustable acceptance. By suitably setting the current in one of the magnets in the spectrometer, particles within a selected momentum range were accepted by the spectrometer. Thus, the acceptance could be tuned to the mass of the decaying particle being studied. (Because of this feature, this type of detector is sometimes referred to as a "mass focusing" spectrometer.)

The spectrometer, shown in Figure 2.1, consists of the following components :

- beam monitor
- silicon micro-vertex detector
- acceptance-control magnet (SM12)

- beam dump
- upstream tracking station
- momentum analysis magnet (SM3)
- downstream tracking stations
- ring imaging Čerenkov counter (RICH)
- electromagnetic calorimeter
- hadronic calorimeter
- muon detector

Some of these components were inherited from E605 and E772 which were predecessors to E789, others were specifically designed for this experiment.

2.4.1 Beam Monitor

The beam monitors in the E789 spectrometer consisted of an ion chamber (ME3IC), a secondary emission monitor (SEM3), and an interaction monitor (AMON). ME3IC and SEM3 were used to measure the intensity of the proton beam. Two different types of intensity monitors were required because the beam intensity used by E789 fell near the non-linear range of ME3IC but near the bottom of the sensitivity range of SEM3. The interaction monitor, a stack of lead and scintillator planes that viewed the target at 90 degrees relative to the beam line in the X-Z plane, monitored the fraction of the beam that interacted with the target [39, 40, 41].

A constant *targeting fraction*, that is the fraction of the proton beam interacting with the target, was achieved by monitoring the ratio of the count rates of AMON and ME3IC. (Recall that the target was thinner in Y than the height of the beam.) To determine the absolute targeting fraction a *target scan* was performed. In this procedure, the target was moved vertically in Y in 200 μm steps, corresponding to the height of the target. The ratio of AMON vs. ME3IC was measured at each step. With the data collected from the target scan, the instantaneous targeting fraction during normal running could be determined with equation 2.1.

$$\text{Targeting Fraction at time } t = \frac{1}{N}\frac{\text{AMON}(t)}{\text{ME3IC}(t)} \tag{2.1}$$

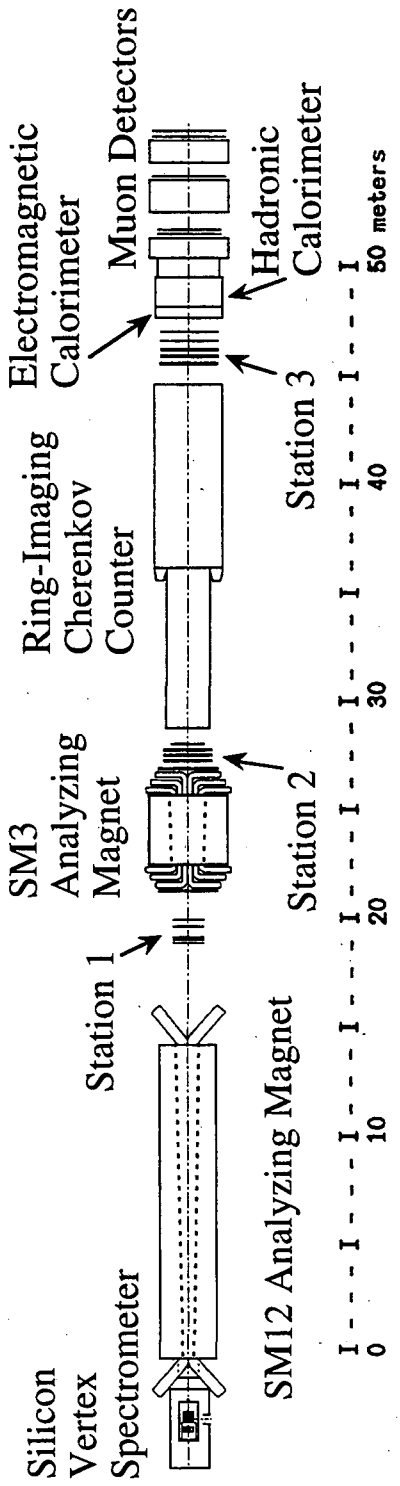

Figure 2.1: E789 spectrometer.

where

$$N = \sum_i \frac{\mathrm{AMON}_i}{\mathrm{ME3IC}_i} \tag{2.2}$$

and where AMON(t) and ME3IC(t) are the AMON and ME3IC counts at time t and AMON_i and $\mathrm{ME3IC}_i$ are the counts from AMON and ME3IC at step i in the target scan. By averaging over three target scans, the factor $\frac{1}{N}$ was determined to be [38] :

$$\frac{1}{N} = (4.074 \pm 0.172) \tag{2.3}$$

The SEM determined absolute beam intensity by measuring the number of δ rays produced by the interaction of the monitor with the proton beam. The calibration of the SEM was accomplished through the following steps. First, a copper foil was placed in the beam line. The copper foil and the SEM were then exposed to the proton beam. The SEM output was integrated over the exposure time. Next, the foil was removed and the amount of ^{24}Na created in the foil by the proton beam was determined by measuring the rate of ^{24}Na decay in the foil. Given the cross-section for the production of ^{24}Na by protons on copper and the number of created ^{24}Na atoms, the absolute flux of protons was determined. This was then compared with the integrated output of the SEM, giving a calibration of 1 SEM count = $(.80 \pm .04) \times 10^8$ protons [42].

In addition to ME3IC, AMON and SEM3, a segmented wire ion chamber (SWIC) was used to monitor the beam position and profile. However, the SWIC was removed from the beam line during data taking to reduce the background.

2.4.2 Silicon Micro-Vertex Detector

One new addition to the spectrometer was the silicon micro-vertex detector. Located just behind the target, it consisted of 16 planes of 50 micron-pitch silicon micro-strip detectors and two scintillators. The 16 planes were divided into two groups of 8, the first group located in the "upper" arm of the spectrometer (above the beam line) and the second group located in the "lower" arm of the spectrometer (below the beam line). Located behind each of these two arms was a scintillator, designated S_U and S_D for (S)cintillator (U)p and (S)cintillator (D)own. Each scintillator covered an area of 5.08 cm $\times$ 5.08 cm and was 1 mm thick. The scintillators were used to provide a fast trigger to indicate the presence (or absence) of a charged particle(s) passing through the upper or lower arm of the micro-vertex detector.

Plane No.	Plane Name	Z Position (cm)	Y Position (cm)	Plane View	Arm	Number of Strips
1	Y1B	-294.54	-2.125	Y	Lower	316
2	Y1T	-291.36	0.949	Y	Upper	316
3	U2B	-286.92	-2.300	U	Lower	372
4	U2T	-283.74	1.066	U	Upper	372
5	Y3B	-279.30	-2.758	Y	Lower	436
6	Y3T	-276.12	1.548	Y	Upper	436
7	V4B	-271.68	-2.865	V	Lower	500
8	V4T	-268.50	1.721	V	Upper	500
9	Y5B	-264.07	-3.364	Y	Lower	572
10	Y5T	-260.88	2.217	Y	Upper	572
11	U6B	-256.44	-3.566	U	Lower	628
12	U6T	-253.26	2.289	U	Upper	628
13	Y7B	-248.82	-4.018	Y	Lower	692
14	Y7T	-245.64	2.805	Y	Upper	692
15	V8B	-241.20	-4.154	V	Lower	756
16	V8T	-238.02	2.925	V	Upper	756

Table 2.1: Information about the detector planes in the Silicon Micro-Vertex detector.

Each silicon plane in the micro-vertex detector had an active area of 5 cm $\times$ 5 cm and was 300 microns thick. The planes were located from 37 cm to 94 cm downstream of the target, covering an angular region of 20 mr to 60 mr above and below the beam-line in the Y-Z plane. The planes were cooled to $10°C$ by helium gas to reduce the leakage current in the detectors that resulted from the accumulated effects of radiation damage that occurred during the course of the run. Each silicon plane was oriented in one of the three directions, Y, U, or V, where the strips were oriented 0 degrees, +5 degrees and -5 degrees from horizontal, respectively [43]. Table 2.1 gives additional information about the micro-vertex detector.

2.4.3 Beam Dump

Located downstream of the silicon micro-vertex detector and inside of the magnetic volume of SM12 was the beam dump. The beam dump was designed to absorb non-interacting protons and low P_t (transverse momentum) particles generated in the proton-target interaction. It consisted of a water cooled block of copper shaped to allow the decay

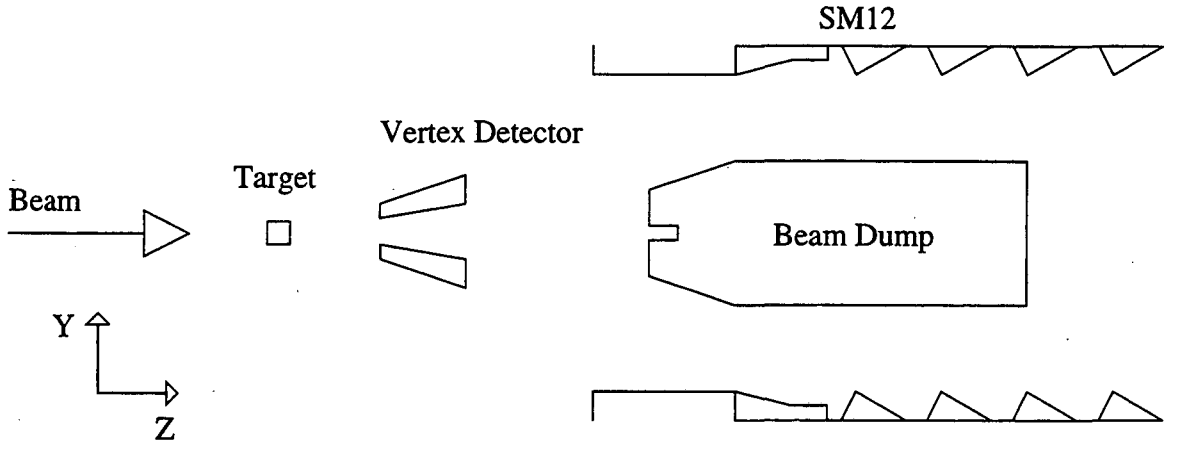

Figure 2.2: Schematic of the region around the target, SM12 and beam dump.

particles of interest to travel above or below the dump (See Figure 2.2.) The front face of the dump was located at Z = 172.72 cm and its middle was located at Z = 439.5 cm. The dump extended across the entire horizontal aperture of the SM12 magnet (discussed in section 2.4.4). Although it was 4.27 m long, a 30.5 cm recession in the front face of the block left only about 4 m or 26.5 interaction lengths separating the beam from the rest of the spectrometer [40]. Finally, because of some settling of the foundation of the dump, the center-line of the dump was located 6.3 mm ($\frac{1}{4}$ in.) below the beam line.

2.4.4 SM12 Magnet

Surrounding the beam dump was the principle bend magnet, SM12, which was designed to control the acceptance of the spectrometer. The magnet was a conventional dipole magnet measuring 14.5 meters long and weighing 1200 tons. It was wedge shaped and had an upstream aperture of 15.2 cm × 102.9 cm and a downstream aperture of 86.4 cm × 120.7 cm. It was capable of generating a horizontal field up to 1.3 T when run with the maximum current of 4000 A. At this field intensity, charged particles were given a P_t kick of 7 GeV/c [40]. With the beam dump positioned in the middle of the volume of SM12, only charged particles within a select transverse and longitudinal momentum range traversed the length of SM12. Figures 2.3, 2.4 and 2.5 show the geometric acceptance of the spectrometer for the various modes of interest (see equations 1.12, 1.13 and 1.14) as a function of the SM12 magnet current. During the *b*-run, the current was set at 1500 A which translated to a P_t kick of 2.6 GeV/c. This value was a compromise between good $B \rightarrow J/\psi \rightarrow \mu^+\mu^-$

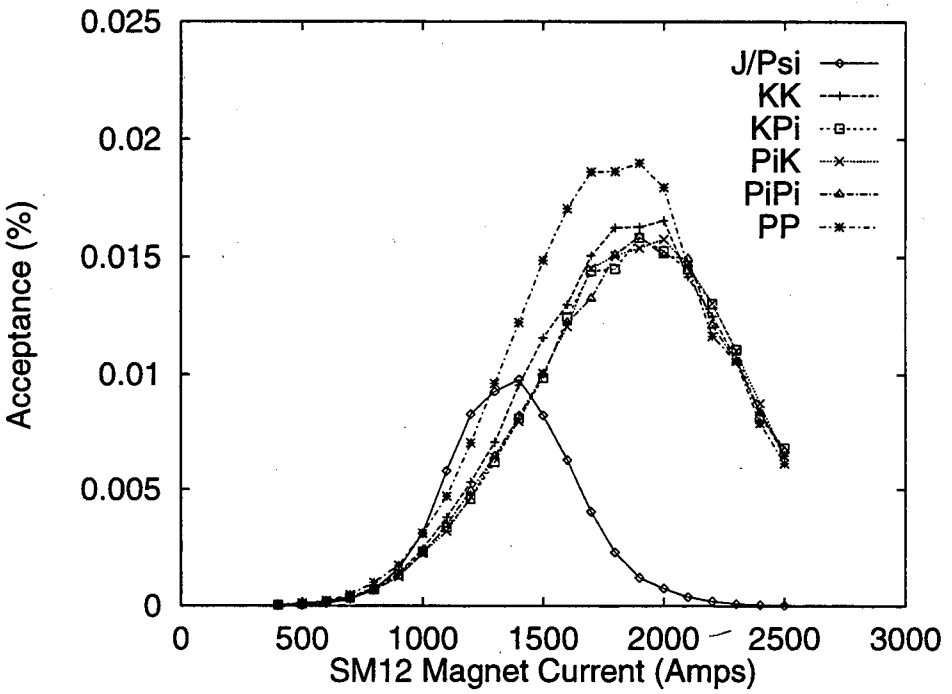

Figure 2.3: Acceptance of the spectrometer for various B_d decays as a function of SM12 current.

acceptance and good $B \to h^+h^-$ acceptance.

In order to reduce multiple scattering, the magnet volume was filled with helium gas. However, due to cracks in the magnet, it was estimated that a substantial fraction of the helium leaked out. A further attempt to reduce multiple scattering in the spectrometer was made by filling the space between SM12 and the first tracking station (See section 2.4.5) with helium contained in a poly-vinyl chloride bag.

2.4.5 Tracking Stations

The charged particles within the acceptance of SM12 were tracked with hodoscopes and wire chambers located downstream of SM12. These hodoscopes and wire chambers were grouped into three tracking stations labeled 1, 2, and 3. Each station consisted of a set of closely spaced hodoscope planes and drift chambers. Stations 1 and 2 were positioned just upstream and downstream of the analysis magnet, SM3. Station 3 was positioned between the RICH and the calorimeters.

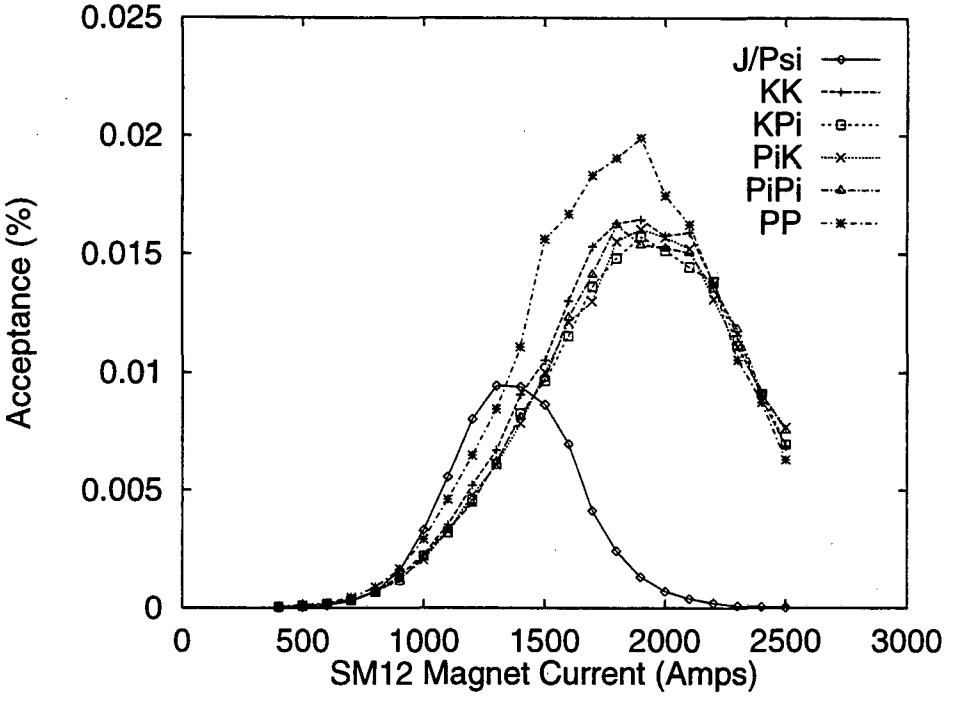

Figure 2.4: Acceptance of the spectrometer for various B_s decays as a function of SM12 current.

Hodoscopes

Tracking stations 1 and 3 each contained a pair of hodoscope planes. Each plane in the pair was tiled by hodoscope paddles in an N × M pattern. The N designates the number of paddles along the X direction and M designates the number of paddles along the Y direction. The planes can be grouped into two categories, 2 × M and N × 2 planes. The 2 × M planes were referred to as "Y" planes since they had finer Y resolution than X resolution. Conversely, the N × 2 planes were called "X" planes. Unlike the other tracking stations, station 2 possessed only a single Y hodoscope plane. Table 2.2 gives more detailed information about the hodoscopes in each tracking station. The names of the hodoscope planes are given as HXn or HYn where n denotes the tracking station and X or Y denotes the plane type. (Note that the standard E789 name for these hodoscope planes do not contain the H prefix. The H prefix was added in this description to avoid confusion with the drift chamber planes.) Hodoscope planes HY4 and HX4 constituted part of the muon detector (see section 2.4.9).

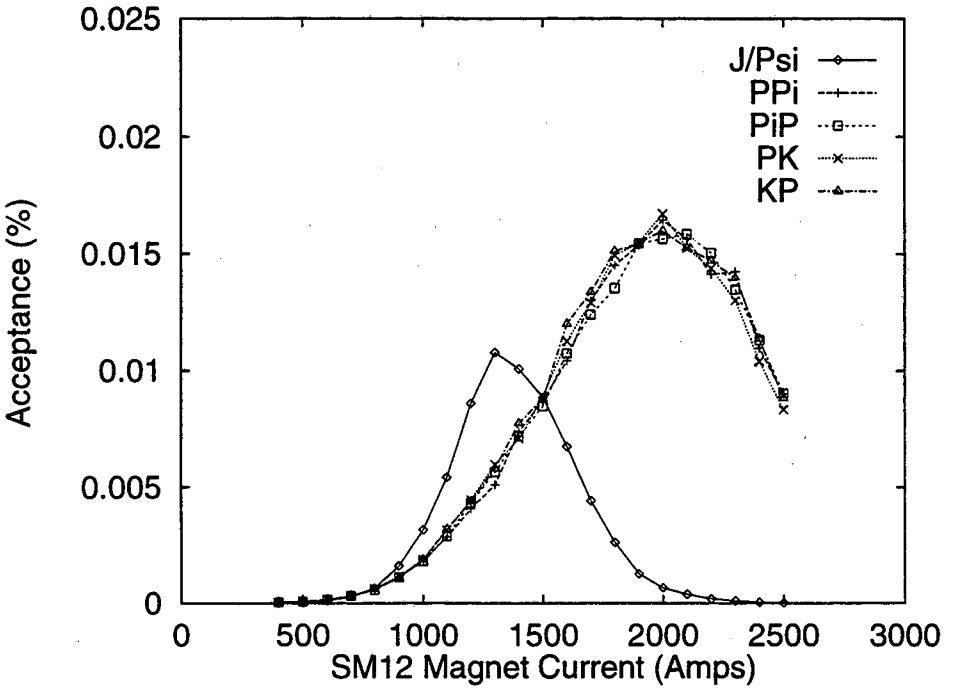

Figure 2.5: Acceptance of the spectrometer for various Λ_b decays as a function of SM12 current.

Plane Name	Z Position (cm)	Plane View	Number Counters	Aperture	
				X (cm)	Y (cm)
HX1	1959.61	X	12x2	120.75	76.20
HY1	1995.80	Y	2x12	120.35	77.95
HY2	2831.95	Y	2x16	163.83	123.51
HX3	4627.88	X	12x2	267.16	233.68
HY3	4653.28	Y	2x13	264.16	233.68
HY4	5170.17	Y	2x14	294.64	254.00
HX4	5413.04	X	16x2	320.04	289.56

Table 2.2: Information about the hodoscope planes.

Plane Name	Z Position (cm)	Plane View	Number of wire	Wire Spacing (cm)
V1	1879.8	V	208	0.508
V1′	1885.0	V	208	0.508
Y1	1904.5	Y	160	0.508
Y1′	1909.7	Y	160	0.508
U1	1930.3	U	208	0.508
U1′	1935.5	U	208	0.508

Table 2.3: Information about the drift chambers in station one.

Wire Chambers

In addition to the hodoscope planes, each station contained 6 planes of drift chambers. These 6 planes were divided into 3 pairs with each pair oriented in a different direction, e.g., V1–V1′. The wires within a pair of planes, however, were oriented in the same directions. The plane pairs that contained wires parallel to the X axis were labeled as Y planes. The other two plane pairs contained wires that were rotated by 14 degrees (U planes) and -14 degrees (V planes) about the Z axis with respect to the wires in the Y planes. See equation 2.4 for the exact definition of the U and V unit vectors. Note that the U and V planes (or views) of the wire chambers do NOT coincide with the U and V views in the silicon micro-vertex detector.

$$\begin{aligned} \hat{\mathbf{u}} &= \cos(\theta)\hat{\mathbf{y}} - \sin(\theta)\hat{\mathbf{x}} \\ \hat{\mathbf{v}} &= \cos(\theta)\hat{\mathbf{y}} + \sin(\theta)\hat{\mathbf{x}} \\ \text{where } \theta &= \tan^{-1}(\frac{1}{4}) \end{aligned} \tag{2.4}$$

The sense wires, and hence the chamber "cells", in the paired planes were offset by half a cell to resolve the left-right ambiguity problem. The drift chambers were filled with a $50\% - 50\%$ mixture of argon and ethane that was bubbled through ethanol at 27°F. The aperture of the drift chambers in stations 1, 2 and 3 were 119.4 cm × 81.3 cm, 167.6 cm × 130.0 cm and 269.6 cm × 242.6 cm respectively [38]. Additional information about the drift chambers in these tracking stations are tabulated in Tables 2.3, 2.4 and 2.5.

Plane Name	Z Position (cm)	Plane View	Number of wire	Wire Spacing (cm)
V2	2751.8	V	160	0.986
V2′	2757.2	V	160	0.986
Y2	2776.8	Y	128	1.106
Y2′	2782.1	Y	128	1.106
U2	2802.3	U	160	0.986
U2′	2807.6	U	160	0.986

Table 2.4: Information about the drift chambers in station two.

Plane Name	Z Position (cm)	Plane View	Number of wire	Wire Spacing (cm)
V3	4546.8	V	144	2.021
V3′	4553.8	V	144	2.021
Y3	4572.5	Y	112	2.083
Y3′	4579.5	Y	112	2.083
U3	4598.0	U	144	2.021
U3′	4605.0	U	144	2.021

Table 2.5: Information about the drift chambers in station three.

2.4.6 SM3 Analysis Magnet

SM3 was the primary momentum analysis magnet. Located at $Z = 25.5$ m, between tracking stations 1 and 2, its purpose was to determine the momentum of charged particles passing through the spectrometer. It provided a P_t kick of up to 0.914 GeV/c, in the vertical direction, at its maximum rated current of 4268 A. During the *b*-run, the current was set at 4200 A, resulting in a 0.9 GeV/c P_t kick in the direction opposite to that provided by SM12. The magnet had an aperture of 1.35 m $\times$ 1.68 m in X and Y, and was 3.23 m long. Like SM12, the magnet volume was filled with a helium bag.

The components of the magnetic field generated in SM3 (and also SM12) were measured in detail with the Fermilab "zip-track" apparatus at several current settings. The apparatus provided measurements of the magnetic field at 2.54 cm intervals along the Z axis. The field at other currents was determined by interpolation.

2.4.7 Ring Imaging Čerenkov Counter

Occupying the space between tracking stations 2 and 3 was the Ring Imaging Čerenkov (RICH) detector. Consisting of a tank approximately 17 m long, the RICH detector was designed to identify charged particles from their Čerenkov radiation in helium. Originally built for E605, the RICH was unused in E772 and then brought back into operation for E789. However, the detector was read out for about half of the *b*-run, therefore, the analysis in this thesis does not use the information generated by the RICH. For a detailed description of the RICH, interested readers are referred to other references [44, 45, 46].

2.4.8 Calorimeter

The identification of hadrons and electrons in this experiment was accomplished with a calorimeter that was located between tracking station 3 and the muon detector. The E789 calorimeter was a sampling calorimeter which meant that the cascade of charged particles generated by an incident particle was sampled by detector planes located at discrete points along the Z axis and oriented perpendicular to the beam line. It consisted of two distinct sections, an electromagnetic (EM) calorimeter and a hadronic (H) calorimeter. In both sections, the operating principle was essentially identical. An incident particle initiated a shower of charged particles in the calorimeter volume. These shower particles were then detected by the scintillator planes that were interleaved with the shower initiating material.

Since the total energy of the particle shower is proportional to the energy of the incident particle, the output of the scintillators should be proportional to the energy of the incident particle. Thus the calorimeter could measure the total energy of the incident particle.

Electromagnetic Calorimeter

The electromagnetic calorimeter, located just downstream of tracking station 3 and upstream of the hadronic calorimeter, was designed to absorb the total energy of incident electrons or photons. The electromagnetic calorimeter was constructed of 32 layers of 6 mm thick scintillators alternating longitudinally with 32 layers of 3 mm thick lead sheets. The material present in the calorimeter represented 19 radiation lengths of material but only approximately one hadronic interaction length [47].

The 32 layers were grouped, for readout purposes, into 4 modules consisting of 4, 9, 9, and 10 layers respectively. These modules were identified as E1 through E4. Each scintillator plane contained an active area of 296.7 cm $\times$ 243.8 cm. In order to provide some spatial localization, each plane of scintillators was segmented vertically into 12 sections and horizontally into two halves. This corresponded to an individual scintillator segment size of 148 cm (58.4 in.) in X and 20.3 cm (8 in.) in Y.

Hadronic Calorimeter

The hadronic calorimeter, located behind the electromagnetic calorimeter, was designed to absorb the total energy of incident hadrons. It consisted of two modules, H1 and H2, one behind the other. The first module, H1, consisted of 12 layers of 6 mm thick scintillators alternating with 12 layers of 2.5 cm thick iron sheets. The second module consisted of 20 layers of 6 mm thick scintillators alternating with 20 layers of 5 cm thick iron sheets. The material in H1 and H2, when combined, represented approximately eight interaction lengths and 75 radiation lengths of material. Each scintillator plane covered an area 309.4 cm by 264.2 cm. Like the electromagnetic calorimeter, each scintillator plane was segmented horizontally and vertically, in this case into 2 and 13 sections respectively. This corresponded to a scintillator segment size of 154.7 cm (60.9 in.) in X and 20.3 cm (8 in.) in Y.

Plane Name	Z Position (cm)	Plane View	Number of wire	Aperture	
				X (cm)	Y (cm)
PTY1	5186.04	Y	120	297.2	304.8
PTX	5425.12	X	135	343.9	308.6
PTY2	5589.90	Y	143	359.4	363.2

Table 2.6: Information about the proportional chambers in the muon detector.

2.4.9 Muon Detector

Located behind the hadronic calorimeter was the muon detector. It consisted of a pair of hodoscope planes, three multi-wire proportional tube chambers and blocks of hadron absorbing material. The characteristics of the two hodoscope planes are shown in Table 2.2 (See section 2.4.5.) Of the three proportional tube chambers, two had wires oriented to provide Y views and one had wires oriented to provide an X view. Each chamber consisted of two planes of proportional tubes constructed of aluminum with a square cross section. The second plane was offset by half a cell from the first plane, covering the dead region of the first plane. The size of the cells in each plane was 2.54 cm. The gas mixture used in the proportional tube chambers was identical to the mixture used in the drift chambers. Additional information about the proportional chambers in the muon detector is shown in Table 2.6.

The first tracking plane in the muon detector was hodoscope plane HY4. To prevent background from leakage of a hadronic shower from the calorimeter, 81 cm of concrete, 92 cm of zinc and 10 cm of lead separated the calorimeter from HY4. Located immediately behind HY4 was the first proportional tube plane PTY1. Separating the second hodoscope, HX4, and proportional counter, PTX, from HY4 and PTY1 was 92 cm of concrete. Another 92 cm of concrete separated HX4 and PTX from the final detector, PTY2, in the muon detector [42]. A total of 21.6 interaction lengths of material was interspersed between the planes in the muon detector. In addition, a total of 16.6 interaction lengths of material stood between HY4, the first detector plane in the muon detector, and tracking station 3. (Discussed in section 2.4.5.)

Detector Name	Associated Detector Planes
Silicon Lower Arm	Y1B, U2B, Y3B, V4B, Y5B, U6B, Y7B, V8B, SD
Silicon Upper Arm	Y1T, U2T, Y3T, V4T, Y5T, U6T, Y7T, V8T, SU
Tracking Station 1	HX1, HY1, V1, V1′, Y1, Y1′, U1, U1′
Tracking Station 2	HY2, V2, V2′, Y2, Y2′, U2, U2′
Tracking Station 3	HX3, HY3, V3, V3′, Y3, Y3′, U3, U3′
EM Calorimeter	E1, E2, E3, E4
Hadronic Calorimeter	H1, H2
Muon Detector	HX4, HY4, PTY1, PTX, PTY2

Table 2.7: Overview of the detectors in the E789 spectrometer.

2.4.10 Detector Name Summary

Table 2.7 briefly summarizes the major detector groups in the spectrometer and their constituent detectors. The ordering of the detector groups corresponds roughly with their Z ordering.

2.5 Trigger

Assuming a total pp cross section of 42 mb [48] and an $A^{0.77}$ dependence [49], the expected interaction rate for protons on a 3 mm long gold target is on the order of 40 MHz. But the cross section for $pN \rightarrow b\bar{b}$ is measured to be $5.7 \pm 1.5 \pm 1.3$ nb/nucleon [50], corresponding to a 5 Hz production rate. This means that the majority of the proton – target interactions will contain uninteresting events. In addition, only a small fraction of the events of interest are in the acceptance of the spectrometer. Therefore, a triggering system was required to indicate which events contained interactions that should be recorded.

A two level trigger was used to select events during the b-run of E789. The first

level trigger, TFI, was a loose trigger designed to flag dihadron and dimuon events. The second level trigger, TGO, was the "physics" trigger for the experiment. It was used to make a loose classification of the event and also ensure that the dihadron (dimuons) in the event were roughly consistent with target generated dihadrons (dimuons). Events that passed both the TFI and TGO triggers were recorded. Note that order is important, the TFI trigger must occur before the TGO trigger is checked. Also, provisions were made in the trigger system to discard events that occurred when the data acquisition system was busy processing a previous event.

2.5.1 Level One Trigger : TFI

The definition of the TFI trigger is shown in equation 2.5. The + indicates a logical OR and the · indicates a logical AND.

$$\mathrm{TFI} = 4/4\mu\mathrm{LR} + (\mathrm{E_H} \cdot \mathrm{RF}) + (2/4\mathrm{M} \cdot 2\mathrm{Y4}) + (\mathrm{e_L} \cdot \mathrm{RF}) \tag{2.5}$$

The components of the TFI trigger are as follows :

$4/4\mu$LR This component was designed to be a loose dimuon trigger. It was the logical AND of two component signals, $4/4\mu$L and $4/4\mu$R, where L and R correspond to left and right. To generate these two components, the hodoscope planes HX1, HY2, HX4, and HY4 (see Table 2.2) were split into two halves, left and right. $4/4\mu$L (R) was the logical AND of the signals from the left (right) halves of these four hodoscope planes. $4/4\mu$L and $4/4\mu$R were ON when two muons were detected, one in the left half of all four hodoscope planes and one in the right half.

($\mathrm{E_H} \cdot$ RF) This component of the TFI trigger consisted of an analog sum of the dynode signals from all the photomultiplier tubes in the H1 and H2 sections of the hadronic calorimeter and the E1 and E4 sections of the electromagnetic calorimeter logically AND'ed with the accelerator RF clock. The subscript H denotes that the analog sum was *discriminated* at a high level, i.e. was required to be above a high threshold. (There was also an $\mathrm{E_L}$ signal that was obtained from the same analog sum but was required to be above a low threshold.) AND'ing the calorimeter signal with the RF clock signal forced the calorimeter signal to be "in time" with the beam. The ($\mathrm{E_H} \cdot$ RF) component of the trigger was therefore a loose hadron trigger.

(2/4M · 2Y4) This component of the TFI trigger consisted of 2Y4 which was derived from the HY4 hodoscope plane and 2/4M which was derived from HY1, HY2, and HY3. The 2Y4 signal was ON when at least 2 out of the 28 scintillator sections in HY4 detected a particle. The 2/4M component was derived from the four quadrants of the *matrix* trigger. The matrix trigger is discussed in section 2.5.2, the section describing the TGO trigger. The 2/4M trigger required that at least 2 out of the 4 matrix triggers "fired". The (2/4M · 2Y4) was basically another muon trigger. (Note that 2X4, in place of 2Y4, was also used.)

(e_L · RF) This component of the TFI trigger consisted of an analog sum of the dynode signals from all the photomultiplier tubes in the E2 and E3 sections of the electromagnetic calorimeter [38] logically AND'ed with the RF clock. The subscript L denotes that the analog sum was discriminated at a low level, i.e. was required to be above a low threshold. The (e_L · RF) component of the trigger was therefore a loose electron trigger.

2.5.2 Level Two Trigger : TGO

The TGO trigger was the "physics" or level two trigger. The definition of the TGO trigger is shown in equation 2.6.

$$\begin{aligned} \text{TGO} &= h^+h^- + \mu^+\mu^- + e^+e^- + e^\pm\mu^\mp \\ &\quad + h^\pm h^\pm/16 + \mu^\pm\mu^\pm + e^\pm e^\pm + e^\pm\mu^\pm + \text{TFI}/4096 \end{aligned} \tag{2.6}$$

Each component of the TGO trigger selected a particular type of event of interest. For example, the $h^\pm h^\pm$ and h^+h^- components flag like-sign and opposite-sign dihadron events. Similarly, $e^\pm e^\pm$ and e^+e^- select like-sign and opposite-sign dielectron events. The divide-by-N notation in TFI/4096 means that every Nth trigger was included in the computation of TGO. The quantity N is called the pre-scale factor.

The composition of each of the components of the physics trigger is shown in Table 2.8. Each of the different components of the physics trigger share common elements, with each element being obtained from the different scintillators in the spectrometer. These elements are described below.

Trigger Name.	Description
h^+h^-	$M_U \cdot M_D \cdot S_U \cdot S_D \cdot \overline{NX1} \cdot \overline{NX3} \cdot E_H$
$\mu^+\mu^-$	$M_U \cdot M_D \cdot S_U \cdot S_D \cdot \overline{NX1} \cdot \overline{NX3} \cdot \frac{2}{4}X4 \cdot \frac{2}{4}Y4$
e^+e^-	$M_U \cdot M_D \cdot S_U \cdot S_D \cdot \overline{NX1} \cdot \overline{NX3} \cdot e_H$
$e^\mp\mu^\pm$	$M_U \cdot M_D \cdot S_U \cdot S_D \cdot \overline{NX1} \cdot \overline{NX3} \cdot e_L \cdot X4 \cdot Y4$
$h^\mp e^\pm$	$M_U \cdot M_D \cdot S_U \cdot S_D \cdot \overline{NX1} \cdot \overline{NX3} \cdot E_L \cdot e_L$
$h^\mp\mu^\pm$	$M_U \cdot M_D \cdot S_U \cdot S_D \cdot \overline{NX1} \cdot \overline{NX3} \cdot E_L \cdot X4 \cdot Y4$
$h^\pm h^\pm$	$M_{LIKE} \cdot (S_U + S_D) \cdot \overline{NX1} \cdot \overline{NX3} \cdot E_H$
$\mu^\pm\mu^\pm$	$M_{LIKE} \cdot (S_U + S_D) \cdot \overline{NX1} \cdot \overline{NX3} \cdot \frac{2}{4}X4 \cdot \frac{2}{4}Y4$
$e^\pm e^\pm$	$M_{LIKE} \cdot (S_U + S_D) \cdot \overline{NX1} \cdot \overline{NX3} \cdot e_H$
$e^\pm\mu^\pm$	$M_{LIKE} \cdot (S_U + S_D) \cdot \overline{NX1} \cdot \overline{NX3} \cdot e_L \cdot X4 \cdot Y4$
$h^\pm e^\pm$	$M_{LIKE} \cdot (S_U + S_D) \cdot \overline{NX1} \cdot \overline{NX3} \cdot E_L \cdot e_L$
$h^\pm\mu^\pm$	$M_{LIKE} \cdot (S_U + S_D) \cdot \overline{NX1} \cdot \overline{NX3} \cdot E_L \cdot X4 \cdot Y4$

Table 2.8: Components of the physics triggers.

Trigger Name.	Description
M_U	$M_{UL} + M_{UR}$ Hodoscope hits consistent with a track passing through the upper half of the spectrometer
M_D	$M_{DL} + M_{DR}$ Hodoscope hits consistent with a track passing through the lower half of the spectrometer
M_{LIKE}	$(M_{UL} \cdot M_{UR}) + (M_{UL} \cdot M_{UR})$ Hodoscope hits consistent with two tracks passing through the upper half (or lower half) of the spectrometer

Table 2.9: Outputs from the matrix trigger.

Matrix Trigger : M_U, M_D and M_{LIKE}

The matrix triggers, M_U, M_D, and M_{LIKE}, were derived from the four basic matrix triggers M_{UL}, M_{UR}, M_{DL}, and M_{DR} as shown in Table 2.9. These four basic triggers, in turn, were derived from information obtained from the three Y hodoscope planes, HY1, HY2, and HY3. (See Figure 2.6.) Particles produced at the target that traversed the entire spectrometer (with the possible exception of the muon station) fired only selected combinations of hodoscope sections in HY1, HY2, and HY3. The M_{UL}, M_{UR}, M_{DL}, and M_{DR} matrix trigger logic were designed to signal TRUE when hodoscope hit patterns corresponded to the presence of target generated charged particle tracks in each of the four quadrants of the spectrometer. For example, M_{UL} was TRUE when the hits in the hodoscopes were consistent with a target generated particle that passed through the upper left quadrant of the spectrometer. (The U/D in the M_{xy} name designated up/down while the L/R designated left/right.)

The matrix triggers were implemented with a lookup table using fast ECL static RAM [51]. Counters in the three Y hodoscope planes were used to specify an entry in the lookup table. Each entry in the lookup table contained a value that specified whether or not the combination of hodoscope hits was consistent with a charged particle track coming from the target. The entries in the lookup table were generated from a Monte Carlo simulation of the detector and the decay processes of interest. With this latter step, only events with

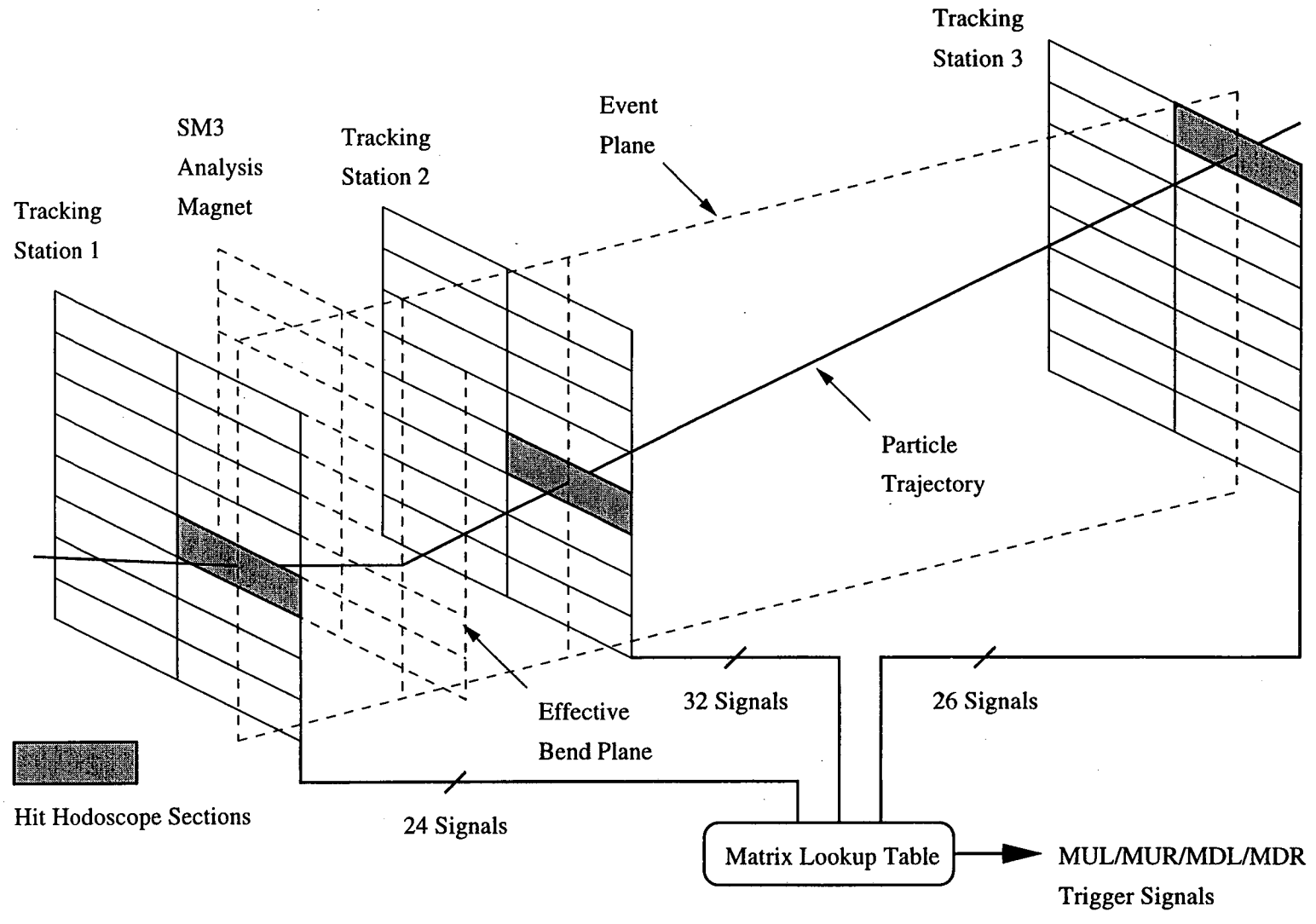

Figure 2.6: Schematic of the construction of the matrix trigger.

charged particle tracks from desired decays would be selectively enhanced.

Micro-Vertex Scintillator Trigger : S_U and S_D

The silicon micro-vertex scintillator trigger was used to signal the presence of a charged particle exiting an arm of the micro-vertex detector. The triggers were generated from the outputs of the S_U and S_D scintillators which were positioned behind the upper and lower arms of the silicon micro-vertex detector. The AND'ed signal, $S_U \cdot S_D$, was TRUE if two particles passed through the silicon micro-vertex detector, one in the upper arm and one in the lower arm. Hence, $S_U \cdot S_D$ signaled the presence of at least two oppositely charged particles.

Multiplicity Veto : $\overline{NX1}$ and $\overline{NX3}$

Two veto signals were created from the hodoscope planes to flag the presence of high multiplicity events. Designated $\overline{NX1}$ and $\overline{NX3}$, these two flags registered FALSE if the number of charged particles traversing hodoscope planes HX1 or HX3, respectively, were greater than a preset value. The particle count was obtained by making a digital count of the number of scintillator segments that registered a hit. For the *b*-run, $\overline{NX1}$ signaled FALSE when more than 10 counters fired while $\overline{NX3}$ signaled FALSE when more than 9 counters fired.

Muon Trigger : nX4 and nY4

The trigger elements $\frac{2}{4}$X4, $\frac{2}{4}$Y4, X4, and Y4 signaled the presence of muons. The X4 (Y4) trigger was generated from the HX4 (HY4) hodoscope plane. X4 and Y4 signaled the presence of a single muon. $\frac{2}{4}$X4 and $\frac{2}{4}$Y4 were used to signal the presence of two distinct muons. The $\frac{2}{4}$ designates that 2 out of 4 quadrants of the hodoscope plane must register the presence of a charged particle.

Calorimeter Trigger : e_L, e_H, E_L and E_H

Examination of the energy deposition in the calorimeter was the primary means of making a fast, but crude, determination of the presence of a hadron or an electron in an event. The triggers that were generated from the signals obtained from the electromagnetic and hadronic calorimeters were e_L, e_H, E_L and E_H.

The triggers e_L and e_H were generated from an analog sum of the outputs from the E2 and E3 modules of the electromagnetic calorimeter [38]. E_L and E_H were generated from an analog sum of the outputs from the H1 and H2 modules of the hadronic calorimeter and the E1 and E4 modules of the electromagnetic calorimeter. The subscripts L and H signify different triggering thresholds, L meaning low and H meaning high. These energy triggers were also recorded with ADC's so that they could be analyzed offline.

Dimuon and Dihadron TGO Trigger Components

The events of interest in this thesis were the opposite-sign dihadron and dimuon events. The h^+h^- and $\mu^+\mu^-$ components of the TGO trigger, shown in equations 2.7 and 2.8, were responsible for flagging those events.

$$h^+h^- = M_U \cdot M_D \cdot S_U \cdot S_D \cdot \overline{NX1} \cdot \overline{NX3} \cdot E_H \quad (2.7)$$

$$\mu^+\mu^- = M_U \cdot M_D \cdot S_U \cdot S_D \cdot \overline{NX1} \cdot \overline{NX3} \cdot \frac{2}{4}X4 \cdot \frac{2}{4}Y4 \quad (2.8)$$

Looking more closely at the factors in the two triggers, it is clear how they flagged opposite-sign dihadron and dimuon. The $S_U \cdot S_D$ term required there to be at least two oppositely charged particle in the silicon micro-vertex detector, one in each arm (up/down). The $M_U \cdot M_D$ term required the presence of at least two oppositely charged, target generated particles passing through hodoscope planes HY1, HY2, and HY3. The E_H term in h^+h^- required large energy deposition in the hadron calorimeter, thus preferentially selecting dihadron events. The $\frac{2}{4}X4 \cdot \frac{2}{4}Y4$ term in $\mu^+\mu^-$ required the presence of tracks in the muon station, thus singling out dimuon events. Finally, the $\overline{NX1} \cdot \overline{NX3}$ term in both trigger components vetoed high multiplicity events.

2.6 Run Statistics

Utilizing the spectrometer in the configuration outlined in the previous paragraphs, a total of 667 2.3 GB 8 mm tapes of data were collected. The integrated number of protons incident on the target (ignoring the targeting fraction) was 2.78×10^9 SEM3 counts or 2.2×10^{17} protons. Figure 2.7 shows the integrated number of protons incident on the target as a function of tape number. A total of 9.65×10^8 TGO triggers were recorded on tape during the 2 month duration of the *b*-run. Figure 2.8 shows the integrated TGO trigger count as a function of tape number. Figure 2.9 shows the DAQ live time as a function of

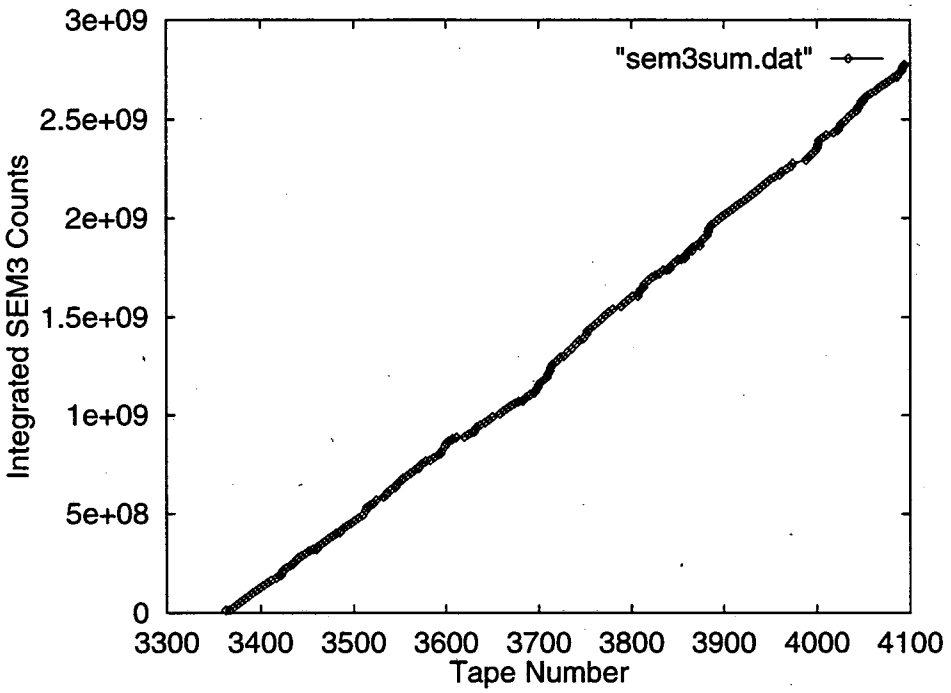

Figure 2.7: Integrated number of incident protons (in SEM3 counts) as a function of tape number.

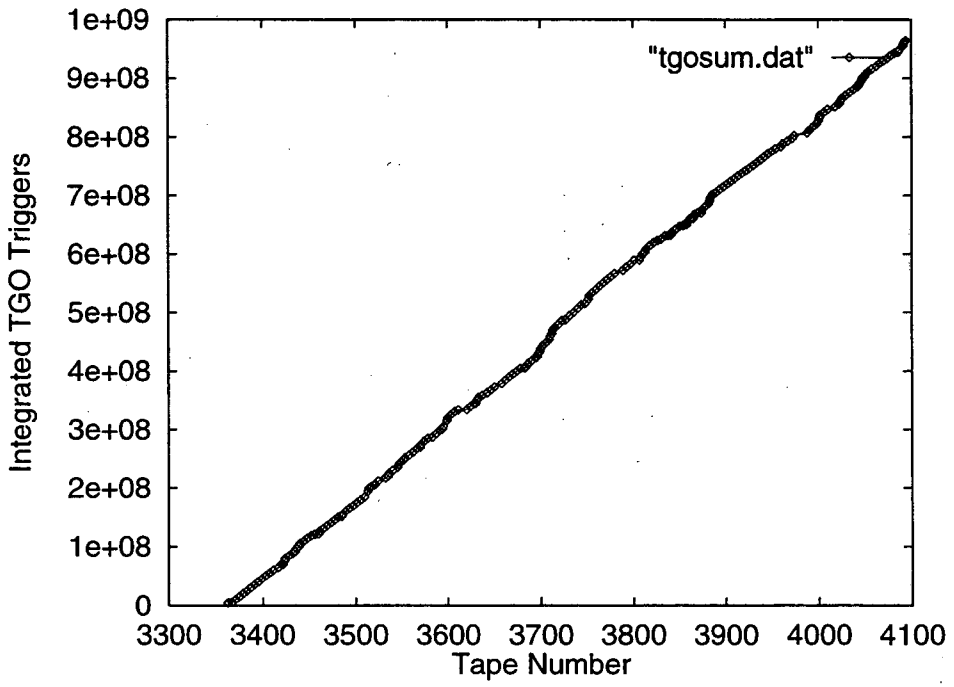

Figure 2.8: Integrated number of TGO triggers as a function of tape number.

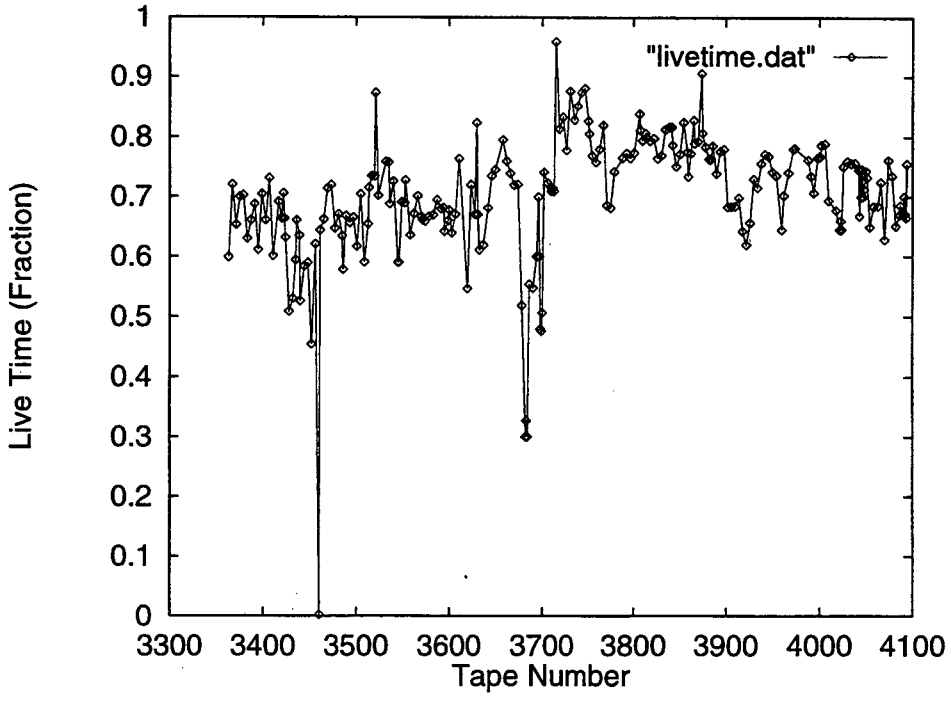

Figure 2.9: DAQ live time (fraction) as a function of tape number.

tape number. Figure 2.10 shows the average number of TGO triggers per spill as a function of tape number. As mentioned in section 3.4.4, there was a change in the $M_U \cdot M_D$ trigger that resulted in a change in the acceptance of dihadron events. This change occurred at tape number 3666. The integrated number of protons incident on the target at the end of the first running period (i.e., before the change in the $M_U \cdot M_D$ trigger) was 1.03×10^9 SEM3 counts. A total of 3.89×10^8 TGO triggers were recorded on tape during this run.

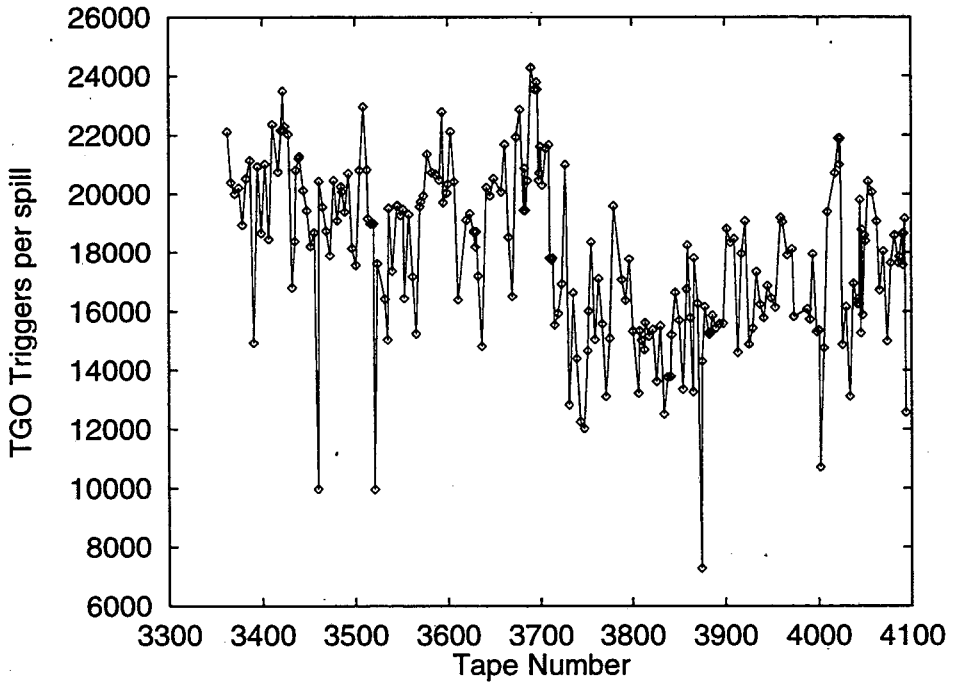

Figure 2.10: Average number of TGO triggers per spill as a function of tape number.

Chapter 3

Analysis

The goal of this analysis was to determine the branching ratios of the modes given in section 1.3.1 from the data collected from the 1991 b-physics run of E789. This involved determining a procedure for extracting the information from the 667 2.3 GB 8mm tapes (corresponding to 4×10^{13} interactions) that were written during the 2 month run.

3.1 Analysis Overview

The technique used to establish an upper bounds on the different B^0 and Λ_b branching ratios was to compare the observed rate of the decay modes of interest to that of a known decay mode of the b-hadron in the same experiment. The chosen reference decay was the cascade decay $B \to J/\psi + X \to \mu^+\mu^- + X$, where B is any b-hadron and X is anything. The advantages of this technique can be seen from the following analysis.

The number of reference events reconstructed from the data, N_{ref}, is given by equation 3.1, where $\epsilon_{ref}(t)$ is the product of the reconstruction efficiency and detector acceptance for the mode, BR_{ref} is the branching ratio for $B \to J/\psi + X \to \mu^+\mu^- + X$, σ is the total cross section for b-hadron production in the interaction of 800 GeV/c protons on gold (Au), $\mathcal{L}(t)$ is the luminosity, i.e., the number of protons per unit time per unit area impinging on the target, and T is the total running time of the experiment.

$$\begin{aligned} N_{ref} &= \int_0^T \epsilon_{ref}(t)\mathrm{BR}_{ref}\sigma\mathcal{L}(t)dt \\ &= \mathrm{BR}_{ref}\sigma \int_0^T \epsilon_{ref}(t)\mathcal{L}(t)dt \end{aligned} \tag{3.1}$$

The number of rare dihadron events in channel i reconstructed from data, N_i, is given by equation 3.2, where $\epsilon_i(t)$ is the combination of the reconstruction efficiency and detector acceptance for mode i, f_i is the fraction of produced b-hadrons that are of the type of interest, in this case B_d^0, B_s^0 or Λ_b, and BR_i is the branching ratio for mode i.

$$\begin{aligned} N_i &= \int_0^T \epsilon_i(t) f_i \mathrm{BR}_i \sigma \mathcal{L}(t) dt \\ &= \mathrm{BR}_i \sigma f_i \int_0^T \epsilon_i(t) \mathcal{L}(t) dt \end{aligned} \tag{3.2}$$

Dividing equation 3.2 by equation 3.1 yields the relationship given in equation 3.3. Note that σ has dropped out of the equation.

$$\frac{N_i}{N_{ref}} = \left(\frac{\mathrm{BR}_i f_i}{\mathrm{BR}_{ref}}\right)\left(\frac{\int_0^T \epsilon_i(t)\mathcal{L}(t)dt}{\int_0^T \epsilon_{ref}(t)\mathcal{L}(t)dt}\right) \tag{3.3}$$

If the ratio of $\epsilon_i(t)$ and $\epsilon_{ref}(t)$ is time independent, that is $\epsilon_i(t)$ and $\epsilon_{ref}(t)$ can be written as $\epsilon_i'\epsilon_0(t)$ and $\epsilon_{ref}'\epsilon_0(t)$, then the fraction $\frac{N_i}{N_{ref}}$ can be written as :

$$\frac{N_i}{N_{ref}} = \left(\frac{\mathrm{BR}_i f_i \epsilon_i'}{\mathrm{BR}_{ref}\epsilon_{ref}'}\right) \tag{3.4}$$

A slight re-arrangement of terms in equation 3.4 gives equation 3.5 which is the equation that was used to determine the branching ratios.

$$\mathrm{BR}_i = \frac{\epsilon_{ref}' \mathrm{BR}_{ref} N_i}{\epsilon_i' f_i N_{ref}} \tag{3.5}$$

Assuming that the ratio of $\epsilon_i(t)$ and $\epsilon_{ref}(t)$ is truly time independent, the determination of BR_i becomes independent of many factors that are difficult to determine absolutely. For example, the absolute magnitude of the efficiencies, ϵ_{ref}' and ϵ_i' need not be determined, only the ratio of the efficiencies needs to be determined. Hence, any *common mode* errors and uncertainties in the determination of these efficiencies, i.e. those that affect equally the determination of both efficiencies, will partially or completely cancel in the ratio. Examples of such errors are event losses due to tape errors, DAQ readout errors, (non physics) processing errors, and DAQ live-time.

From equation 3.5, it is clear what steps need to be taken in order to determine the branching ratios of the desired processes, these are :

- Count the number of reference $B \to J/\psi + X \to \mu^+\mu^- + X$ events, N_{ref}, in the data.

- Count the number of dihadron b-decays of interest, N_i, in the data.
- Determine the efficiency, ϵ_{ref}, for accepting and reconstructing the reference events.
- Determine the efficiency, ϵ_i, for accepting and reconstructing the signal events.

The data analysis process can be divided into the following five non-orthogonal steps which are given below in roughly chronological order.

- Event reconstruction;
- Monte Carlo studies;
- Acceptance and efficiency studies;
- Event selection;
- Background estimation.

Given the iterative nature of the data analysis these steps are not completely independent nor completely sequential; however, in order to give a coherent discussion, the steps will be described in the order given above.

3.2 Event Reconstruction

By design, the E789 spectrometer recorded a spatially quantized description of an event, i.e., the positions of the particles that traversed the spectrometer were recorded at discrete points in the longitudinal (Z) direction. In the case of the proportional chambers, drift chambers and silicon detectors, only one transverse coordinate was recorded per particle per detector plane. With the hodoscopes, only extremely coarse $X - Y$ position information was recorded for each charged particle per detector plane. In order to extract the physics out of the data, the 3-dimensional trajectory of each particle in each event had to be reconstructed. The next step in the event reconstruction process was the determination of the origin of the particles, since in this analysis only events with particles originating from the target region were of interest. The third step in the reconstruction process was the identification of the types of particles in each event. The final step in the reconstruction process was the reconstruction of the exact location of the source of the particles in each event. Since the events of interest involved the decay of relatively long lived b-hadrons,

the primary goal was to find events with oppositely charged tracks that traced back to a common vertex which was downstream of the target. This required a precise reconstruction of the particle trajectories near the target, made possible by the silicon micro-vertex detector, and the reconstruction of the decay vertex from these trajectories with a vertexing algorithm. In summary, the reconstruction process proceeded in the following *phases* :

- Spectrometer track reconstruction
- Particle identification
- Silicon track reconstruction
- Vertex reconstruction

Note that a distinction is being made between the *phases* discussed here and *passes* discussed next.

As outlined above, the reconstruction process can be separated into logically distinct phases. In principle, the reconstruction phases could have been accomplished in a single pass over the data; however, for several reasons, the reconstruction was separated into multiple passes. First, the signal to noise ratio, as measured by the number of interactions containing b-decays versus the total number of events due to proton–nucleon interaction was small (see Table 1.6). Although the online trigger system (section 2.5) was designed to increase the signal to noise ratio, a substantial number of events which passed the trigger were still uninteresting events. When coupled with the volume of data to be processed and the length of time required to completely process an event, the decision was made to separate the reconstruction into multiple passes (*analysis pipelining*) that successively reduced the size of the data set. The second reason for separating the reconstruction into separate passes was to provide time for refinements in later phases of processing while still allowing for the timely completion of the complete analysis. The final reason for partitioning the analysis was to reduce the amount of processing required should a particular phase need to be rerun.

In this analysis, the reconstruction was partitioned into three separate passes. The first two passes involved spectrometer reconstruction and particle identification. The final reconstruction pass involved silicon reconstruction and vertex reconstruction. Subsequent *physics* analysis of the data did not involve further event reconstruction; instead, it utilized the information obtained from these three passes. The analysis codes used in the three

reconstruction passes were developed by the E789 collaboration from code developed for the E605 and E772 experiments [52, 53, 39, 45, 46, 47]. The pass 3 analysis code, particularly the silicon reconstruction and vertex reconstruction algorithms, were designed and tuned by the E789 collaboration for the measurement of the production of neutral D-mesons [43] and for the measurement of the production of bottom quarks [50]. The first analysis pass was made at Fermilab and the second and third analysis passes were made at the Lawrence Berkeley National Laboratory.

3.2.1 Pass 1

The first pass over the data reconstructed tracks in stations 1, 2 and 3, made preliminary particle identification and made loose *cuts* on the track origin. The goal of this pass was to quickly extract events from the *raw* data tapes that contained at least 2 tracks that originated from the target region and traversed the complete length of the spectrometer. All the cuts used to separate signal events from noise events were loose to prevent unintentional signal loss. In order to increase the probability that signal events were retained, first pass analysis depended primarily on the information in the downstream section of the spectrometer, in particular, tracking stations 1, 2, and 3. In this region, particle multiplicities were the lowest and track separation was the greatest, thus tracks were less ambiguous and easier to reconstruct.

Hit reconstruction

The first step in pass 1 was the merging of hits from each pair of drift chamber detector planes in a common view, e.g., $V1 - V1'$, into virtual hits on a single virtual plane. (Recall that the primed and unprimed planes in a pair contained wires oriented in a common direction, offset by one half cell to help resolve left-right ambiguities and adjacent in Z. See section 2.4.5.) The hits in each virtual plane were separated into two classes depending on how they were formed. A virtual hit was either a combination of hits from a primed and an unprimed plane (an *associated* hit) or a hit from only one plane (an *unassociated* hit). The association of hits from a primed and an unprimed plane was based on the proper matching of drift-time information from the two hits. The goal of this process was to assign some quality metric to the hits, with associated hits being "better" than unassociated hits. Next, virtual hits from the three virtual planes in a tracking station were combined to form

triplets and *doublets*. Each triplet (doublet) consisted of a combination of 3 (2) virtual hits, each from a different virtual plane, that was consistent with a single track. (Recall that each tracking station consisted of 3 paired planes, e.g., V1 – V1′, U1 – U1′, and Y1 – Y1′, a sufficient number to construct a point in 3-space.) Each triplet was required to contain at least one associated hit and each doublet was required to contain two associated hits. In addition, each doublet could not be part of a triplet.

Downstream track reconstruction

Once a list of triplets and doublets was made for each tracking station, an attempt was made to construct the downstream tracks (i.e., downstream of the SM3 analysis magnet) from the doublets and triplets in tracking stations 2 and 3. Figure 3.1 is a flow chart of the downstream track reconstruction process. Each track consisted of a triplet or doublet from station 2 and a triplet or doublet from station 3. Each track, however, was required to contain at least one triplet. The generated tracks were then projected to SM3 and to the target in the XZ plane. Since neither SM12 nor SM3 bent tracks in the XZ plane, a target cut was made in X, $|x| < 3$ in. at z_{target}, for the reconstructed tracks. Figures 3.2 and 3.3 show the distribution of x for muon and hadron tracks that survive through pass 3 of the analysis chain. The plots show that the $|x|$ cut loses no events. An SM3 aperture cut, $|x| < 28$ in. and $|y| < 32$ in. at z_{SM3}, was also made on the tracks. What resulted was a set of downstream tracks that were roughly consistent with tracks originating from the target region which traversed the downstream half of the spectrometer.

In order to weed out poorly reconstructed tracks and fake tracks, two track quality cuts were made. First, a cut was made on the quality of the hits contained in a track. The quality metric was the *checksum*. In this metric, the track angle and the drift distances for primed and unprimed hits in the associated hits in a track were used to determine if the paired hits were consistent with two measurements of the same track or with measurements of two different tracks. Triplet/triplet tracks were required to have at least one associated hit with a good checksum in each triplet. Triplet/doublet tracks had the same requirement for the triplet but were required to have two associated hits with good checksums for the doublet. Second, a chi square cut, $\chi^2 < 50$, was made on the tracks. The resulting track list was then stripped of duplicate tracks.

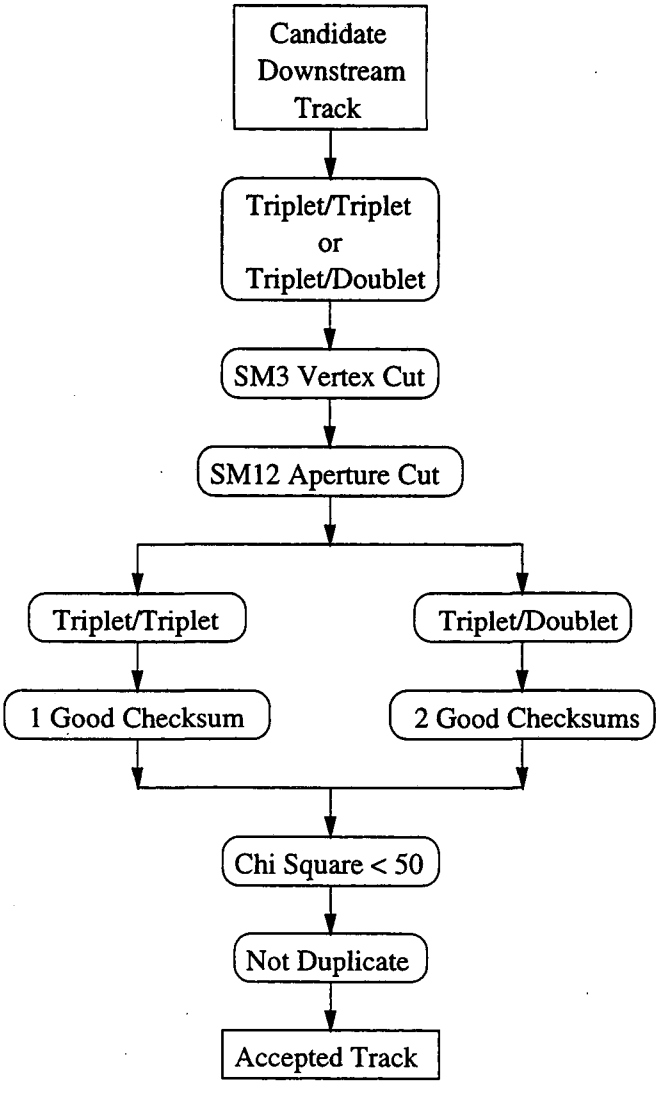

Figure 3.1: Flow chart of the downstream track reconstruction algorithm.

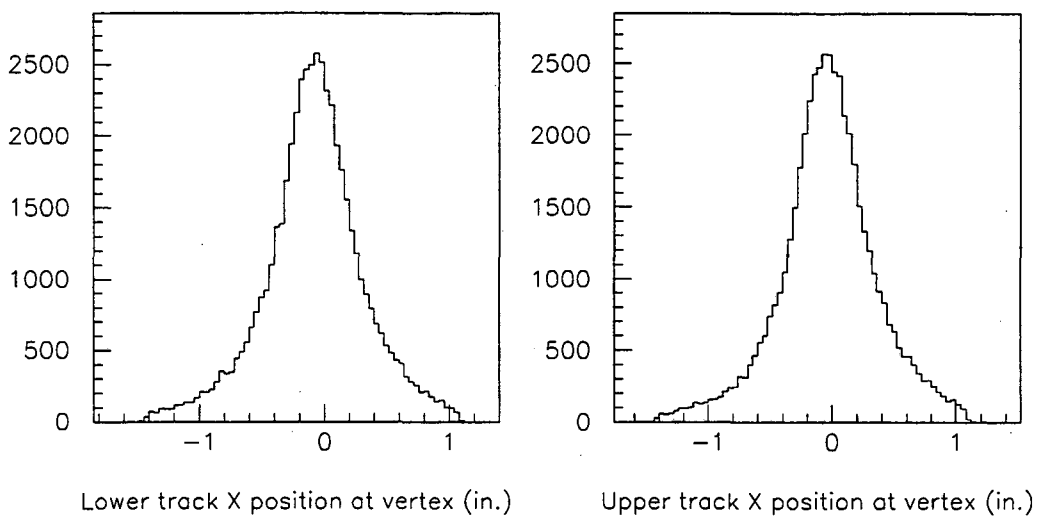

Figure 3.2: Distribution of the projected X position of the reconstructed downstream track at the target for a subset of the muon data set. The distribution for tracks in the lower (upper) arm of the spectrometer is shown on the left (right). (Units are in inches.)

Upstream track reconstruction

Once a list of unique, high quality downstream tracks was constructed, an attempt was made to find its upstream segment. Figure 3.4 is a flow chart of the upstream track reconstruction process. The first step in this process was the propagation of the downstream track through SM3 using a single bend plane approximation. An upstream track was created from the position of the downstream track at the x–y plane at the center of SM3 and each triplet/doublet in station 1 that fell within a window around the projected Y position of the downstream track. The limits of the window corresponded to the projected Y positions of 10 GeV/c tracks of particles with positive and negative charges. Each upstream track was then projected to the front of the beam dump and then to the target. For speed, a single bend plane approximation was used to characterize the effects of SM12 for this projection. Each upstream track was required not to point to the dump, $|y| > 3.0$ in. near the front face of the dump, and required to point to the target, $|x| < 2.0$ in. and $|y| < 2.0$ in. at the target Z position. These cuts were subsequently relaxed in later processing to $|y| > 2.5$ in. at the beam dump and $|x| < 3.0$ in. and $|y| < 4.5$ in. at the target. In all cases, the

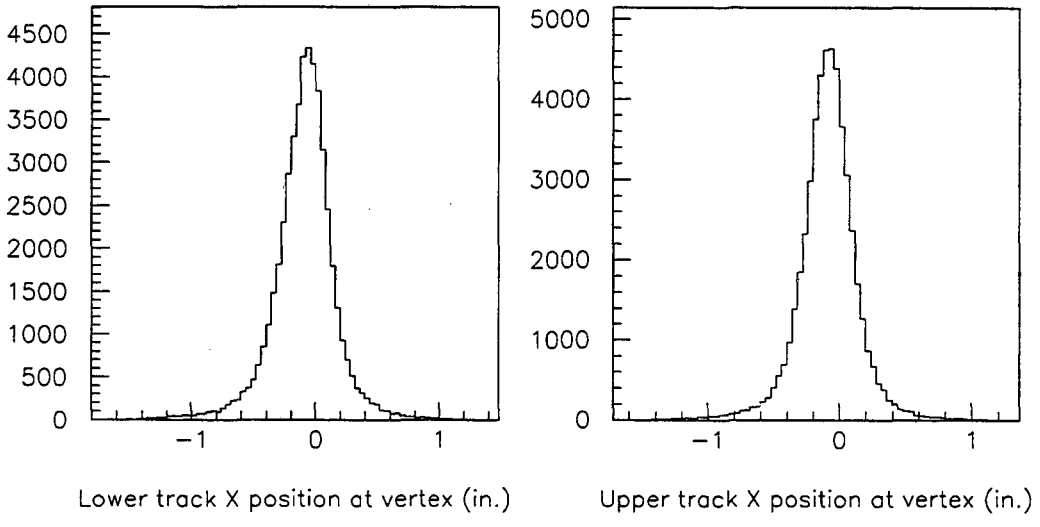

Figure 3.3: Distribution of the projected X position of the reconstructed downstream track at the target for a subset of the hadron data set. The distribution for tracks in the lower (upper) arm of the spectrometer are on the left (right). (Units are in inches.)

apertures used in the beam dump cut were larger than the actual aperture of the beam dump/SM12 magnet combination.

Given the types of cuts used in upstream reconstruction, it was critical that the trace-back procedure through SM3 and SM12 be completely understood. In particular, it was essential that the errors in track propagation be the result of position measurement uncertainty and hit mis-assignment but not due to errors in the propagation through the magnetic fields in SM3 and SM12. Previous analyses verified that the errors in the trace-back were not caused by errors in the magnetic field map. This was accomplished by the comparison of vertex position distributions, reconstructed mass distributions and other distributions generated from data and the same distributions generated via Monte Carlo simulation [54].

Complete spectrometer track reconstruction

For each acceptable upstream track found, a complete spectrometer track was constructed. Each spectrometer track was required to contain at least 12 hits (counting

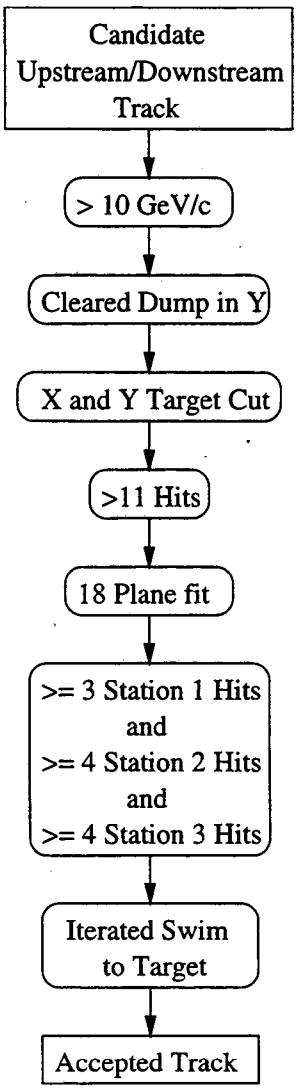

Figure 3.4: Flow chart of the upstream track reconstruction algorithm.

primed and unprimed hits separately). A full 18-plane fit on the surviving upstream – downstream pairs was then made. The track was then compared to previously found tracks in the event. If an identical track existed, the new track was not stored. A final requirement of greater than or equal to three hits in station 1 and four hits in each of the other tracking stations was applied to all tracks before being accepted.

Target Trace-Back

Once a list of acceptable quality spectrometer tracks was obtained, the tracks were iteratively traced through SM12 using a multi-bend plane approximation for SM12. First, the tracks were traced back from SM3 to $z_{scatter}$ = 6.67 m in 45.7 cm (18 in.) steps. The position of $z_{scatter}$ coincided with the position where the effects of multiple scattering on a track between the target position and SM3 could be most accurately modeled by scattering at a single point. This was accomplished by choosing the value of $z_{scatter}$ that minimized the width of the $J/\psi \rightarrow \mu^+\mu^-$ mass distribution. At discrete intervals in Z in this trace-back, the position of the track was compared with the magnet aperture to ensure that the track didn't hit the magnet. Tracks that successfully traversed this section of the magnet volume were then iteratively traced to the center of the target, again in 18 in. steps.

At z_{target} the transverse position of each track was compared to the beam position. If the track missed the target by more than $\Delta X = 0.01$ in. or $\Delta Y = 0.001$ in., the angle of the track in X and/or Y was adjusted at $z_{scatter}$ and the track was retraced to the target from $z_{scatter}$. (The assumption was that the angle error was due to multiple scattering of the track between the target and SM3.) The adjustment to the scattering angle was computed using the formulas shown in equations 3.6 and 3.7.

$$\theta_x(i+1) = \theta_x(i) + \frac{x_{target}(i)}{z_{scatter} - z_{target}} \tag{3.6}$$

$$\theta_y(i+1) = \theta_y(i) + \frac{y_{target}(i)}{z_{scatter} - z_{target}} \tag{3.7}$$

The adjustment formula was derived through the following steps. First, the magnetic field of SM12 resulted in a time rate of change of the momentum (of a particle passing through SM12's magnetic volume):

$$\frac{dP_y}{dt} = eB_x v_z \tag{3.8}$$

$$\frac{dP_z}{dt} = -eB_x v_y \tag{3.9}$$

Defining

$$\tan\theta = \frac{dy}{dz} = \frac{P_y}{P_z} \tag{3.10}$$

it can be shown using equations 3.8, 3.9 and 3.10 [54] and recognizing that $|\vec{P}| = constant$ and hence $P_y = \alpha v_y$ and $P_z = \alpha v_z$, that :

$$\frac{d}{dz}(\tan\theta) = \frac{eB_x}{P\cos^3\theta} \tag{3.11}$$

Integrating over dz twice yields equation 3.12:

$$y(z) = y(z_{target}) + (z - z_{target})\tan\theta(z_{target}) + \frac{e}{P}\int_{z_{target}}^{z} dz' \int_{z_{target}}^{z'} dz'' \frac{B_x(z'')}{cos^3\theta(z'')} \tag{3.12}$$

Evaluating the equation at $z_{scatter}$ and treating the last term as a constant (with respect to small variations in θ), and rewriting the integral, equation 3.12 can be rewritten as:

$$y(z_{scatter}) = y(z_{target}) + (z_{scatter} - z_{target})\tan\theta(z_{scatter}) + F(z_{scatter}) \tag{3.13}$$

Solving for $y(z_{target})$ yields:

$$y(z_{target}) = y(z_{scatter}) - (z_{scatter} - z_{target})\tan\theta(z_{scatter}) + F(z_{scatter}) \tag{3.14}$$

If $y(z_{scatter})$, $z_{scatter}$ and z_{target} are assumed to be correctly determined, then the real Y position of the particle at the target should satisfy the following equation:

$$y(z_{target})_{real} = y(z_{scatter}) - (z_{scatter} - z_{target})\tan\theta(z_{scatter})_{real} + F(z_{scatter}) \tag{3.15}$$

Subtracting equation 3.15 from equation 3.14 yields:

$$y(z_{target}) - y(z_{target})_{real} = -(z_{scatter} - z_{target}) \times (\tan\theta(z_{scatter}) - \tan\theta(z_{scatter})_{real}) \tag{3.16}$$

Solving for $\theta(z_{scatter})_{real}$ yields:

$$\tan\theta(z_{scatter})_{real} = \tan\theta(z_{scatter}) + \frac{y(z_{target}) - y(z_{target})_{real}}{z_{scatter} - z_{target}} \tag{3.17}$$

Making a small angle approximation yields:

$$\theta(z_{scatter})_{real} = \theta(z_{scatter}) + \frac{y(z_{target}) - y(z_{target})_{real}}{z_{scatter} - z_{target}} \tag{3.18}$$

This equation was then turned into an iterative equation as follows:

$$\theta(z_{scatter})_{i+1} = \theta(z_{scatter})_i + \frac{y(z_{target})_i - y(z_{target})}{z_{scatter} - z_{target}} \tag{3.19}$$

Equation 3.19 yields equation 3.7 if the true position of the particle was assumed to be $y(z_{target}) = 0.0$. (Note that the above analysis also holds for the X direction, except that the integral over the magnetic field would not be present.)

The iteration of the trace-back procedure was attempted up to a maximum of 10 times for each track. If the track failed to converge on the target within the above tolerances ($\Delta X = 0.01$ in. or $\Delta Y = 0.001$ in.), the track was thrown out. Like the trace-back from SM3 to $z_{scatter}$, the transverse position of the track was compared with the magnet/beam dump aperture at discrete points in Z. Tracks that hit the beam dump or the magnet were removed from the track list. (Note that aperture cuts were made intentionally loose, i.e. wider than the real aperture.) Finally, only events containing two or more reconstructed tracks that originated from the target region were placed into the pass 1 data summary tapes (DST). The total number of events passing all the cuts was 333,743,381.

Miscellaneous pass 1 processing

In addition to track reconstruction, pass 1 analysis also utilized silicon track information to reconstruct the interaction vertex on a spill by spill basis [38]. This interaction vertex was stored for use by later passes. Also, an attempt at particle identification using information from the electromagnetic and hadronic calorimeter and the muon station was made. However, neither the silicon track information nor the particle identification information were used in this pass of the analysis.

3.2.2 Pass 2

From the set of pass 1 DST's, two smaller data sets were generated, a set containing dimuon events and a set containing dihadron events. In addition to sorting the events, more stringent track quality cuts were applied in pass 2 to the tracks in each event. The cuts that were applied are the following :

- Track momentum (20 GeV/c $< P <$ 800 GeV/c).
- Minimum number of drift chamber hits (≥ 13).
- Minimum number of hodoscope hits (≥ 3).
- Chi square per degree of freedom ($\chi^2/DOF \leq 5$).

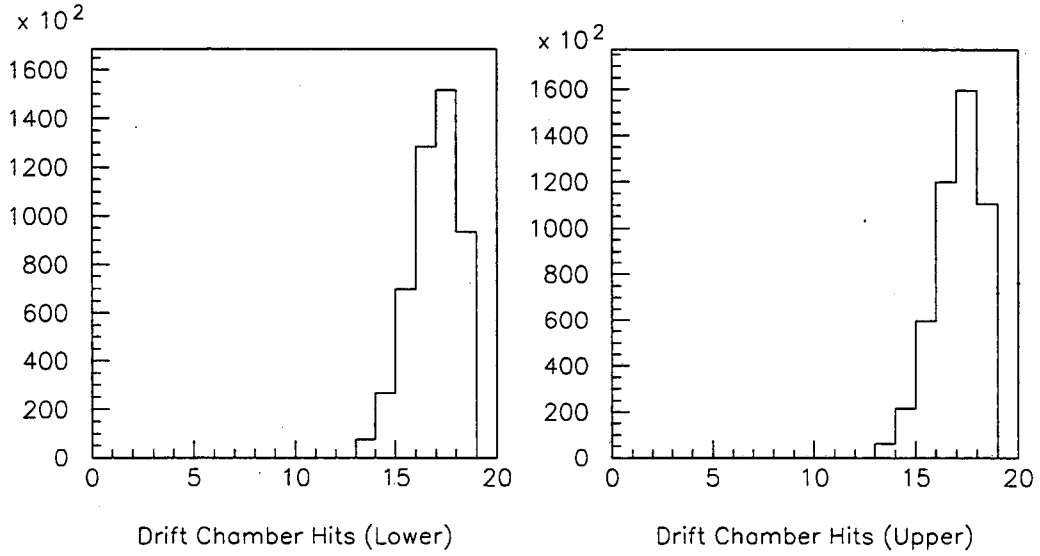

Figure 3.5: Distribution of the number of drift chamber hits in accepted muon tracks. The distribution for tracks in the lower (upper) arm of the spectrometer are on the left (right).

Figures 3.5 and 3.6 show the distribution of drift chamber hits for accepted muon and hadron tracks. It shows that the cut loses very few signal events. Figures 3.7 and 3.8 show the distribution of the number of hodoscope hits (not including the muon station hodoscope planes) for accepted tracks. Again, the distributions show that loss of signal events was minimal. Finally, Figures 3.9 and 3.10 show the distribution of the χ^2 per degree of freedom for accepted tracks. The total event loss due to these track quality cuts was approximately 6% .

Particle identification

In order to sort events into dimuon and dihadron categories, it was necessary to identify the particle type associated with each track in each event. Ideally, exact particle identification would have been desirable, e.g., muon, electron, pion, kaon. However, without the RICH, only incomplete particle identification, muon or electron or hadron, was possible. The key to the particle identification algorithm was the utilization of energy deposition information from the calorimeter. The E789 particle identification algorithm was partitioned into three components, cluster-finding, calorimeter particle identification and spectrometer

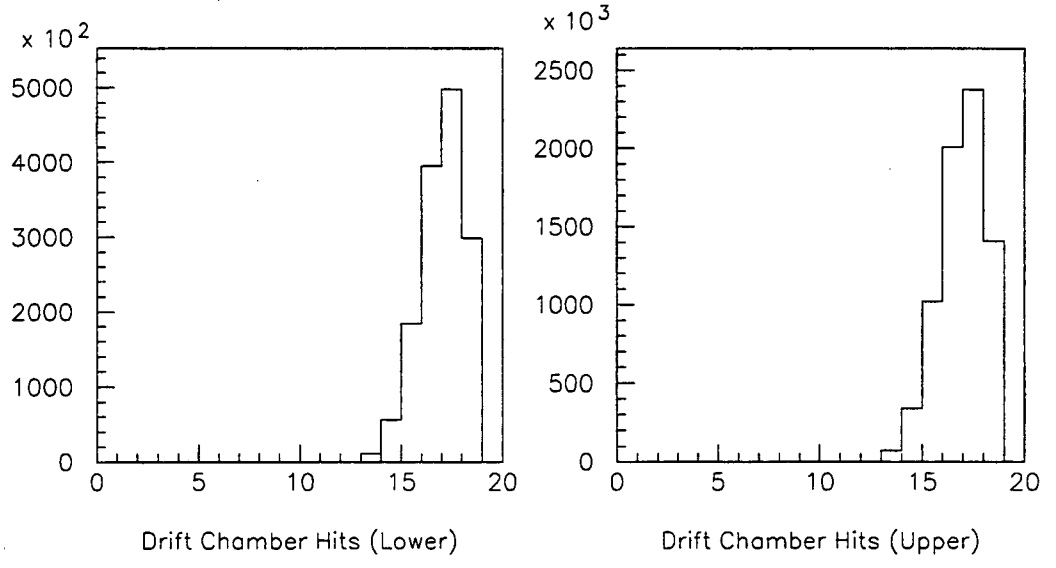

Figure 3.6: Distribution of the number of drift chamber hits in accepted hadron tracks. The distribution for tracks in the lower (upper) arm of the spectrometer are on the left (right).

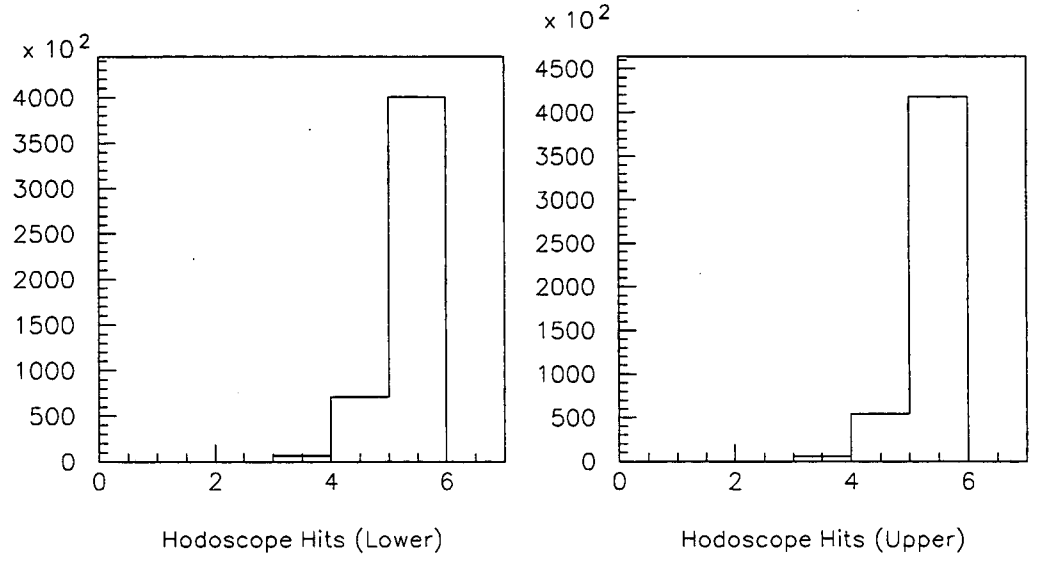

Figure 3.7: Distribution of the number of hodoscope hits in accepted muon tracks. The distribution for tracks in the lower (upper) arm of the spectrometer are on the left (right).

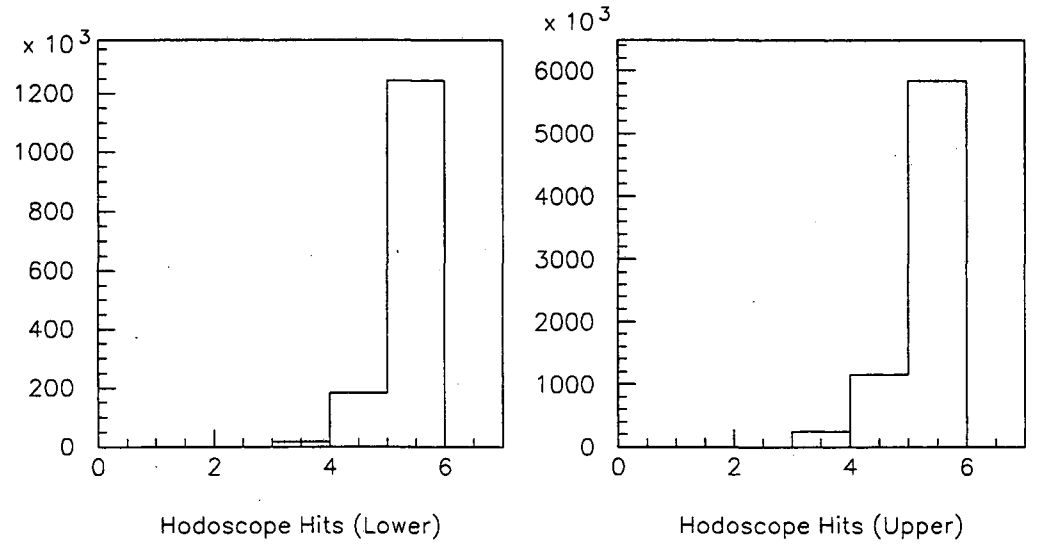

Figure 3.8: Distribution of the number of hodoscope hits in accepted hadron tracks. The distribution for tracks in the lower (upper) arm of the spectrometer are on the left (right).

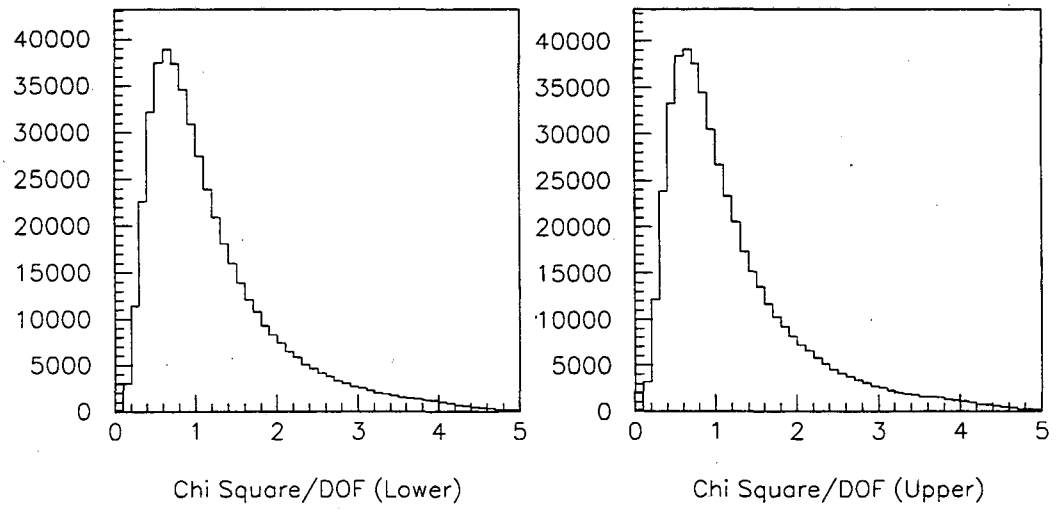

Figure 3.9: Distribution of the χ^2 per degree of freedom for accepted muon tracks. The distribution for tracks in the lower (upper) arm of the spectrometer are on the left (right).

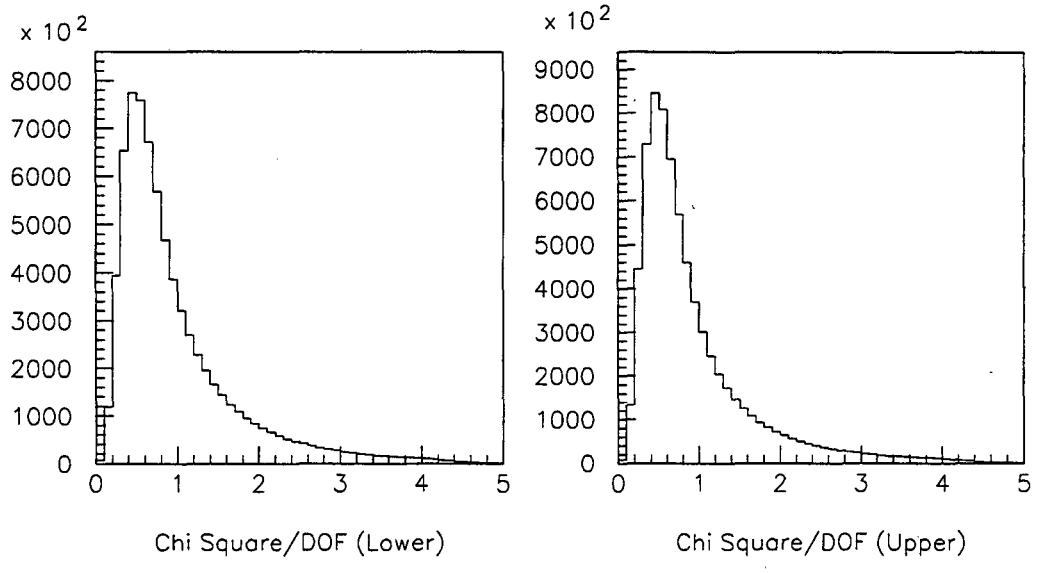

Figure 3.10: Distribution of the χ^2 per degree of freedom for accepted hadron tracks. The distribution for tracks in the lower (upper) arm of the spectrometer are on the left (right).

particle identification.

The first step in the particle identification process was the categorization of the tracks as isolated or overlapping in a process called cluster finding. Figure 3.11 shows the structure of the algorithm and the classification made by the algorithm. The cluster finding process was separated into two separate processes, shown in the figure by the boxes with the rounded corners. The first process handled events with two tracks and the second handled events with three or more tracks. The algorithm classified clusters into one of four categories, shown as square cornered boxes in the Figure 3.11 and listed below:

1. Isolated track.
2. Two overlapping hadron/electron tracks.
3. Two overlapping muon tracks.
4. Unresolvable.

Figure 3.12 is a flow chart of the algorithm used to categorize two-track events. The end product of the algorithm was the classification of tracks into one of the following

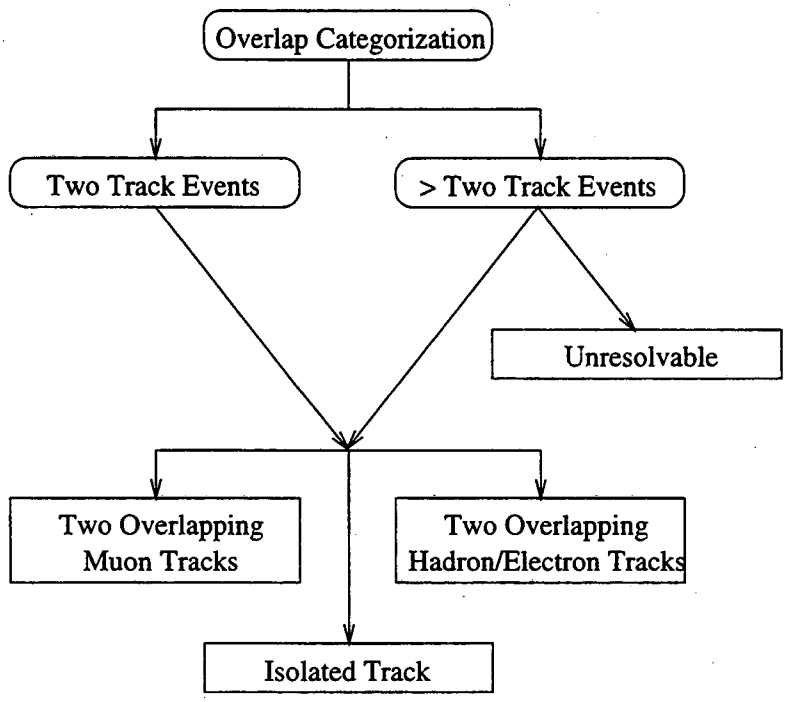

Figure 3.11: Overview of the overlap categorization algorithm.

three categories: isolated tracks, two overlapping hadron/electron tracks or two overlapping muon tracks. The steps in the identification process are outlined below:

1. Determine the Y separation of the two tracks, ΔY, at the EM and hadron calorimeters.

2. Declare tracks as isolated if $\Delta Y > 16$ in. at both calorimeters. This separation allowed for a finite shower size and corresponded to a separation of 2 calorimeter sections. (Recall that the calorimeter was segmented into 12 sections in the Y direction and split in half in the X direction.)

3. Determine the X positions of the two tracks at the face of the last hadron calorimeter section.

4. If both tracks were in different halves (left–right) of the calorimeter and neither was within 20 in. of the dividing line between the two halves of the calorimeter, the two tracks were declared to be isolated. This criteria handles the possibility of shower leakage between the left and right halves of the calorimeter.

5. If neither of the above criteria were satisfied, then the energy deposition in the

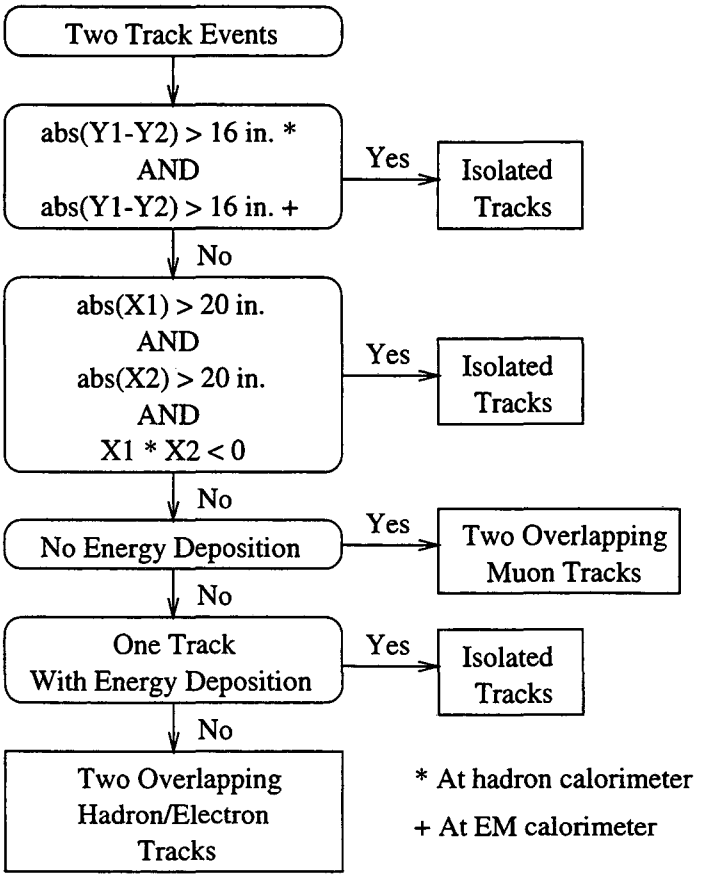

Figure 3.12: Flow chart of the overlap categorization algorithm for two-track events.

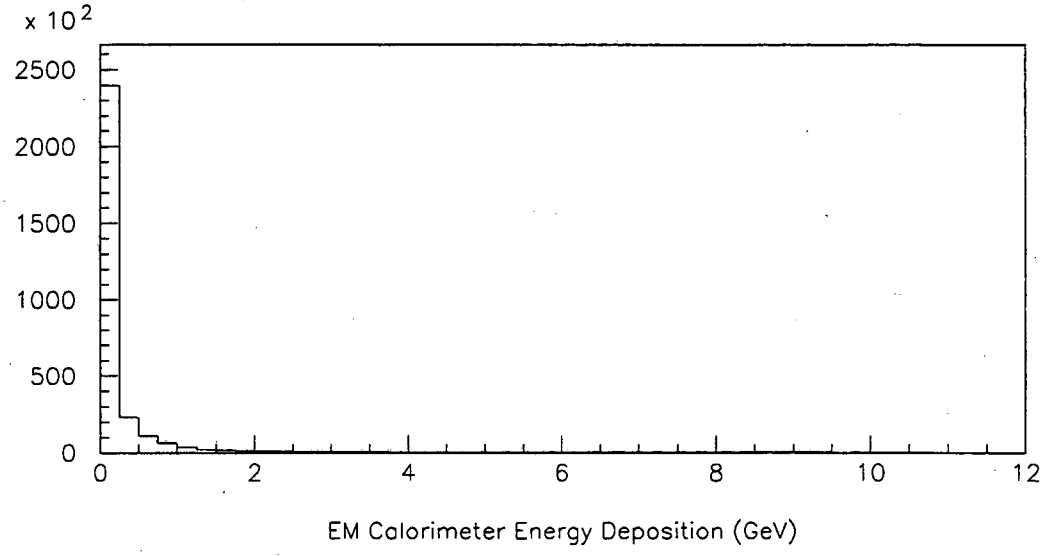

Figure 3.13: Distribution of the energy deposited in the EM calorimeter by good muons.

calorimeter was examined.

6. If the energy deposited around each track in the calorimeter was individually less than 5.0 GeV and 7.5 GeV in the EM and hadron calorimeters respectively, then the two tracks were declared to be two overlapping muons. (The tracks were assumed to be isolated when the energy deposition was determined.)

7. Otherwise, if the energy deposition in the calorimeter for only one of the tracks was greater than these thresholds, the two tracks were declared to be isolated. (The assumption here was that one of the tracks was probably a muon.)

8. Otherwise, the two tracks were declared to be overlapping hadron/electron tracks.

The effect of the cuts on EM and hadron calorimeter energy deposition when deciding if two overlapping tracks were two muons can be determined by looking at the energy deposited by good muons in the EM and hadron calorimeters. Figures 3.13 and 3.14 show the energy deposited in the EM and hadron calorimeters by good muon tracks, where good is defined to be an isolated track with hits in all of the muon hodoscope and proportional counter planes.

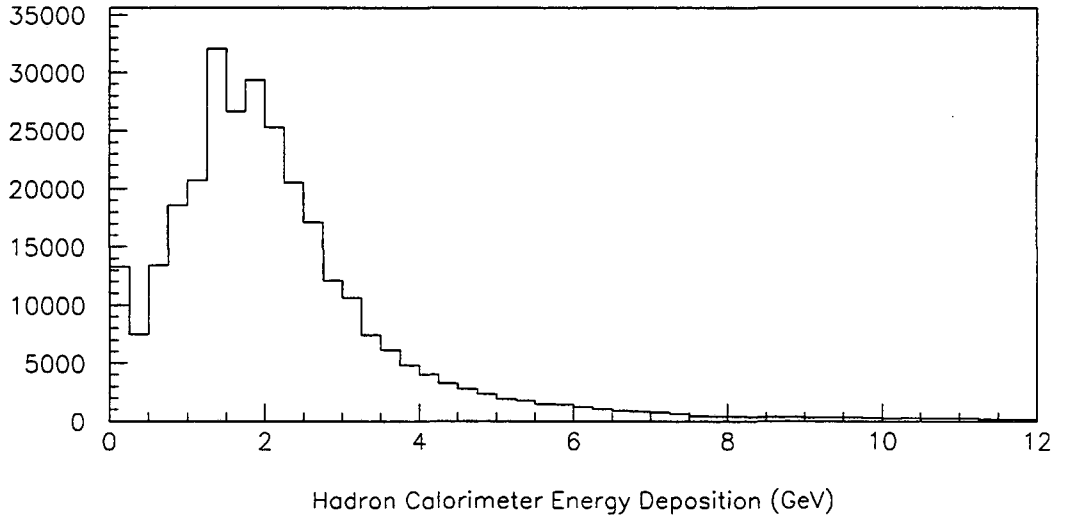

Figure 3.14: Distribution of the energy deposited in the hadron calorimeter by good muons.

The cluster-finding algorithm for events with three or more tracks is shown in Figure 3.15. The steps in the algorithm are outline below:

1. All tracks in events with greater than 5 tracks were labeled as unresolvable.
2. For all other events, tracks were sorted into clusters, where a cluster was defined to be all tracks that were within 16 in. in Y (at the hadron calorimeter) of each other and that were either in the same X half-plane or within 20 in. of the dividing line between the two X half-planes.
3. All tracks in clusters with three or more tracks were labeled as unresolvable.
4. All tracks in two-track clusters were categorized using the two track algorithm mentioned in the previous paragraph.
5. All tracks in clusters with one track were categorized as isolated tracks.

Once tracks were classified into clusters, particle identification was attempted using the profile of the energy deposited in the calorimeter. The two keys to the identification of particles by the calorimeter were the $(E-P)/\sqrt{P}$ ratio and the EM fraction. Electrons and hadrons deposit all of their energy within the calorimeter, whereas muons pass through

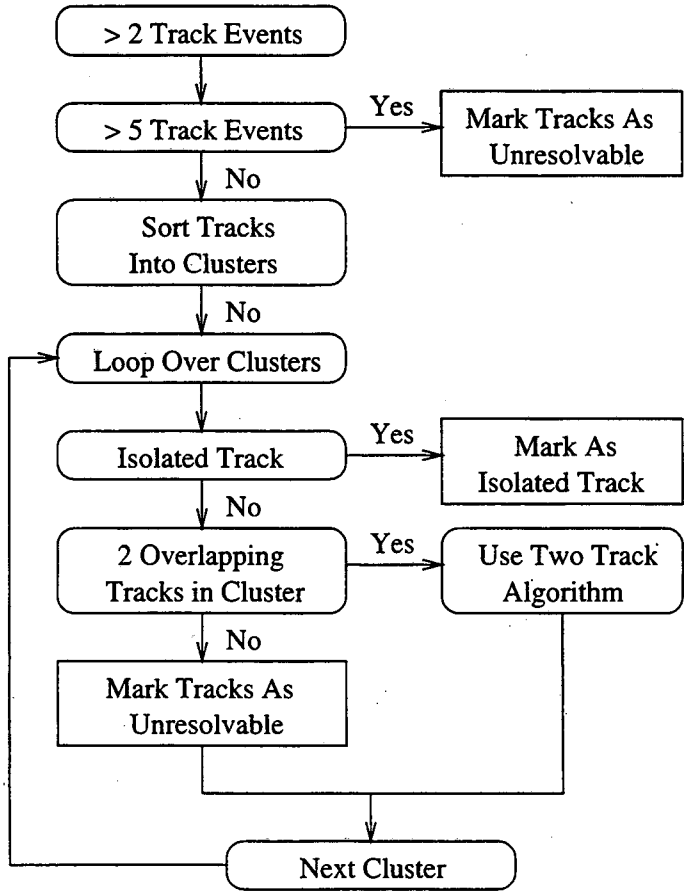

Figure 3.15: Flow chart of the overlap categorization algorithm for events with three or more tracks.

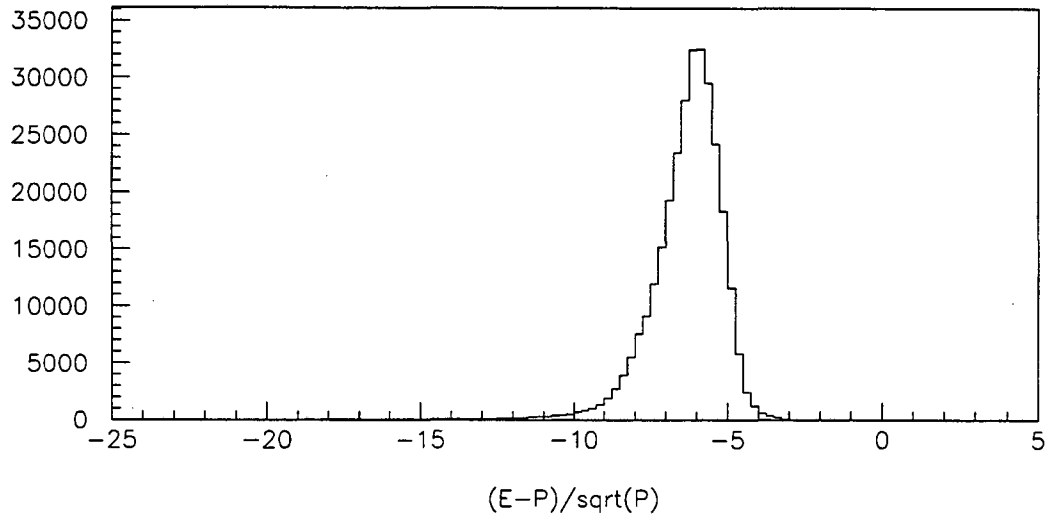

Figure 3.16: Distribution of $(E-P)/\sqrt{P}$ for good muon tracks.

the calorimeter with relatively little energy deposition. (See section 2.4.8 and 2.4.8 for the amount of material in radiation lengths and hadronic interaction length in the calorimeter sections.) This is the result of the fact that hadrons interact strongly with nuclei in the calorimeter and electrons, being relatively light, lose energy in material through bremstrahlung. In contrast, muons only interact electromagnetically and weakly with the material in the calorimeter. As a result, the $(E-P)/\sqrt{P}$ ratio, where E is the energy deposited by a track in the calorimeter and P is the momentum of the track as measured by SM3, should be centered around zero for electrons and hadrons. However, the ratio should be negative for muons. Figure 3.16 shows the distribution of $(E-P)/\sqrt{P}$ for tracks identified as good isolated muons (where good means that the track was isolated and had hits in all three muon hodoscope planes and hits in both muon proportional counters). Figure 3.17 shows the distribution for tracks identified as isolated hadrons with no hits in the muon hodoscopes or muon proportional counters (good hadrons). (From this plot, it is clear that the calibration of the calorimeter was not optimal; however, given the cuts used for isolating hadrons, $|(E-P)/\sqrt{P}| < 3.2$, its clear that this was not a problem. Note also that the linearity of the calorimeter calibration was fairly good as can be seen in the E versus P plot for isolated hadrons, shown in Figure 3.18, so the energy–momentum relationship is

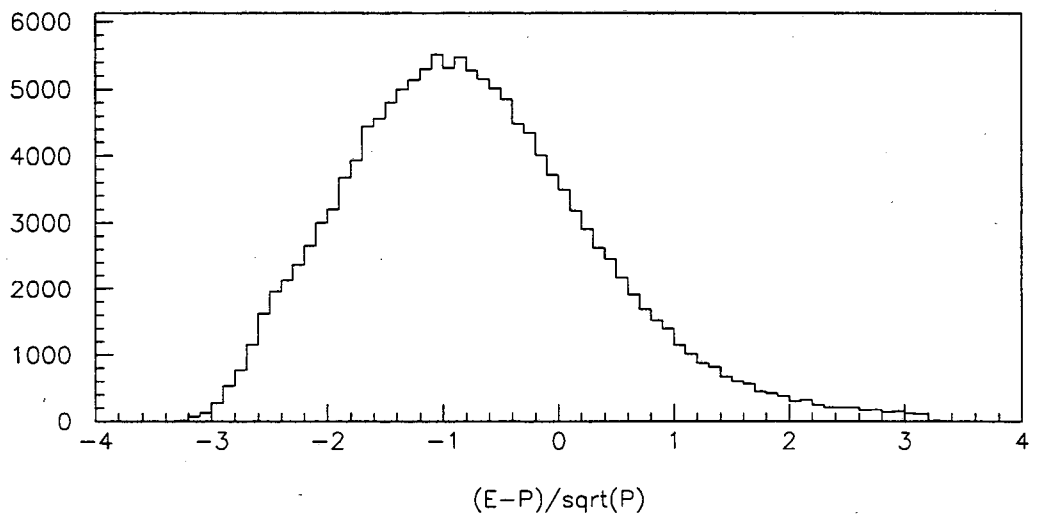

Figure 3.17: Distribution of $(E-P)/\sqrt{P}$ for good hadron tracks.

reasonable.) Given the different energy deposition characteristic in the calorimeter, the value of $(E-P)/\sqrt{P}$ was a way of separating muons from hadrons and electrons.

Once muons were separated from the hadrons and electrons, a method of separating electrons from hadrons was required. Since electrons lose energy rapidly in material because of bremstrahlung, most of their energy was deposited in the EM calorimeter. Hadrons on the other hand deposit more of their energy in the hadron calorimeter. Hence, the ratio of the energy loss in the EM calorimeter to the total energy loss in the calorimeter, the EM fraction, was peaked at one for electrons and much more broadly distributed for hadrons.

An overview of the calorimeter particle identification algorithm and its output is shown in Figure 3.19. The algorithm was divided into three components:

1. Isolated track identification.

2. Two overlapping non-muon track identification.

3. Two overlapping track identification (with one or more muon-like).

The isolated track identification component of the algorithm handled track clusters which were identified as isolated tracks or two overlapping muon tracks by the cluster-finding code. The last two components of the algorithm handled track clusters that had been identified

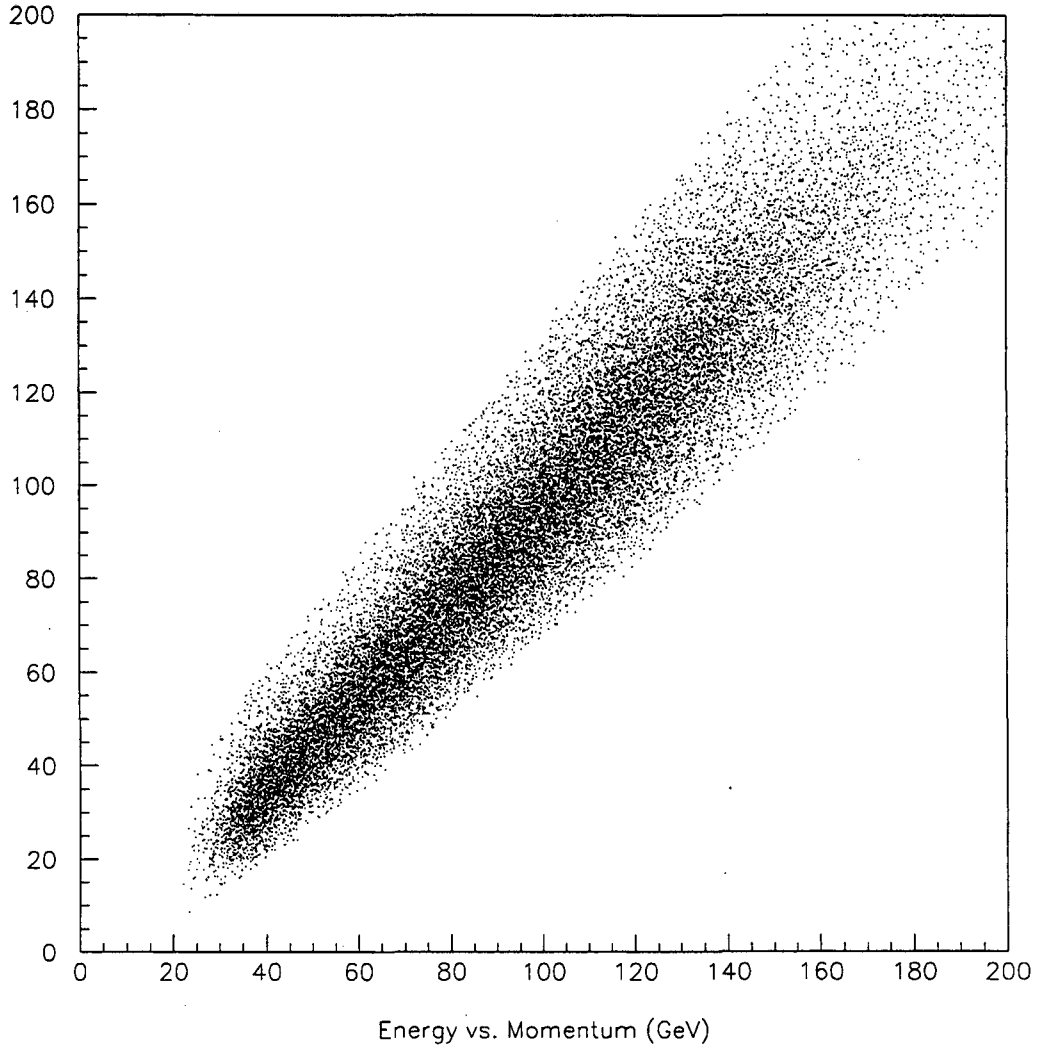

Figure 3.18: Distribution of E versus P for good hadron tracks. (Units are in GeV.)

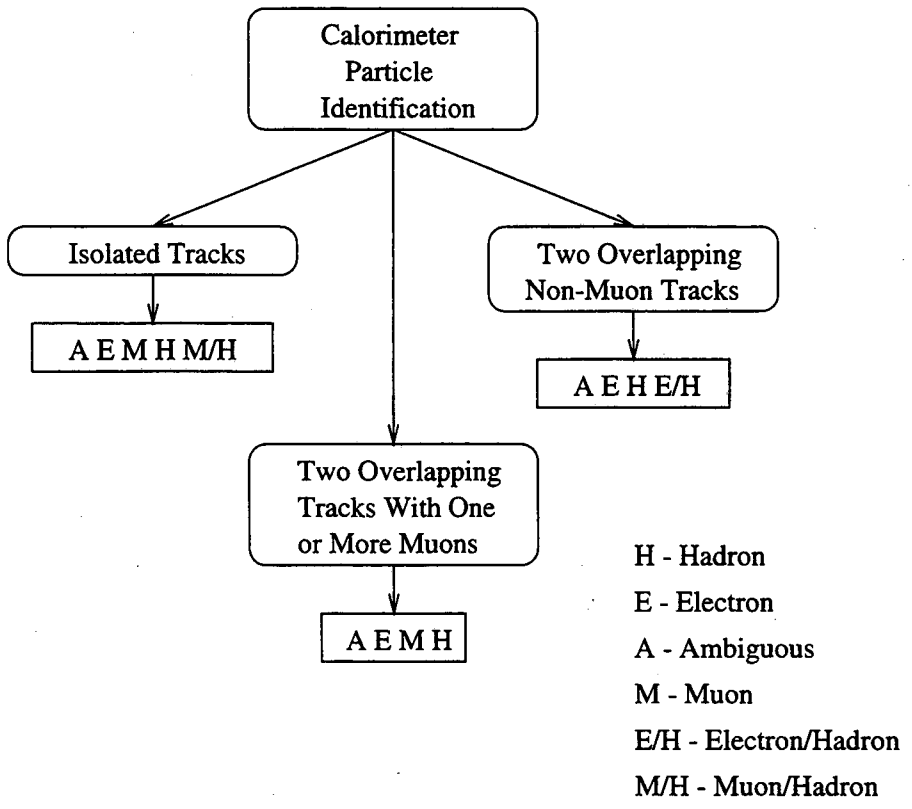

Figure 3.19: Overview of the calorimeter particle identification algorithm and its outputs.

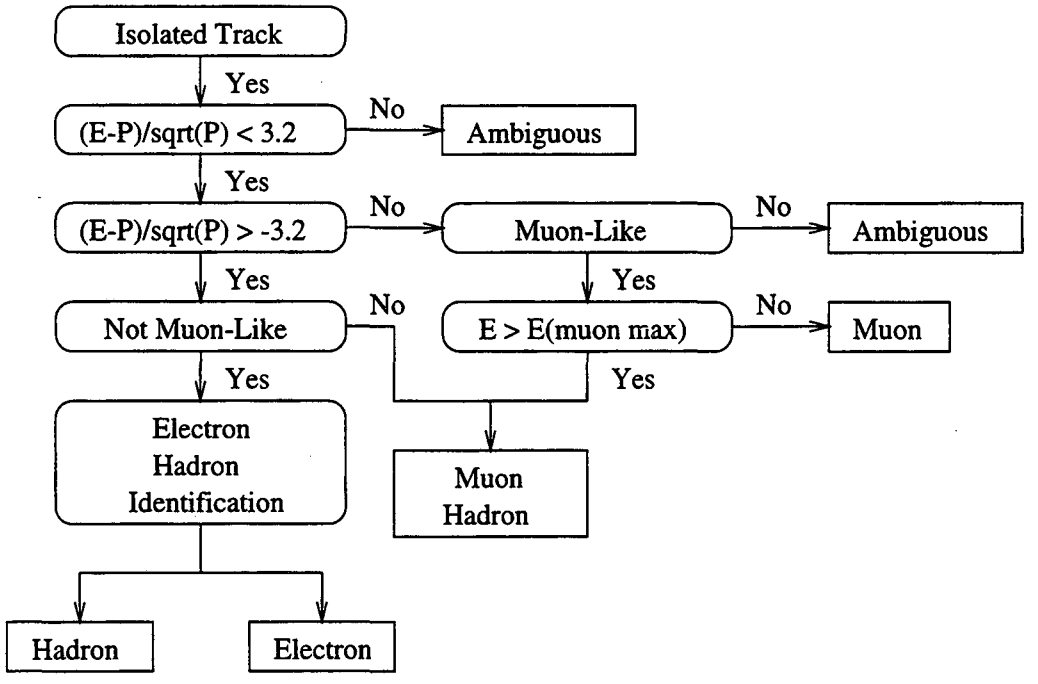

Figure 3.20: Flow chart of the calorimeter isolated particle identification algorithm.

as two overlapping hadron/electron tracks by the cluster-finding code. The tracks in each cluster were placed into one of the following six categories:

1. Hadron
2. Electron
3. Muon
4. Hadron/Electron
5. Muon/Hadron
6. Ambiguous

Note that all tracks in the unresolved clusters were identified as ambiguous.

The algorithm used by the calorimeter particle identification code to identify isolated tracks as muons, electrons or hadrons is shown in Figure 3.20. The steps in the algorithm are as follows:

1. The ratio $(E-P)/\sqrt{P}$ was calculated, where E is the energy deposited in the calorimeter in the region around the track and P is the momentum of the track as measured by SM3.

2. If the ratio was greater than 3.2, the track was classified as ambiguous.

3. If the ratio was less than -3.2 and the track was not muon-like then the track was classified as ambiguous. The assignment of the muon-like/not muon-like label was based on the number of hits in the muon station that were consistent with the track. A muon-like track required at least three hits in the muon station, with at least one hit being in one of the muon hodoscope planes.

4. If the ratio was less than -3.2 and the track was muon-like and deposited an amount of energy that was consistent with a muon ($E(\mu)_{max} < 12.5$ GeV), then the track was classified as a muon.

5. If the ratio was less than -3.2 and the track was muon-like and deposited an amount of energy that was not consistent with a muon, then the track was classified as both a muon and a hadron.

6. If the ratio was greater than -3.2 and the track was muon-like, then the track was classified as both a muon and a hadron.

7. If the ratio was greater than -3.2 and the track was not muon-like, then the track was classified as either a hadron or an electron by the electron–hadron identification code (discussed in the next paragraph).

The effects of the $E(\mu)_{max} < 12.5$ GeV cut for muons can be seen by looking at the distribution of energy deposition in the calorimeter by good muons shown in Figure 3.21. Note also that the isolated track identification algorithm was also used to identify the particles in two overlapping tracks where both particles had been tentatively identified as muon-like by the cluster-finding code.

The hadron–electron identification code used the EM fraction, defined as the ratio of the energy deposited in the electromagnetic calorimeter and the total energy deposited in both calorimeters by the track, to distinguish electrons from hadrons. A flow chart of the algorithm is shown in Figure 3.22. If the EM fraction was less than 0.95 then the track

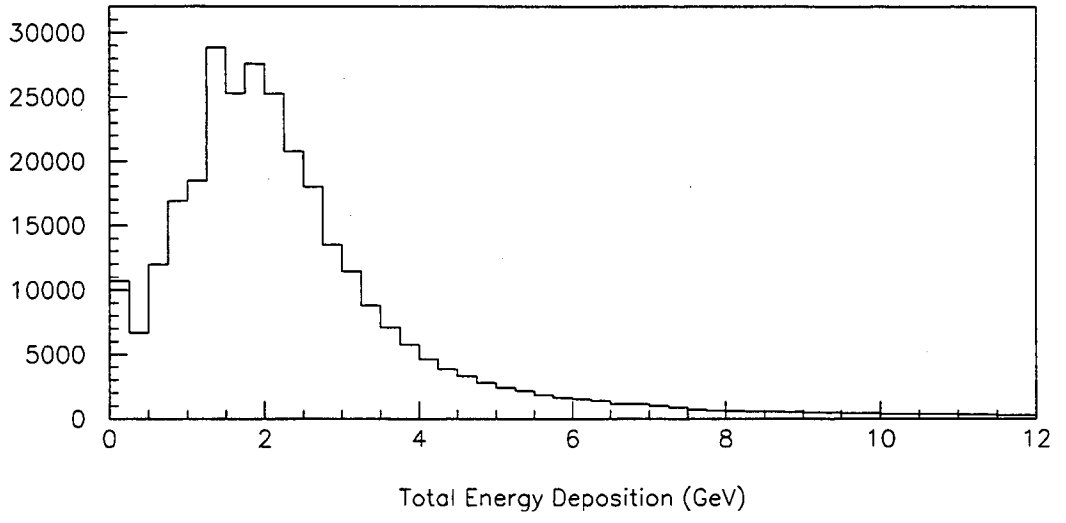

Figure 3.21: Distribution of the total energy deposited by good muons in the calorimeter.

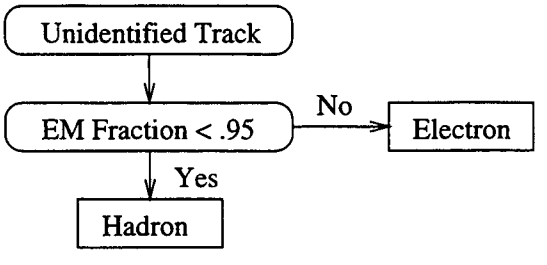

Figure 3.22: Flow chart of the calorimeter electron–hadron particle identification algorithm.

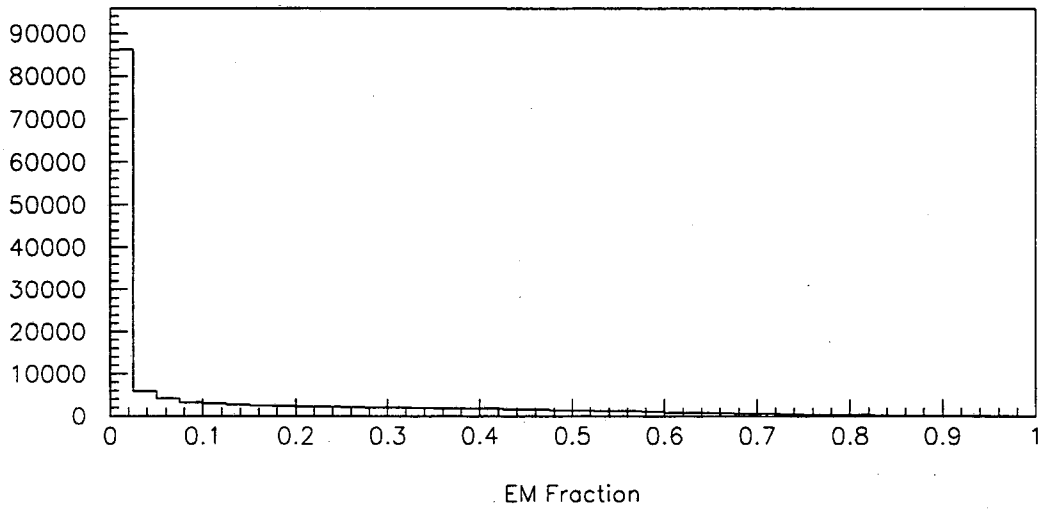

Figure 3.23: Distribution of the EM fraction for good hadrons.

was identified as a hadron. If the EM fraction was greater than 0.95, it was identified as an electron. Figure 3.23 shows a plot of the EM fraction for good hadrons. The less than 0.95 cut clearly picks up most if not all of the hadrons.

The second component of the calorimeter particle identification code, used to identify two overlapping non-muon tracks (as determined by the cluster finding code), is shown in Figure 3.24. The algorithm proceeded in the following steps:

1. The ratio $(E_{sum} - P_{sum})/\sqrt{P_{sum}}$ was calculated, where E_{sum} is the energy in the calorimeter in the region around the two tracks and P_{sum} is the scalar sum of the momenta of the two tracks.

2. If the ratio was greater than 3.2, then both particles were identified as ambiguous.

3. If the ratio was greater than -3.2, then the tracks were passed to the overlapping electron–hadron identification code. (See Figure 3.25.)

4. If the ratio was less than -3.2, then the quantity $|(E_{sum} - P_i)/\sqrt{P_i}|$ was calculated for the i^{th} track.

5. If $|(E_{sum} - P_1)/\sqrt{P_1}|$ was less than 3.2, then the energy in the calorimeter was assigned

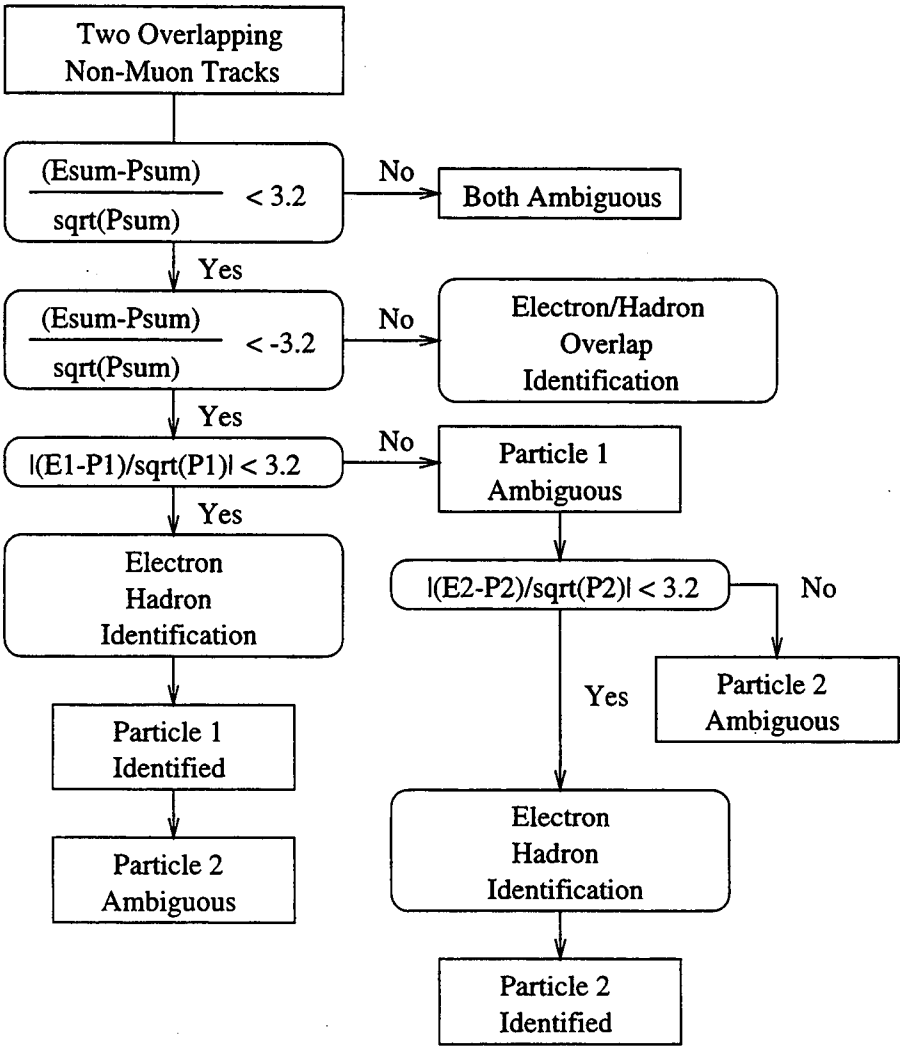

Figure 3.24: Flow chart of the calorimeter overlapping non-muon track particle identification algorithm.

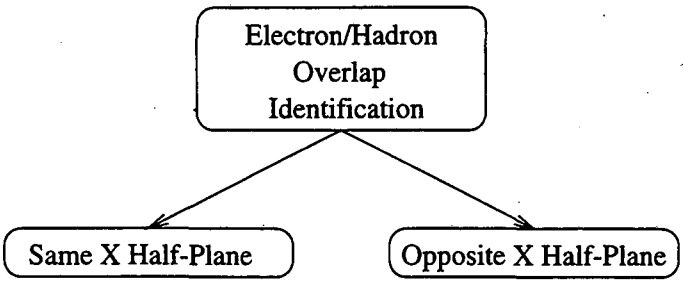

Figure 3.25: Flow chart of the overlapping electron–hadron track calorimeter particle identification algorithm.

to the first track, which was then identified as either an electron or a hadron using the electron–hadron identification algorithm. (See Figure 3.22.) The second track was then tagged as ambiguous.

6. If $|(E_{sum} - P_1)/\sqrt{P_1}|$ was greater than 3.2 and $|(E_{sum} - P_2)/\sqrt{P_2}|$ was less than 3.2, then the first track was tagged as ambiguous and the second track was identified as either an electron or a hadron.

7. If both $|(E_{sum} - P_i)/\sqrt{P_i}|$'s were greater than 3.2, then both tracks were tagged as ambiguous.

The asymmetry in the identification code with respect to tracks 1 and 2 was because track 1 was always a higher quality track than track 2.

The overlapping electron–hadron identification code, used by the above code (see Figure 3.24), was split into two components, shown in Figure 3.25. The first part handled the identification of two tracks that were in opposite X half-planes. The second handled the case where the two tracks were in the same X half-plane.

Figures 3.26 is a flow chart of the algorithm that handled two tracks in opposite X half-planes. The steps in the identification were as follows:

1. Particle 1 was tentatively identified using the electron–hadron identification algorithm shown in Figure 3.22. However, the energies in the separate calorimeters were calculated assuming a zero radius shower.

2. Next, the ratio $(E_1 - P_1)/\sqrt{P_1}$ was calculated assuming a zero radius shower.

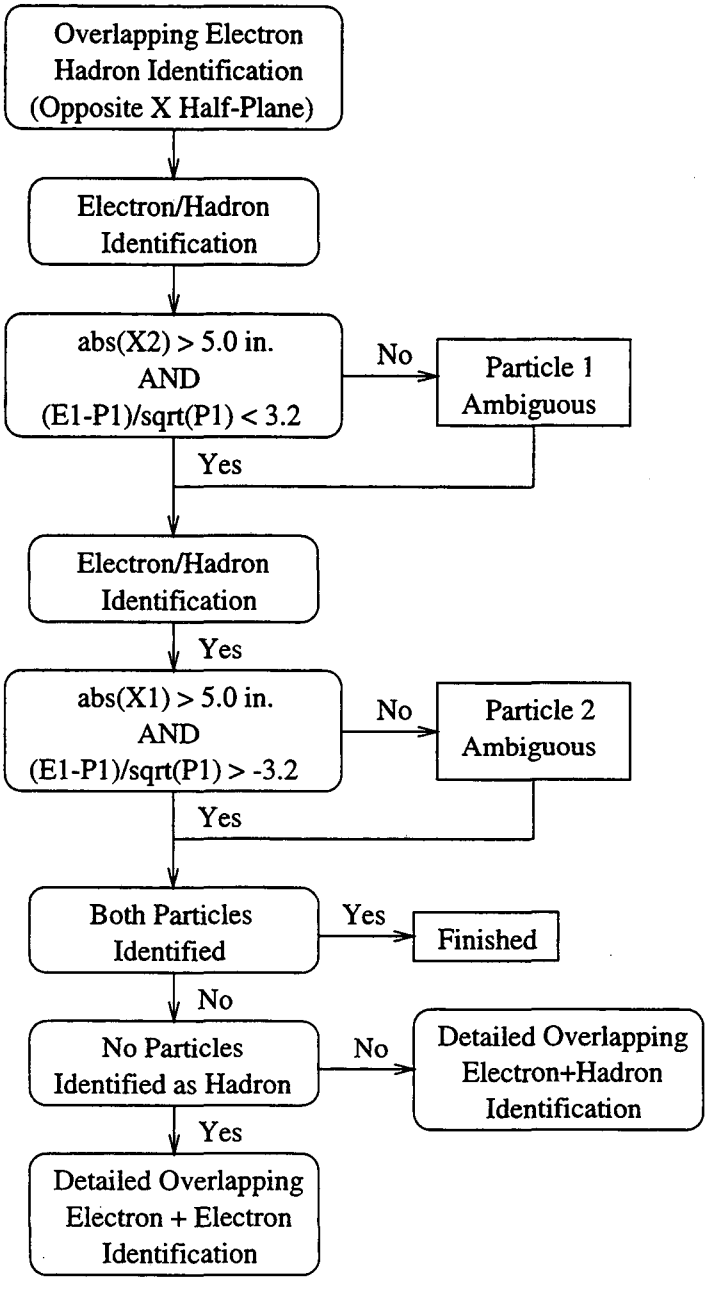

Figure 3.26: Flow chart of the opposite X half-plane overlapping electron–hadron identification algorithm.

3. If the ratio was greater than 3.2 or particle 2 was less than 5 in. from the left–right dividing line then the identity of particle 1 was reset to ambiguous.

4. Next, particle 2 was tentatively identified using the electron–hadron identification algorithm, again assuming a zero radius shower.

5. If the $(E_1 - P_1)/\sqrt{P_1}$ ratio was greater than 3.2 and particle 1 was less than 5 in. from the left–right dividing line, then the identity of particle 2 was reset to ambiguous.

6. If both particles were identified (i.e., not identified as ambiguous), then the two tracks were declared to be identified.

7. Otherwise, if one of the tracks was identified as a hadron and the other was ambiguous, then the two tracks were identified using the detailed electron–hadron identification code in Figure 3.27.

8. Otherwise, if neither track was identified as a hadron, then the two tracks were identified using the detailed electron–electron identification code. (See Figure 3.28.)

The detailed overlapping electron–electron identification algorithm, shown in Figure 3.27, calculated the EM fraction for the combined pair of tracks. If the EM fraction was greater than 0.95, then both tracks were identified as electrons. If the EM fraction was less than 0.95, then the preliminary particle identification, made by the zero shower radius approximation outlined in the previous paragraph, was examined. If neither track was identified as an electron, both particles were identified as hadrons. If one of the tracks was identified as an electron, then a modified EM fraction was calculated for each track. This modified EM fraction was the ratio of the energy deposited in the first section of the EM calorimeter and the energy deposited in all four sections of the EM calorimeter. If the ratio was less than 0.95, then the track was identified as a hadron, otherwise it was identified as an electron and a hadron.

The detailed overlapping electron–hadron identification code, shown in Figure 3.28, used the modified EM fraction to identify the ambiguous tracks flagged by the overlapping electron–hadron identification code. (See Figure 3.26.) If the modified EM fraction was less than 0.95 for the ambiguous track, then it was identified as a hadron, otherwise, it was identified as both an electron and a hadron.

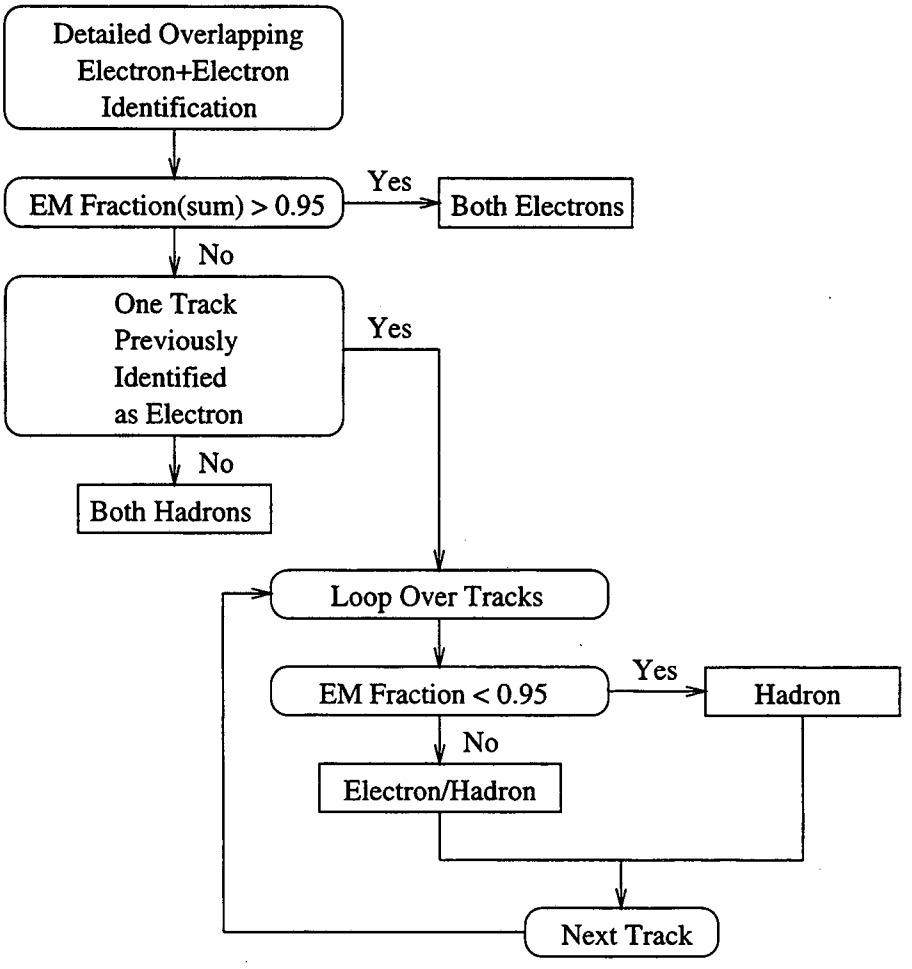

Figure 3.27: Flow chart of the detailed opposite X half-plane overlapping electron–electron identification algorithm.

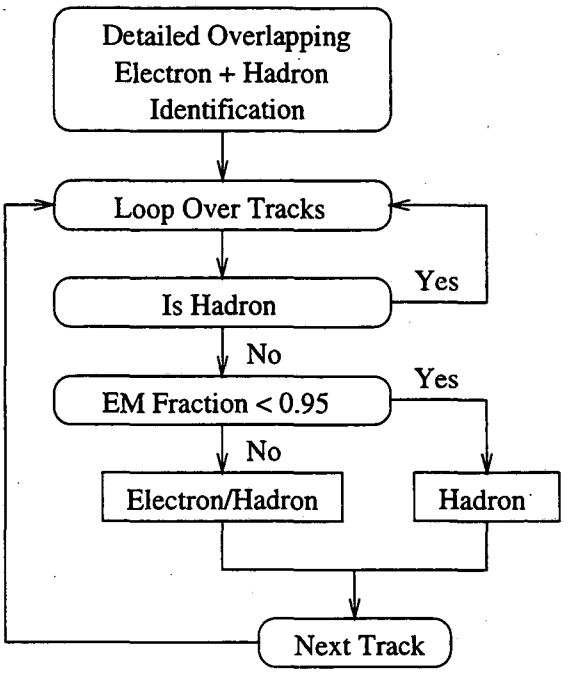

Figure 3.28: Flow chart of the detailed opposite X half-plane overlapping electron–hadron identification algorithm.

The same X half-plane overlapping electron–hadron identification code in Figure 3.29 calculated the EM fraction for the combined track pair. If the EM fraction was greater than 0.95 then both tracks were identified as electrons. Otherwise both tracks were identified as hadrons.

The final component of the calorimeter particle identification code was the component that handled two overlapping tracks where one or more of the tracks was identified as a muon by the muon station (three hits in the muon station, with at least on hit being in one of the hodoscope planes). Figure 3.30 shows the flow chart for the algorithm. The steps were as follows:

1. If both tracks were identified as muons by the muon station and the energy deposited in the calorimeter by the two tracks was less than 20 GeV, then both tracks were identified as muons.

2. If both tracks were identified as muons by the muon station and the energy deposited was greater than 20 GeV, then both tracks were declared to be ambiguous.

3. If only one track was identified as a muon by the muon station, then the $(E-P)/\sqrt{P}$

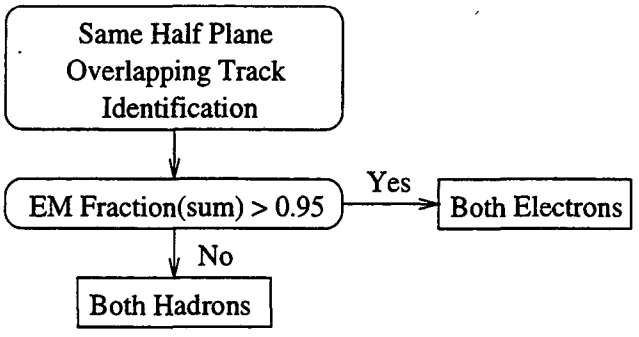

Figure 3.29: Flow chart of the same X half-plane overlapping electron hadron plane identification algorithm.

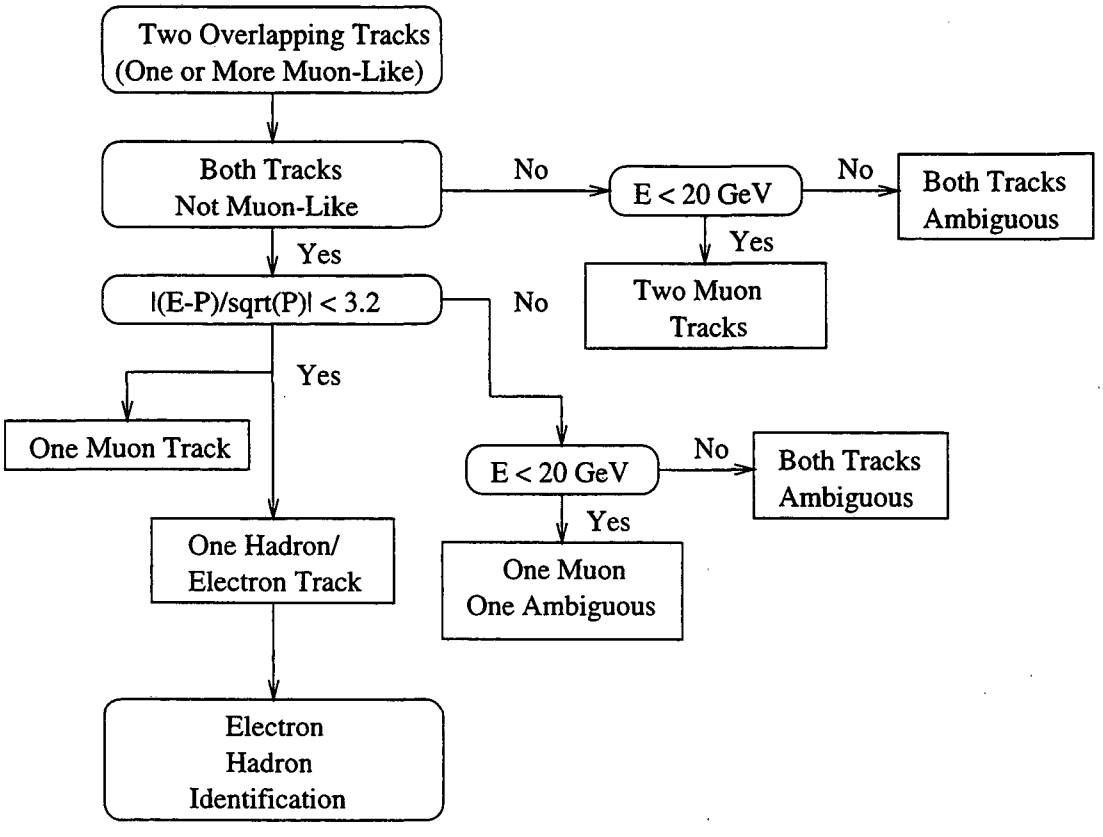

Figure 3.30: Flow chart of the algorithm for the calorimeter overlapping track particle identification algorithm where one or more tracks is a muon.

ratio was calculated for the other track. In the calculation of this ratio, the average energy deposited by muons was subtracted from the energy in the calorimeter.

4. If the absolute value of the ratio was less than 3.2 then the muon track was declared to be a muon and the other track was passed to the electron–hadron identification code to be classified as either a hadron or an electron.

5. If the absolute value of the ratio was greater than 3.2 and the total energy in the calorimeter was less than 20 GeV then the muon track was declared to be a muon and the other track was declared to be ambiguous.

6. If the absolute value of the ratio was greater than 3.2 and the total energy in the calorimeter was greater than 20 GeV then both tracks were declared to be ambiguous.

The previous paragraphs described the calorimeter particle identification code. The final assignment of particle identities was made using the information from the calorimeter code and the hits in the muon station. A flow chart of the final particle identity assignment algorithm is shown in Figure 3.31. Muons were required to register hits in at least 3 planes in the muon station, of which one hit must be a muon hodoscope hit. Particles which were not identified as muons and were identified by the calorimeter as an electron and not a hadron were designated as electrons. Conversely, particles which were not identified as muons and were identified by the calorimeter as hadrons and not electrons were tagged as hadrons. Finally, all particles not falling into any of these three categories were identified as ambiguous. Additional, information on the performance of the particle identification algorithm can be found in reference [47]. Once the particles in each event were identified, the events were sorted into dimuon and dihadron events.

Dimuon selection

The goal of the dimuon selection was to isolate those events that contained dimuons from $J/\psi \rightarrow \mu^+\mu^-$ decays. This meant selecting dimuon events that had the invariant mass of the two muons near the mass of the J/ψ (3.096 GeV) [37]. For the dimuon set, events were placed into three classes, two-body, three-body and N-body, depending on the number of reconstructed tracks in the event. All N-body events containing opposite-sign dimuon tracks were retained. All three-body events containing only two muons were retained if the muons were oppositely charged and had an invariant mass between 2.0 GeV and 6.0 GeV. All

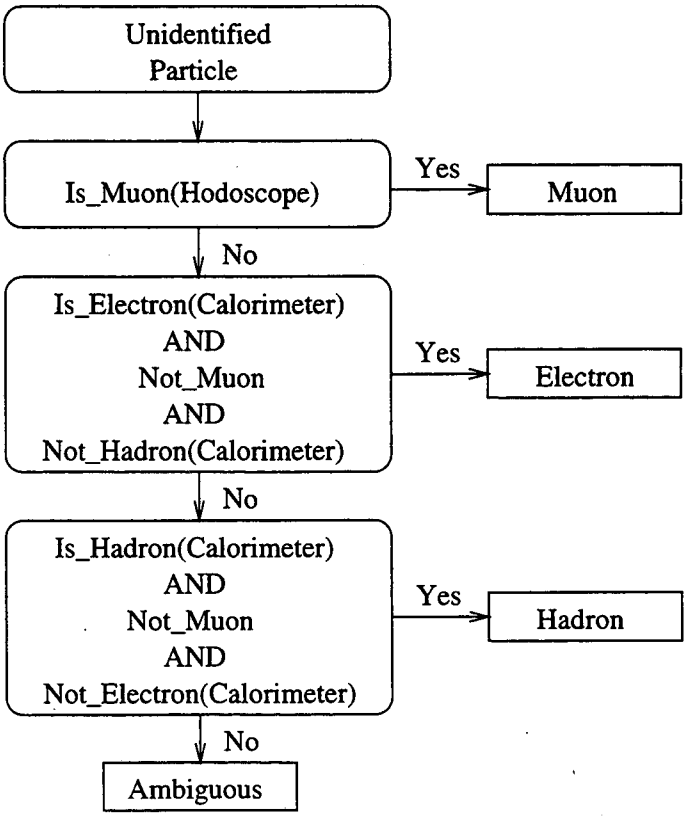

Figure 3.31: Final particle identification algorithm.

three-body events containing three muons were retained if they contained oppositely charged muons. All two-body events containing oppositely charged muons with invariant mass between 2.0 GeV and 6.0 GeV were retained. The resulting data set contained 7,983,432 events. (Note that trigger information was not used in the selection of the events.)

Dihadron selection

For the dihadron set, events were again placed into two-body, three-body and N-body classes. For two-body events, all opposite-sign dihadron events with invariant mass between 5.0 GeV and 6.0 GeV were retained. Three-body events were retained if they contained an opposite-sign hadron pair in the 5.0 GeV and 6.0 GeV mass region. For N-body events, only events with two or three reconstructed hadrons with a pair of opposite-sign hadron tracks in the 5.0 GeV and 6.0 GeV mass region were retained. In the calculation of the invariant mass, the possible particle assignments made were π-π, π-K, K-π, and K-K. Note that the pp mass combination was not one of the particle assignments. The resulting data set contained 7,608,808 events. (Note that trigger information was not used in the selection of the events.)

3.2.3 Pass 3

The primary goal of pass 3 was to reduce the size of the dimuon and dihadron data sets. This was accomplished by sorting the events into one of two categories, event with two uncorrelated hadrons (muons), which are background events, and events with two hadrons (muons) originating from the decay of a single particle, the signal events. This was accomplished by attempting to reconstruct a decay vertex for each pair of hadrons (muons) in each event. This required the reconstruction of the trajectories of the hadrons (muons) in the silicon micro-vertex detector.

SM12 Aperture Cuts

In order to reconstruct the trajectory of each particle in the silicon micro-vertex detector, an accurate estimate of the expected position of each spectrometer track at each silicon detector plane was required. This required an accurate trace-back of each track through the SM12 and beam dump region. This in turn required a more accurate characterization of the field within the SM12 volume than was available in pass 1 and pass 2.

Z (in)	$abs(Y_{min})$ (in)	$abs(Y_{min})$ (in)
68.0	2.50	21.25
104.0	3.75	18.25
176.0	4.75	20.25
236.0	4.75	21.25

Table 3.1: The apertures for SM12 magnet used in the pass 3 analysis.

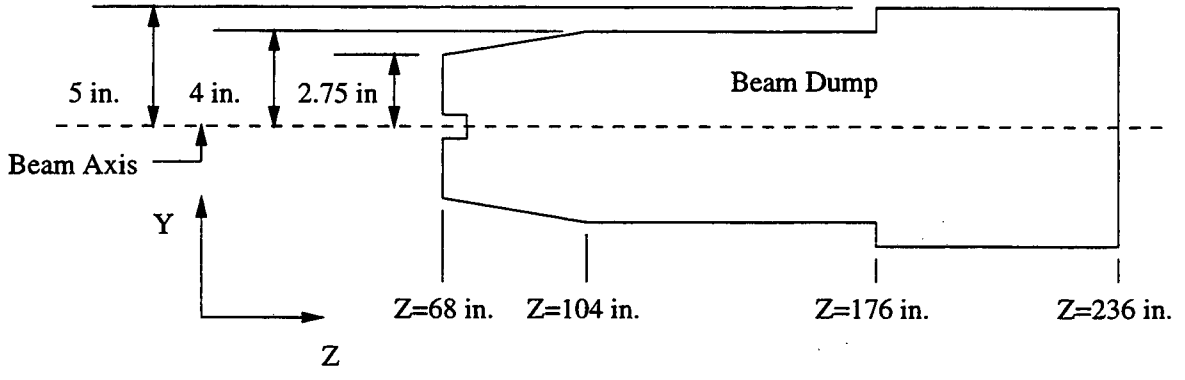

Figure 3.32: Schematic of the Y–Z profile of the beam dump.

With the better understanding of the magnetic field available in pass 3 processing, it was also possible to tighten the SM12–beam dump aperture cuts.

The apertures used in pass 3 are shown in Table 3.1. (Note that in the analysis code, adjustments were made for the drop in the beam dump position which was mentioned in section 2.4.3.) These apertures should be compared with the profile of the beam dump shown in Figure 3.32. As before, an iterated swim using 18 in. steps was made through SM12. The fraction of dimuon events surviving the tighter aperture cuts was significantly lower than the fraction of dihadron events ($\sim$ 10% versus $\sim$ 90%). The source of the large difference can be seen by looking at the distributions of the hadron (muon) positions at the locations of the aperture cuts. Figures 3.33 and 3.34 show the distribution of hadron and muon events at $Z = 104$ in., $Z = 176$ in., and $Z = 236$ in. for the hadrons (muons) in the upper and lower arms of the spectrometer. The hadron distributions are much sharper than the muon distribution because the muons can traverse sections of the beam dump, scatter and lose energy, before propagate through the rest of the spectrometer. In contrast, the hadrons are stopped by the beam dump.

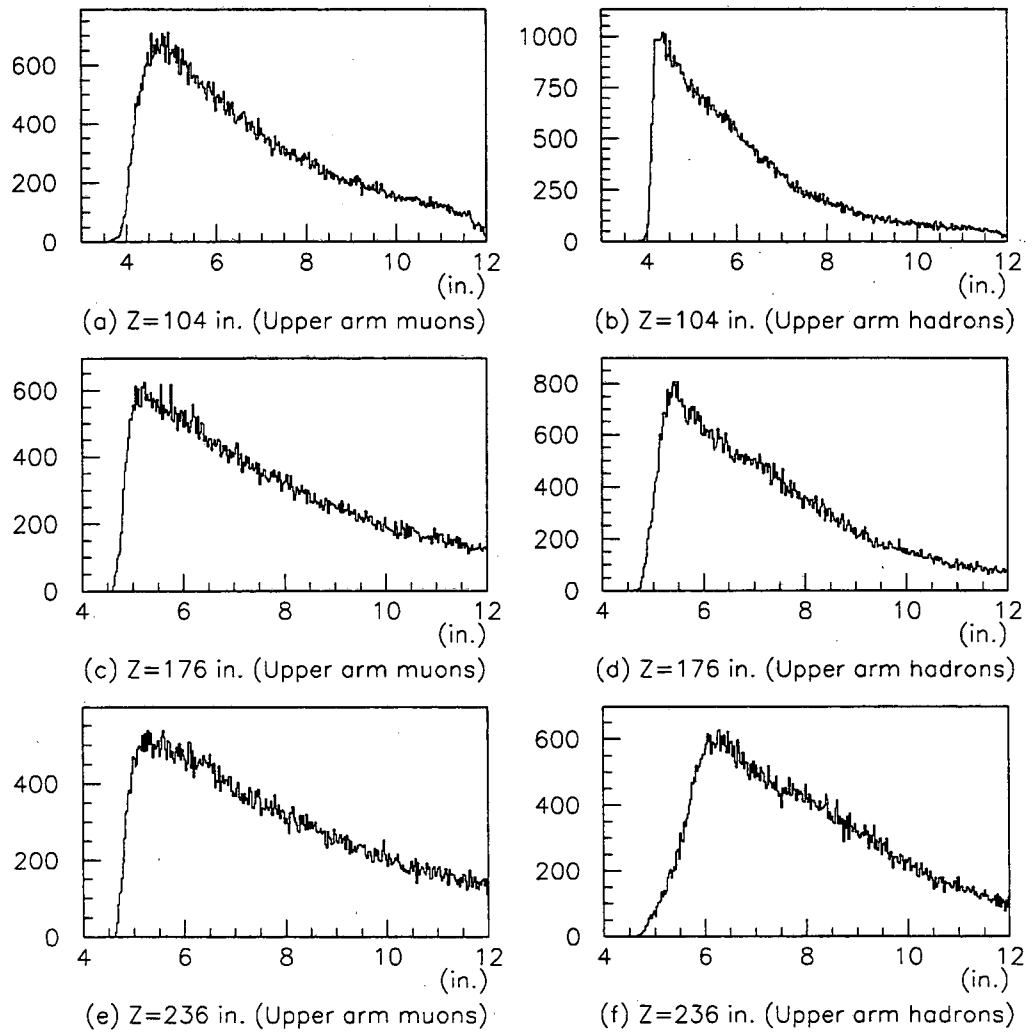

Figure 3.33: Distribution of track Y-positions in the upper arm of the spectrometer at $Z = 104$ in., $Z = 176$ in., and $Z = 236$ in. for the muon (left) and hadron (right) data sets.

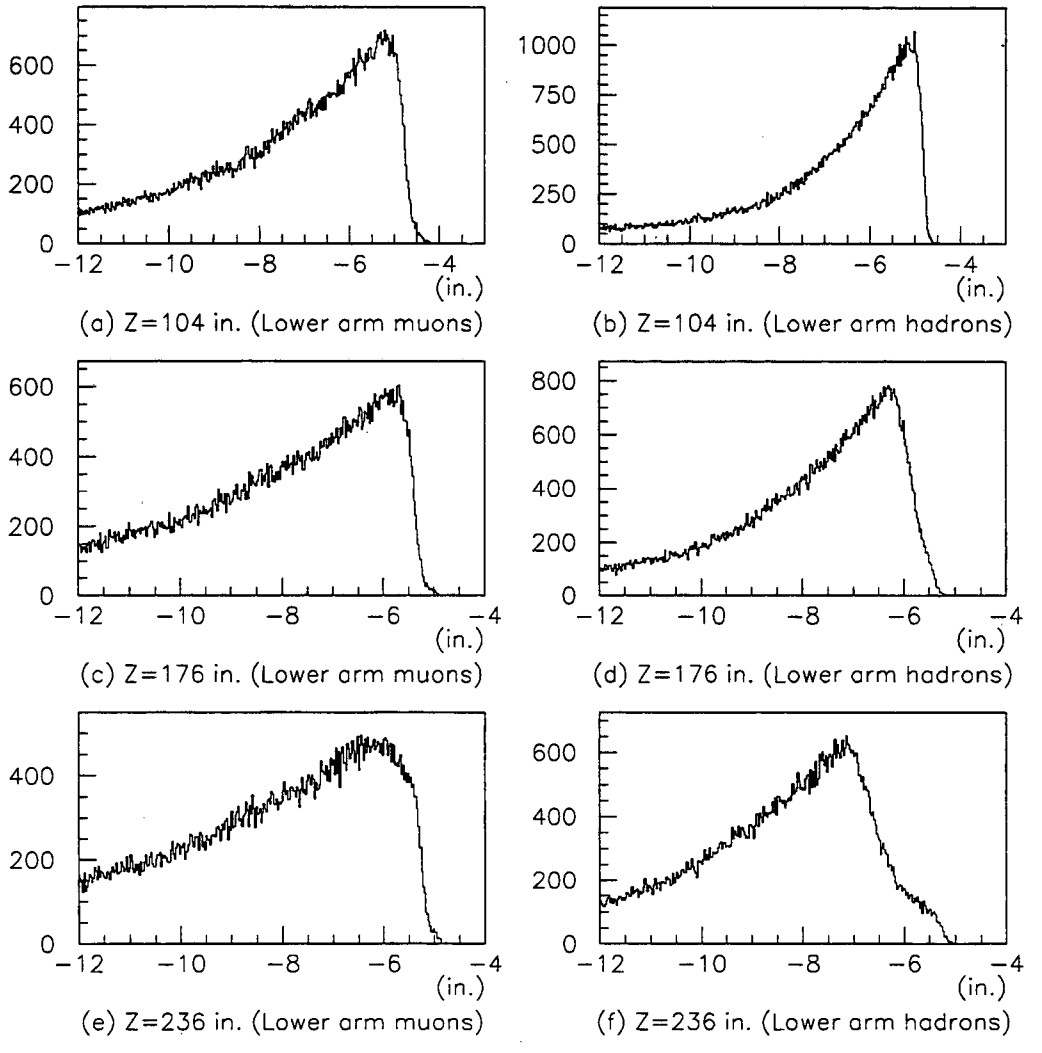

Figure 3.34: Distribution of track Y-positions in the lower arm of the spectrometer at $Z = 104$ in., $Z = 176$ in., and $Z = 236$ in. for the muon (left) and hadron (right) data sets.

Silicon track reconstruction

In the silicon track reconstruction phase, the spectrometer tracks that survived the cuts in passes 1 through 3 were traced through the silicon micro-vertex detector and an attempt was made to associate the hits on the planes in the detector with each of the spectrometer tracks. The reconstruction process was separated into 3 phases, hit filtering, Y-track reconstruction and YUV-track reconstruction. The first phase created a "road" in the silicon detector around the spectrometer track from which hits, used to create silicon tracks, were selected. Y-track reconstruction involved the reconstruction of tracks from the hits within the road in the Y planes in the silicon detector. YUV-track reconstruction involved the reconstruction of a 3-space trajectory from the Y-tracks and hits in the U/V planes. A flow chart of the complete silicon track reconstruction process is shown in Figure 3.35.

For each spectrometer track, only a selected subset of hits in each individual silicon plane was used in the reconstruction of the track's trajectory in the silicon micro-vertex detector. This "hit filtering" involved selecting only those hits in a given plane that were within a narrow Y window around the projected position of each spectrometer track at that plane. The half width of the Y window was defined to be:

$$\Delta Y = 0.015 \text{ in.} + (\text{Plane Num} - 1) * 0.0005 \text{ in.} + |\text{Track Slope}| * 2 \text{ in.} \tag{3.20}$$

for the Y planes and

$$\Delta Y = 0.015 \text{ in.} + (\text{Plane Num} - 1) * 0.0005 \text{ in.} + |\text{Track Slope}| * 2 \text{ in.} + 0.005 \text{ in.} \tag{3.21}$$

for the U/V planes. The first term in each equation took into account the uncertainty in the trace-back of the track, the second term compensated for multiple scattering in the silicon planes and the third term allowed for upstream/downstream decays to occur to within 2.0 in. of the target position. The additional 0.005 in. term (corresponding to about three silicon strips) was added for the U and V planes to compensate for the uncertainty in the X position of the track. Figures 3.36 and 3.37 show the distributions, for the muon data set, of the distance between the hits on a silicon plane and the iterated position of a spectrometer track at that plane, for each silicon plane in the spectrometer. (The B/T suffix at the end of each detector plane name denotes the lower/upper arm of the detector.) The dashed line in each plot was the distribution before hit filtering, the solid line was the

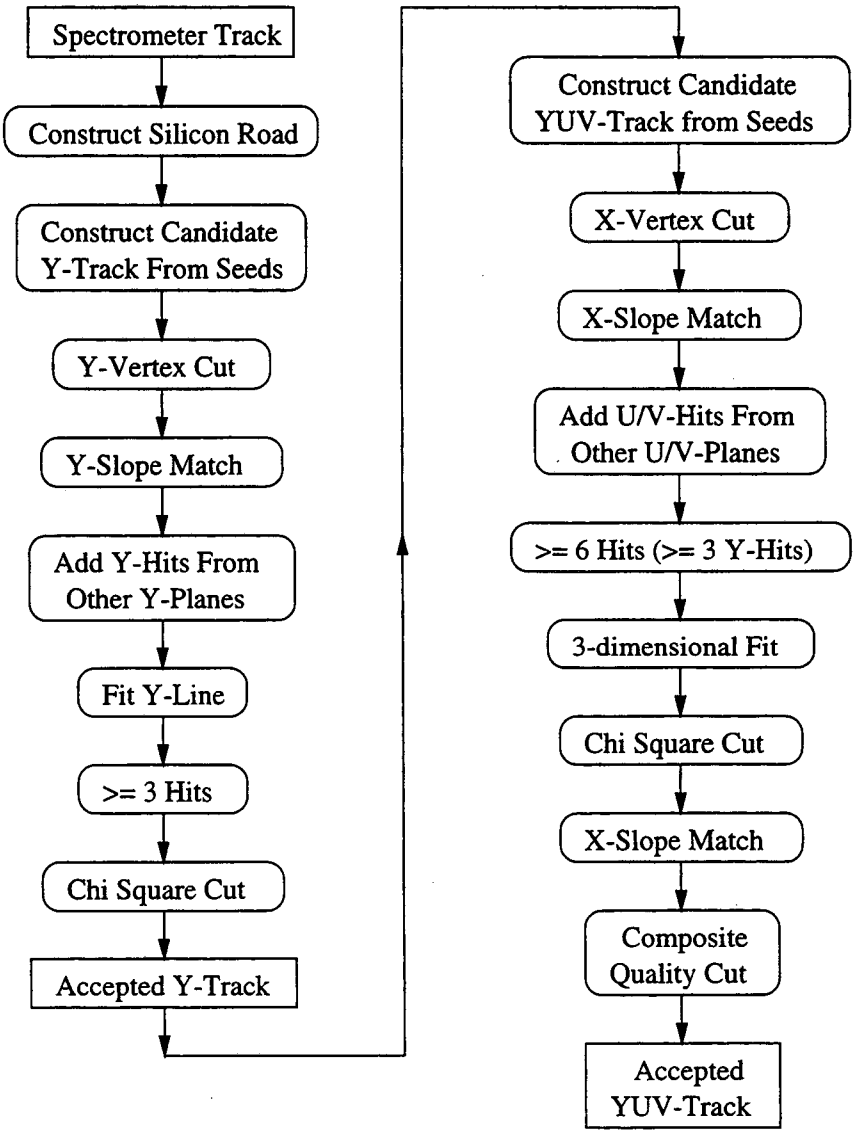

Figure 3.35: Flow chart of the silicon track reconstruction algorithm.

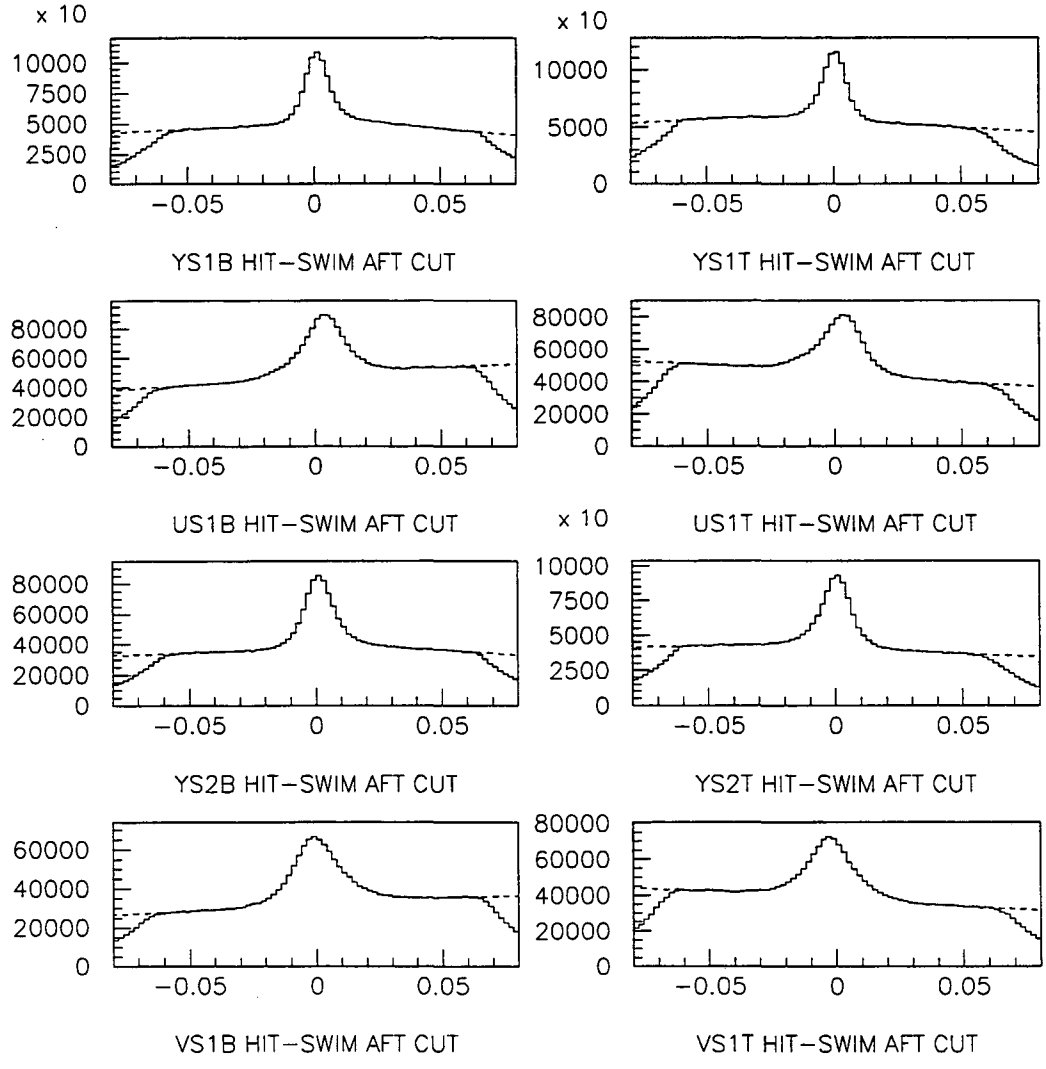

Figure 3.36: Distribution of the distances between the hits on a plane and the iterated Y position of the spectrometer track at that plane for a subset of the muon data set. (Units are in inches.)

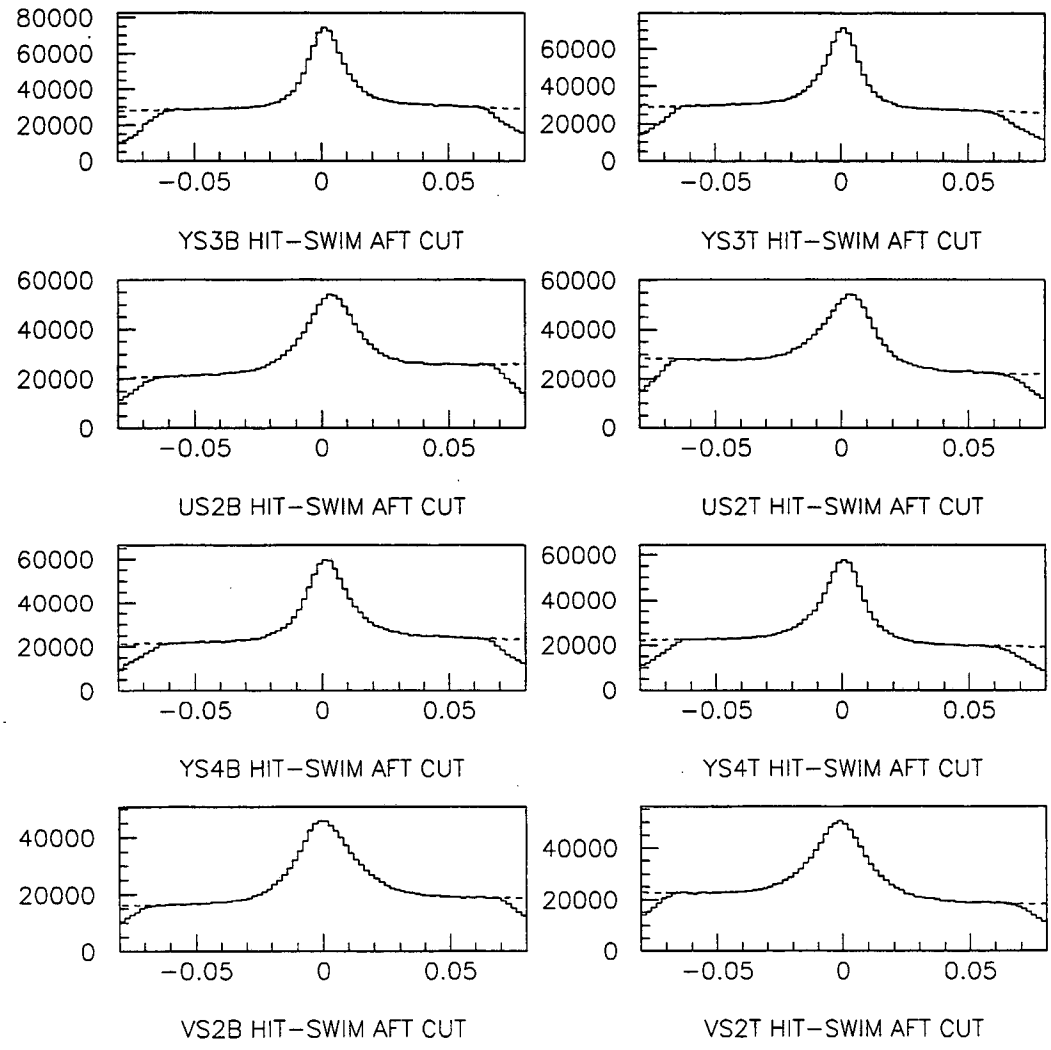

Figure 3.37: Distribution of the distances between the hits on a plane and the iterated Y position of the spectrometer track at that plane for a subset of the muon data set (cont'd). (Units are in inches.)

distribution after hit filtering. Figures 3.38 and 3.39 show the same distributions for the dihadron data set. Both sets of figures clearly shows that the cut removed unimportant hits. The higher "shoulders" and wider peaks in the distributions for the muon data set, relative to the hadron data set, was the result of the fact that the muons can multiple scatter in the beam dump and continue propagating through the rest of the spectrometer, whereas the hadrons are stopped by beam dump.

Next, candidate Y-tracks were constructed by using the restricted hits on a pair of Y planes as seeds for Y-tracks. The plane-pairs were obtained from all possible combinations of the two upstream Y planes and the two downstream Y planes in each arm of the silicon vertex detector. The candidate Y-track from a pair of hits was required to pass within $\pm$(0.012 in. + |Track Slope| * 2 in.) of the primary vertex, as determined in pass 1, in the Y direction. Figure 3.40 are the residual distributions showing the affects of this cut on the muon and hadron data sets. The dashed line in the plots show the distribution of the distance between the track and the primary vertex, $y_{target} - y_{track}(z_{target})$, before the cut and the solid line shows the distribution after the cut. The slope of the Y-track was also required to match that of the spectrometer track to within $\pm$0.0007. To see the effects of this requirement, Figures 3.41 and 3.42 show the distribution of the difference in the Y slope for the candidate Y-track and the spectrometer track before the cut for the muon and hadron data sets, respectively.

Once an acceptable two-hit candidate Y-track was found, hits from the other silicon Y planes were added to it. Only those hits on the other Y planes that were closest to the track and within $\pm$0.004 in. of it were added to the track. Figures 3.43 and 3.44 show the distribution of the distance to the closest hit (in Y) in the non-seed planes for the dimuon and dihadron data sets, respectively. A straight line was then fitted to the track and cuts were made on the quality of the track. Only Y-tracks with at least 3 hits, a Y slope that matched the spectrometer track to within $\pm$0.0007 and a χ^2 per degree of freedom $< 7(5)$ for 3 (4) hits were kept. Figures 3.45 and 3.46 show the distribution of the χ^2 per degree of freedom for three and four hit candidate Y-tracks. Figures 3.47 and 3.48 show the distribution of the Y slope difference between silicon and spectrometer tracks for a subset of the muon and hadron data sets before the cut. The effect of this second Y slope cut was minimal.

From each candidate Y-track, an attempt was made to construct a full 3-space YUV-track. As in the construction of candidate Y-tracks, candidate YUV-tracks were

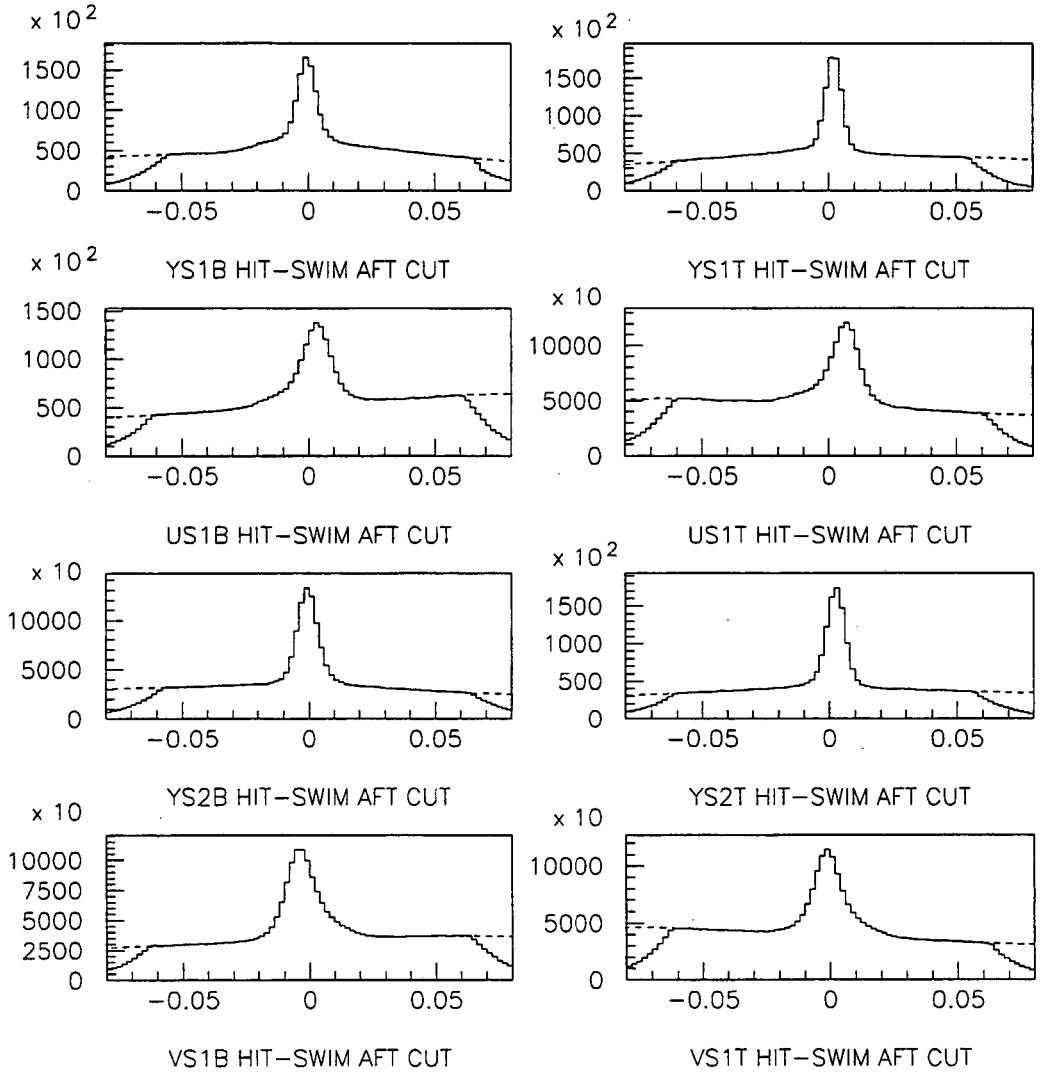

Figure 3.38: Distribution of the distances between the hits on a plane and the iterated Y position of the spectrometer track at that plane for a subset of the hadron data set. (Units are in inches.)

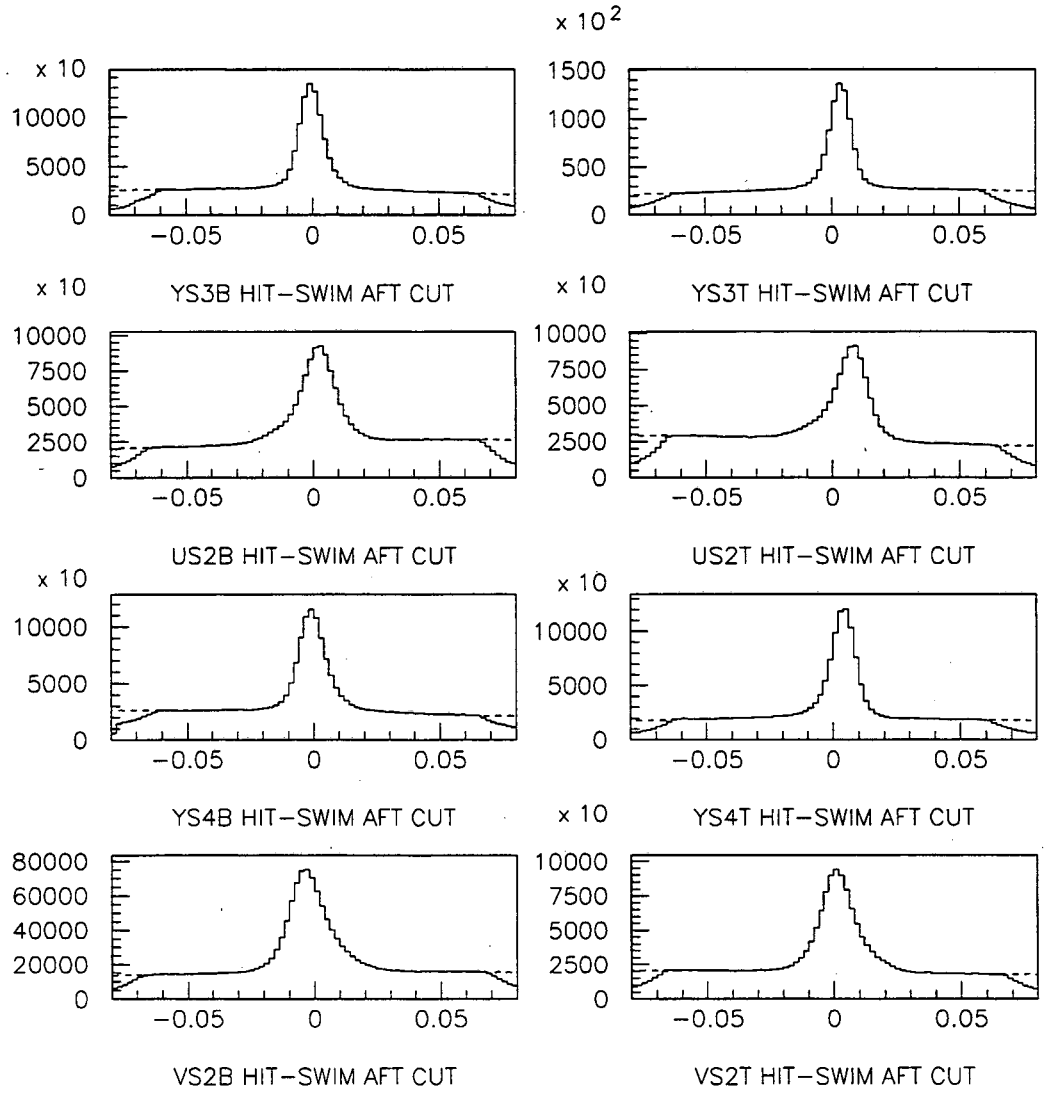

Figure 3.39: Distribution of the distances between the hits on a plane and the iterated Y position of the spectrometer track at that plane for a subset of the hadron data set (cont'd). (Units are in inches.)

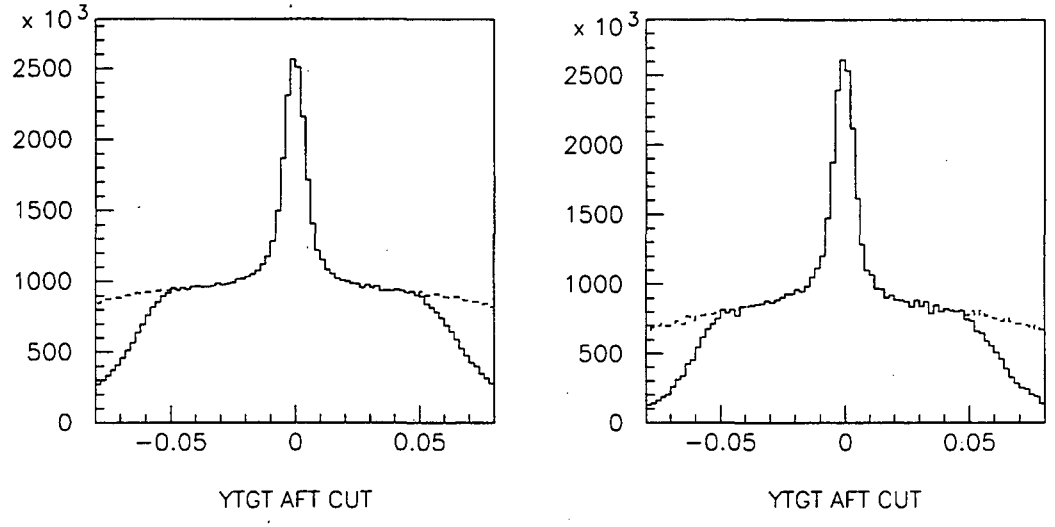

Figure 3.40: Distribution of $y_{target} - y_{track}(z_{target})$ for a subset of the muon data set (left) and hadron data set (right). (Units are in inches.)

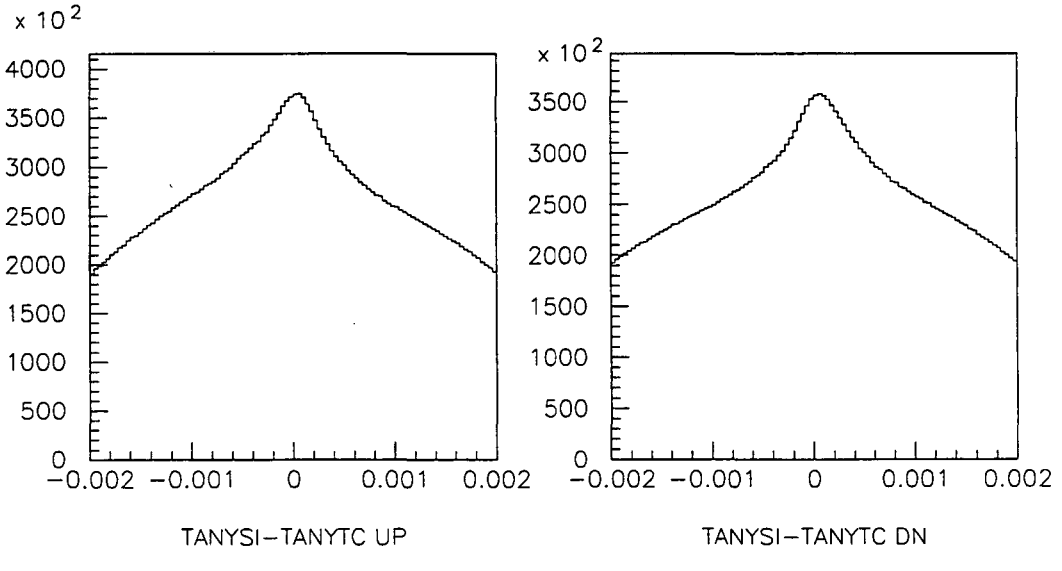

Figure 3.41: Distribution of ΔY_{slope} for a subset of the muon data set. The left (right) plot shows the distribution for the upper (lower) arm of the silicon micro-vertex detector.

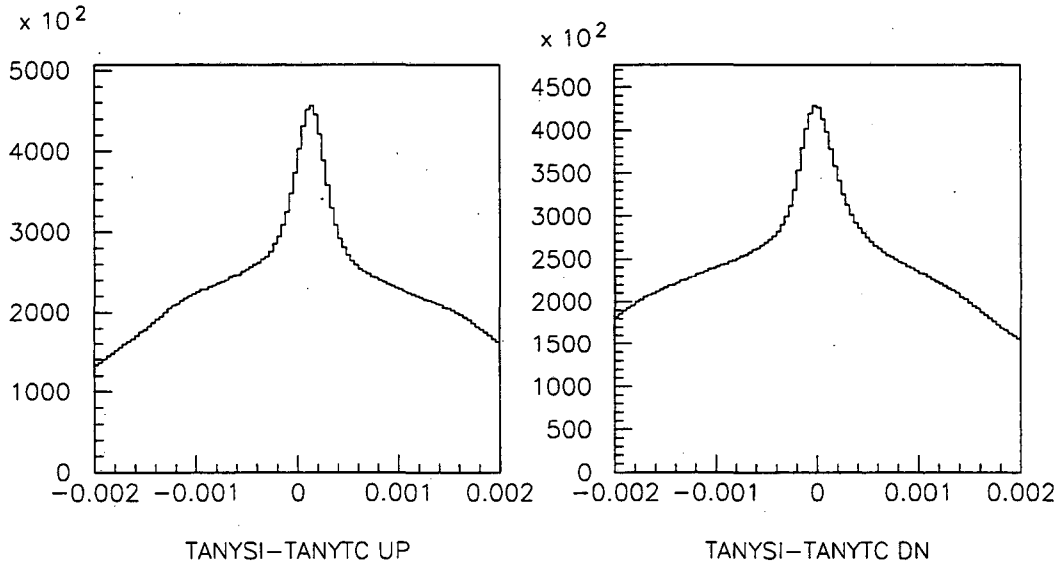

Figure 3.42: Distribution of ΔY_{slope} for a subset of the hadron data set. The left (right) plot shows the distribution for the upper (lower) arm of the silicon micro-vertex detector.

constructed from U/V hits on pairs of seed planes. Each seed hit in a plane was required to fall within ±0.2 in. of the projected X position of the spectrometer track at that plane. Figure 3.49 and 3.50 show the distribution for the distance between the spectrometer track X position and the hits in the different U/V planes. Pairs of acceptable seed hits were required to form a track that passed within 0.25 in. of the primary vertex (beam centroid) in X and matched the X slope of the spectrometer track to within ±0.004. Figure 3.51 shows the distributions of the distance between the target X position and the X position of the candidate X track at the target Z position for a subset of the muon and hadron data sets. Figures 3.52 and 3.53 show the distributions of the slope differences for a subset of the muon and hadron data sets. Tracks that passed these criteria were then filled with hits from the remaining two U/V planes. In each case, the closest hit within a 0.05 in. window of the X position of the track was taken and the line that resulted from the hit and the seed hit in the upstream plane was required to pass within 0.25 in. of the primary vertex in X. Figure 3.54 shows the distribution of the distance to the closest hit (in X) on the non-seed U/V planes for the dimuon and dihadron data sets.

The YUV-tracks that survived the cuts in the previous paragraph were subject to

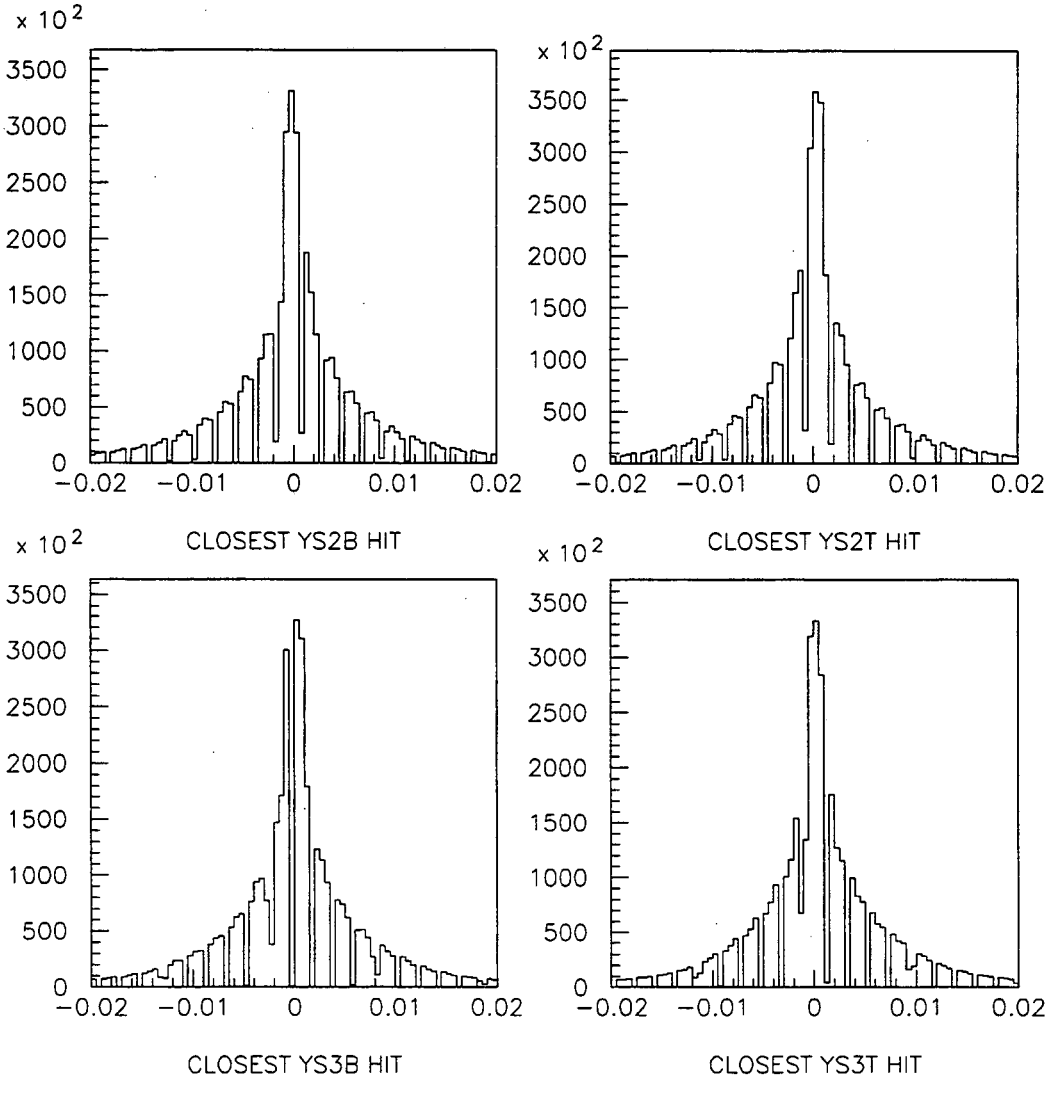

Figure 3.43: Distribution of the distances between the closest hits on the non-seed silicon Y planes and the candidate Y-track for a subset of the muon data set. (Units are in inches.)

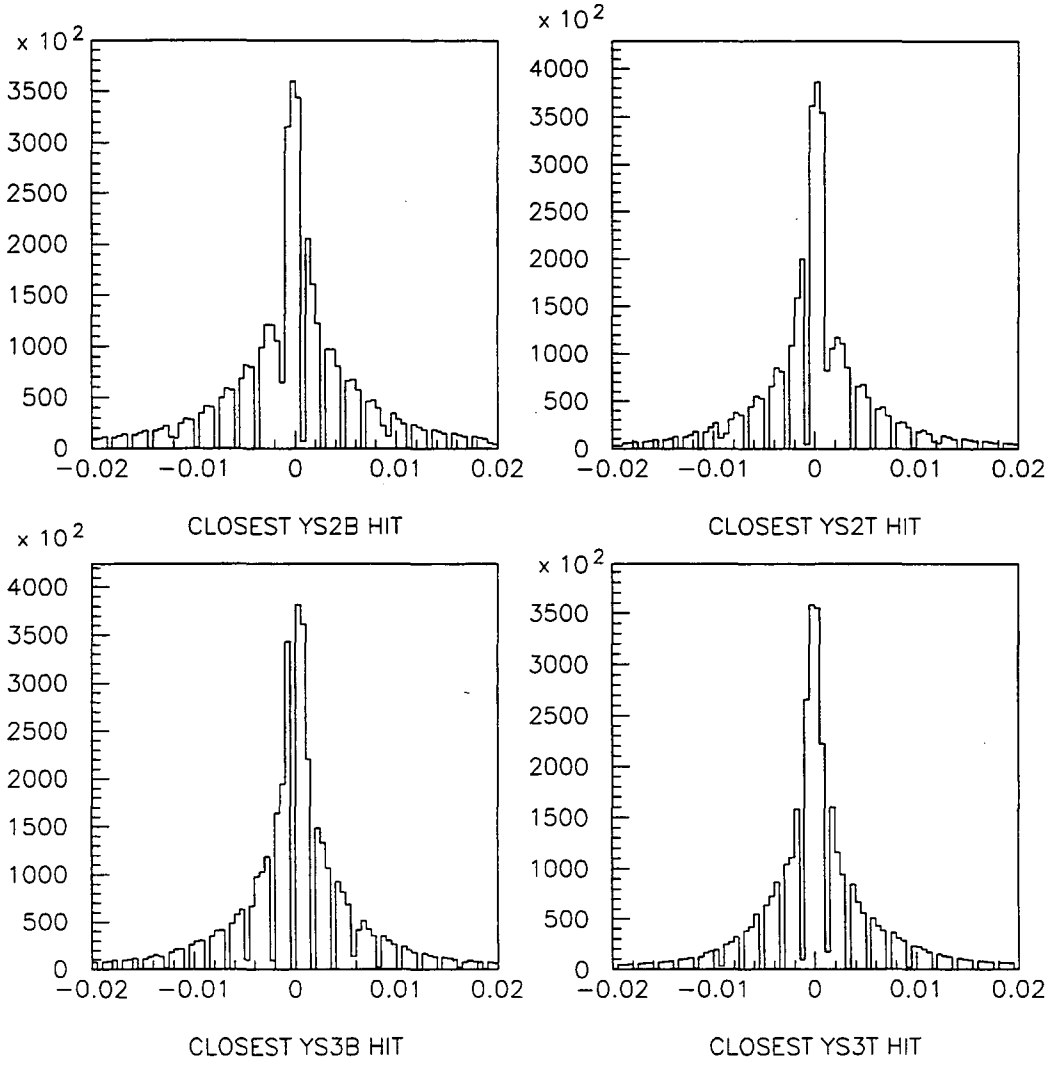

Figure 3.44: Distribution of the distances between the closest hits on the non-seed silicon Y planes and the candidate Y-track for a subset of the hadron data set. (Units are in inches.)

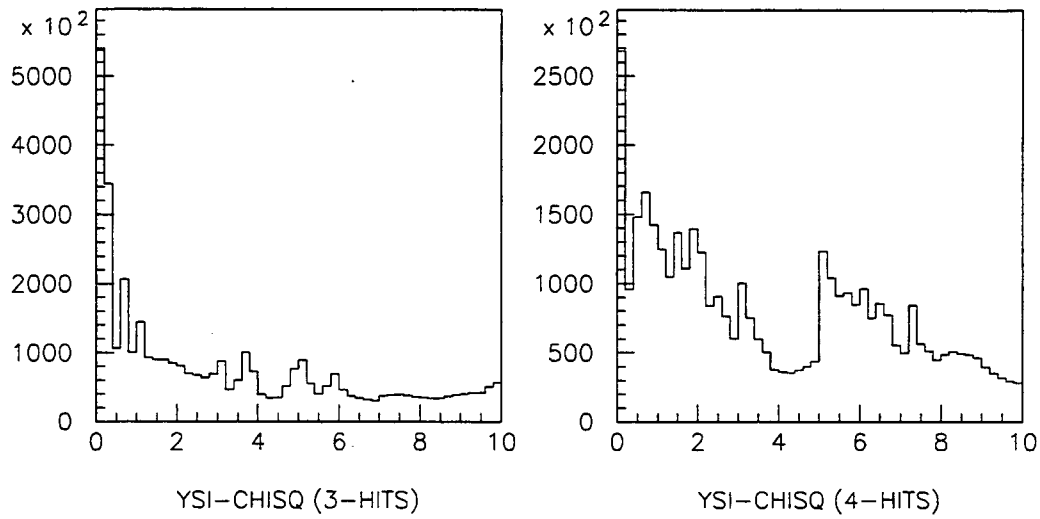

Figure 3.45: Distribution of the χ^2 per degree of freedom for 3 and 4 hit candidate Y-tracks in a subset of the muon data set.

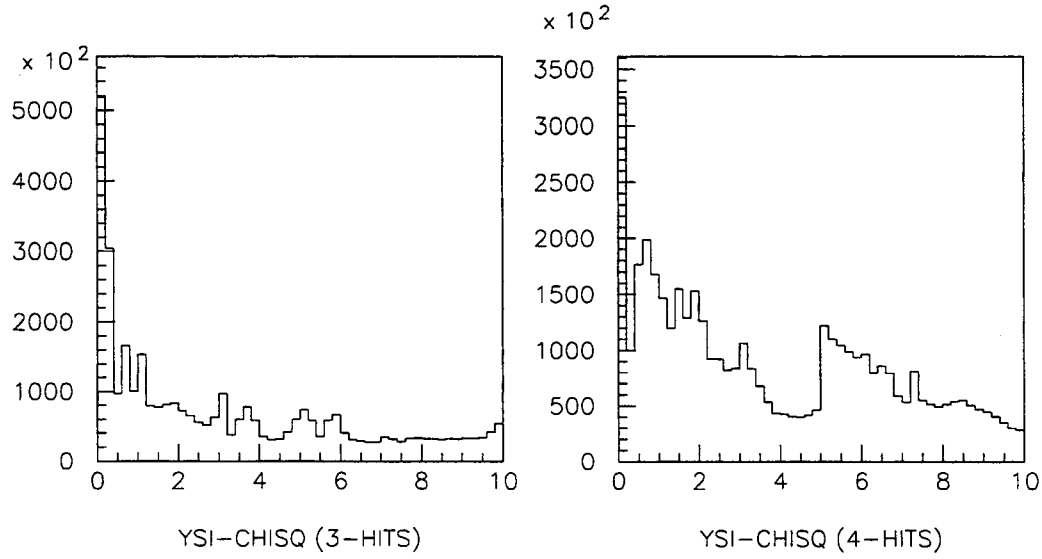

Figure 3.46: Distribution of the χ^2 per degree of freedom for 3 and 4 hit candidate Y-tracks in a subset of the hadron data set.

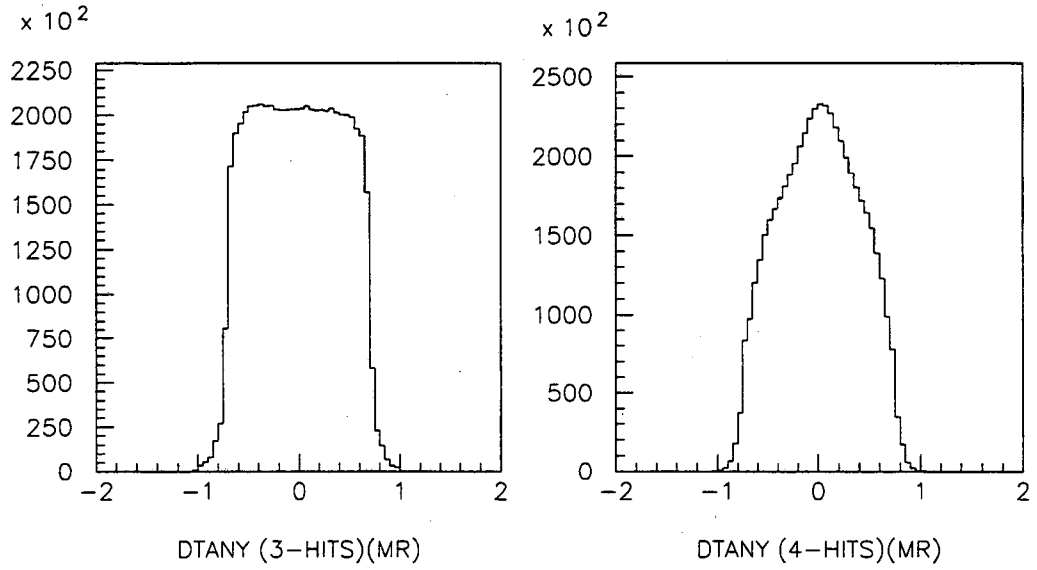

Figure 3.47: Distribution of ΔY_{slope} for the muon data set. The left plot shows the distribution for tracks with 3 hits and the right for 4 hit tracks. (Units are in milli-radians.)

three final cuts. First, they were required to have at least 6 hits (out of a possible 8), where at least 3 were Y hits. Second, a full 3-dimensional straight line fit to all the silicon hits was required to yield a χ^2 per degree of freedom less than 5. Finally, the X slope of the fit was required to match the X slope of the spectrometer track to within ± 0.004. The effects of the χ^2 cut can be seen in Figures 3.55 and 3.56 The effects of the X slope cut can be seen in Figures 3.57 and 3.58 which are the distributions of the slope differences before the cut was applied.

The result of the YUV-track finding process was a set of silicon tracks for each spectrometer track. Figure 3.59 shows the distribution of the number of silicon tracks found for each spectrometer track. From this set of silicon tracks, only the best track was kept. The metric used in the selection process was the following :

$$\text{Quality} = P(\chi^2) \times P(\Delta tan_x) \times P(\Delta tan_y) \times (\text{No. Hits}) \tag{3.22}$$

where $P(\chi^2)$ is the probability of the track fit χ^2 per degree of freedom for the track and $P(\Delta tan_x)$ and $P(\Delta tan_y)$ are the probabilities of the χ^2 per degree of freedom for the silicon–spectrometer X and Y slope differentials. For the latter two probabilities, the sigmas

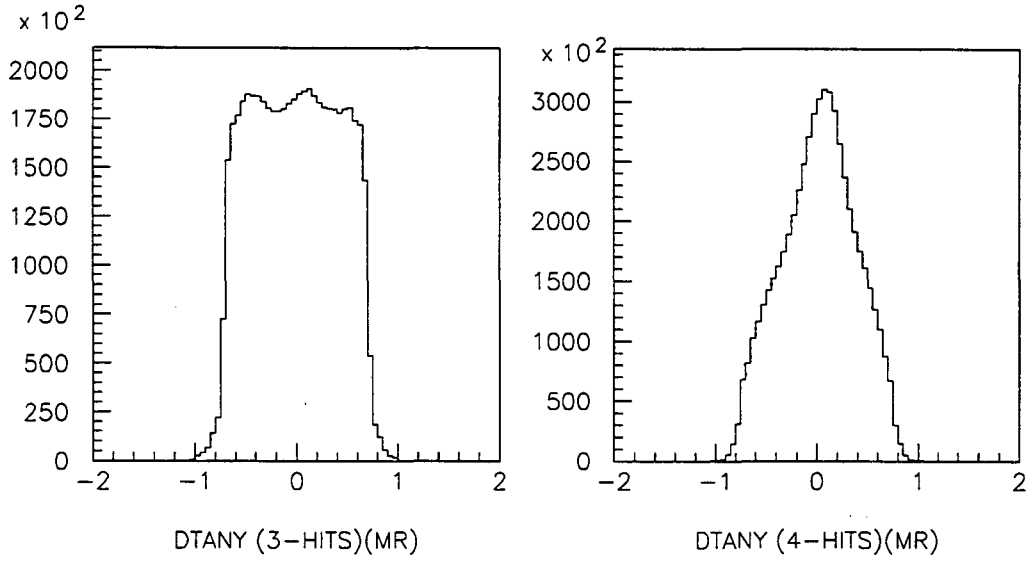

Figure 3.48: Distribution of ΔY_{slope} for a subset of the hadron data set. The left plot shows the distribution for tracks with 3 hits and the right for 4 hit tracks. (Units are in milli-radians.)

that were used in calculating the χ^2 probabilities were 0.001 and 0.0003 respectively. (In other words, Δtan_x and Δtan_y where assumed have a Gaussian distribution with sigmas of 0.001 and 0.0003 respectively.) Figures 3.60 and 3.61 show the distributions of ΔX_{slope} and ΔY_{slope} before this final cut. Figure 3.62 shows the track fit χ^2 distribution, for a subset of the muon and hadron data sets, that was used in the final cut.

Vertex reconstruction

The vertexing algorithm used in the pass 3 analysis code was relatively simple. The algorithm first calculated the distance of closest approach between each pair of silicon tracks in an event. Those pairs with a distance of closest approach greater than 0.08 in. were immediately eliminated from further consideration. In order to see the effects of this cut, Figure 3.63 shows the distribution of distance of closest approach for a subset of the muon and hadron data sets. For those pairs that satisfied the distance of closest approach criteria, the Z intersection point of the YZ lines for the pair of tracks was determined. The transverse position of one of the tracks in the pair at the Z intersection point was

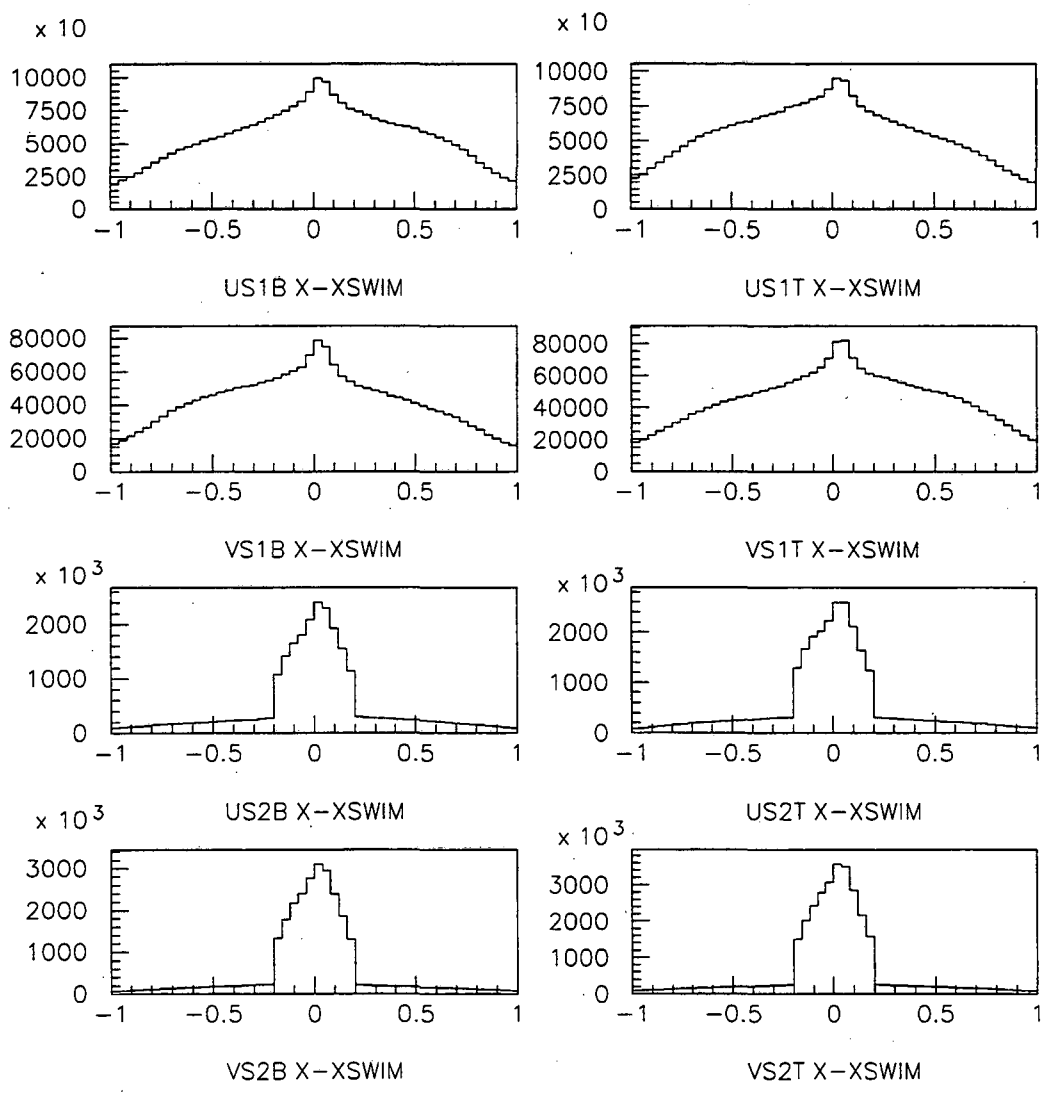

Figure 3.49: Distribution of the distances between the closest silicon hits on the various U/V planes and the iterated X position of the spectrometer track at the respective planes for a subset of the muon data set. (Units are in inches.)

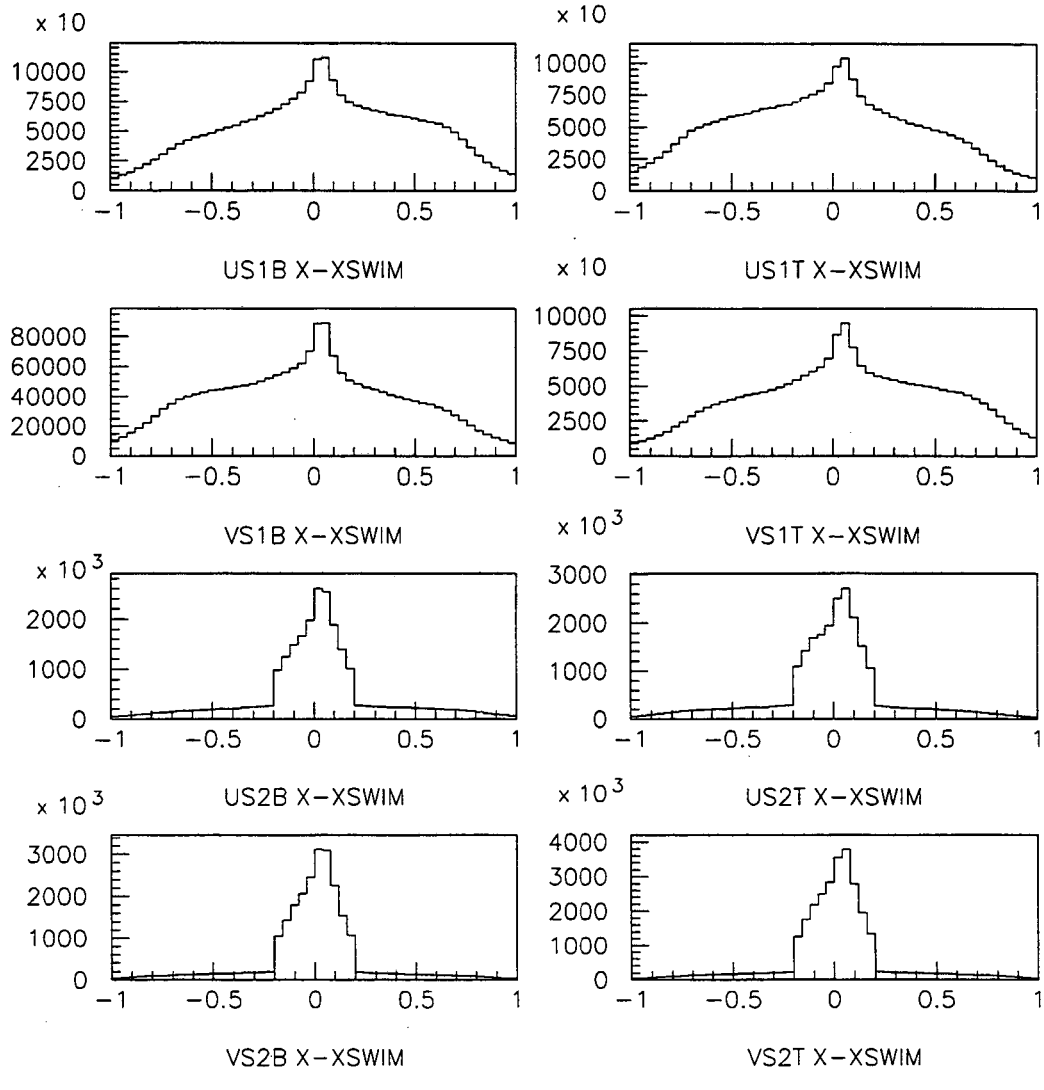

Figure 3.50: Distribution of the distances between the closest silicon hits on the various U/V planes and the iterated X position of the spectrometer track at the respective planes for a subset of the hadron data set. (Units are in inches.)

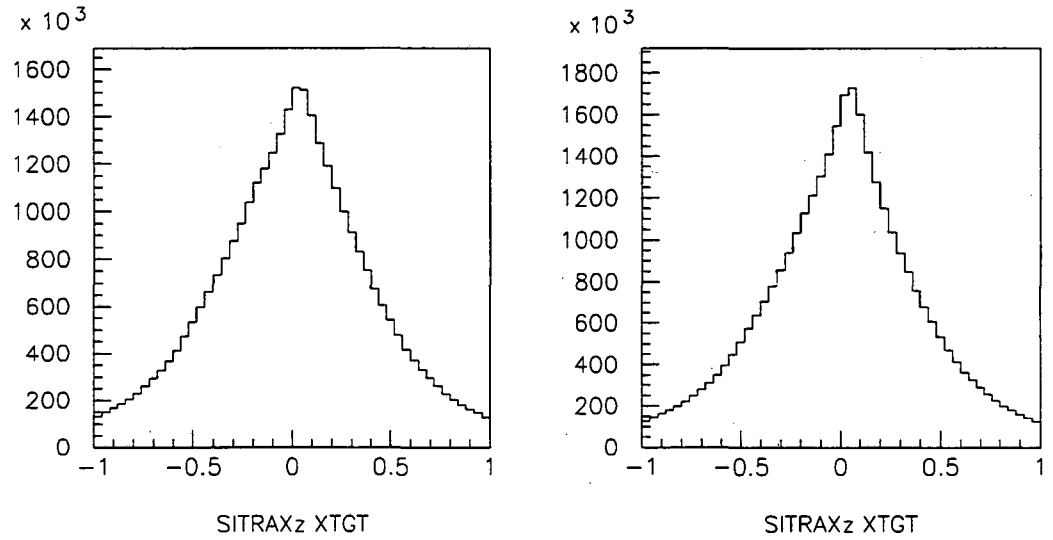

Figure 3.51: Distribution of the distance between the target position in X and the position of the candidate X track at the target Z position for a subset of the muon data set (left) and hadron data set (right). (Units are in inches.)

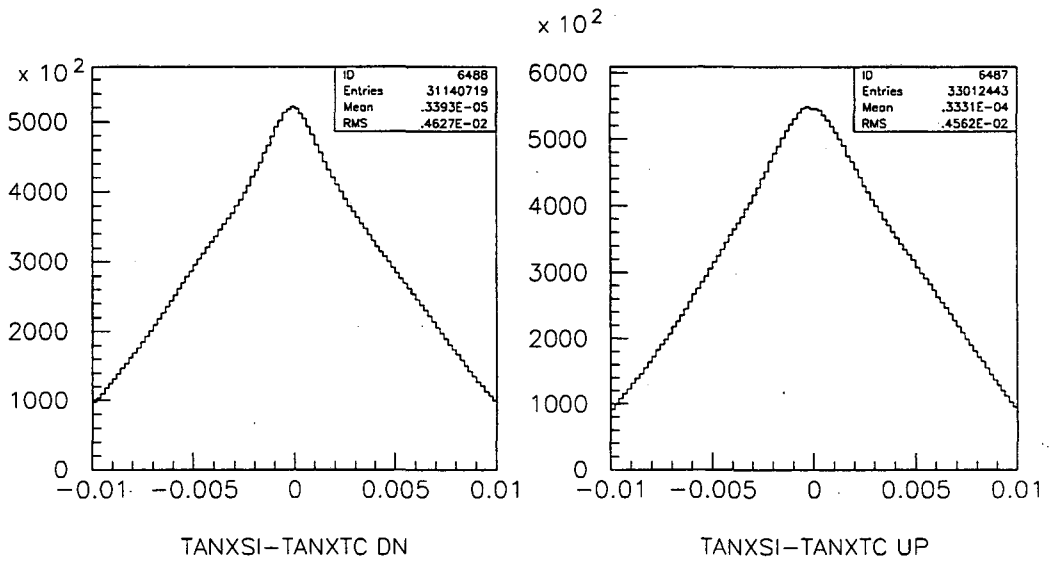

Figure 3.52: Distribution of ΔX_{slope} for the muon data set. The left (right) plot shows the distribution for tracks in the lower (upper) arm of the silicon detector.

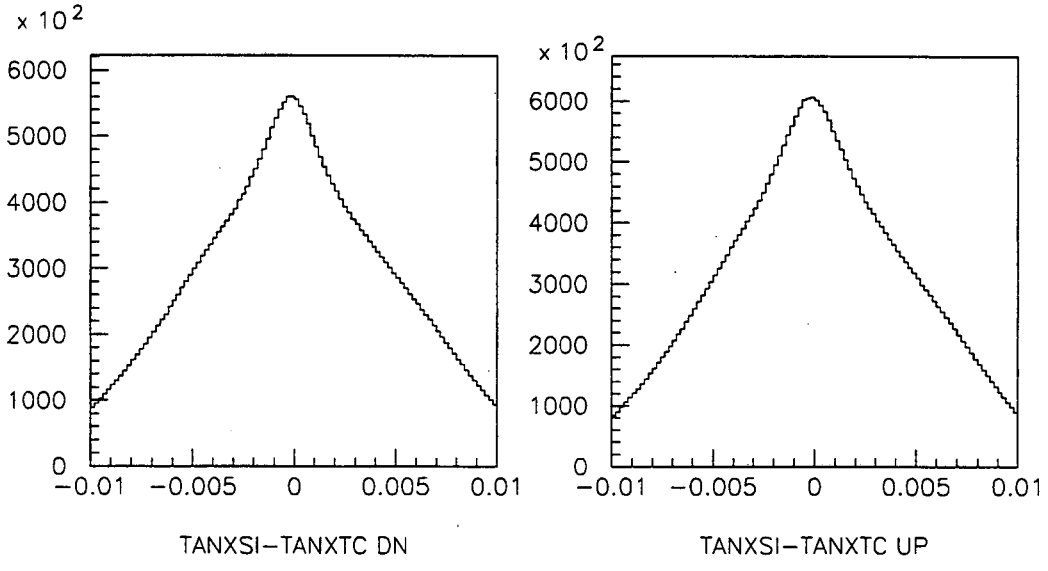

Figure 3.53: Distribution of ΔX_{slope} for a subset of the hadron data set. The left (right) plot shows the distribution for tracks in the lower (upper) arm of the silicon detector.

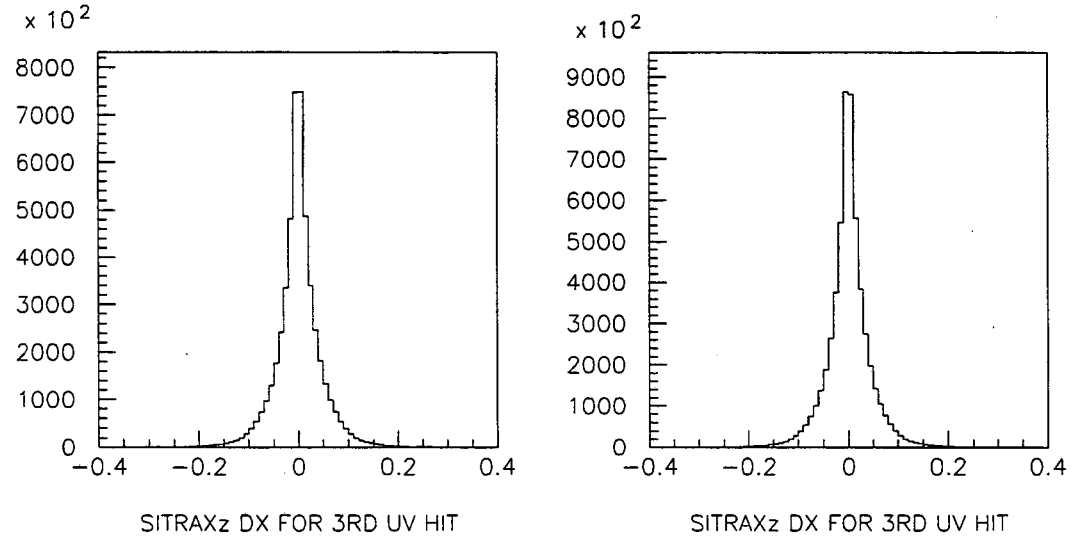

Figure 3.54: Distribution of the distances between the closest hits on the non-seed silicon X planes and the candidate X track's position for a subset of the muon (left) and hadron (right) data set. (Units are in inches.)

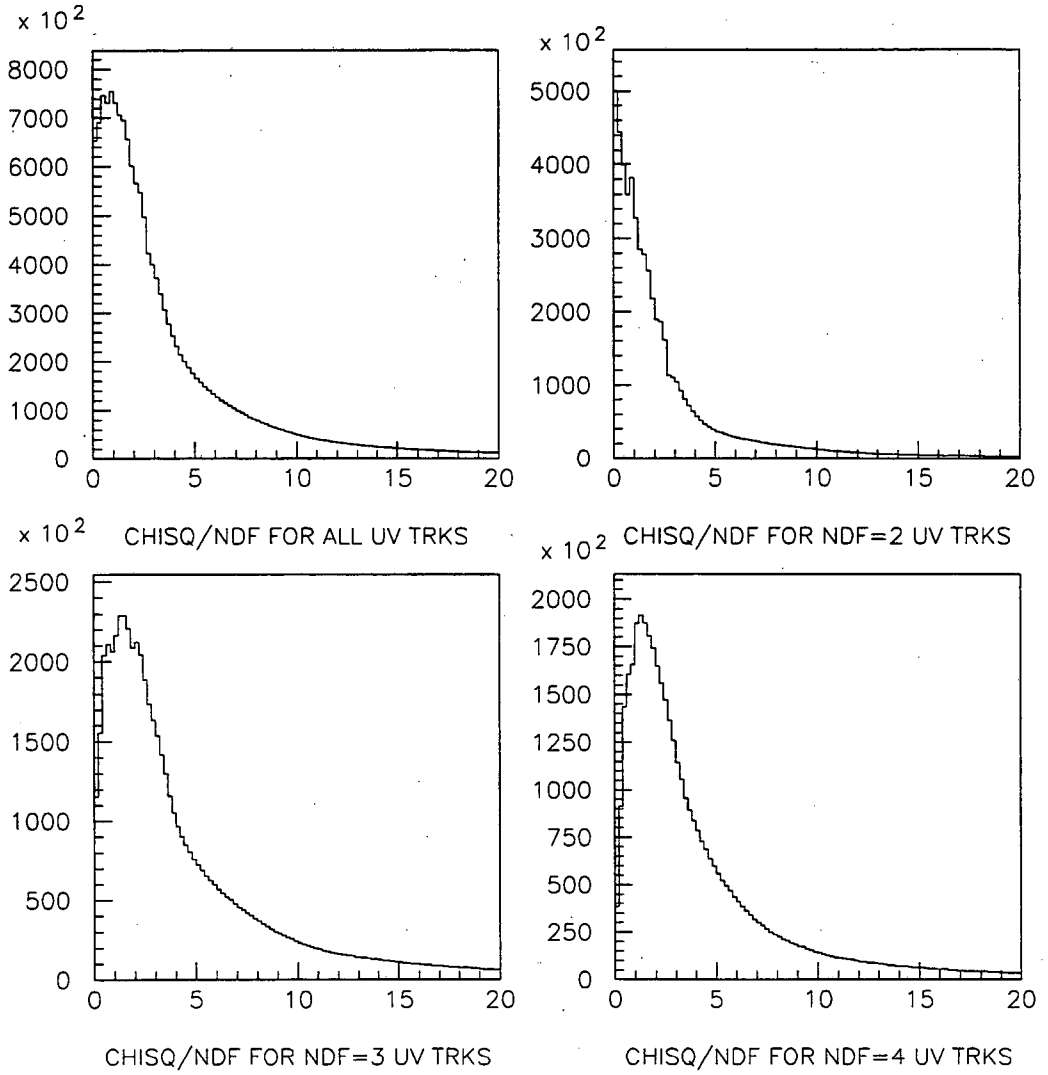

Figure 3.55: Distributions of the χ^2 per degree of freedom for tracks with 6 or more hits, 6 hits, 7 hits and 8 hits for a subset of the muon data set.

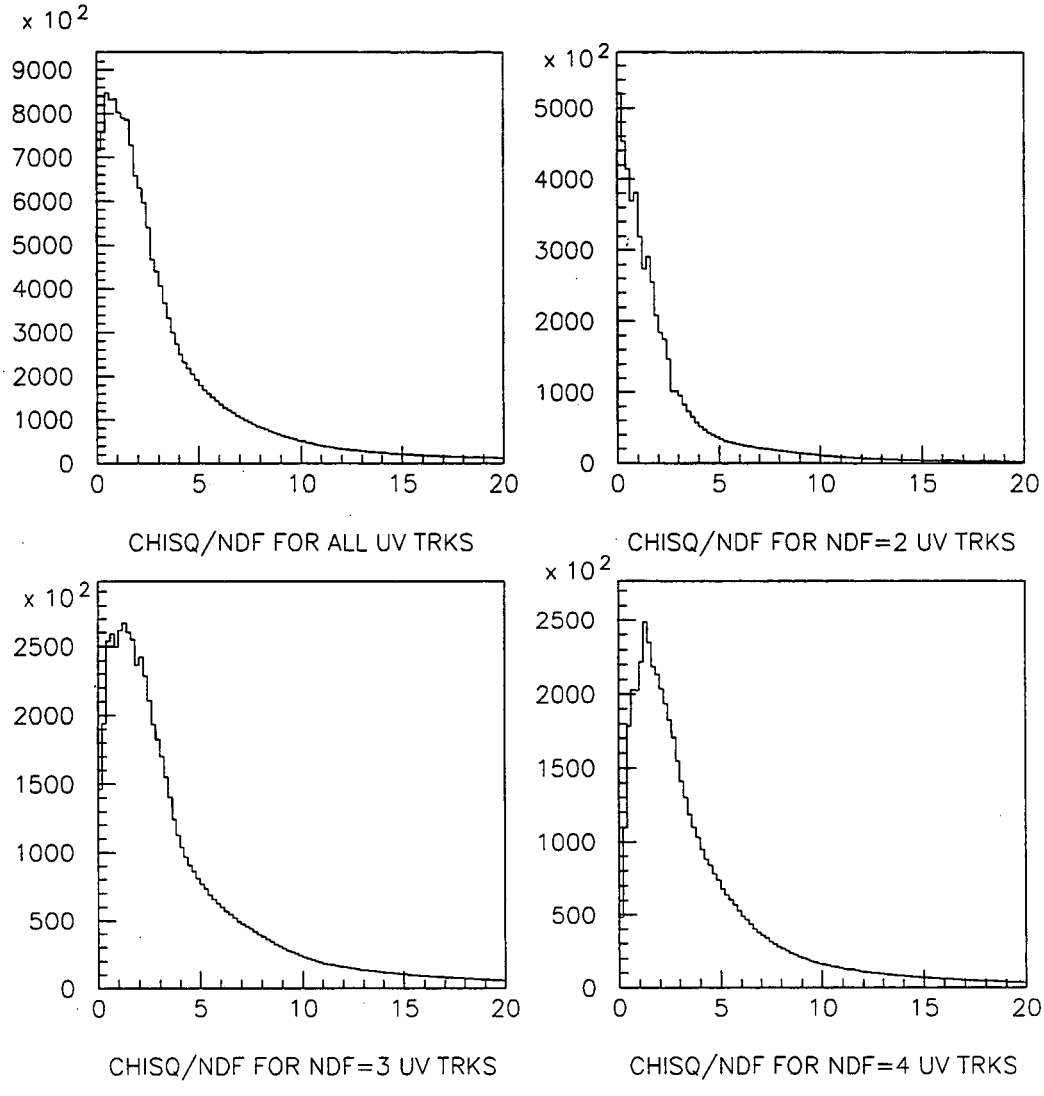

Figure 3.56: Distributions of the χ^2 per degree of freedom for tracks with 6 or more hits, 6 hits, 7 hits and 8 hits for a subset of the hadron data set.

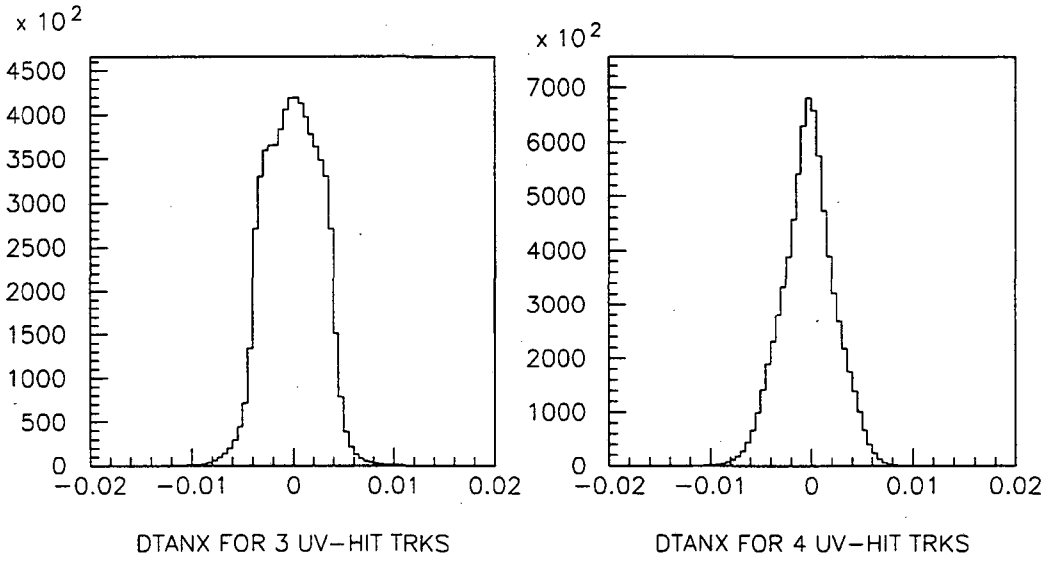

Figure 3.57: Distribution of ΔX_{slope} for a subset of the muon data set. The left plot shows the distribution for 3-hit UV tracks and the right, for 4-hit UV tracks.

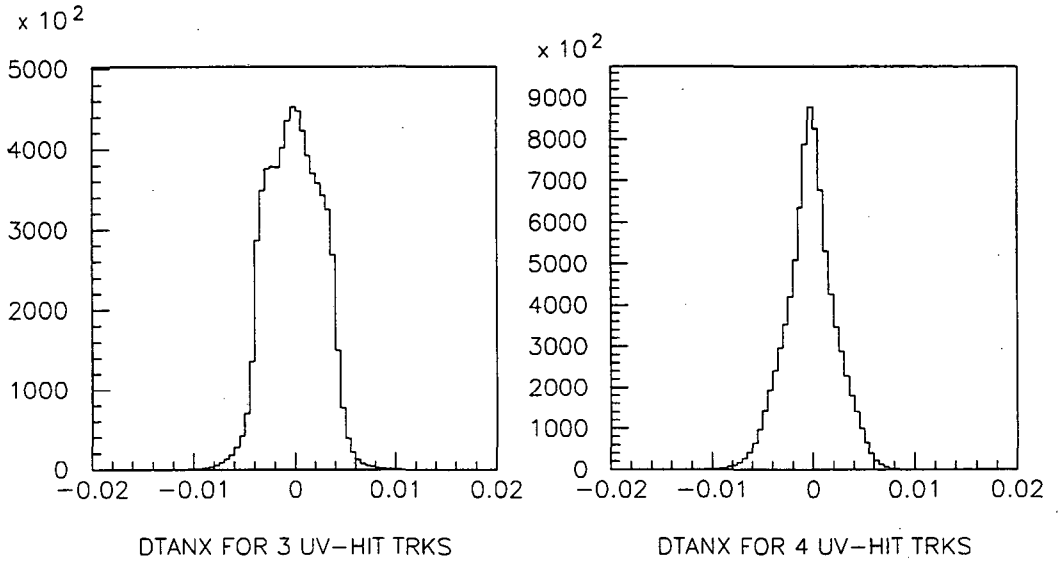

Figure 3.58: Distribution of ΔX_{slope} for a subset of the hadron data set. The left plot shows the distribution for 3-hit UV tracks and the right, for 4-hit UV tracks.

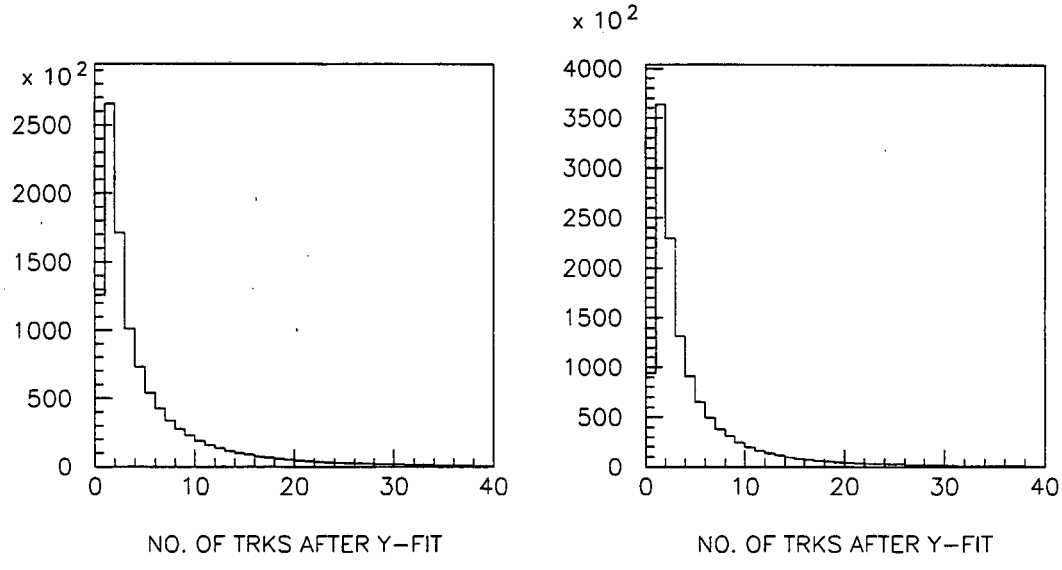

Figure 3.59: Distribution of the number of silicon tracks found for each spectrometer track for a subset of the muon (left) and hadron (right) data sets.

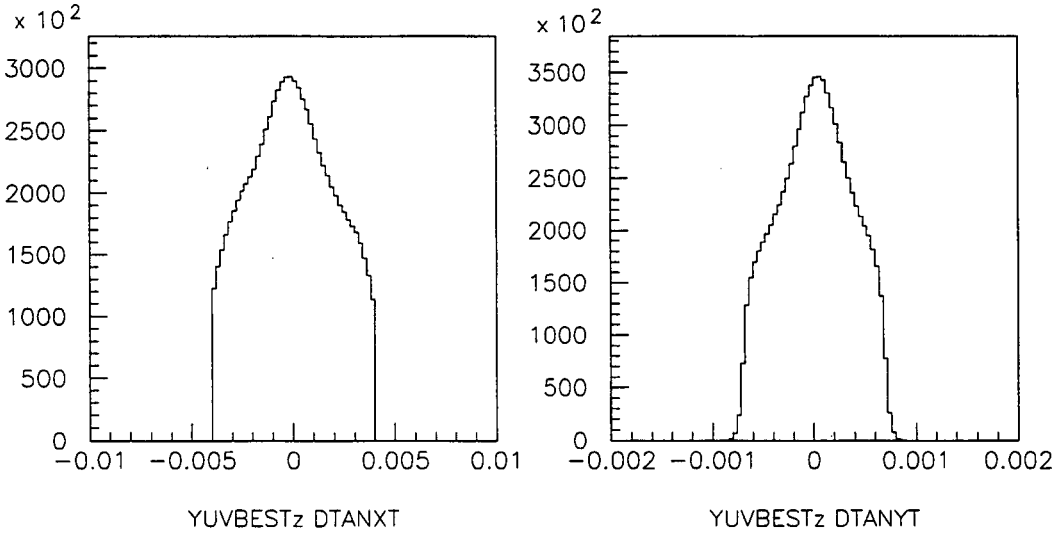

Figure 3.60: Distribution of ΔX_{slope} (left) and ΔY_{slope} (right) for a subset of the muon data set before the final cut.

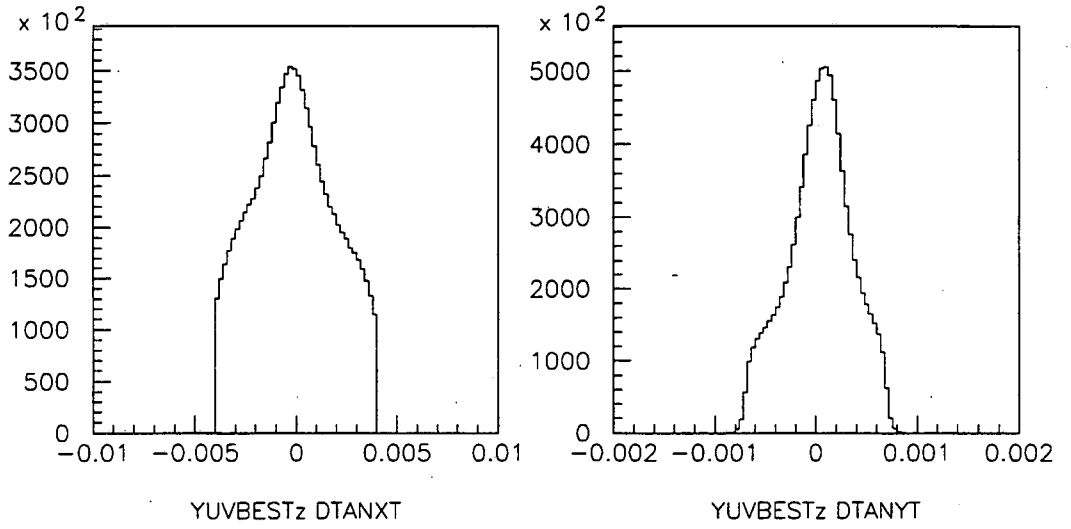

Figure 3.61: Distribution of ΔX_{slope} (left) and ΔY_{slope} (right) for a subset of the hadron data set before the final cut.

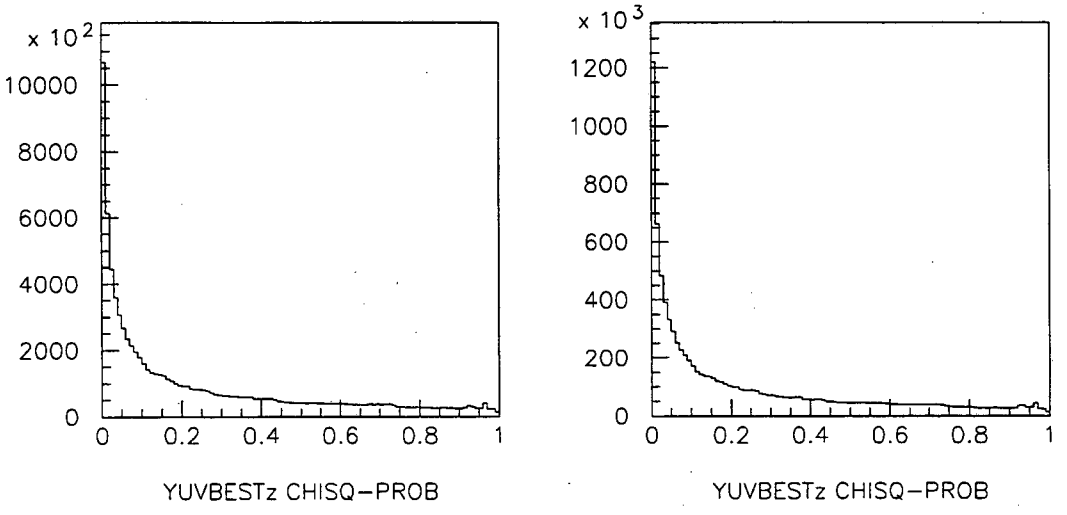

Figure 3.62: Distribution of the probability for the track fit χ^2 per degree of freedom, for a subset of the muon (left) and hadron (right) data sets, used in the final silicon track cut.

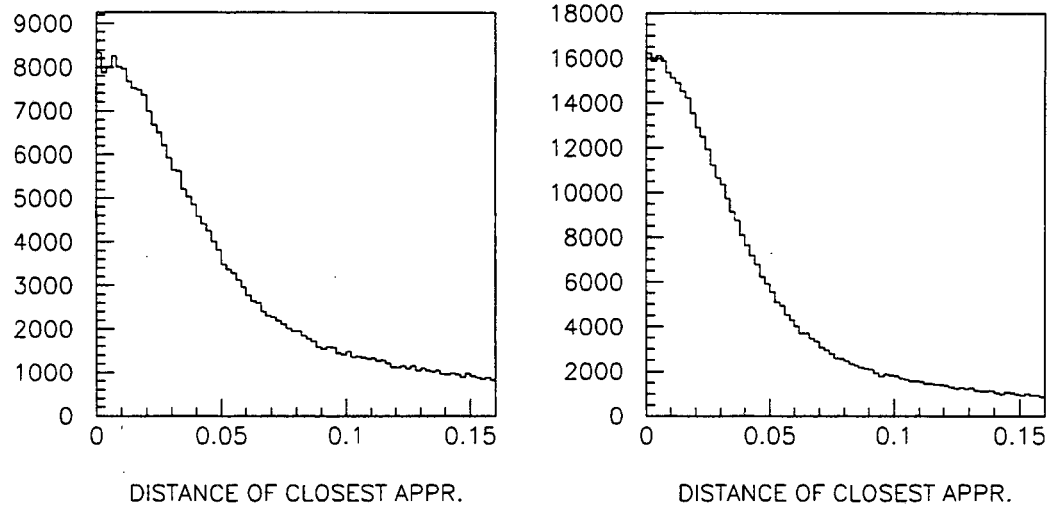

Figure 3.63: Distribution of the distance of closest approach for opposite-sign muon tracks (left) and hadron tracks (right), from a subset of the data, used in the final event cut. (Units are in inches.)

then used as the transverse position of vertex. (The intersection point in the YZ plane was used because the spectrometer's Y resolution was better than its X resolution.) Only pairs with vertex positions within $|\Delta X| < 2.0$ in. and $|\Delta Y| < 0.05$ in. of the nominal beam position were kept. Figures 3.64 and 3.65, which plot the distributions of ΔX and ΔY for a subset of the muon and hadron data sets, show that the impact of the cuts was minimal. Finally, from the list of surviving track pairs in an event, the pair with the best matching silicon–spectrometer slope, given by equation 3.23, was retained.

$$\text{Slope} - \text{Match Metric} = P_1(\Delta tan_x) \times P_1(\Delta tan_y) \times P_2(\Delta tan_x) \times P_2(\Delta tan_y) \qquad (3.23)$$

3.3 Monte Carlo

A Monte Carlo simulation of the b-hadron production, the b-hadron decay processes and the spectrometer was vital in the analysis. In particular, it was used to determine tracking efficiency, trigger efficiency, and detector acceptance. Of major importance was its use in determining the relative efficiencies and acceptances for the different decay

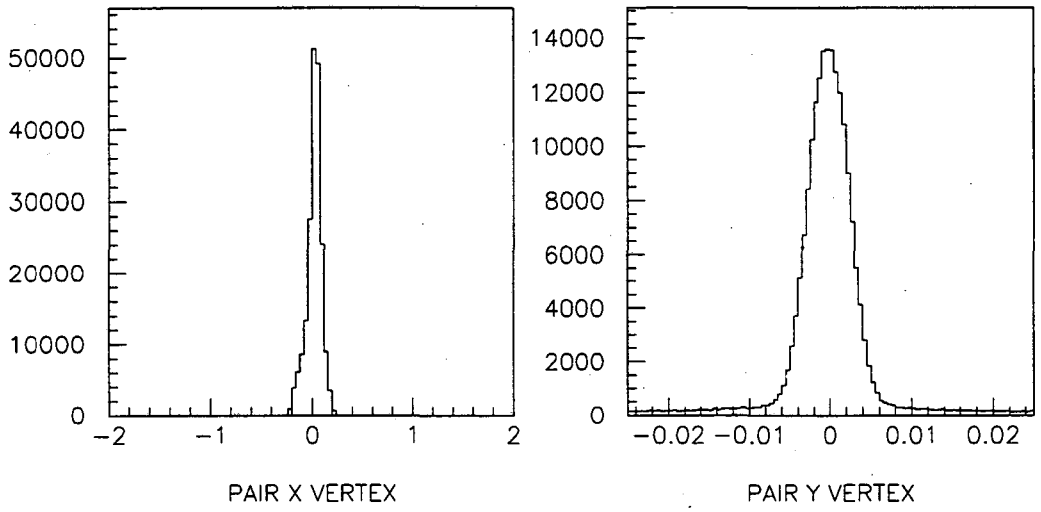

Figure 3.64: Distribution of the distance in X and Y to the target position from the decay vertex for a subset of the muon data set. The plot on the left is the X distance and the right is the Y distance. (Units are in inches.)

channels. The Monte Carlo used in this analysis was developed from the code used in the E605 and E772 experiments [52, 53, 39, 45, 46, 47]. The E789 Monte Carlo can be separated into two halves, the physics generator and the detector simulation. The physics generator generated b-decay events and was partitioned into two pieces, the b-hadron generator and the b-hadron decay generator. The detector simulation, inherited from the E605 and E772 Monte Carlo code, was responsible for simulating the response of the E789 spectrometer to the b-decay events. The b-hadron generator was developed by the E789 collaboration for the measurement of the production of bottom quarks [50]. Portions of the b-hadron generator were modified for this analysis from the version used in the measurement of the production of bottom quarks [50] to take into account new information on the top quark mass and the nucleon structure function [55, 11, 12]. The b-hadron $\rightarrow J/\psi + X \rightarrow \mu^+\mu^-$ decay generators used in the measurement of the production of bottom quarks by the E789 collaboration was directly utilized (with minor bug fixes), whereas the b-hadron $\rightarrow h^+h^-$ decay generator was modified in this analysis to handle dihadrons with unequal masses.

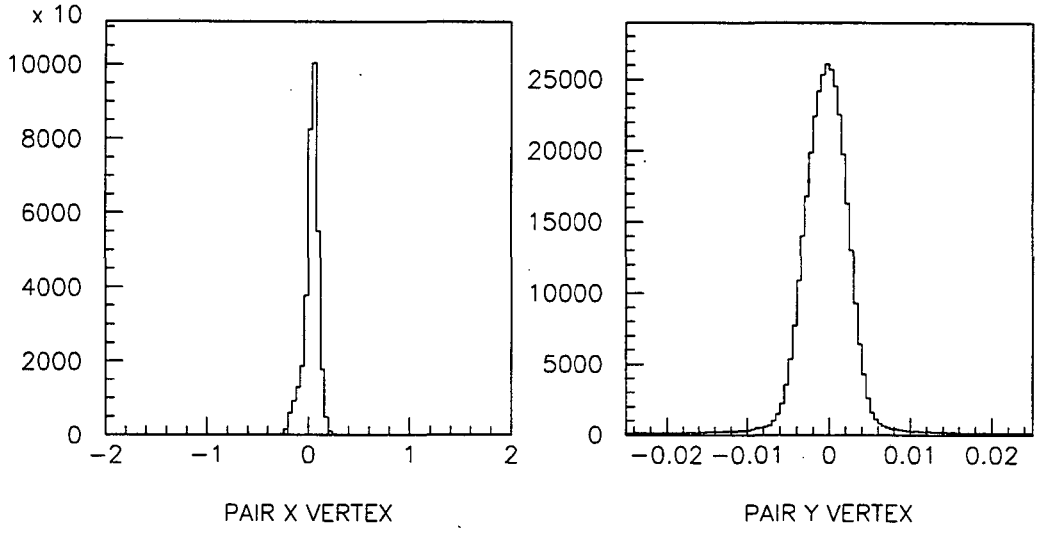

Figure 3.65: Distribution of the distance in X and Y to the target position of the decay vertex for a subset of the hadron data set. The plot on the left is the X distance and the right is the Y distance. (Units are in inches.)

3.3.1 *b*-hadron Production Model

In the E789 Monte Carlo, the first step in generating the *b*-hadron momentum spectrum was the generation of the *b*-quark hadro-production spectrum. The second step was the fragmentation of the *b*-quark into a *b*-hadron.

b-quark production model

A Fortran program using leading order (LO) and next to leading order (NLO) effects was used to generate the *b*-quark differential production spectrum [56, 57]. The adjustable parameters in the Fortran program were the *b*-quark mass (m_b), factorization scale (μ_f), renormalization scale (μ_r) and parton distribution function (F_{pdf}). The nominal values used for these parameters were $m_b = 4.75$ GeV, $\mu_f = m_b$, $\mu_r = m_b$, and $F_{pdf} = MRS - (A)$ (with top mass = 180 GeV) [55, 11, 12]. Figure 3.66 shows the *b*-hadron transverse momentum (P_t) and longitudinal momentum (P_l) production spectrum in the center of mass produced by the Fortran program using the nominal values. (The longitudinal and transverse directions are with respect to the incident protons.) Figure 3.67 show the

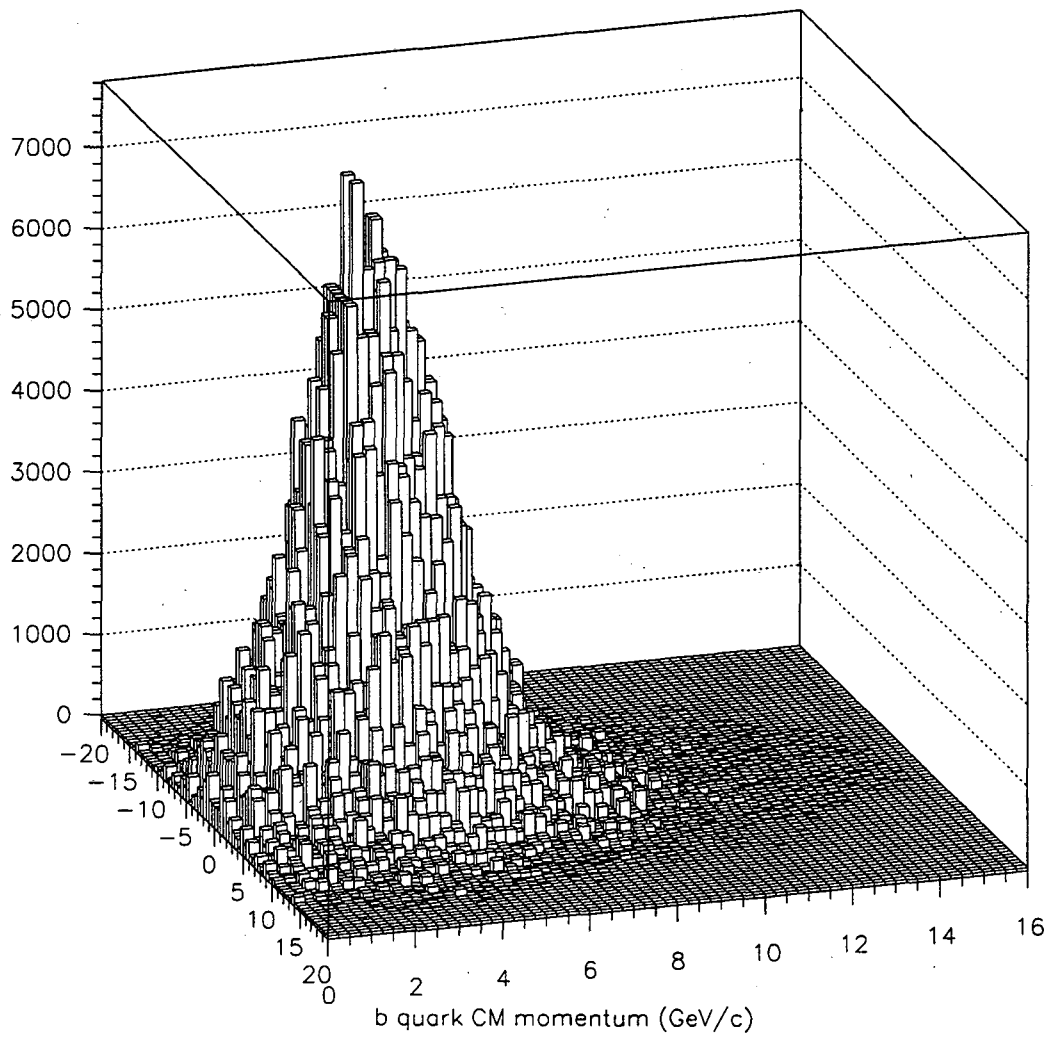

Figure 3.66: Production (P_l, P_t) spectrum (center of mass) for b-quarks produced in proton on proton interaction (Monte Carlo). The P_t axis is on the bottom with the range (0,16), the P_l axis is on the left with the range (-20,20).

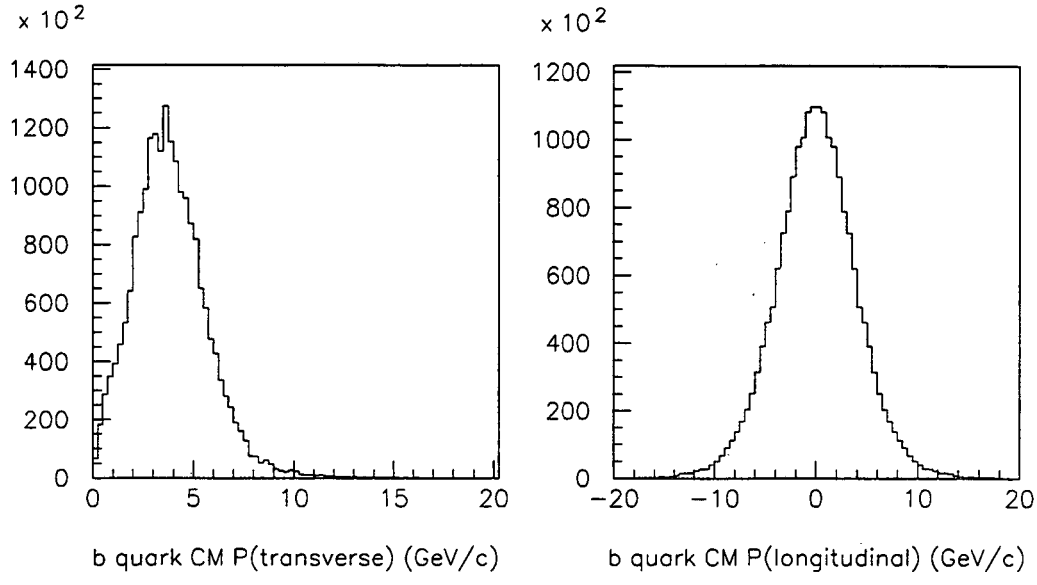

Figure 3.67: b-quark production spectrum projected onto the P_t (left) and P_l (right) axes (Monte Carlo).

distribution projected onto the transverse momentum and longitudinal momentum axes.

b-quark fragmentation

The generated b-quark production spectrum was not directly usable since it was the b-hadron spectrum which was of interest. A b-hadron spectrum was obtained from that of the b-quark by fragmenting the b-quark into a b-hadron using a Peterson fragmentation function [58].

The exact algorithm used to generate a b-hadron was as follows :

1. The four momentum of the b-quark was randomly generated from the b-quark production spectrum.

2. A transverse momentum (relative to the b-quark) for the b-hadron was randomly generated from a P_t^2 distribution of the form shown in equation 3.24 and Figure 3.68. The constants C_0 and C_1 were chosen such that the mean transverse momentum was 0.35 GeV/c.

$$f(P_t^2) = C_0 * \left[\frac{1}{(1 + C_1 * P_t^2)}\right]^4 \tag{3.24}$$

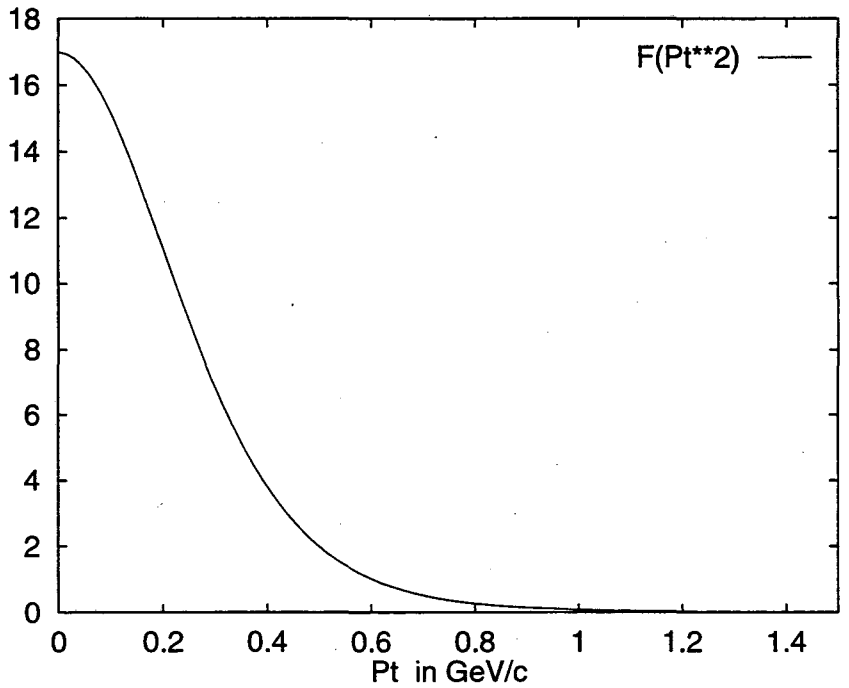

Figure 3.68: b-hadron P_t spectrum.

3. The longitudinal momentum of the b-hadron was determined from the b-quark momentum and the Peterson fragmentation function shown in equation 3.25.

$$D(z) = \frac{1}{z\left(1 - 1/z - \epsilon/(1-z)\right)^2} \tag{3.25}$$

The variable z is defined as follows:

$$z = (E_{hadron} + P_{\|})/(E_{quark} + P_{quark}) \tag{3.26}$$

and ϵ was set to 0.006 [59, 60]. The function is plotted in Figure 3.69.

4. A cut was made that required the generated b-hadron energy to be less than or equal to the b-quark energy. ($E_{hadron} < E_{quark}$.)

5. Finally, the effect of the "intrinsic" k_t of the partons in the proton and nucleon was modeled by an additional transverse momentum factor. In this case, the added transverse momentum had a Gaussian distribution with a $\langle {k_t}^2 \rangle$ of $(0.5\ \mathrm{GeV/c})^2$.

Figures 1.12 and 1.13, in section 1.4.1, show the P_t and X_F spectrums of the b-hadrons produced by the described hadronization model.

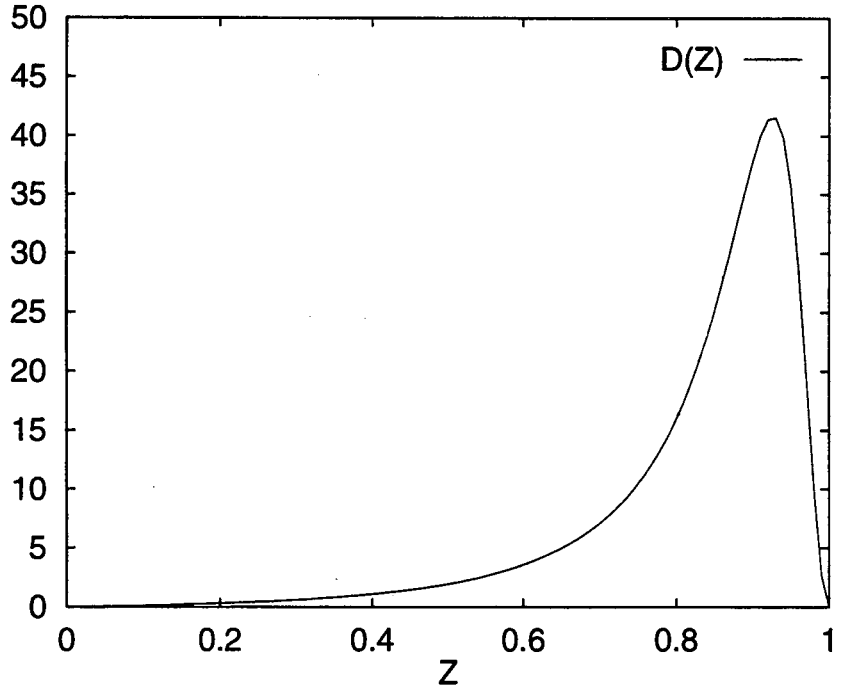

Figure 3.69: Peterson fragmentation function for $\epsilon = 0.006$.

3.3.2 b-hadron Decay

Once the b-hadron production spectrum was determined, the momentum spectrum of its decay products was determined. More specifically, the dihadron spectrum from direct b-decays was generated, as well as the dimuon spectrum from the J/ψ produced from the decay of the b-hadron.

Dihadron b decays

The simpler of the two decay processes was the b-hadron to dihadron decay mode. Since $B^0_{d,s}$ mesons are spin zero, in the rest frame of the B-meson, the momenta of the two hadrons are isotropically distributed. The magnitudes of the momenta are such that the invariant mass of the two hadrons is equal to the rest energy of the decaying B-meson. For the case of the Λ_b, the baryon was assumed to be produced in a random polarization state. (This is justified since the Λ_b's are produced with a mean transverse momentum of zero.) This meant that the dihadrons from its decay would also be isotropically distributed in the rest frame of the Λ_b. The nominal values used for the mass of the three b-hadrons were $M(B_d) = 5.279$ GeV, $M(B_s) = 5.374$ GeV and $M(\Lambda_b) = 5.641$ GeV [37].

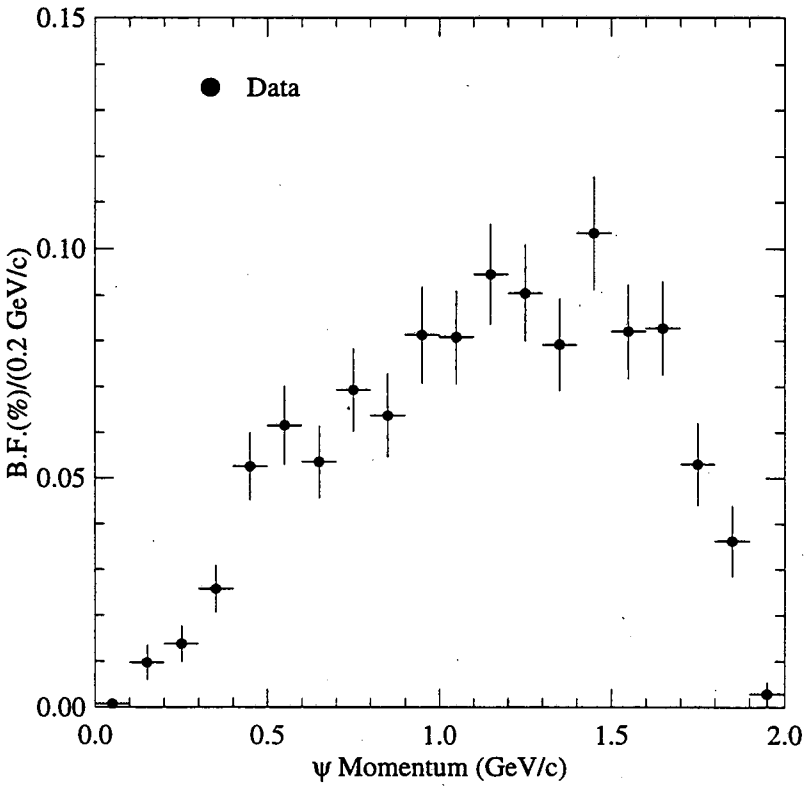

Figure 3.70: J/ψ momentum spectrum from b-hadron decays.

Inclusive B decays to J/ψ

Modeling the B to J/ψ to dimuon process was much more complex. The problem is that the polarization and momentum distributions of the J/ψ are not well known. In the Monte Carlo, the momentum distribution of the J/ψ was obtained from the inclusive J/ψ momentum spectrum measured by the CLEO collaboration in B to J/ψ events [14]. (See Figure 3.70.) However, there was a problem with directly utilizing the measured J/ψ distribution. The momentum distribution was measured in the CM frame of the colliding e^+e^- particles. In this frame, the B-mesons are produced with a finite momentum. Simple calculation shows that the B-meson momentum can be up to 0.34 GeV/c. Furthermore, in the rest frame of the B-meson, the J/ψ can have a momentum up to 1.73 GeV/c. Hence, the effect of the finite B-meson momentum was not small. Unfortunately, the CLEO J/ψ momentum distribution was fairly coarse and the process of deconvolving the B-meson

momentum spectrum was not trivial. The solution that was taken was to "fold" the J/ψ spectrum at the 1.73 GeV/c kinematic limit. That is, the area under the curve above 1.73 GeV/c was added to the interval between 1.6 and 1.73 GeV/c.

The next hurdle to overcome was the problem of the polarization of the J/ψ. The J/ψ from a B decay is known to be partially polarized, which will affect the distribution of the dimuons from the decay of the J/ψ [15]. However, the exact polarization of the J/ψ is not well known, therefore, the only solution was to try multiple dimuon distributions. The nominal distribution used was $(1+\alpha cos^2\theta)$ with $\alpha = 0.436 \pm 0.115$ [50], where θ is the polar angle of the positively charged muon in the J/ψ decay measured with respect to the J/ψ momentum vector in the B rest frame.

3.3.3 Detector simulation

The Monte Carlo of the E789 spectrometer simulates the propagation of particles through the entire volume of the spectrometer. Included in the simulation were :

- Multiple scattering effects throughout the entire spectrometer volume.
- Propagation of charged particles through SM12 using a detailed field map and through SM3 using a single bend plane approximation.
- Efficiencies of the drift chambers, proportional chambers and silicon planes.
- Efficiencies of the hodoscope planes.
- Modeling of dead channels.
- Trigger simulation including matrix, dimuon and dihadron.
- Noise simulation through event overlays and the addition of random hits. (The noise includes electronic noise and background event noise.)
- Event-output compatible with the analysis code input format.

By taking these effects into account, the detector Monte Carlo provided the means to calculate the acceptances and efficiencies that were needed in the determination of the branching ratios. Since the details of the simulation were closely coupled to the calculation of the acceptances and efficiencies, a more detailed discussion of the simulation is given in the section on acceptance and efficiency. (Section 3.4.)

In order to gauge the accuracy of the Monte Carlo simulation a comparison of some of the distributions in Figures 3.2 through 3.63 with the same distributions generated by the Monte Carlo is in order. This comparison is best made between the distributions from the dimuon data set and those generated by a Monte Carlo simulation of prompt J/ψ decays to dimuons. This is because a significant fraction of the dimuon events in the data were from the decays of J/ψ that were generated in the primary interaction.

Figures 3.71 and 3.72 show the residuals for each silicon plane for Monte Carlo generated muon track(s). These distributions should be compared with the same distributions for real events shown in Figures 3.36 and 3.37. The "shoulders" at ± 0.05 in. in the plot are the effects of the Y window cut in the silicon.

Figure 3.73 is a plot of the difference between the extrapolated Y position of a candidate silicon Y-track at the target Z position and the target Y position. The candidate Y-track was constructed from two hits in the silicon detector. The Y vertex cut begins to effect the distribution near ± 0.05 in. The extrapolated vertex distribution should be compared with the distribution from data in Figure 3.40.

Figure 3.74 plots the difference in the Y slope of the silicon track and the Y slope of the track reconstructed in the rest of the spectrometer. The distribution shows that the requirement of $|\Delta_{slope}| < 0.0007$ was reasonable.

Figure 3.75 shows the distribution of the closest Y hits in the non-seed silicon Y planes. The distributions mirror those of the dimuon events shown in Figure 3.43. An accurate matching of Monte Carlo distributions with the real dimuon event distributions is necessary because of the ± 0.004 in. cut used in choosing if a hit should or should not belong to a track.

Figure 3.76 shows the distribution of the χ^2 per degree of freedom for reconstructed Monte Carlo prompt J/ψ dimuon events. The distributions contain the same gross features of the distributions in real dimuon events shown in Figure 3.45.

Figure 3.77 shows the Y slope match between "fully populated" silicon Y-tracks and spectrometer tracks. The distributions exhibit the same features as those for the real dimuon events shown in Figure 3.47.

Figure 3.78 shows the distance between the projected X positions of a fully reconstructed silicon Y-track in the U/V planes and the closest hits in those planes. The Monte Carlo distributions show that the correct U/V hits are within the ± 0.2 in. window used to decide if a U/V hits is part of the silicon track. The distributions should be compared with

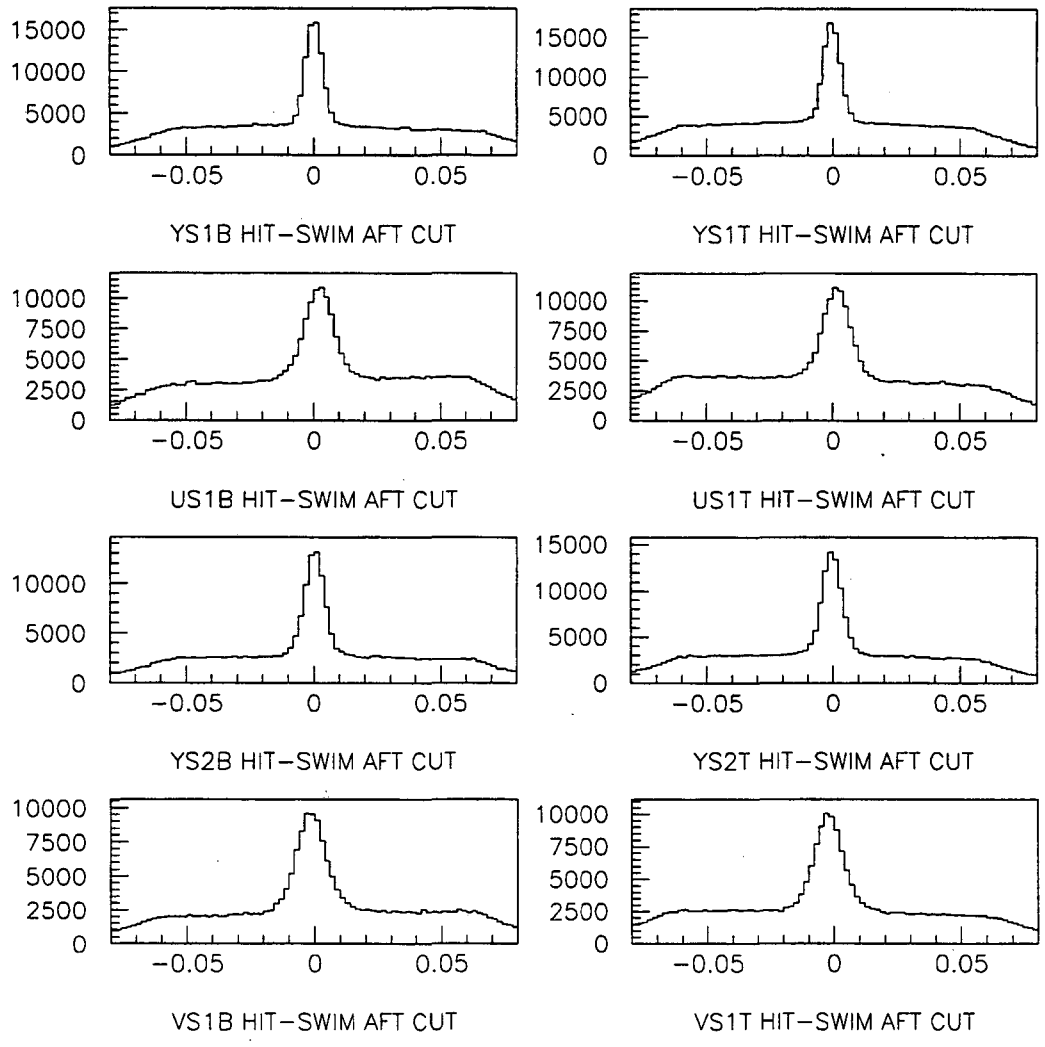

Figure 3.71: Distribution of the distances between the hits on a plane and the iterated Y position of the spectrometer track at that plane for Monte Carlo generated prompt J/ψ decays to two muons. (Units are in inches.)

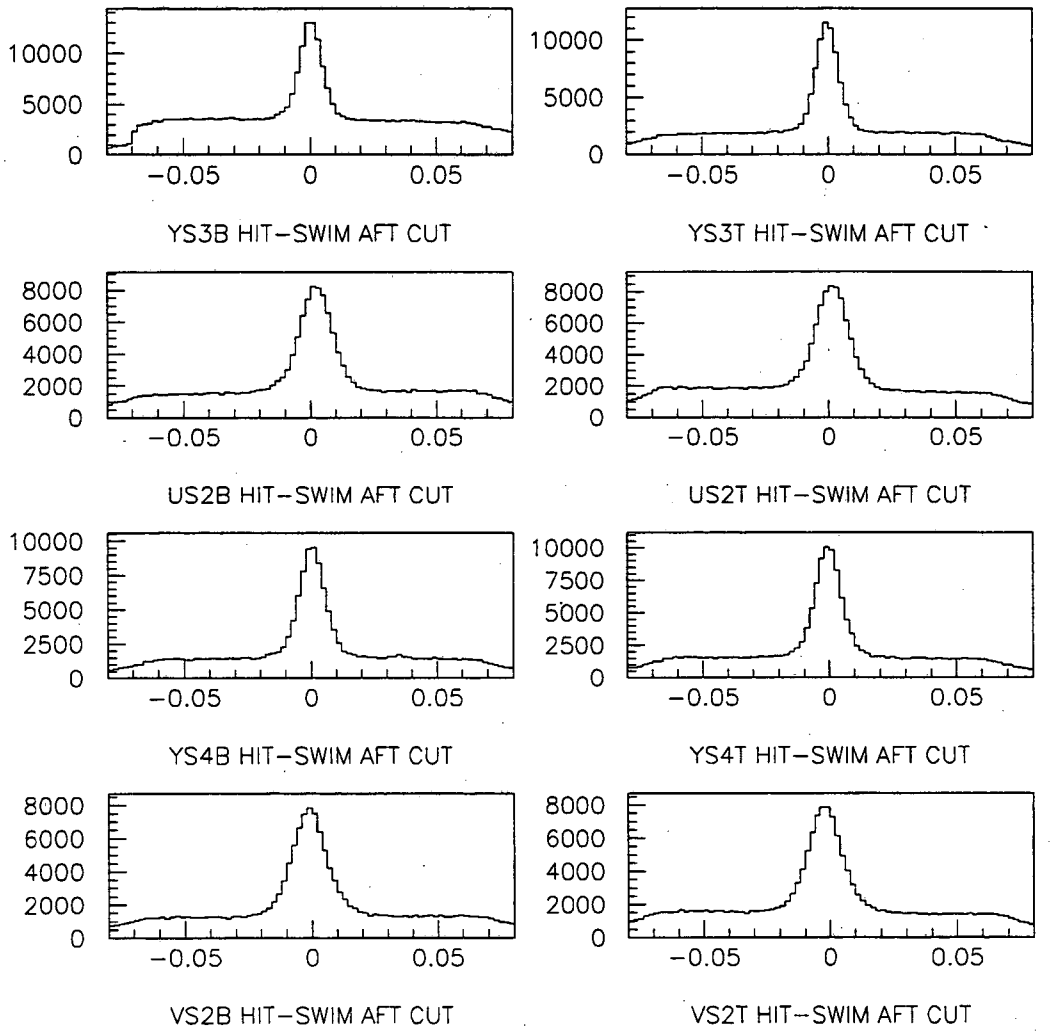

Figure 3.72: Distribution of the distances between the hits on a plane and the iterated Y position of the spectrometer track at that plane for a Monte Carlo generated prompt J/ψ decays to two muons (cont'd). (Units are in inches.)

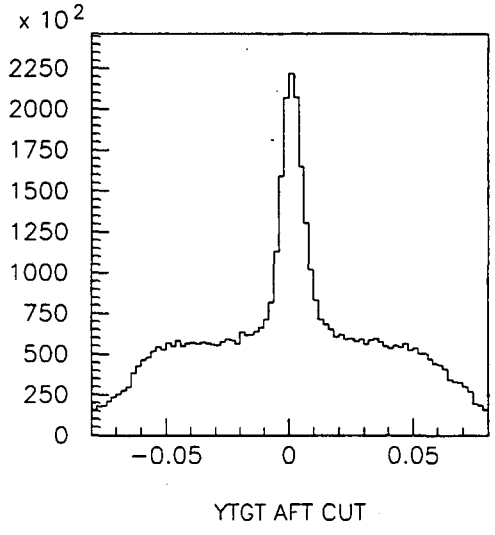

Figure 3.73: Distribution of $y_{target} - y_{track}(z_{target})$ for Monte Carlo generated prompt J/ψ decays to two muons. (Units are in inches.)

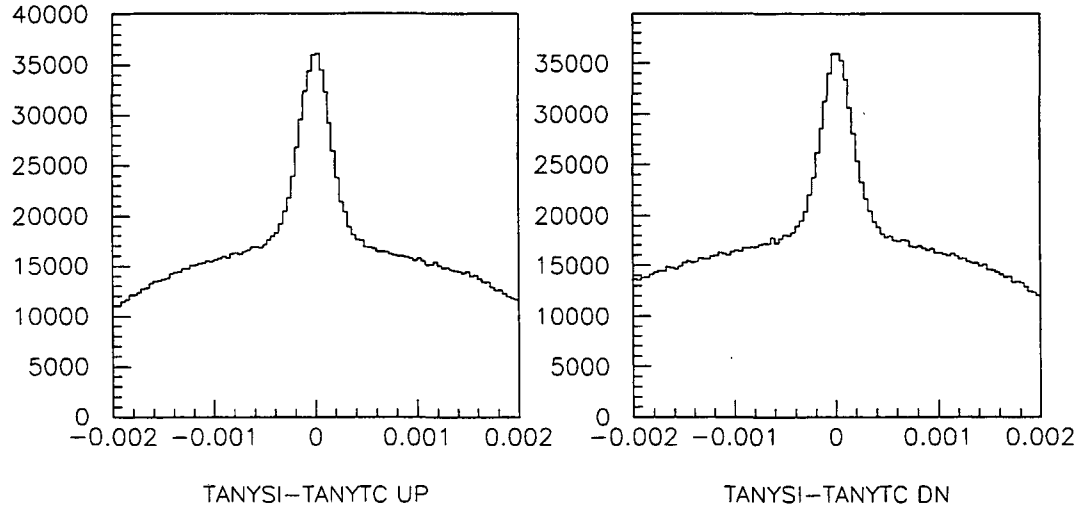

Figure 3.74: Distribution of ΔY_{slope} for Monte Carlo generated prompt J/ψ decays to two muons. The left plot shows the distribution for the upper arm of the silicon detector, the right plot is for the lower arm

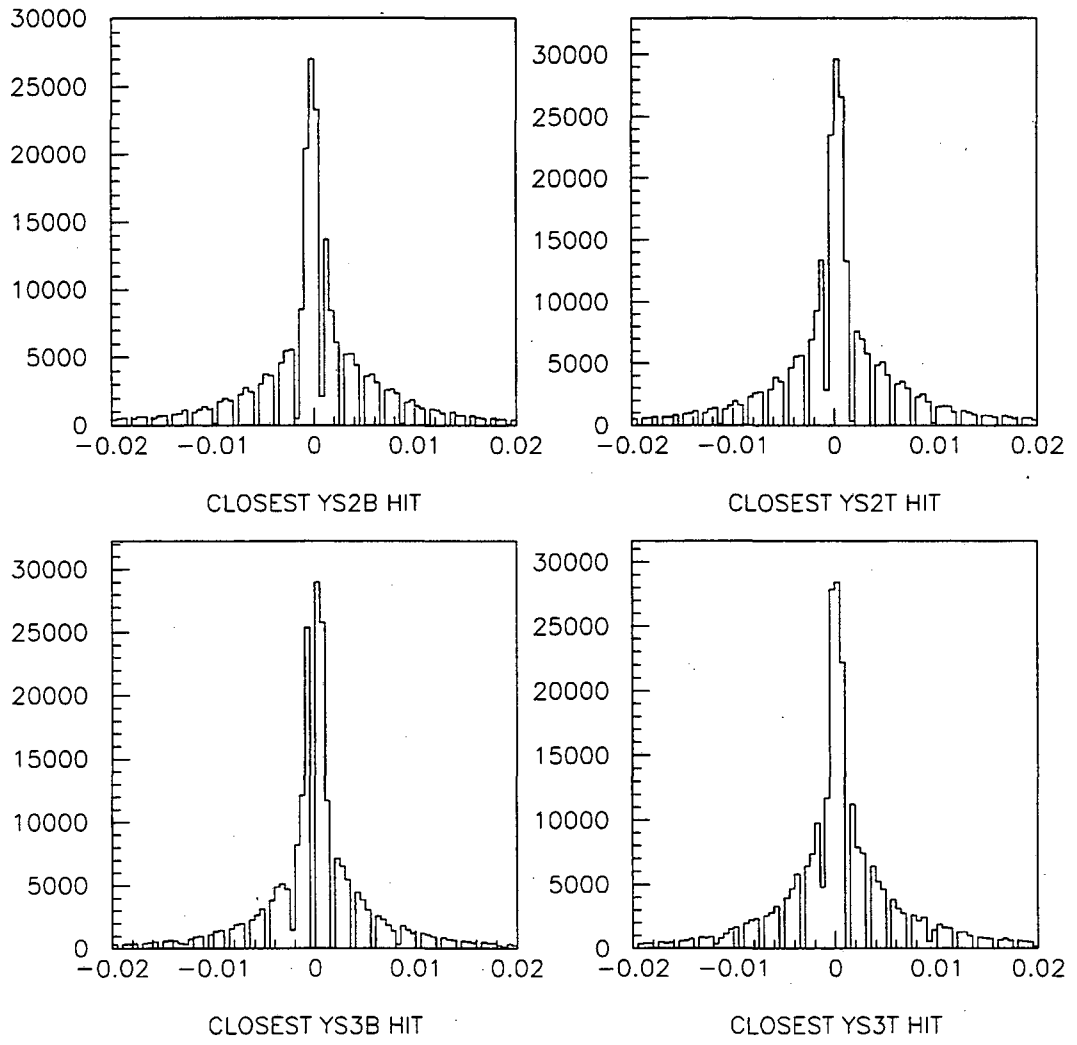

Figure 3.75: Distribution of the distances between the closest hits on the non-seed silicon Y planes and the candidate Y-track for Monte Carlo generated prompt J/ψ decays to two muons. (Units are in inches.)

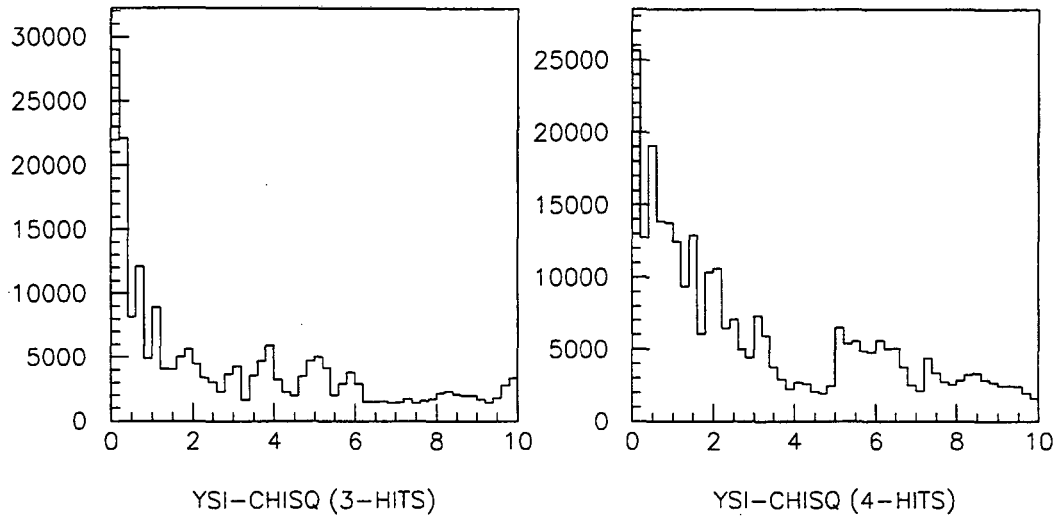

Figure 3.76: Distribution of the χ^2 per degree of freedom for 3 and 4 hit candidate Y-tracks for Monte Carlo generated prompt J/ψ decays to two muons.

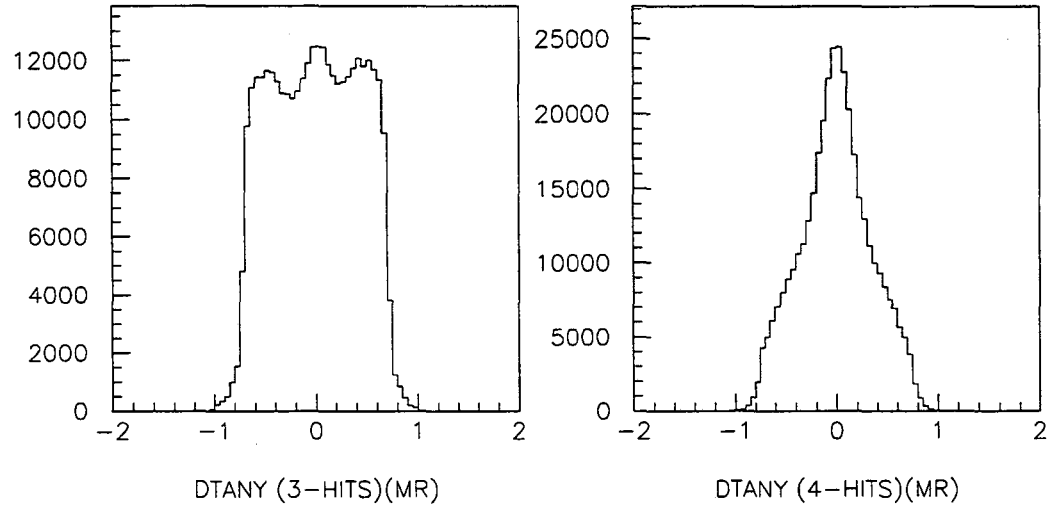

Figure 3.77: Distribution of ΔY_{slope} for Monte Carlo generated prompt J/ψ decays to two muons. The left plot shows the distribution for tracks with 3 hits and the right for 4 hit tracks. (Units are in milli-radians.)

Figure 3.49.

Figure 3.79 shows the extrapolated X-position of a candidate silicon X-track at the target Z position. Recall that there was a ±0.25 in. cut for accepted silicon X-tracks.

Figure 3.80 shows the difference between the X-slope of the silicon track and the spectrometer track. The distribution shows that the signal is contained mostly within the ±0.004 window cut used in the reconstruction code.

Figure 3.81 shows the distribution of the distance to the closest X hit from a candidate YUV-track in the non seed U/V planes. The distribution closely mimics the true distribution shown in Figure 3.54.

Figure 3.82 shows the χ^2 per degree of freedom distribution of reconstructed silicon tracks after a full 3-dimensional fit. The distributions are similar to the real dimuon distributions shown in Figure 3.55.

Figure 3.83 shows the X-slope match between the YUV-track and the spectrometer track. The distributions clearly shows the signal is embedded within the ±0.004 final slope cut. The distributions should be compared with Figure 3.57.

For a given spectrometer track, one or more silicon tracks may be reconstructed. Figure 3.84 shows the distribution of silicon tracks found for a single spectrometer track. The distribution should be compared to that of the real dimuon events shown in Figure 3.59. In order to choose the best silicon track for each spectrometer track, a track quality metric was used. (see equation 3.22.) The basis of the metric was the X and Y slope-match between the silicon and spectrometer tracks. Figure 3.85 shows the distribution of the X and Y slope matches between the best silicon track and the spectrometer track for Monte Carlo events. The plots shows the basis for the standard deviation values of 0.001 and 0.0003 used in the calculation of $P(\Delta tan_x)$ and $P(\Delta tan_y)$. The corresponding distribution for real dimuon events is shown in Figure 3.60. Figure 3.86 shows the distribution of the silicon track χ^2 used in the calculation of the quality metric.

Figure 3.87 shows the distribution of the distance of closest approach between opposite-sign muon tracks in each event. The distribution shows that the 0.08 in. cut was reasonable. The distribution should be compared with the distribution of real dimuon events in Figure 3.63.

Finally, Figure 3.88 shows the difference between the position of the reconstructed J/ψ decay vertex and the position of the primary interaction.

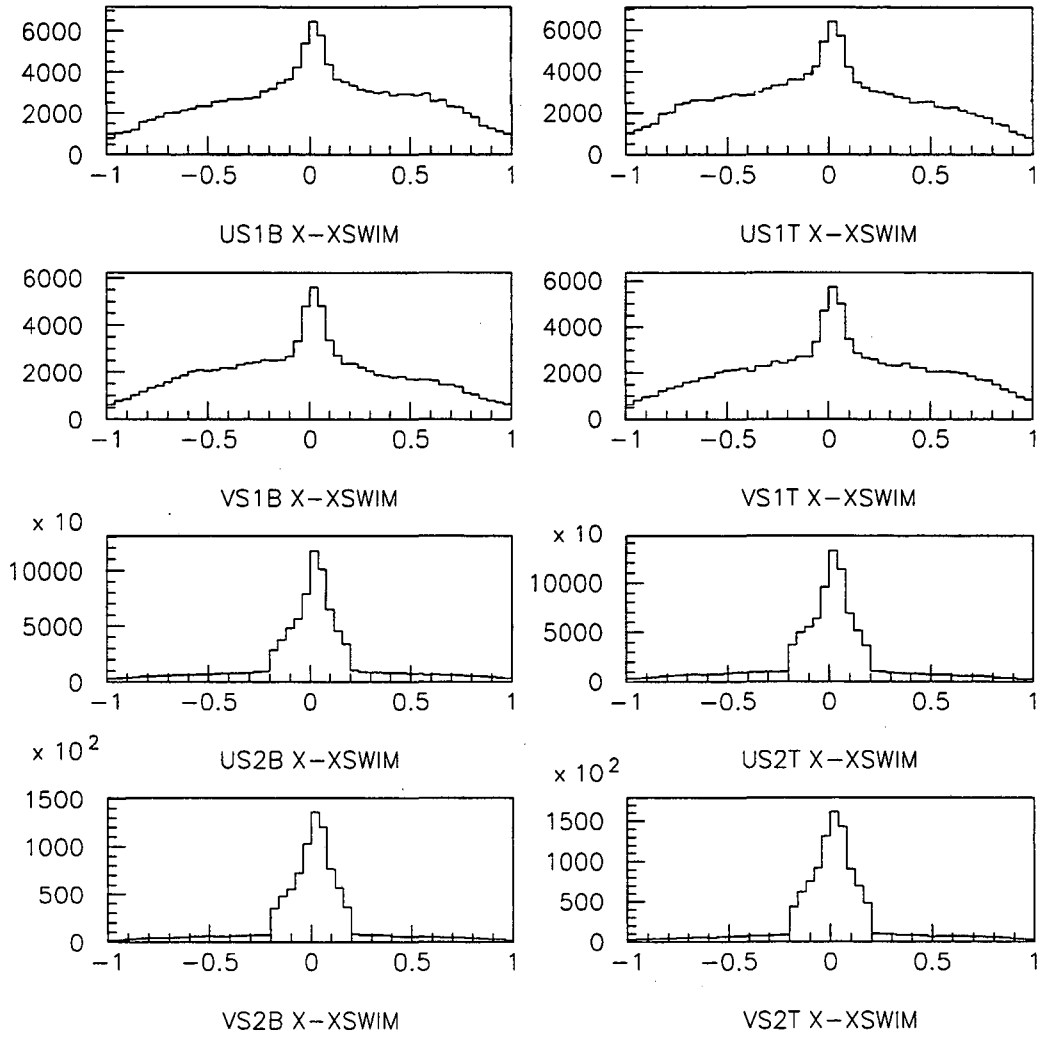

Figure 3.78: Distribution of the distance between the silicon hits on U/V planes and the iterated X position of the spectrometer track for Monte Carlo generated prompt J/ψ decays to two muons. (Units are in inches.)

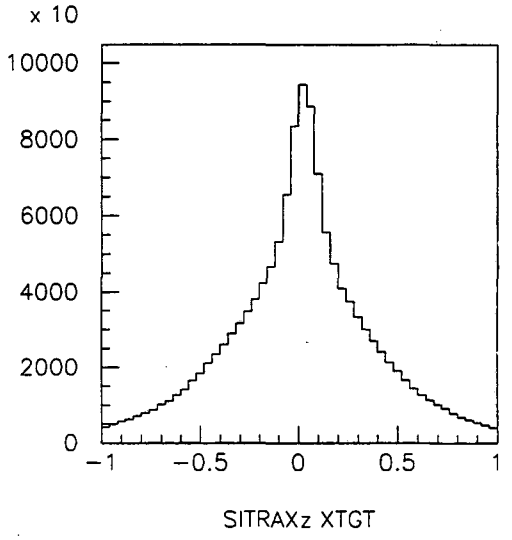

Figure 3.79: Distribution of the distance between the target position in X and the position of the candidate X track at the target Z position for Monte Carlo generated prompt J/ψ decays to two muons. (Units are in inches.)

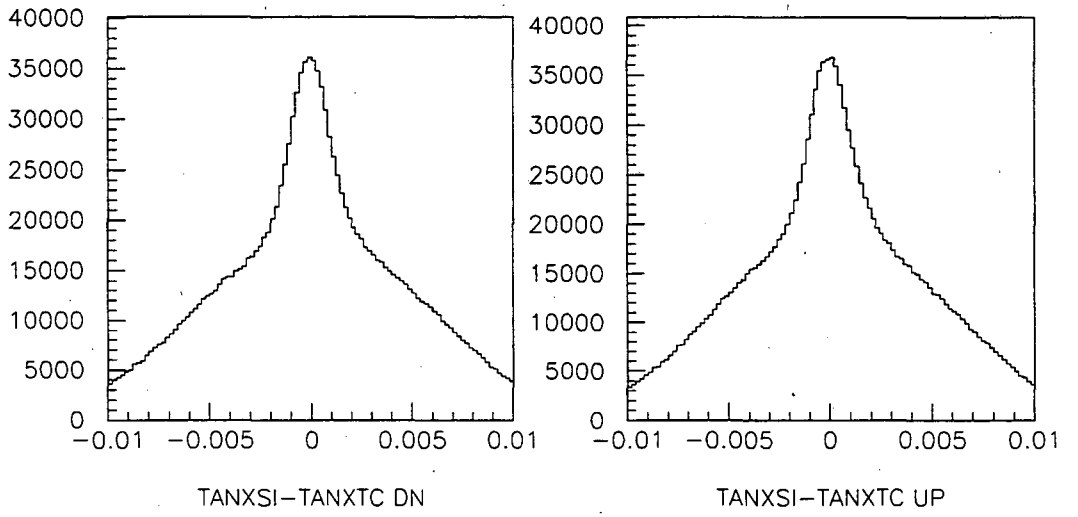

Figure 3.80: Distribution of ΔX_{slope} for Monte Carlo generated prompt $J/\psi \rightarrow \mu^+\mu^-$. The left (right) distribution is for tracks in the lower (upper) arm of the silicon detector.

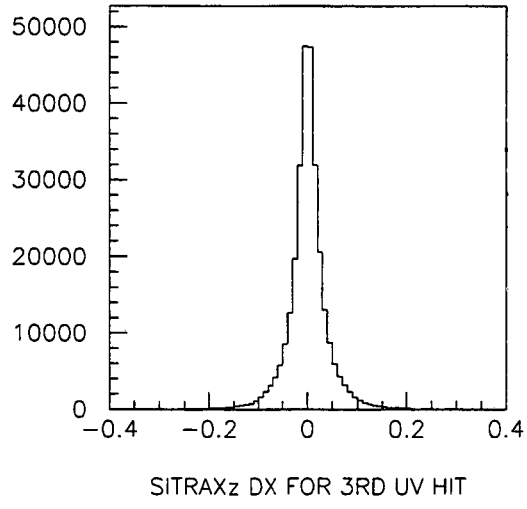

Figure 3.81: Distribution of the distances between the closest hits on the non-seed silicon X planes and the candidate X track for Monte Carlo generated prompt J/ψ decays to two muons. (Units are in inches.)

The reconstructed Monte Carlo tracks that survive through pass 3 analysis have characteristics that are similar to the reconstructed real dimuon tracks. Figures 3.89 and 3.90 show the distribution of the number of drift chamber and hodoscope hits, respectively, of the accepted dimuon tracks. These distributions should be compared with the ones in Figures 3.5 and 3.7 for the dimuon data set. Figure 3.91 shows the distribution of the χ^2 per degree of freedom for accepted muon tracks. The distributions are close to the distributions for the real muon tracks shown in Figure 3.9.

The final check on the accuracy of the Monte Carlo simulation is the comparison of the reconstructed prompt J/ψ mass specta. Figure 3.92a and 3.92b shows the dimuon invariant mass spectrum obtained from the Monte Carlo and real data, respectively. (Note that the non-J/ψ background in the Monte Carlo data was added to the mass plot.) Figure Figure 3.93 shows the two distributions overlayed on top of each other. The reconstructed mass of the J/ψ is centered at 3.098 GeV for the Monte Carlo events and 3.097 GeV for the data. The mass resolution (after background subtraction) is 14 MeV and 16 MeV respectively.

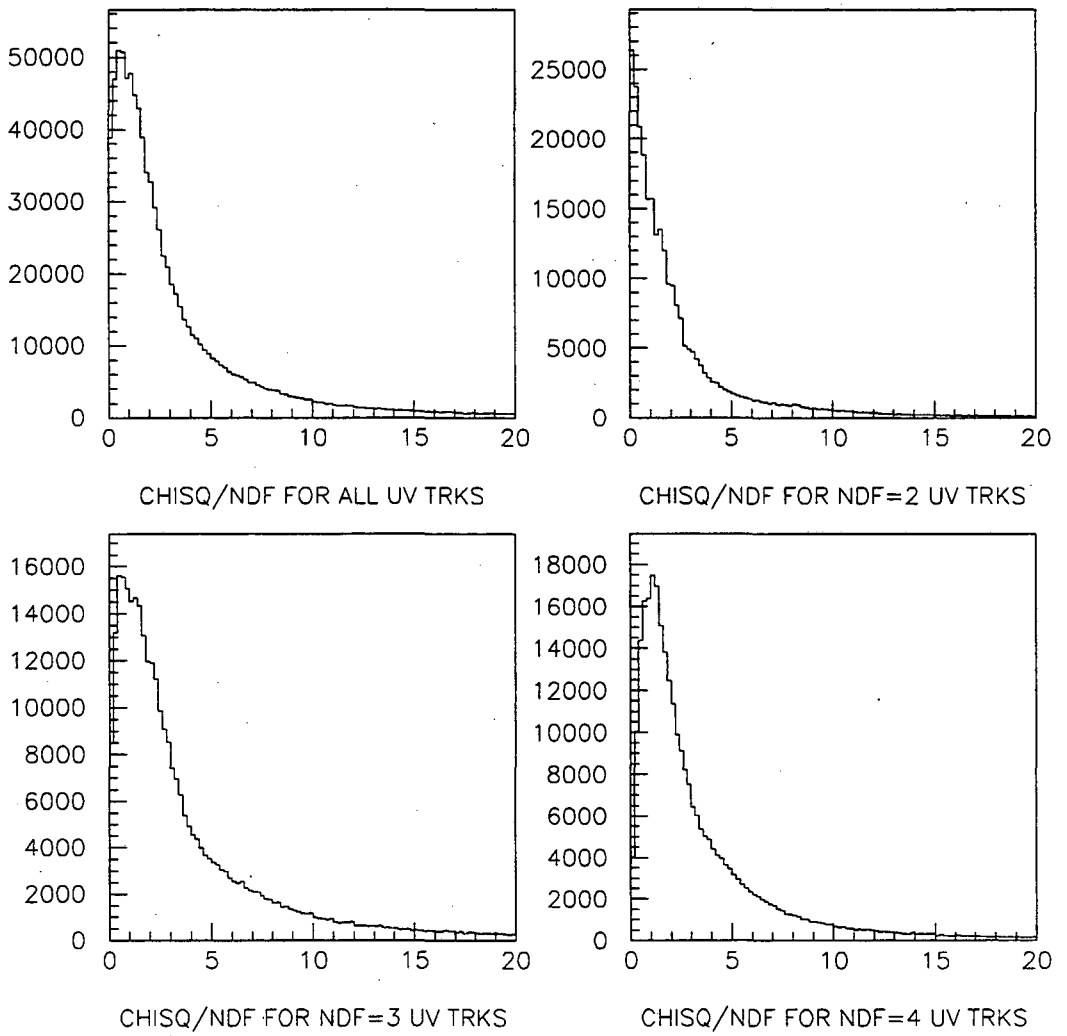

Figure 3.82: Distribution of the χ^2 per degree of freedom distributions for tracks with 6 or more hits, 6 hits, 7 hits and 8 hits for Monte Carlo generated prompt J/ψ decaying to two muons.

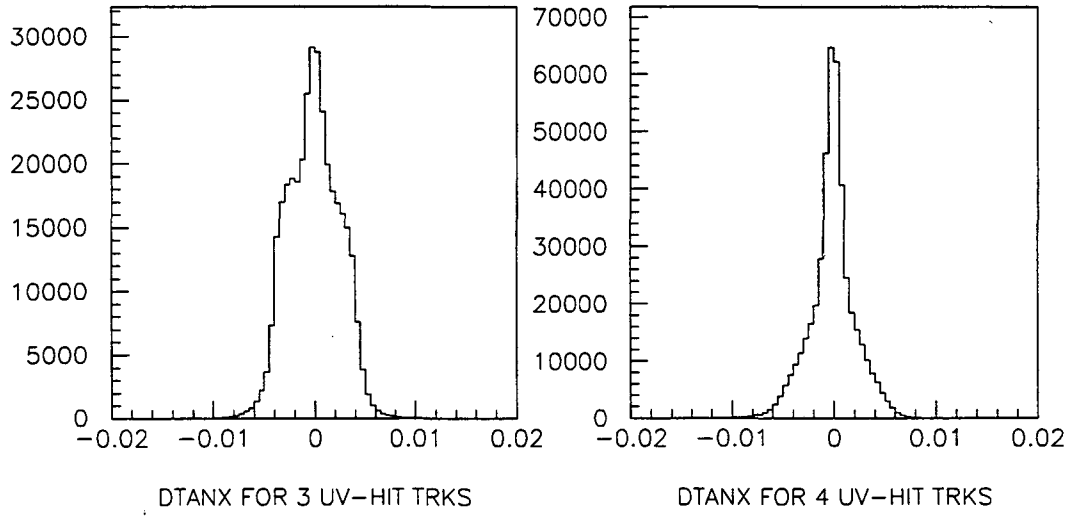

Figure 3.83: Distribution of ΔX_{slope} for Monte Carlo generated prompt J/ψ to two muons. The left plot shows the distribution for 3-hit UV tracks and the right, for 4-hit UV tracks.

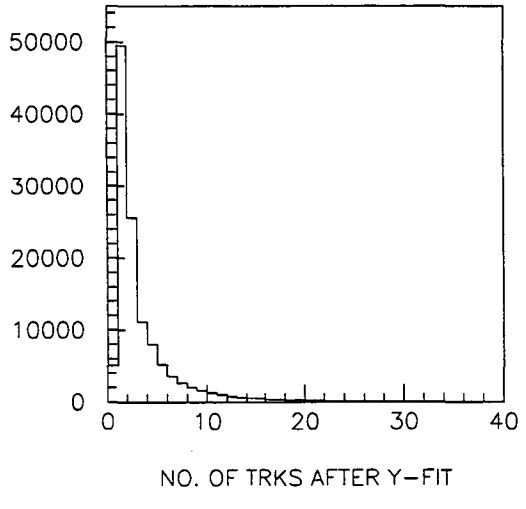

Figure 3.84: Distribution of the number of silicon tracks found for each spectrometer track for Monte Carlo generated prompt J/ψ decays to two muons.

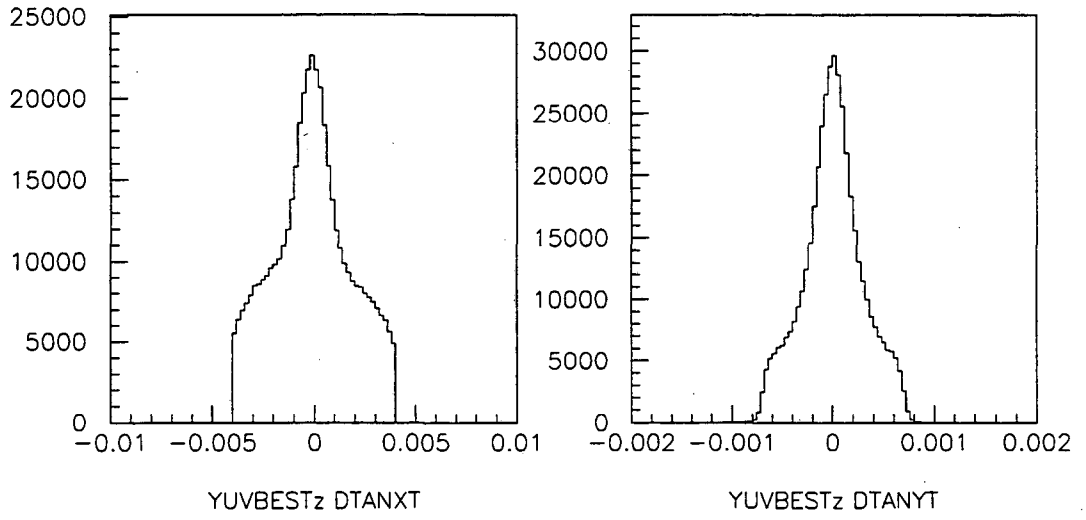

Figure 3.85: Distribution of ΔX_{slope} (left) and ΔY_{slope} (right) for Monte Carlo generated prompt J/ψ decays to two muons before the final cut.

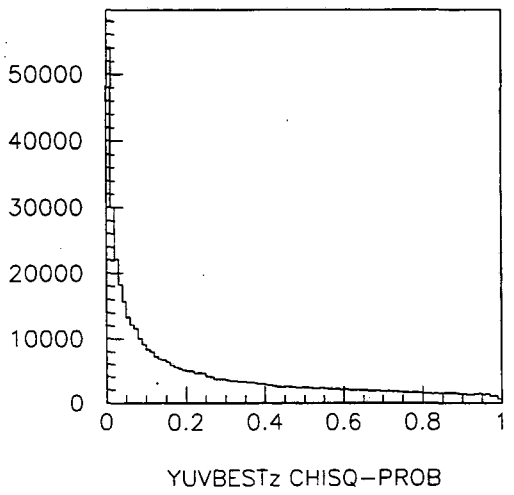

Figure 3.86: Distribution of the probability for the track fit χ^2 per degree of freedom, for Monte Carlo generated prompt J/ψ decays to two muons, used in the final silicon track cut.

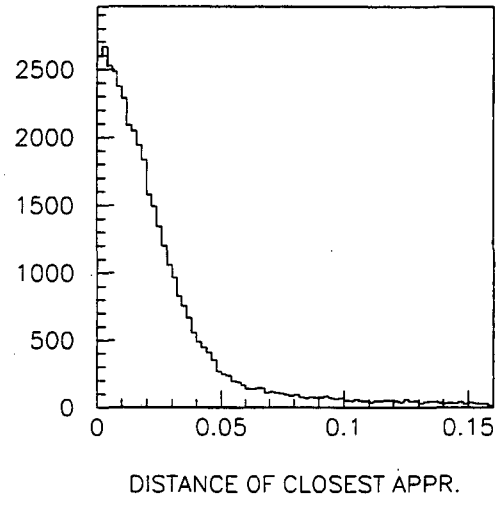

Figure 3.87: Distribution of the distance of closest approach between $\mu^+\mu^-$ tracks in Monte Carlo generated prompt J/ψ decays to two muons (left). (Units are in inches.)

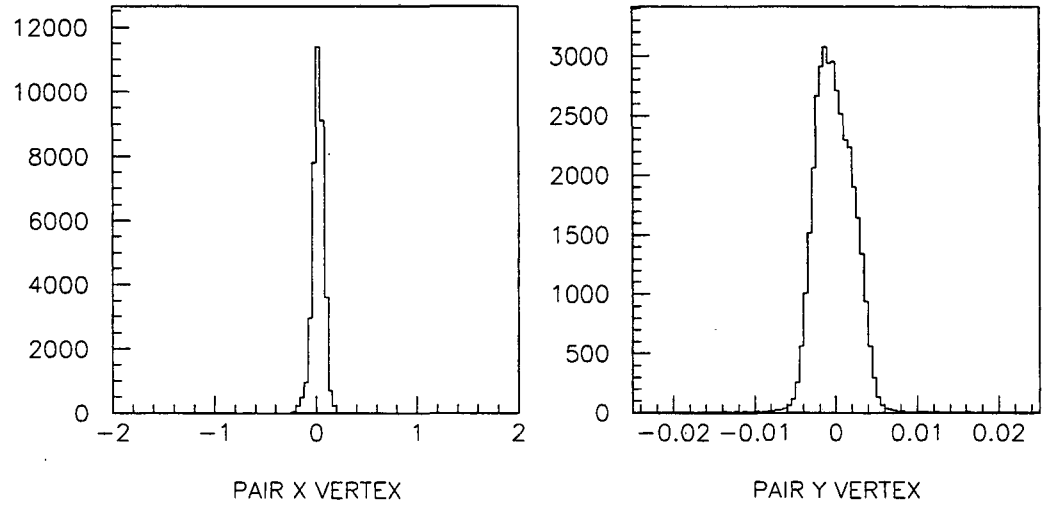

Figure 3.88: Distribution of the distance in X and Y to the primary interaction vertex position from the decay vertex for Monte Carlo generated prompt J/ψ decays to two muons. The plot on the left is the X distance and the right is the Y distance. (Units are in inches.)

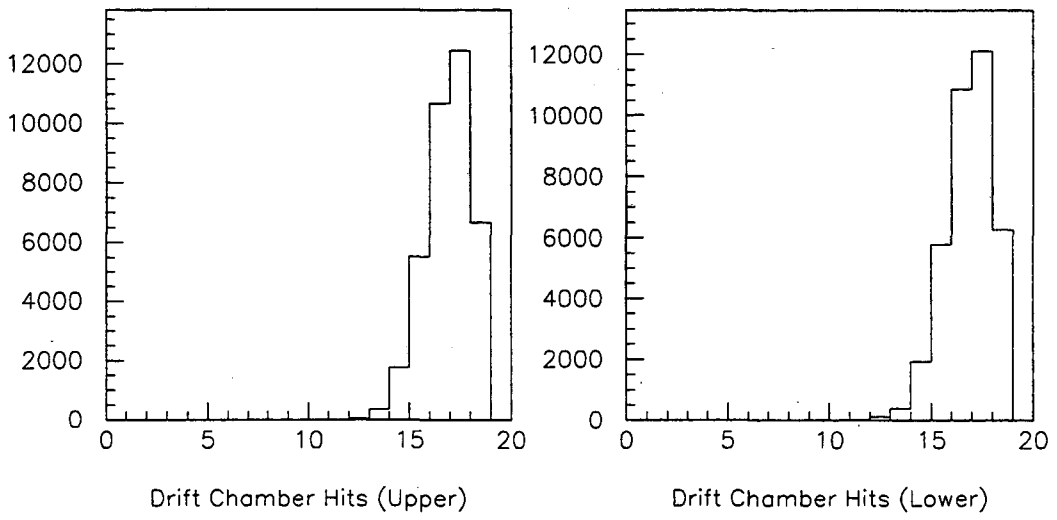

Figure 3.89: Distribution of the number of drift chamber hits in accepted upper (left) and lower (right) arm muon tracks for Monte Carlo generated prompt J/ψ decays to $\mu^+\mu^-$.

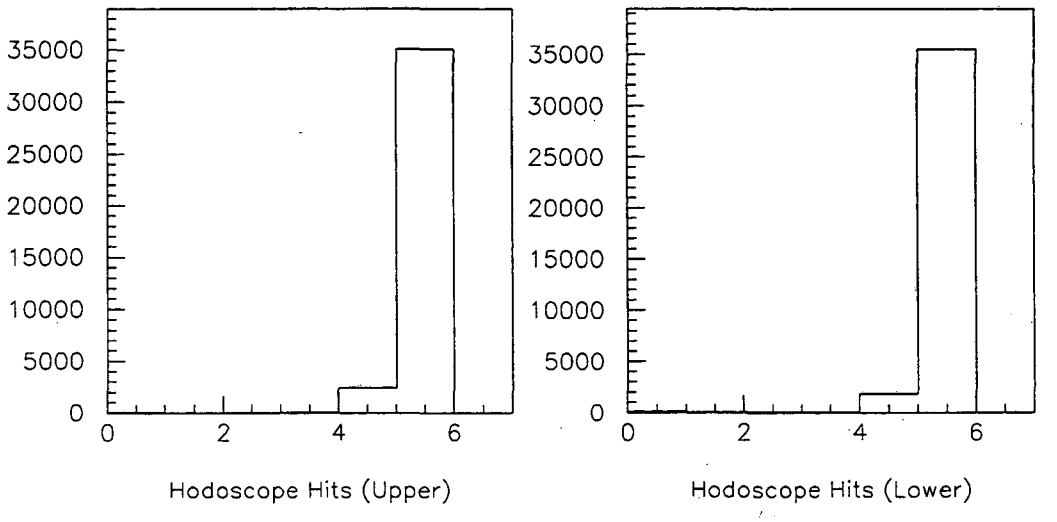

Figure 3.90: Distribution of the number of hodoscope hits in accepted upper (left) and lower (right) arm muon tracks for Monte Carlo generated prompt J/ψ decays to $\mu^+\mu^-$.

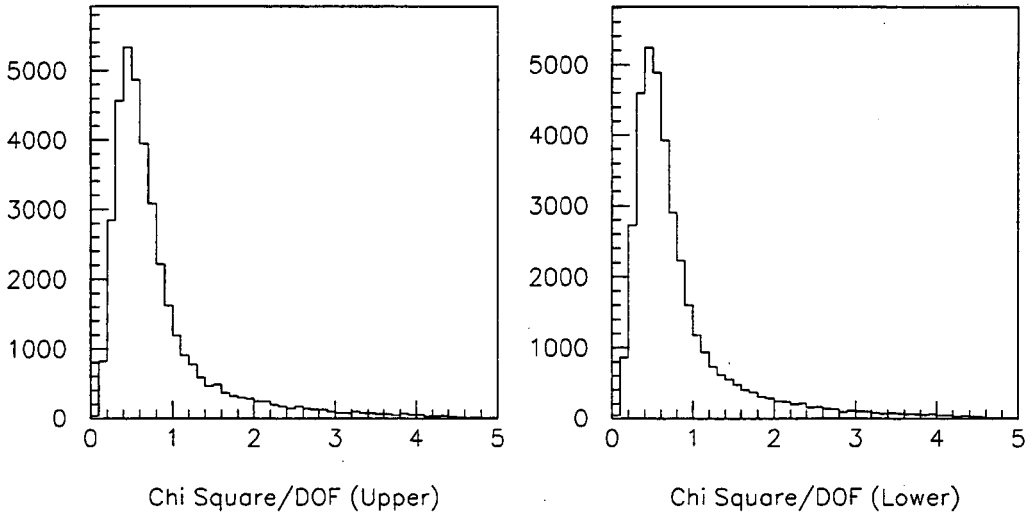

Figure 3.91: Distribution of the χ^2 per degree of freedom for accepted upper (left) and lower (right) arm muon tracks from Monte Carlo generated prompt J/ψ decays to two muons.

3.4 Acceptance and Efficiency

In the calculation of the branching ratio, BR_i (see equation 3.5), a critical factor was the determination of the ratio of the efficiencies ϵ_i and ϵ_{ref}. Each efficiency is the ratio of the number of events in a given channel that should have be seen in the data on tape and the number of events in the same channel that occurred in the beam–target interaction during the b-run. Conceptually, each ϵ_i is the product of a series of acceptances and efficiencies (see equation 3.27) that measure the loss of signal events at various stages of data collection and data analysis.

$$\epsilon_i = \epsilon_{geom}\epsilon_{trig}\epsilon_{live}\epsilon_{tape}\epsilon_{recon}\epsilon_{select} \tag{3.27}$$

The factors in ϵ_i are :

- ϵ_{geom} – Geometric acceptance. The ratio of the number of signal events that were fully contained within the active region of the detector to the number of signal events generated in the proton on nucleon interaction.

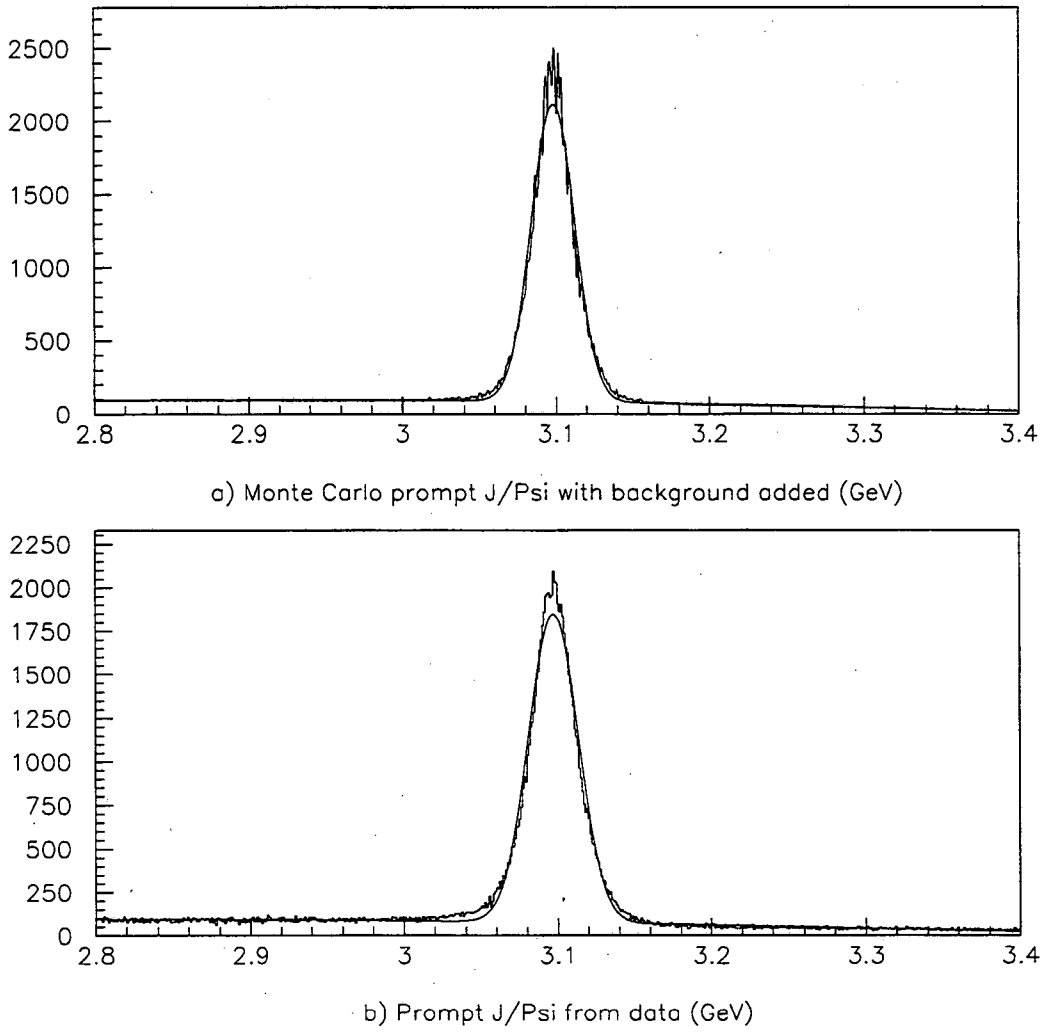

Figure 3.92: Invariant mass of Monte Carlo generated prompt J/ψ with added background (a) and real dimuon events (b).

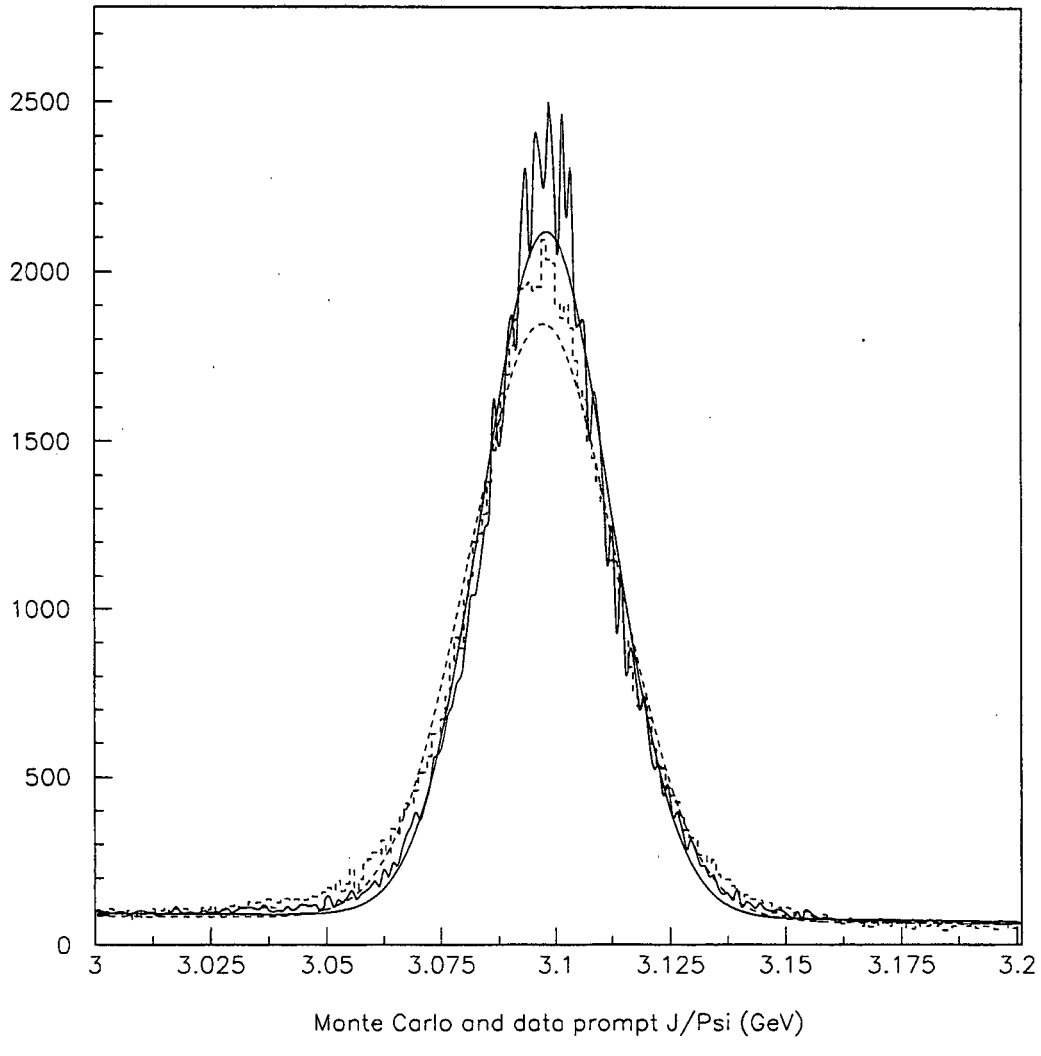

Figure 3.93: Invariant mass of Monte Carlo generated prompt J/ψ dimuon events (solid line) and real dimuon events (dotted line) and fits to the Monte Carlo generated (smooth solid curve) and real dimuon (dotted smooth curve) background and signal.

- ϵ_{trig} – Trigger efficiency. The ratio of the number of signal events triggered by the triggering system to the number of signal events within the geometric acceptance of the spectrometer.

- ϵ_{live} – Data acquisition system live time. The ratio of the number of signal events accepted by the triggering system when the readout system was ready to accept a new event to the number of signal events triggered by the triggering system.

- ϵ_{tape} – Tape read back efficiency. The fraction of events that were successfully read back from the data tapes at the different stages of processing . (Event loss was due to tape failures and event format errors.)

- ϵ_{recon} – Reconstruction efficiency. The fraction of signal events that were reconstructed. (Event loss was due to the various cuts applied in the reconstruction process.)

- ϵ_{select} – Event selection efficiency. The fraction of reconstructed signal events which survived the event selection cuts.

Note that these efficiency factors can be products of sub-efficiencies and some may be decay channel dependent. In addition, the factors may be correlated.

As was stated previously, many of these efficiencies were determined with Monte Carlo calculations. This was accomplished in the following steps. First, the Monte Carlo was used to generate a known number of events in a particular decay mode. These events were then propagated through the simulation of the detector, taking into consideration the above efficiency and acceptance effects. Next, the surviving events were combined with "noise" hits in the silicon detector and wire chambers that were obtained from data. These noise overlayed Monte Carlo events were then placed into a DST file which was processed by the analysis code. (The noise hits were designed to simulate event background in the silicon detector and the drift chambers.) The ratio of the number of events reconstructed to the number of events initially generated by the Monte Carlo gave an estimate for most of the factors that comprise ϵ_i.

In the following sections, the methods by which each of the efficiencies and acceptances, shown in equation 3.27, were incorporated into the overall efficiency determination are discussed. The discussion of efficiency and acceptance effects is broken down into the following sections:

- Detector Efficiencies
- Miscellaneous Efficiencies
- Geometric Acceptance
- Trigger Efficiency
- Reconstruction Efficiency
- Event Selection Efficiency

3.4.1 Detector Efficiencies

A key component of the determination of the overall efficiencies for the acceptance and reconstruction of the various decay modes was the efficiencies of the individual detector planes (and in some cases, their components). The planes that were of interest are the hodoscope planes in stations 1, 2 and 3, the muon station hodoscope planes, the silicon micro-vertex detector planes, and the wire chamber planes. The efficiencies of the hodoscopes are particularly important because they were an integral component of the triggers. The efficiencies of the silicon and drift planes are important in the determination of the tracking efficiencies.

Hodoscope Efficiencies

A detailed understanding of the efficiencies of the hodoscope planes in stations 1, 2, and 3 was required in order to estimate the efficiencies of the matrix ($M_U \cdot M_D$) trigger. This meant that the efficiencies of the individual hodoscope sections in each hodoscope plane needed to be determined. This was accomplished by looking at unbiased events in the data tapes that contained tracks that passed through different sections of the hodoscope planes and seeing what fraction of the time the sections registered a hit. The key to this technique was the selection of an unbiased sample of events, i.e., events that did not require the hodoscopes to fire.

The steps used to calculate the hodoscope efficiencies are outlined below:

1. Choose a sample of data tapes to be analyzed. In this case, 11 data tapes were chosen for analysis.

2. Save all prescaled TFI events that have the $E_H \cdot RF$ component ON. This guarantees that the events used in the analysis were unbiased.
3. Using those selected events, reconstruct the tracks in the event using only the drift chambers in stations 1, 2 and 3.
4. Select only high quality tracks.
   (a) Choose only high momentum tracks, i.e., > 50 GeV/c, since the effects of multiple scattering are smaller.
   (b) Choose tracks with greater than 15 drift chamber hits (out of a possible 18 hits).
   (c) Choose tracks with a chi square per degree of freedom < 3.
5. Project the high quality tracks into each hodoscope plane.
6. For tracks that pass within the fiducial area of a hodoscope section, count the number of times the tracks were registered by the section. (The fiducial area of the detector excludes a small strip around the perimeter of each hodoscope section.)
7. For each hodoscope section, divide the number of registered hits by the expected number of hits.

This procedure assumes that the DAQ efficiency for reading out each hodoscope section was the same. It also assumes no rate-dependent effects and that the edge effects were decay channel independent.

The efficiencies of the hodoscope planes are shown in Table 3.2. These efficiencies have been compared with efficiencies calculated by other methods and are consistent with them [40, 50].

Muon Hodoscope Efficiencies

The efficiencies of the muon hodoscopes are important in the determination of the efficiency of the muon triggers as well as in the efficiency of muon track reconstruction. The efficiencies that were used in this analysis for each muon hodoscope section were taken from previous analyses [40, 50]. The technique used to determine the muon hodoscope efficiencies was similar to the technique used to determine the efficiencies of the station 1, 2 and 3 hodoscopes. The muon hodoscope efficiencies used in this analysis are shown in Table 3.3.

Sec.	Hodoscope Plane Efficiency (Percent)									
No.	X1U	X1D	Y1L	Y1R	Y2L	Y2R	X3U	X3D	Y3L	Y3R
1	97	98	68	94	94	100	96	100	100	100
2	98	100	87	98	59	87	97	99	100	78
3	99	99	61	92	97	99	97	99	100	88
4	100	100	98	99	96	100	97	100	99	94
5	100	100	95	99	95	100	99	100	100	94
6	100	100	95	97	96	100	99	100	100	99
7	98	100	96	99	99	100	100	66	100	93
8	100	100	97	99	98	98	98	100	99	96
9	99	100	83	99	90	99	98	98	100	88
10	99	99	98	98	94	100	94	83	99	95
11	98	99	92	94	99	99	98	67	100	94
12	99	99	90	92	99	99	51	76	100	86
13	-	-	-	-	98	99	-	-	100	100
14	-	-	-	-	92	98	-	-	-	-
15	-	-	-	-	80	99	-	-	-	-
16	-	-	-	-	100	100	-	-	-	-

Table 3.2: Efficiencies for the hodoscopes in stations 1, 2 and 3.

Tracking Plane Efficiencies

The efficiencies of the tracking planes, i.e., drift chamber planes, proportional chamber planes and silicon micro-vertex planes, were important in determining the efficiency of track reconstruction. For these detectors, individual wire (or strip) efficiencies, however, were not used. Instead, per-plane efficiencies were used. Tables 3.6, 3.4 and 3.5 respectively show the efficiencies that were determined for the silicon, drift and proportional detectors. These efficiencies were also determined from previous analysis of the data from the same experiment [40, 50].

3.4.2 Miscellaneous Efficiencies

In this section, the efficiency factors with simpler dispositions are discussed, notably ϵ_{live} and ϵ_{tape}. Unlike most of the other efficiencies shown in equation 3.27, the effects of these efficiencies were not determined with the Monte Carlo.

Sec. No.	Muon Hodoscope Efficiency (Percent)			
	Y4L	Y4R	X4U	X4D
1	-	-	-	-
2	97	98	100	100
3	100	99	100	100
4	100	100	99	99
5	100	100	99	100
6	100	100	100	100
7	100	100	99	99
8	100	100	99	100
9	100	100	98	100
10	100	100	100	100
11	100	100	99	99
12	100	100	100	99
13	98	99	99	98
14	-	-	100	96
15	-	-	100	100
16	-	-	-	-

Table 3.3: Efficiencies of the muon station hodoscopes.

Plane Name	Drift Chamber Efficiency (Percent)
Y1	89.78
Y1′	87.00
U1	91.16
U1′	88.28
V1	84.96
V1′	89.88
Y2	94.38
Y2′	91.98
U2	89.38
U2′	94.05
V2	90.66
V2′	90.32
Y3	91.98
Y3′	93.81
U3	86.33
U3′	96.28
V3	93.06
V3′	90.77

Table 3.4: Efficiencies of the drift chamber planes.

Plane Name	Muon Proportional Tube Efficiency (Percent)
PTY1	95
PTX	95
PTY2	95

Table 3.5: Efficiencies of the muon proportional tubes.

Plane Name	Silicon Efficiency (Percent)
Y1B	92.76
Y1T	92.95
U1B	93.94
U1T	84.98
Y2B	93.67
Y2T	94.01
V1B	93.25
V1T	91.73
Y3B	93.21
Y3T	90.47
U2B	90.89
U2T	89.90
Y4B	91.45
Y4T	91.12
V2B	93.98
V2T	92.83

Table 3.6: Efficiencies of the planes in the silicon micro-vertex detector.

ϵ_{live} : Data Acquisition Live Time

The dihadron and dimuon data analyzed in this thesis were taken from a single run of the E789 experiment. More specifically, each event in the run was examined for dimuon and dihadron events. Hence, ϵ_{live}, the ratio of the number of signal events recorded on data tape to the number of signal events that generated a trigger, should be the same for both data sets. Therefore, it was assumed that the live time cancelled in the ratio of the dihadron and dimuon efficiencies.

ϵ_{tape} : Tape Read Back Efficiency

The tape read back efficiency, ϵ_{tape}, attempts to quantify the loss of events due to problems in reading raw and DST tapes. Pass 1 processing involved reading the raw data tapes. Since dihadron and dimuon events were intermixed on each raw tape, the fractional event loss for dihadron and dimuon events should be equal. Thus, like ϵ_{live}, the ratio of the fraction of dihadron events and dimuon events that were successfully read from the raw tapes was assumed to be one. (Note that in making this assumption, it was assumed that

any event losses due to event format errors in the raw tapes was independent of the decay channel.) In subsequent stages of processing (e.g., pass 2) there was no event loss. Thus, in the ratio, ϵ_{tape} for the dimuon and dihadron data sets canceled.

3.4.3 Geometric Acceptance

The E789 spectrometer was specifically designed to throw away a considerable fraction of signal events to increase the signal to noise ratio. This was mostly accomplished with the combination of the beam dump and SM12. An additional fraction of events was lost as a result of the limited size of the detector planes downstream of SM12 and the limited aperture of SM3. The geometric acceptance factor, ϵ_{geom}, in ϵ_i quantifies the ratio of signal events that were fully contained in the detector volume and the number of signal events actually generated in all proton-on-nucleon interactions in the b-run.

The effects of the limited acceptance of the spectrometer was incorporated in the Monte Carlo through the use of known geometric apertures located at discrete points along the length of the spectrometer. During the propagation of the decay particles through the detector volume in the software, the position of each particle was compared with the apertures to determine if the particle strayed from the active region of the detector. If either one of the two signal particles, i.e., one of the muons (hadrons) from the J/ψ (b-hadron) decay, landed outside of the acceptance of the detector, the generated event was removed from the Monte Carlo event output stream.

The effect of the geometric acceptance of the spectrometer can be seen in the P_t and X_F distributions for accepted b-events. Figures 3.94 and 3.95 show the P_t and X_F spectrum for accepted B mesons in the $B \to \pi^+\pi^-$ channel. Figures 3.96 and 3.97 show the same distributions for $B \to J/\psi \to \mu^+\mu^-$. These should be compared with the generated P_t and X_F spectrum shown in Figures 1.12 and 1.13 in section 1.4.1. (For completeness, Figures 3.98 and 3.99 show the P_t and X_F spectrum for the J/ψ's in the $B \to J/\psi \to \mu^+\mu^-$ channel.)

3.4.4 Trigger Efficiency

The trigger efficiency is the ratio of the number of signal events flagged by the trigger system and the number of signal events contained within the geometric acceptance of the spectrometer. The trigger efficiency itself was a product of a number of factors

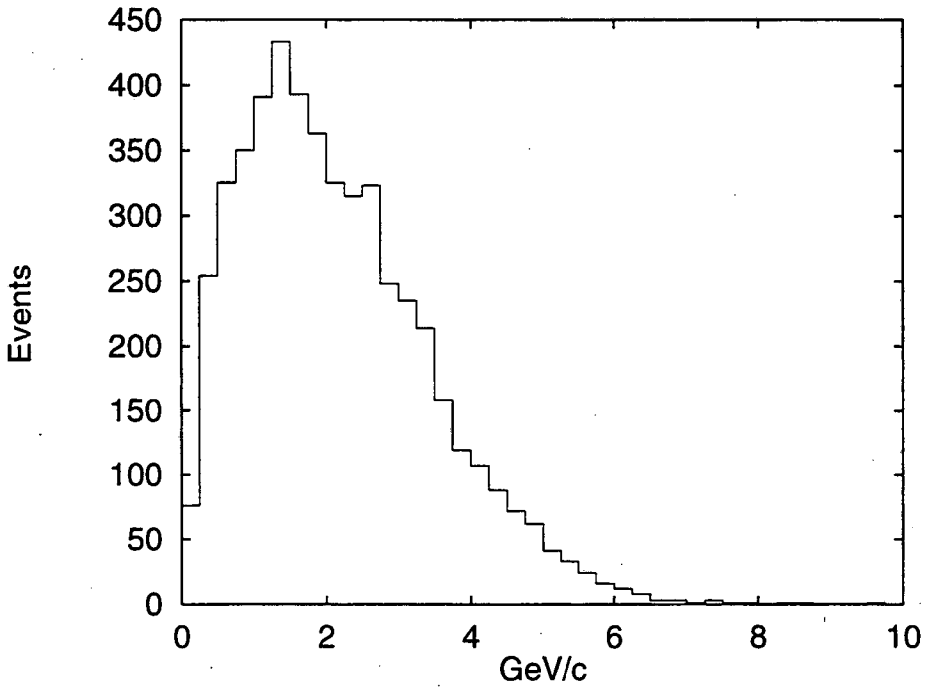

Figure 3.94: P_t spectrum of accepted B mesons for $B \to \pi^+\pi^-$ assuming 100% detector efficiency (Monte Carlo).

since the trigger system itself was the logical AND of many components (see sections 2.5.1 and 2.5.2). The major components of the trigger efficiency were the:

- TFI trigger efficiency,
- $M_U \cdot M_D$ efficiency,
- $S_U \cdot S_D$ efficiency,
- $\overline{NX1} \cdot \overline{NX3}$ efficiency,
- Calorimeter trigger efficiency,
- Muon trigger efficiency.

TFI Trigger Efficiency

As mentioned in section 2.5, the trigger was a two level trigger, the TFI level one trigger and the TGO level two trigger. Assuming no cross contamination between events,

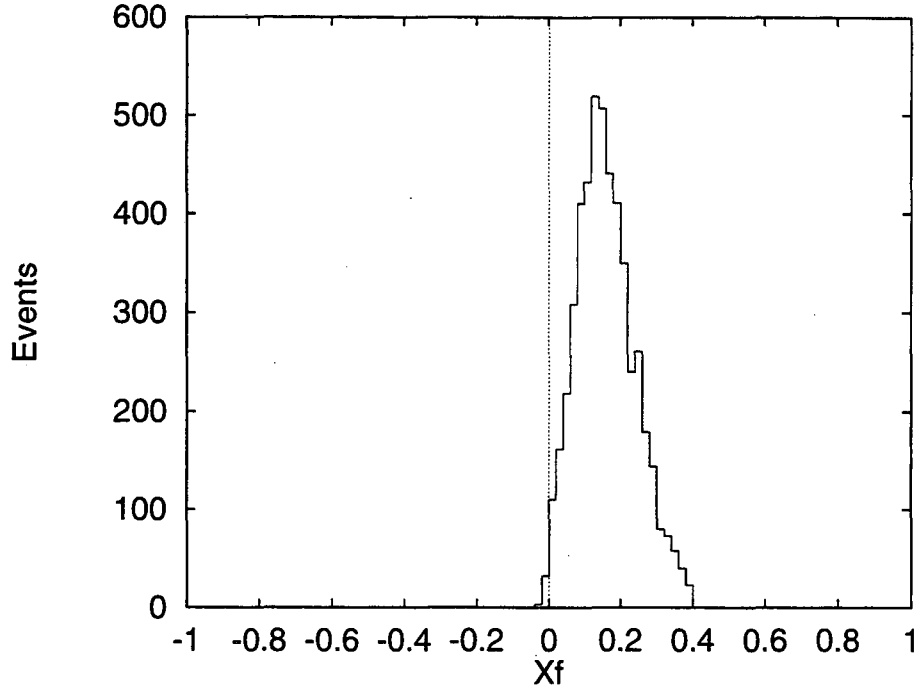

Figure 3.95: X_F spectrum of accepted B mesons for $B \to \pi^+\pi^-$ assuming 100% detector efficiency (Monte Carlo).

i.e., dimuon events were always triggered by the dimuon component of the TGO trigger and dihadron events were always triggered by the dihadron component of the TGO trigger, then the efficiency of the complete trigger system was determined by the efficiency of the TGO trigger. This is due to the fact that TGO dimuon (dihadron) triggers should be a subset of the TFI dimuon (dihadron) triggers. This, in turn, can be seen by looking at the construction of the TFI and TGO triggers.

The TFI trigger logic is shown below:

$$\mathrm{TFI} = 4/4\mu\mathrm{LR} + (\mathrm{E_H} \cdot \mathrm{RF}) + (2/4\mathrm{M} \cdot 2\mathrm{Y4}) + (\mathrm{e_L} \cdot \mathrm{RF}) \tag{3.28}$$

Assuming no cross contamination, all dihadron events trigger $(\mathrm{E_H} \cdot \mathrm{RF})$ and all dimuon events trigger either $4/4\mu\mathrm{LR}$ or $(2/4\mathrm{M} \cdot 2\mathrm{Y4})$. At the TGO level, the dimuon events only fire the $\mu^+\mu^-$ trigger and the dihadrons fire the h^+h^- trigger. (Again, assuming no cross contamination.) The $\mu^+\mu^-$ and h^+h^- triggers were constructed as follows:

$$h^+h^- = \mathrm{M_U} \cdot \mathrm{M_D} \cdot \mathrm{S_U} \cdot \mathrm{S_D} \cdot \overline{\mathrm{NX1}} \cdot \overline{\mathrm{NX3}} \cdot \mathrm{E_H} \tag{3.29}$$

$$\mu^+\mu^- = \mathrm{M_U} \cdot \mathrm{M_D} \cdot \mathrm{S_U} \cdot \mathrm{S_D} \cdot \overline{\mathrm{NX1}} \cdot \overline{\mathrm{NX3}} \cdot \frac{2}{4}\mathrm{X4} \cdot \frac{2}{4}\mathrm{Y4} \tag{3.30}$$

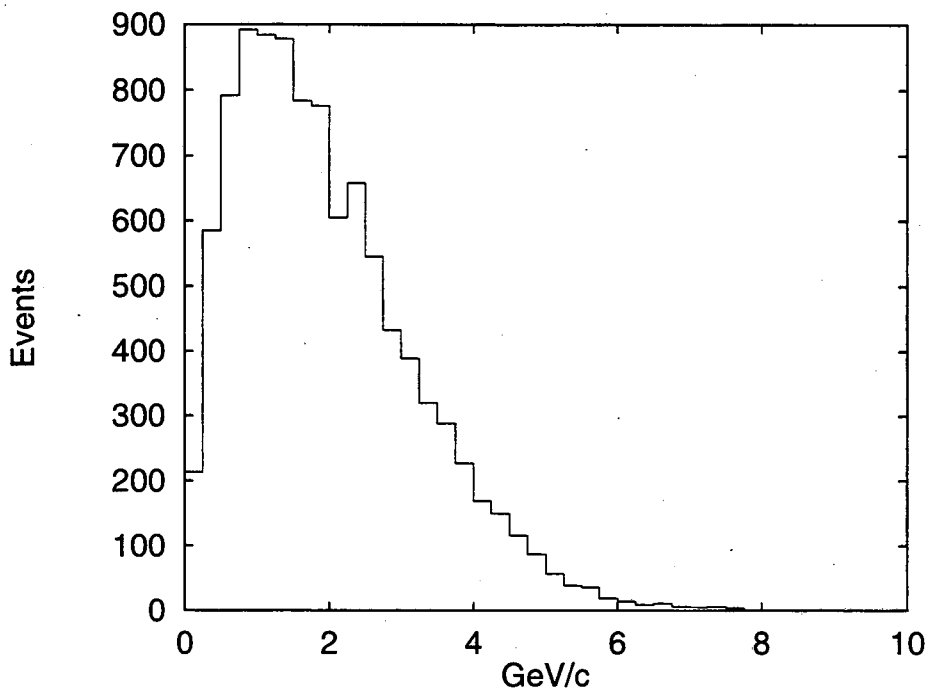

Figure 3.96: P_t spectrum of accepted B mesons for $B \rightarrow J/\psi + X \rightarrow \mu^+\mu^- + X$ assuming 100% detector efficiency (Monte Carlo).

The h^+h^- trigger contained E_H, therefore the dihadron TGO events should be a subset of the TFI dihadron events. The $\mu^+\mu^-$ trigger contained $\frac{2}{4}X4 \cdot \frac{2}{4}Y4$ which consisted of muon hodoscope combinations that also satisfied either $4/4\mu LR$ or $(2/4M \cdot 2Y4)$. Therefore the dimuon TGO events should be a subset of the TFI dimuon events. A consequences of this subset relationship was the dihadron and dimuon trigger efficiencies were determined by the TGO dihadron and dimuon trigger efficiencies.

$M_U \cdot M_D$ Efficiency

The strategy used to determine the efficiencies of the dimuon and dihadron TGO triggers was to determine them by finding the efficiencies of their components. (See equation 3.30 and 3.29.) Looking at the first component, $M_U \cdot M_D$, one might expect that effects due to inefficiencies in this component will cancel in the calculation of the ratio of the branching ratios. However, this assumes that the dimuon events populate the same hodoscope combinations as the dihadron events. If this assumption is not true, then the ratio of the $M_U \cdot M_D$ efficiencies for dimuon events and dihadron events will not cancel. To

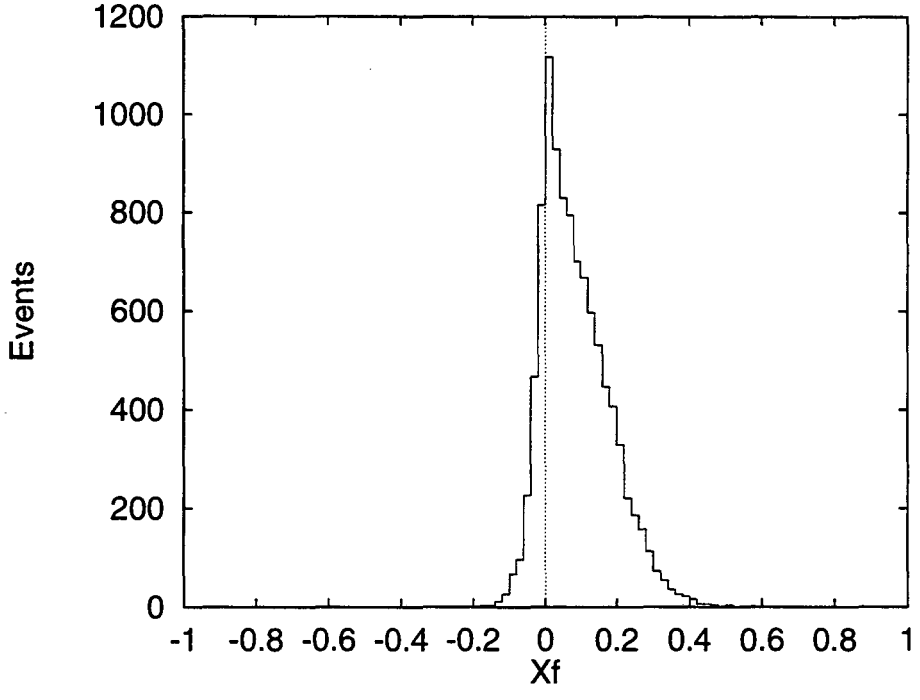

Figure 3.97: X_F spectrum of accepted B mesons for $B \to J/\psi + X \to \mu^+\mu^- + X$ assuming 100% detector efficiency (Monte Carlo).

account for this possibility, Monte Carlo simulations were employed to study the $M_U \cdot M_D$ trigger. The procedure was as follows :

1. Determine the efficiencies of the individual hodoscopes in stations 1, 2, and 3.
2. Generate b-hadron decay events and propagate the decay products through the detector.
3. Determine the hodoscope sections hit by the decay products.
4. Utilize a random number generator and the efficiencies of the hit hodoscope sections to remove some of the hits.
5. Determine if the resulting hodoscope hit patterns were consistent with a valid $M_U \cdot M_D$ trigger.
6. Delete events not satisfying the $M_U \cdot M_D$ trigger.

The key assumption in calculating the $M_U \cdot M_D$ trigger efficiency was that it was dominated by the efficiencies of the hodoscopes. Any inefficiencies in the trigger logic electronics were

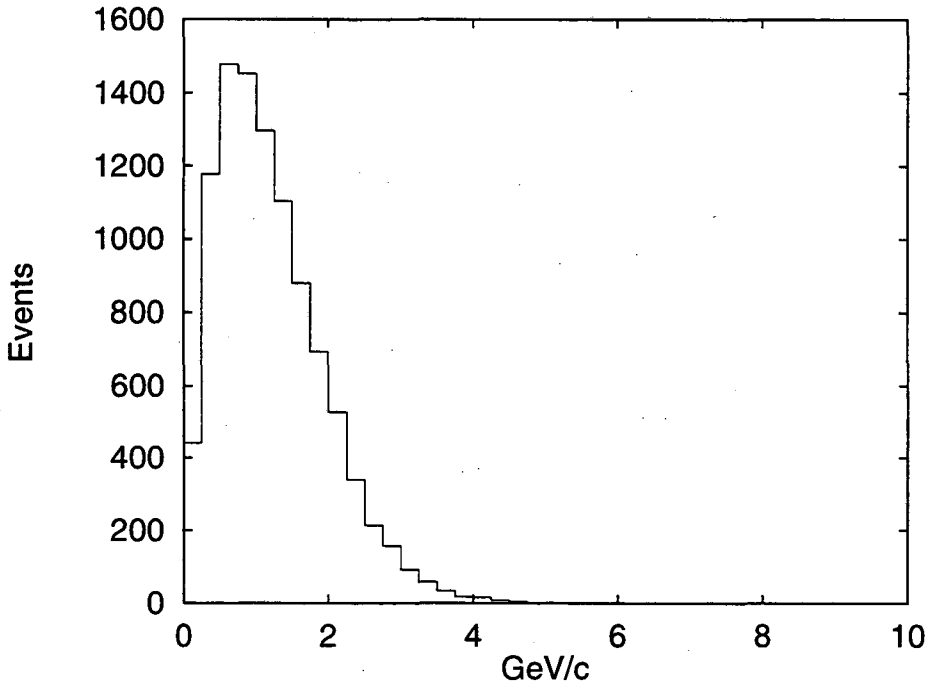

Figure 3.98: P_t spectrum of accepted J/ψ mesons for $B \to J/\psi + X \to \mu^+\mu^- + X$ assuming 100% detector efficiency (Monte Carlo).

assumed to be channel independent.

One minor complication in the analysis of the $M_U \cdot M_D$ trigger efficiency was the fact that two different lookup tables were used during the *b*-run. (See section 2.5.2 for information on the implementation of the $M_U \cdot M_D$ trigger.) The two lookup tables, designated as "Matrix 76" and "Matrix 77" had different acceptance characteristics with respect to dimuons and dihadrons. More specifically, the dimuon acceptances of both lookup tables were approximately the same, whereas the dihadron acceptances of the two tables were quite different. (See sections 3.5.3 and 3.6.2 for more information on the efficiencies of the two lookup tables.)

$S_U \cdot S_D$ Efficiency

The $S_U \cdot S_D$ trigger component was used to signal the presence of two charged tracks passing through the silicon micro-vertex detector, one in the upper arm and one in the lower arm. S_U and S_D were each single small scintillators measuring (5.08 cm $\times$ 5.08 cm $\times$ 1 mm). Given their small dimensions, their efficiency should be relatively insensitive to the distribu-

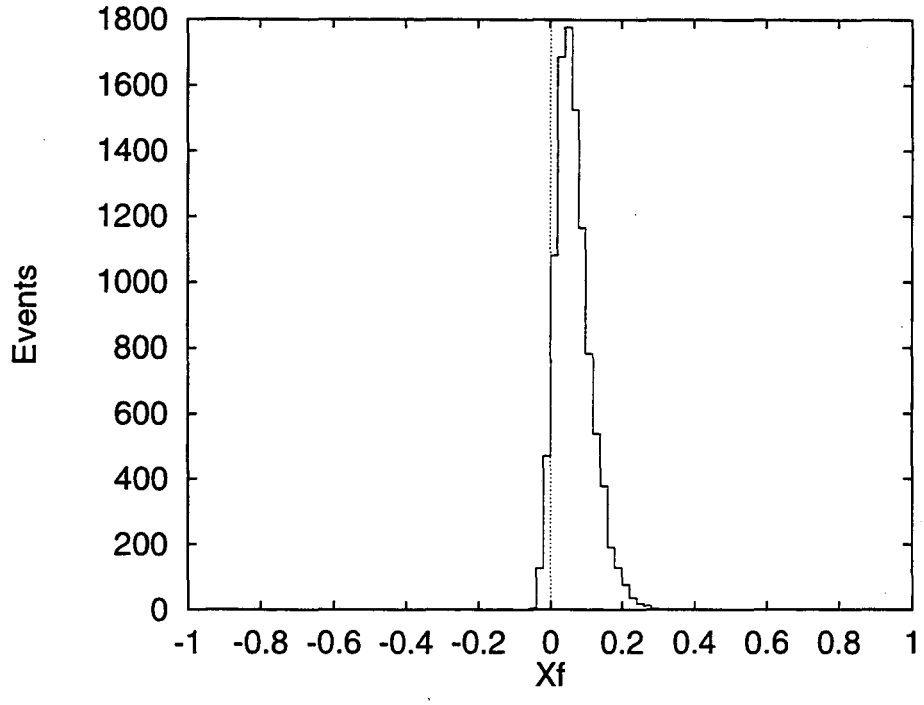

Figure 3.99: X_F spectrum of accepted J/ψ mesons for $B \rightarrow J/\psi + X \rightarrow \mu^+\mu^- + X$ assuming 100% detector efficiency (Monte Carlo).

tion of particles incident on them. Therefore, the $S_U \cdot S_D$ trigger should be equally efficient in triggering on dimuon and dihadron events. This conclusion was verified by looking at the $S_U \cdot S_D$ trigger in unbiased dimuon and dihadron events. The unbiased sample was obtained from the output of pass 3 processing by looking at events that fired the prescaled TFI trigger. From these events, the $S_U \cdot S_D$ trigger was determined to be $(78.3 \pm 2.1)\%$ efficient for dihadron events and $(78.0 \pm 1.2)\%$ efficient for dimuon events.

$\overline{\text{NX1}} \cdot \overline{\text{NX3}}$ Efficiency

The purpose of $\overline{\text{NX1}} \cdot \overline{\text{NX3}}$ was to cut "dirty" events. The assumption was that these dirty events did not contain a substantial number of signal events. The validity of this assumption for NX3 can be seen by looking at the distribution of NX3 (hodoscope plane HX3) hits, shown in Figure 3.100, for dimuon and dihadron events that survive through pass 3 of the processing.

A more accurate analysis of the effects of the $\overline{\text{NX1}} \cdot \overline{\text{NX3}}$ trigger was obtained by looking at the events that were accepted via the prescaled TFI trigger and survived through

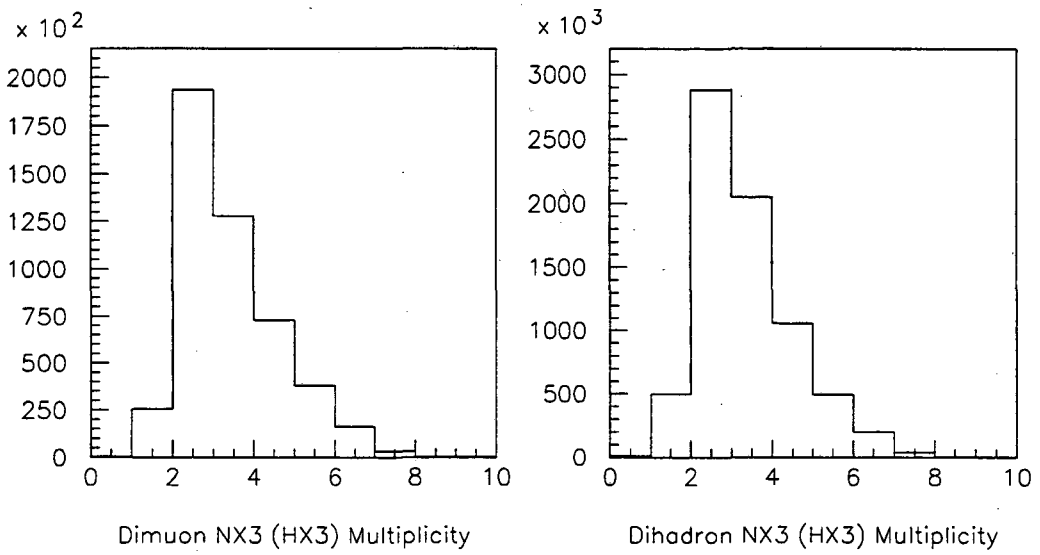

Figure 3.100: NX3 hit multiplicity for target dimuons (left) and dihadrons (right).

pass 3 of the analysis process. The fraction of these events that do not fire the $\overline{\text{NX1}} \cdot \overline{\text{NX3}}$ trigger is a measure of the efficiency of the trigger. For the dihadron events, the efficiency was measured to be $(90 \pm 0.9)\%$, for the dimuon events, the efficiency was measured to be $(92 \pm 1.5)\%$.

Calorimeter E_H Trigger Efficiency

An accurate determination of the efficiency of the E_H component of the opposite-sign dihadron trigger was crucial in determining the b-hadron to dihadron branching ratios. The other components of the dihadron trigger are common to the dimuon trigger whereas E_H was unique to the dihadron trigger; hence, the effects of the other components will tend to cancel in the lowest order in the ratio of the efficiencies while the effects of E_H will not.

A multi-step process was used to determine the efficiency of E_H, a result of the limitation in the available data. The steps were the following:

1. Determine the E_H efficiency as a function of the energy measured by the E1, E2, H1, and H2 sections of the calorimeter, denoted as E_{calc} for the purposes of this discussion. (Recall that the E_H signal was the analog sum of the outputs of these sections of the calorimeter.)

2. Determine the joint probability density function $P(E_{calc}, P_{total})$ where P_{total} is the sum of the magnitudes of the momentum of the two hadrons in the event. (That is, determine the probability that a given pair of hadrons having momentum sum $P_{total} = |\vec{P}_1| + |\vec{P}_2|$ yields a calorimeter trigger signal E_{calc}.)

3. Utilize the joint probability density function $P(E_{calc}, P_{total})$ and the E_H trigger efficiency function to model the calorimeter trigger in the Monte Carlo.

In order to determine the efficiency of E_H as a function of E_{calc}, data from special calorimeter calibration runs, made at set intervals during the *b*-run, were analyzed. At a selected interval, two runs were made, the first run used E_L as the TFI and TGO triggers, the second run used E_H as the TFI and TGO triggers. The ratio of the E_{calc} distributions generated by the E_H and E_L triggered data yielded a scaled version of the E_H versus E_{calc} efficiency curve. (The assumption is that the E_L trigger is 100% efficient over the energy range where the E_H trigger turns on.)

One complication in the generation of this turn-on curve was the determination of E_{calc} for each event. In an ideal world, a direct measurement of E_{calc} would have been desirable, unfortunately, this information was not available. The only alternative was the re-creation of E_{calc} from the ADC outputs of the individual calorimeter sections. The reconstruction of E_{calc} was further complicated by the fact that the ADCs used to record the outputs of the calorimeter sections were quadratic encoders, not linear. As a result, a direct summation of the ADC outputs from the E1, E4, H1, and H2 sections of the calorimeter did not reflect the true value of E_{calc}. To get around this problem, the calorimeter calibration constants determined in Appendix A were used to convert each ADC value into energy deposition in each calorimeter section. The energy measurements in the four sections of the calorimeter were then added up, giving the reconstructed E_{calc}.

Returning to the determination of the E_H turn-on curve, the solid line in Figure 3.101 is the distribution of E_{calc} for events triggered by E_H and the dotted line is the distribution for events triggered by E_L. Figure 3.102 shows the same distributions on a log scale. At the upper energy range, the two curves differ by a scale factor which means that both triggers are 100% efficient. Figure 3.103 is the ratio of the two distributions. (Figure 3.104 is the same distribution on a log scale.) A trigger efficiency curve of the form:

$$A_0 f(E_{calc}) = 0.5 \times A_0 \times (\tanh(A_1 \times (E_{calc} - A_2)) + 1) \tag{3.31}$$

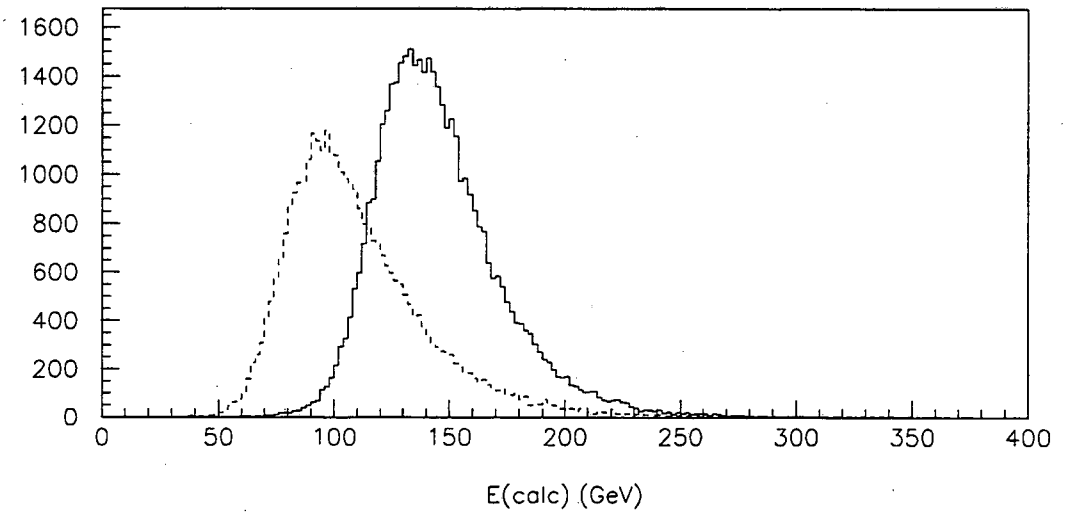

Figure 3.101: Distribution of E_{calc} for events triggered by E_H (solid line) and E_L (dotted line).

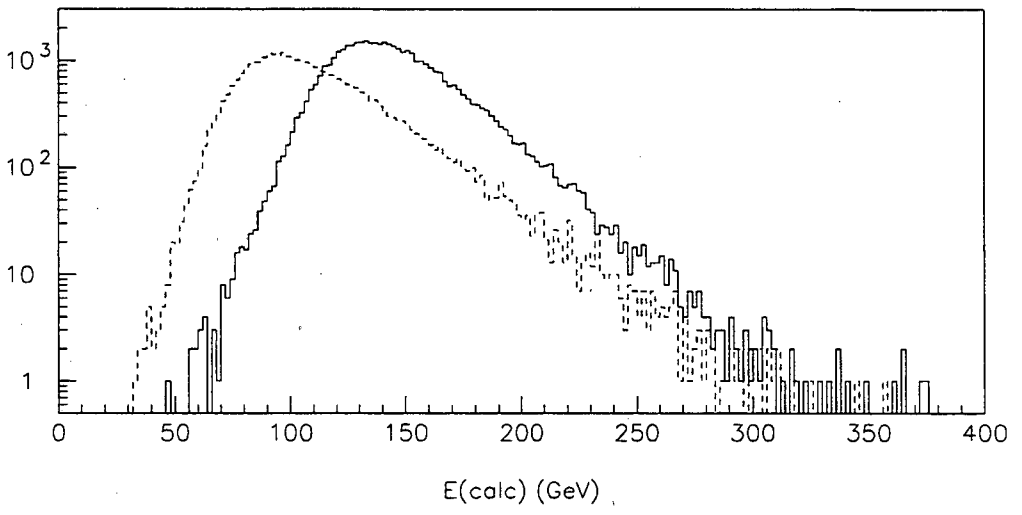

Figure 3.102: Distributions of E_{calc} for events triggered by E_H (solid line) and E_L (dotted line).

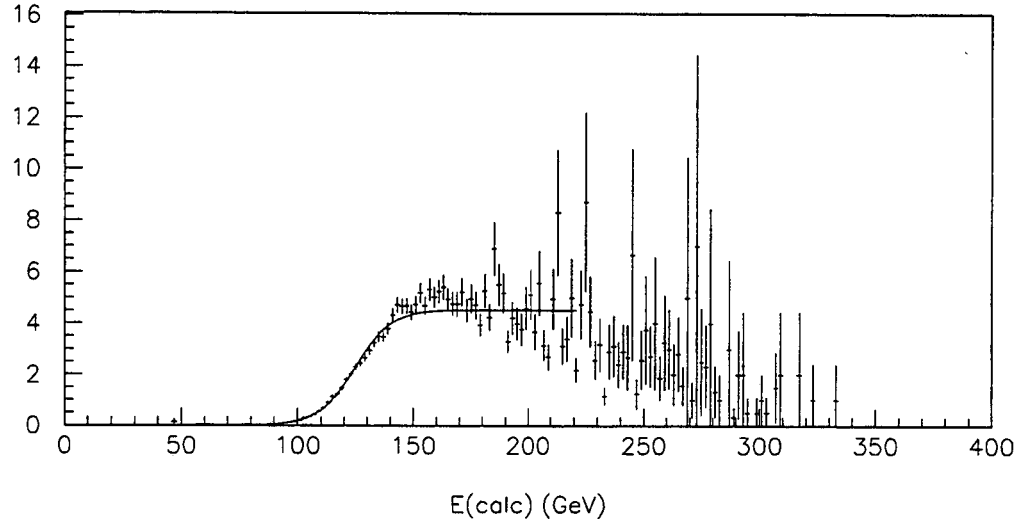

Figure 3.103: Ratio of the distributions of E_{calc} for events triggered by E_H and E_L. (Linear scale.)

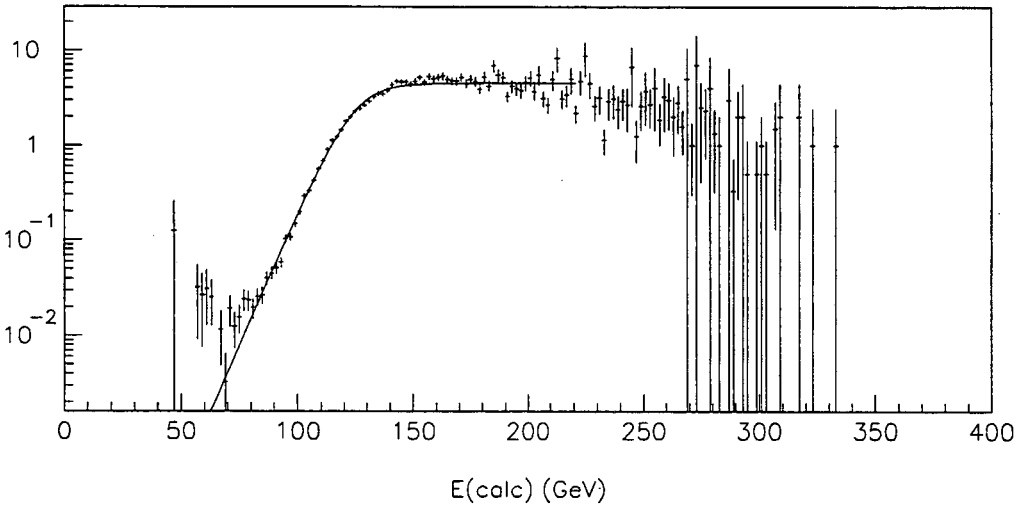

Figure 3.104: Ratio of the distributions of E_{calc} for events triggered by E_H and E_L. (Log scale.)

was then fit to the distribution. The A_0 was an overall scale factor, A_1 controlled the width of the turn-on region, and A_2 was the energy corresponding to the mid-point of the turn-on region. For the curve shown in Figure 3.103, $A_1 = 0.064 \pm .0007$ and $A_2 = 124.7 \pm 0.3$ GeV.

Once the E_H efficiency curve was determined, the joint probability distribution function, $P(E_{calc}, P_{total})$, needed to be determined. (I.e., the probability that an event with a specific value of P_{total} had a particular value of E_{calc}.) This was necessary because the Monte Carlo only provided the momentum of the hadrons in an event. In order to determine whether or not a given Monte Carlo event would fire the calorimeter trigger, a mapping between E_{calc} and P_{total} was required. This mapping was determined by first histogramming E_{calc} and P_{total} for all the events containing dihadrons in the calibration runs triggered by E_L.

The exact procedure for determining the mapping between E_{calc} and P_{total} was as follows:

- All events containing dihadrons (ignoring charge) were selected from the E_L triggered runs in special calibration tapes.

- E_{calc} versus P_{total} was histogrammed for events containing only two hadrons. However, P_{total} was not just the scalar sum of the momenta of the two hadrons in the event. Instead, P_{total} was the scalar weighted sum of the two hadrons, where the weights compensated for the X-dependence of the momentum versus energy relationship discussed in Appendix A.

- To increased statistics, the histograms from all five calibration tapes were combined into one histogram. The key to the validity of this consolidation was a stable E_{calc} versus P_{total} relationship. Figure 3.105 shows a plot of the mean of the Gaussian fitted to the E_{calc} distribution in selected slices of P_{total} for events at selected intervals in the entire *b*-run. The plot shows that the E_{calc} versus P_{total} relationship is indeed stable over the complete *b*-run. (The variations at low momenta are the result of trigger effects.)

- The resulting $P(E_{calc}, P_{total})$ distribution was then sliced into P_{total} strips 10 GeV/c wide. (The slicing procedure is schematically shown in Figure 3.106.)

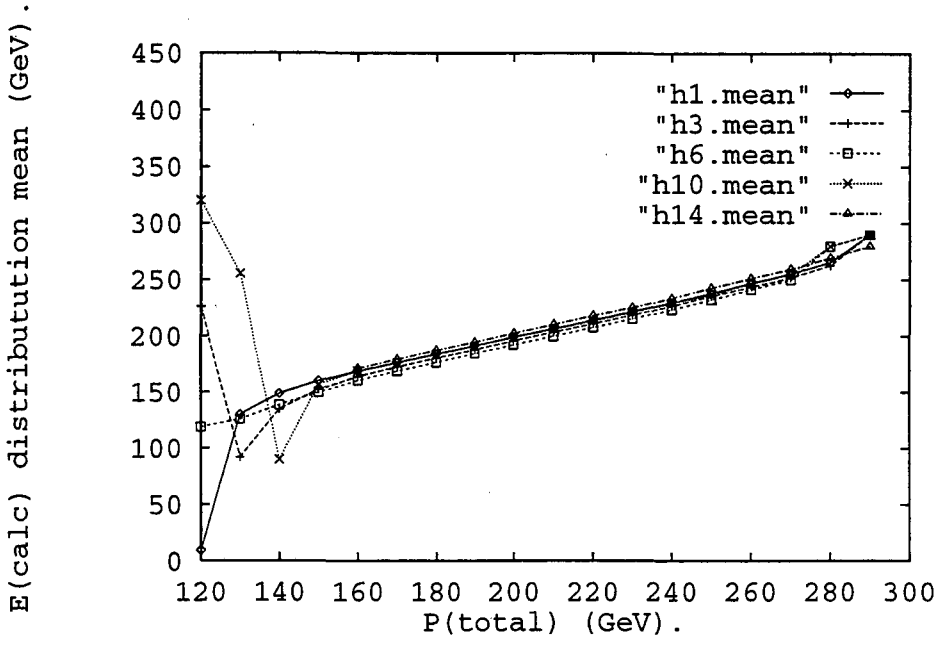

Figure 3.105: Mean of E_{calc} as a function of P_{total} for 5 different runs (triggered by E_H) made at selected intervals in time.

- The E_{calc} distribution for each momentum slice was fitted with the following function:

$$H(x) = C_1 \times G_1(x) + C_2 \times G_2(x) \tag{3.32}$$

where,

$$G_n(x) = \frac{1}{\sigma_n\sqrt{2\pi}} \exp\left(-(x-\mu_n)/2\sigma_n^2\right) \tag{3.33}$$

and where x is E_{calc} and C_n are overall scale factors. Figures 3.107, 3.108, 3.109 and 3.110 plot the the standard deviations and means that was determined from the various momentum slices.

- The parameterizations of the distributions of E_{calc} for discrete values of P_{total} were then used to determine the distribution of E_{calc} for a given value of P_{total}. This was accomplished by interpolating the values of the means and sigmas for E_{calc} at the given value of P_{total} and then using the interpolated values to construct the E_{calc} distribution for P_{total}.

Given the mapping between E_{calc} and P_{total} and the trigger turn-on curve as a

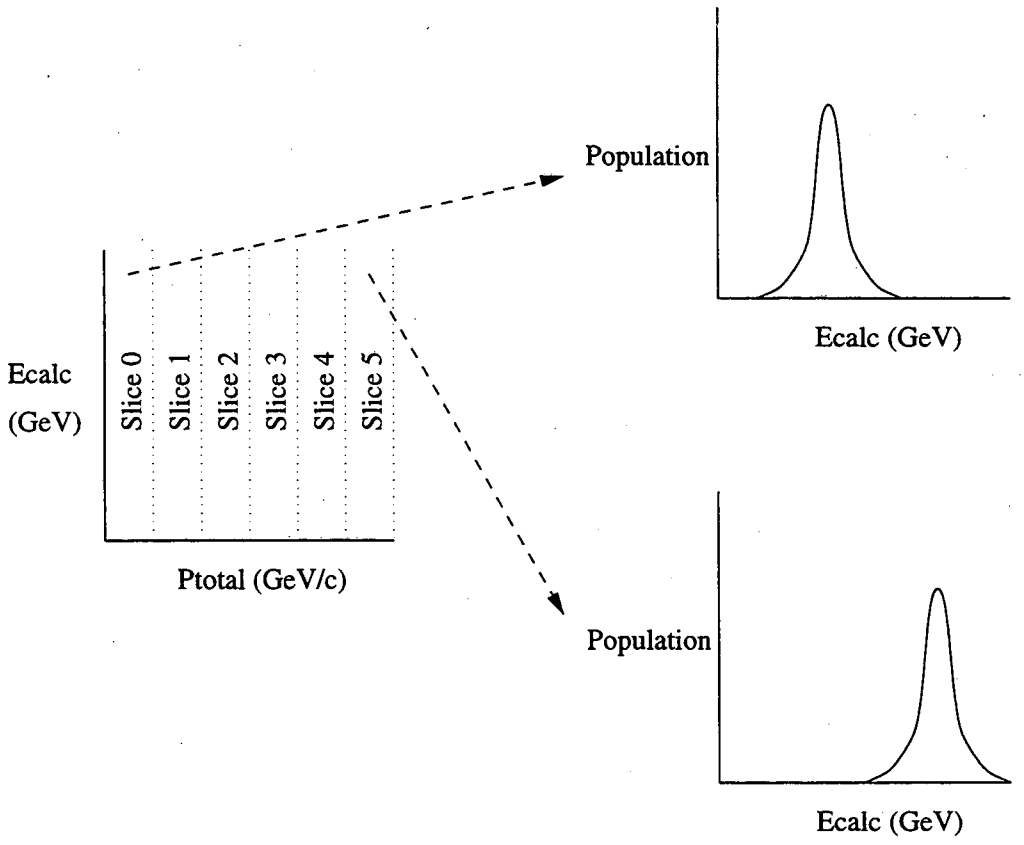

Figure 3.106: Schematic of the momentum slicing procedure for the P_{total} versus E_{calc} distribution.

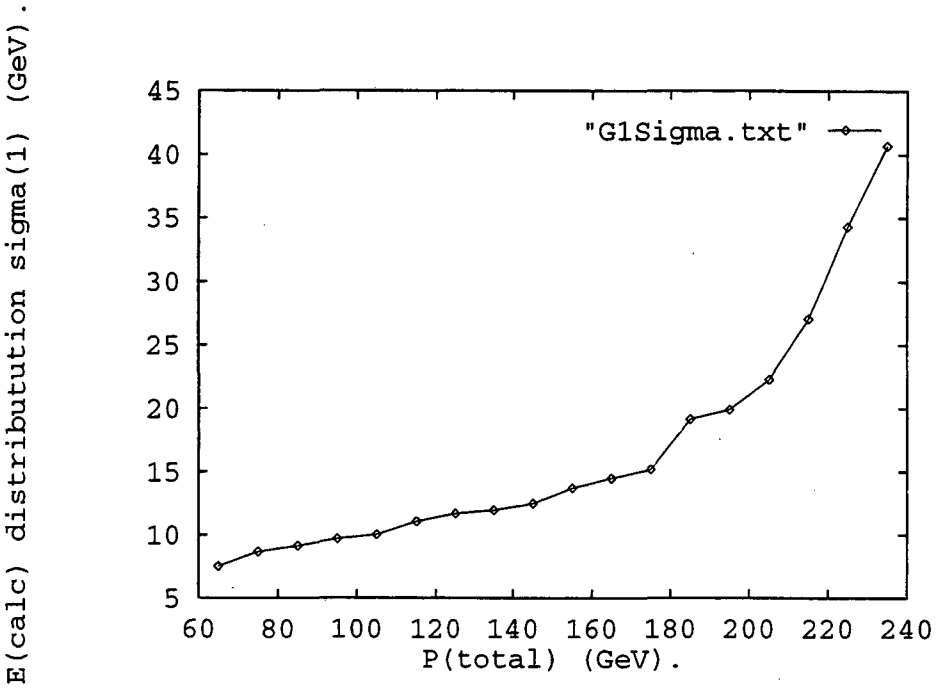

Figure 3.107: Variance (σ_1) of the first Gaussian in the distribution of E_{calc} as a function of P_{total} for events triggered by E_L.

function of E_{calc}, the turn-on curve as a function of P_{total} was then determined. This was done in the following steps :

- Generate a value of P_{total} using a uniform distribution.
- Determine the values for the means and sigmas of the Gaussians that characterize the E_{calc} distribution for that value of P_{total}.
- Use the E_{calc} turn-on curve to determine the probability that the given value of E_{calc} will fire the calorimeter trigger.
- Throw out a fraction of the generated P_{total} events in a manner consistent with the turn-on probability.
- Histogram the generated P_{total}'s.
- Histogram the P_{total}'s that were not thrown out in the above procedure.
- Divide the histogram of surviving P_{total}'s by the histogram of generated P_{total}'s.

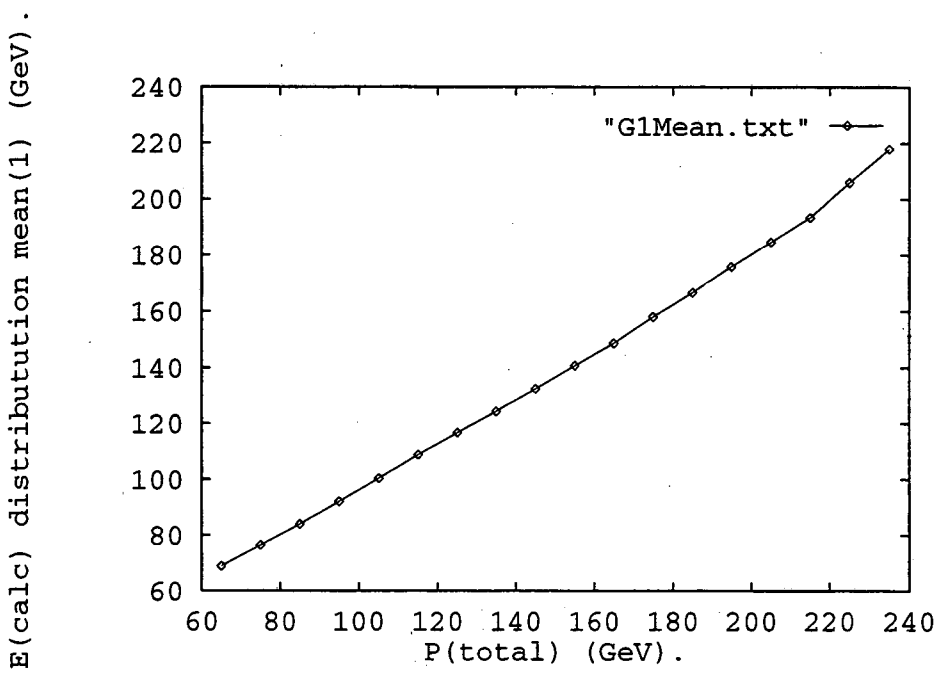

Figure 3.108: Mean (μ_1) of the first Gaussian in the distribution of E_{calc} as a function of P_{total} for events triggered by E_L.

The histogram that results from the final step gives the calorimeter trigger turn-on as a function of P_{total}. Figure 3.111 is a plot of the calorimeter trigger efficiency as a function of P_{total} for two different run periods. Finally, a trigger turn-on function of the form:

$$f(P_{total}) = 0.5 \times (\tanh(A_1 \times (P_{total} - A_2)) + 1) \tag{3.34}$$

was extracted from the histograms to model the calorimeter trigger turn-on in the Monte Carlo.

Once the E_H turn-on curve was determined as a function of P_{total}, a model of the efficiency of the calorimeter trigger could be added to the Monte Carlo. This was done by the following procedure:

- Generate a $B \to h^+h^-$ event.
- Propagate the hadrons through the spectrometer.
- For those events where both daughter hadrons reach the calorimeter, determine the momentum of the hadrons and their X position at the calorimeter.

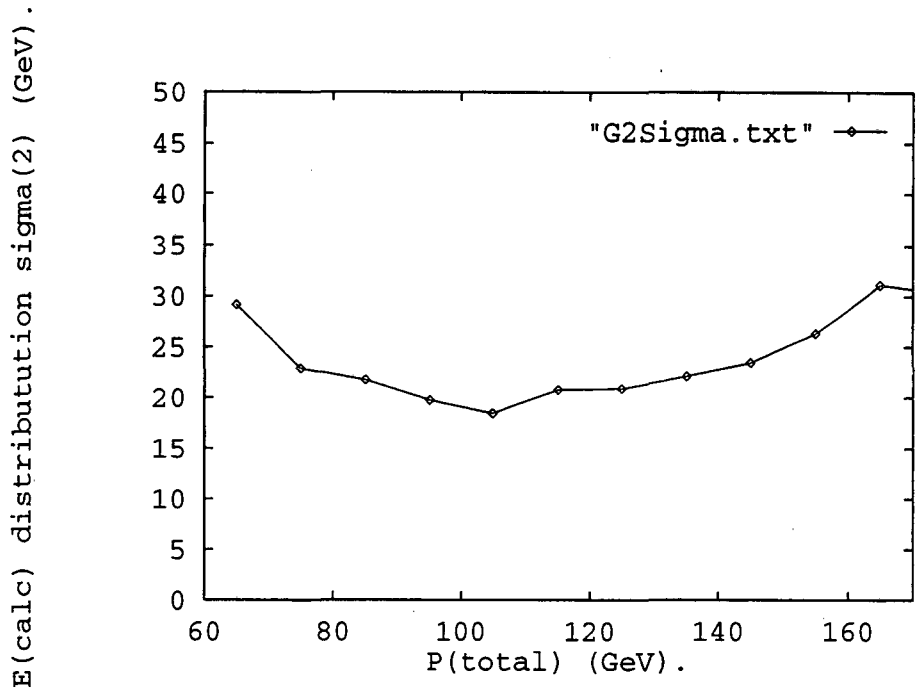

Figure 3.109: Variance (σ_2) of the second Gaussian in the distribution of E_{calc} as a function of P_{total} for events triggered by E_L.

- Determine P_{total} for the two hadrons.
- Utilize the E_H turn-on curve (Equation 3.111) to determine whether or not the event fires the E_H trigger.
- Output those events that fire the trigger to the DST.

Muon ($\frac{2}{4}$X4 · $\frac{2}{4}$Y4) Trigger Efficiency

The efficiency of the muon triggers, like the determination of the efficiency of the $M_U \cdot M_D$ trigger, was determined from the efficiencies of the individual hodoscope sections that comprise the triggers. The efficiencies of the individual hodoscope sections in the muon station were used to model the efficiencies of the muon station in the Monte Carlo. The hit patterns in the muon station for each Monte Carlo generated dimuon event were then analyzed to determine if they satisfied the muon trigger. Those events that did not satisfy the muon trigger (due to hodoscope inefficiencies) were removed from the DST output stream.

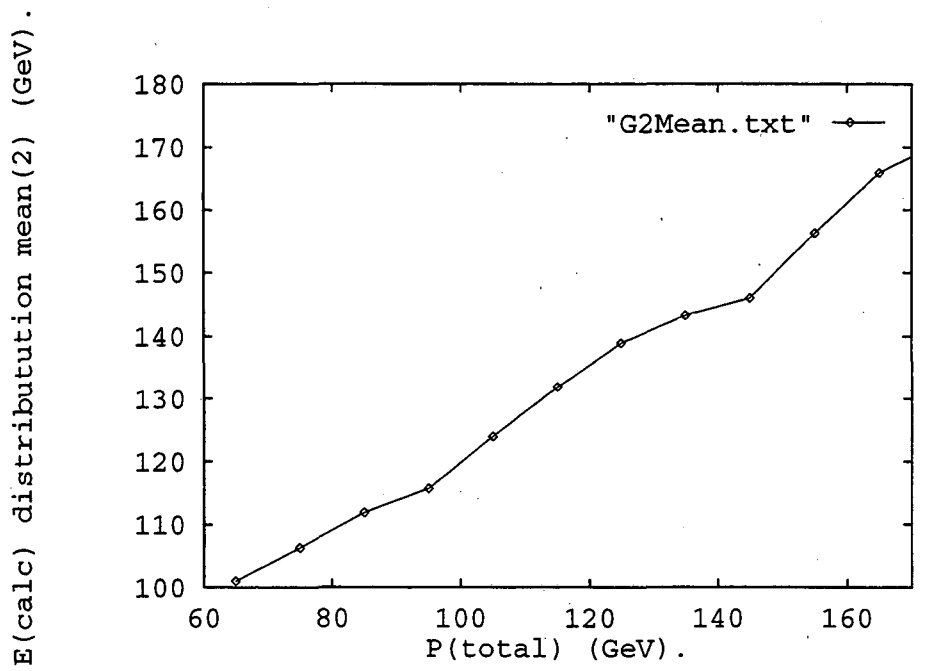

Figure 3.110: Mean (μ_2) of the second Gaussian in the distribution of E_{calc} as a function of P_{total} for events triggered by E_L.

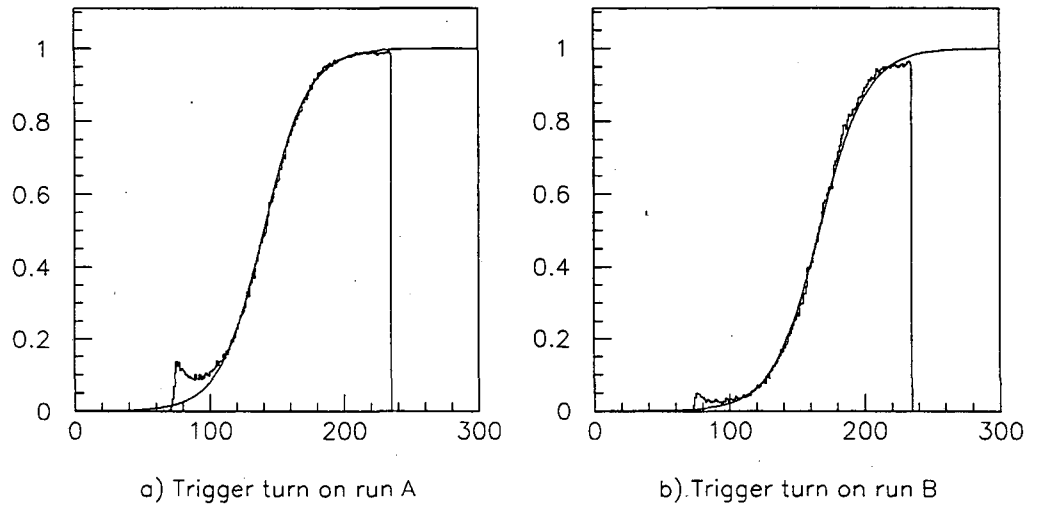

Figure 3.111: The turn-on curve for the E_H trigger as a function of P_{total} for two different run periods.

Physics Trigger Cross Contamination

As was mentioned in the discussion on the efficiency of the TFI trigger, the absence of event cross contamination was crucial in the determination of the overall dihadron and dimuon efficiencies.

Analysis of the final sample of prompt J/ψ events shows that 94.8% of the dimuon events within a ± 0.03 GeV interval around the J/ψ mass fire the $\mu^+\mu^-$ trigger. Of the remaining 5.2%, 88.7% fired the $\mu^\pm\mu^\pm$ trigger. This latter fact is particularly important because it makes it possible to estimate the effects of these "contaminants" on the overall acceptance of dimuon events. Closer examination of these events reveals that virtually 100% of these events fail to fire the $\mu^+\mu^-$ trigger because of the inefficiency of the $S_U \cdot S_D$ trigger. As was mentioned in section 3.4.4, the efficiency of the $S_U \cdot S_D$ trigger was determined to be 78.3%, resulting in a loss of 21.7% of the opposite-sign dimuon events. However, an analysis of the opposite-sign dimuon events that do trigger $\mu^+\mu^-$ shows that 17% of the opposite-sign dimuon events also fire $\mu^\pm\mu^\pm$. Naively, one would expect that the same fraction of opposite-sign dimuon events that fail to fire the $\mu^+\mu^-$ trigger will also fire the $\mu^\pm\mu^\pm$ trigger. Therefore, given 100 produced opposite-sign dimuons, 21.7 will not trigger the $\mu^+\mu^-$ trigger but $21.7 \times 17\% = 3.7$ events will still end up on tape because they fired the $\mu^\pm\mu^\pm$ trigger. As a cross check, out of 100 produced opposite-sign dimuon events, $78.3 + 3.7 = 81.2$ events should end up on the data tapes. Of these events, $78.3/81.2 \times 100\% = 95.5\%$ will fire the $\mu^+\mu^-$ trigger, which is close to the observed value of 94.8%.

The results of the above analysis indicate that the efficiency of the $S_U \cdot S_D$ component of the trigger does not exactly cancel in the ratio of the dihadron and dimuon efficiencies. (Analysis of the dihadron data shows that the fraction of opposite-sign dihadron events that fire the $h^\pm h^\pm$ trigger is negligible.) Utilizing the 94.8% value for the dimuon trigger purity and the 78.3% dimuon $S_U \cdot S_D$ efficiency, a corrected $S_U \cdot S_D$ efficiency of 83% is obtained. Therefore, the ratio of the dimuon and dihadron $S_U \cdot S_D$ efficiencies is 1.06.

Analysis of the final sample of dihadrons shows a similar cross contamination problem. During the first half of the run, approximately $(88 \pm 5)\%$ of all the dihadron events fired the h^+h^-. During the second half of the run, approximately $(78 \pm 7)\%$ of the events fired the h^+h^- trigger. The majority of the events that fail to fire the h^+h^- trigger, failed to fire the E_H component (calorimeter trigger) of the h^+h^- trigger. Examination of

the individual tracks in the events that failed to fire the h^+h^- suggest that these events are valid dihadron events. Hence, for the dihadrons, the h^+h^- trigger is enhanced by a factor of $(1 + 12\%/88\%) = 1.14$ and $(1 + 22\%/78\%) = 1.28$, where the percent uncertainties from the nominal values are $\pm 6\%$ and $\pm 9\%$ respectively. (E.g., the one standard deviation values of 1.28 are $1.28 \times (1.0 \pm 0.09)$.)

3.4.5 Reconstruction Efficiency

Reconstruction efficiency quantifies the probability that the tracks in an event were 1) reconstructed at all 2) reconstructed correctly and 3) survived the various track quality cuts. The loss of real tracks can be attributed to various sources, most notably confusion due to "noise" hits and loss of hits due to detector inefficiencies. Both interact in a complex fashion with the various quality cuts made during track reconstruction which also affect reconstruction efficiency.

The primary method used to measure reconstruction efficiency was to run the reconstruction code on signal events generated with the Monte Carlo and then count the number of events that were correctly reconstructed by the code. Noise hits, from either non-signal tracks or from electronic noise from the spectrometer was modeled by overlaying hits in the silicon and drift chambers from selected events from the experiment data tapes on top of b-decay events generated by the Monte Carlo. Hit loss due to detector inefficiency was handled by the Monte Carlo using the same type of hit loss mechanism that was used for the hodoscope planes. In order that the reconstruction efficiency be correctly determined, it was essential that the Monte Carlo generated events with overlayed noise accurately model real events. From the plots and discussions in section 3.3.3, it is clear that the simulation was fairly accurate in simulating real event data.

Most of the factors that comprise reconstruction efficiency were determined through the use of the Monte Carlo. However, there were two factors that could not be determined with the Monte Carlo. These factors quantified the following effects:

- Effects of unidentified or ambiguously identified tracks in pass 2. (That is the tracks that could not be identified by the particle identification code or were identified as two or more types of particles, e.g., electron-hadron.)
- Effects of the cut on events with more than four hadrons (the 4+ hadron cut) in pass 2.

Particles Identification Efficiency

The first thing to note about the particle identification (PID) algorithm is that it was not a factor in the determination of the overall efficiency for accepting and reconstructing dimuon events. The identification of muons was based solely on the hits in the muon hodoscope planes and the proportional tube planes.

In contrast to the dimuon events, the efficiency of the reconstruction of dihadron events was directly influenced by the particle identification algorithm. This dependence is seen in the algorithm used to make the final decision on particle type shown in Figure 3.31. The diagram shows that the assignment of particle identification in decreasing order of preference is muon, electron, and hadron. In addition to this preference for particle assignment, the assignment of particle identity is dependent on the success or failure of the calorimeter particle identification algorithm to assign a particle identity. As a result of these factors, valid dihadron events could be lost in two different ways:

- Hadrons left unidentified by the calorimeter particle identification code.
- Hadrons that were multiply identified by the calorimeter particle identification code.

To estimate the effects of these factors on the efficiency of the reconstruction of dihadron events, a small subset of the data was re-analyzed through pass 3, but with the particle identification criteria removed. (That is, the cut requiring each dihadron event to contain at least two opposite-sign tracks that were positively identified as only hadrons, was removed.) The results of this analysis showed that less than 2% of the dihadron events were lost as a results of the hadron only cut. A much greater loss of events was due to particles left unidentified by the calorimeter particle identification algorithm. A rough estimate of the event loss due to this later effect was made as follows. First, it was assumed that all the unidentified particle were actually hadrons, which is a good assumption in hadronic collisions. The particle identification efficiency was then determined by the ratio of N_{hh} and N_{xx} where N_{hh} is the number of hadron–hadron event and N_{xx} is the sum of the number of hadron–hadron, no-identity–hadron and no-identity–no-identity events. During the first run period (Matrix 76), the particle identification efficiency was determined to be $(83 \pm 6)\%$. During the second run period (Matrix 77), the particle identification efficiency was determined to be $(84 \pm 2)\%$.

The validity of the assumption that all the no-identity–hadron and no-identity–

no-identity events were really dihadron events was partially supported by the fact that the vast majority of identified particles in the accepted events were hadrons. In the re-analyzed data sample, the ratio of hadrons, electrons, and muons tracks was estimated by looking at the ratio of hadron–hadron, electron–hadron, and muon-hadron events. Assuming that the latter ratio is a valid measure of the former, the ratio of hadrons to electrons to muons was 120:2:1.

A slightly more pessimistic estimate for the particle identification efficiency was made by assuming that in addition to the no-identity–no-identity and no-identity–hadron events, all the electron–no-identity events were actually dihadron events. This decreased the efficiencies from 83% and 84% to 81% and 82% during run periods #1 and #2 respectively. The particle identification efficiencies were therefore assumed to be $(82\pm6)\%$ and $(83\pm3)\%$.

4+ Hadron Event Cut

In pass 2, the dihadron data set was subject to a cut on the number of good hadron tracks in an event. If the number of good hadrons tracks, N_h, was greater than three in events with more than three tracks $N > 3$, the event was thrown out. This resulted in the elimination of 5.2 million events. An estimate of the effect of this cut was made by getting an upper bounds on the number of opposite-sign hadron pairs in events with $N_h > 3$ that fell within an invariant mass interval between 5.0 GeV and 6.0 GeV and comparing that number to the number of opposite-sign hadron pairs within the same mass interval that survived this cut. An assumption was then made that the fraction of signal events (e.g., $B_d \to \pi^+\pi^-$) was the same in both samples.

The first step was determining the number of opposite-sign hadron pairs in a given $N_h > 3$ event. This was accomplished by first looking at the distribution of good tracks, shown in Table 3.7, in all the events prior to the application of the cuts. This table shows that a maximum of 7 good tracks can be contained in these events. In the worst case scenario, the maximum number of opposite-sign pairs that can be obtained from 7 hadrons is $3 \times 4 = 12$ per event.

The next step in the process of determining the effect of the cut was estimating the probability that a given opposite-sign hadron pair within such an event fell within the 5.0 GeV and 6.0 GeV mass interval. This probability was assumed to be equal to the probability that a given opposite-sign hadron pair in an $N_h = 3$ and $N > 3$ event fell within

Number of Tracks per Event	Number of Events
0	880303
1	15643264
2	215320354
3	80317222
4	13464275
5	1195227
6	72625
7	3643
8	0
9	0

Table 3.7: Distribution of good tracks prior to the application of the > 3 hadron cut

that mass interval. (This again is a worst case assumption.) This latter probability was calculated on a tape set by tape set basis for all the analyzed tape sets.

From the probability that a given opposite-sign hadron pair fell within the 5.0 GeV and 6.0 GeV mass interval, an estimate of the number of opposite-sign hadron pairs within the 5.0 GeV and 6.0 GeV mass interval in events where $N > 3$ and $N_h > 3$ can be obtained from the following formula:

$$\text{Lost events} = 12 \times \sum_i N_i(N_h > 3) * P_i \tag{3.35}$$

where the sum over i is a sum over analyzed tape sets, $N_i(N_h > 3)$ is the number of events where $N > 3$ and $N_h > 3$ and P_i is the probability that a given opposite-sign hadron pair is in the appropriate mass interval. (The 12 is the maximum number of opposite-sign hadron pairs that can be obtained from the 7 tracks assumed to be contained in each event.)

Going through the above analysis yielded an estimated value of 180,096 for the number of good opposite-sign dihadron events in the invariant mass interval 5.0 GeV to 6.0 GeV. This should be contrasted with the approximately 5.1 million good opposite-sign dihadron events passed by the pass 1 and pass 2 codes. The 180,096 events corresponds to a variation of +3.5% in the number of good opposite-sign dihadron events at this stage of the processing. Assuming that these cut events contain the same fraction of signal events as the events that passed the cuts, then maximum number of signal events that will be lost is +3.5%.

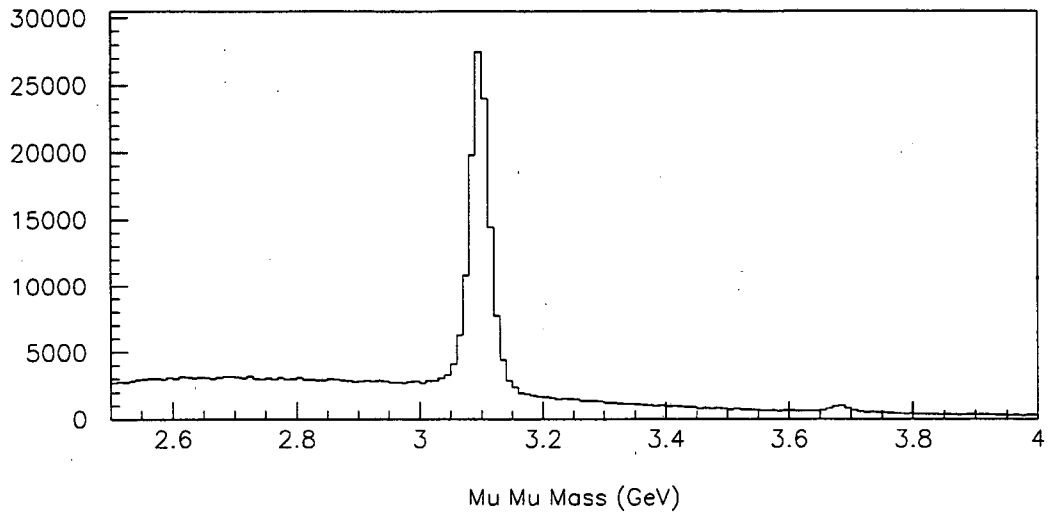

Figure 3.112: Invariant mass spectrum of dimuon events after pass 3. (Units are in GeV.)

3.5 Event Selection

3.5.1 Muon Analysis

The output of pass 3 yielded the sample of J/ψ to dimuon events shown in Figure 3.112. The majority of the J/ψ dimuon events (approximately 98,208 events after background subtraction) are from the decay of prompt J/ψ's, not from the cascade decay $b \to J/\psi \to \mu^+\mu^-$. In order to isolate the desired $b \to J/\psi \to \mu^+\mu^-$ events from the other events in the data sample, i.e., dimuons from the decay of prompt J/ψ's and background dimuon events, needed to be removed. This was accomplished through the application of four cuts. These cuts were identical to the cuts utilized in the previous E789 analysis that measured the production of bottom quarks by searching for $b-\text{hadron} \to J/\psi + X \to \mu^+\mu^-$ decays [50].

The first cut that was made, the elimination of events in which either particle in the event was multiply identified (e.g., muon/electron or muon/hadron), was designed to enhance the signal to noise ratio. The effects of this cut can be seen by comparing the invariant mass spectra in Figures 3.113 and 3.114. Figure 3.113 shows the invariant mass distribution for events where both particles were identified as muons only. The number

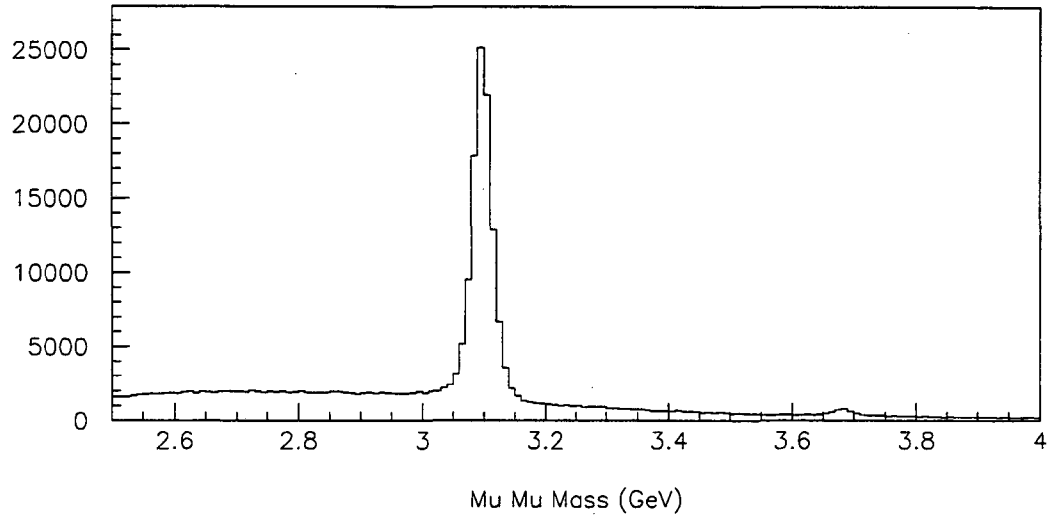

Figure 3.113: Invariant mass spectrum for events where both particles were identified as muons only. (Units are in GeV.)

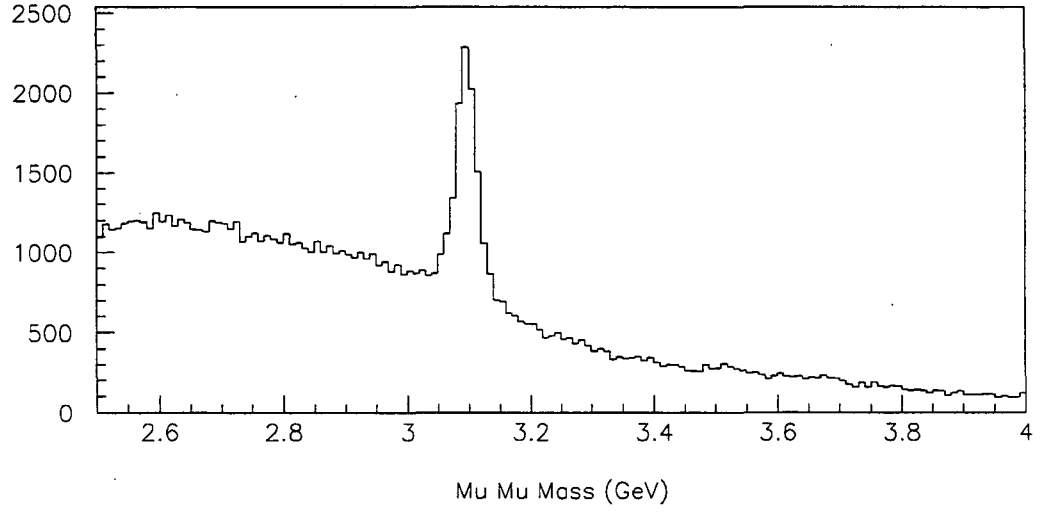

Figure 3.114: Invariant mass spectrum for events where one or both particles were multiply identified. (Units are in GeV.)

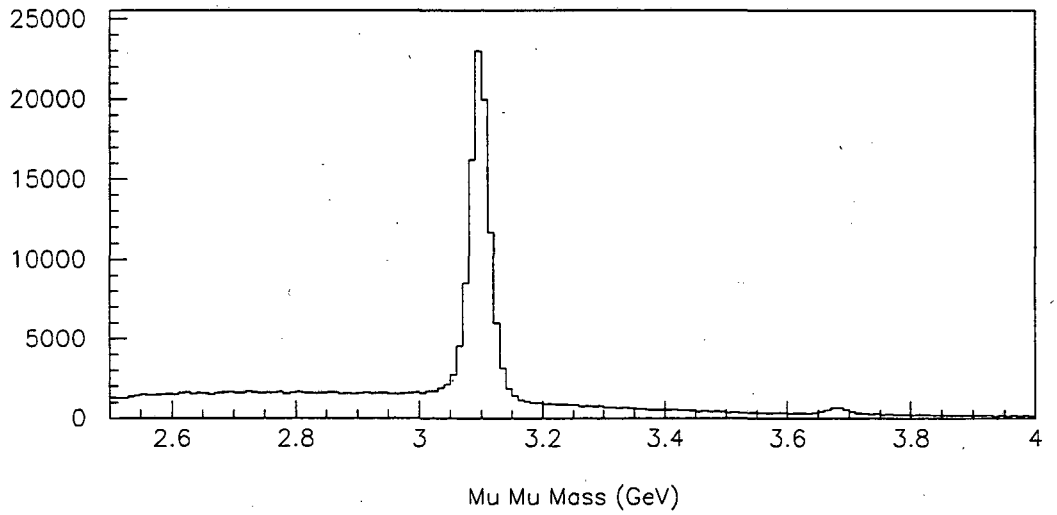

Figure 3.115: Invariant mass spectrum for events where both particles were identified as muons only and where the average silicon hit multiplicity was less than 7. (Units are in GeV.)

of events after background subtraction is 91,731, a loss of 6.6%. Figure 3.114 shows the invariant mass distribution for events where at least one particle was multiply identified. From this plot, the decrease in background was calculated to be 32%.

The second cut that was applied to the dimuon events was the elimination of events where the average number of hits in the silicon planes was greater than 7, the NAVSI < 7 cut. This cut was applied to eliminate poorly reconstructed events caused by hit mis-assignment because of high silicon plane hit multiplicities. Figure 3.115 shows the invariant mass spectrum after this cut. The elimination of these high multiplicity events is designed to reduce the number of poorly reconstructed vertices that might mimic a downstream b decay. The number of true $J/\psi \rightarrow$ dimuon events that were left after background subtraction is 83,562, a loss of 8.9% from the previous cut. In order to gauge the effectiveness this cut, scatter plots of the vertex Z and Y positions for low and high silicon multiplicity events are shown in Figure 3.116 and Figure 3.117. Note the higher density of events in the upstream and downstream zones relative to the density at the primary interaction point. (Specifically, zones 1 and 3 where the zones are numbered as in Figure 3.118.)

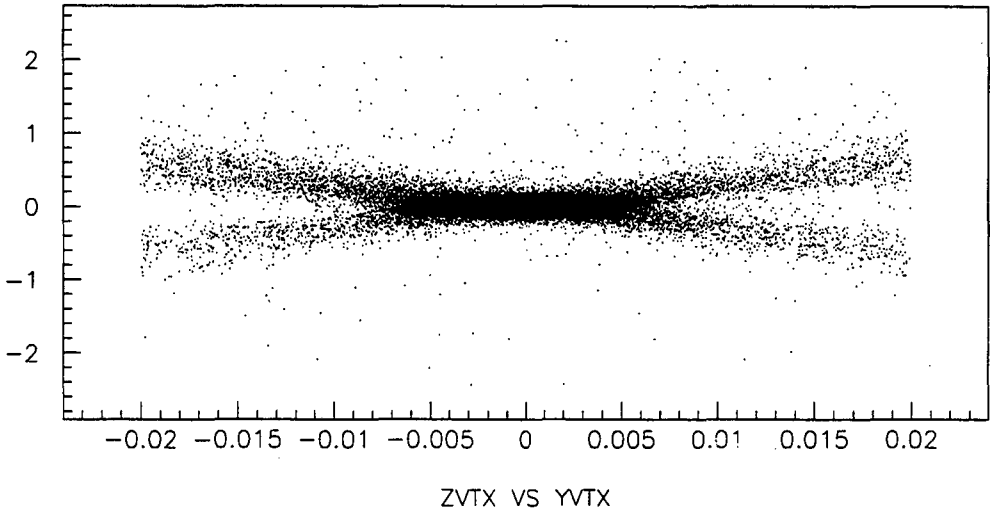

Figure 3.116: A scatter plot of the vertex Z versus Y position for dimuon events where the average silicon hit multiplicity is less than 7. (Units are in inches.)

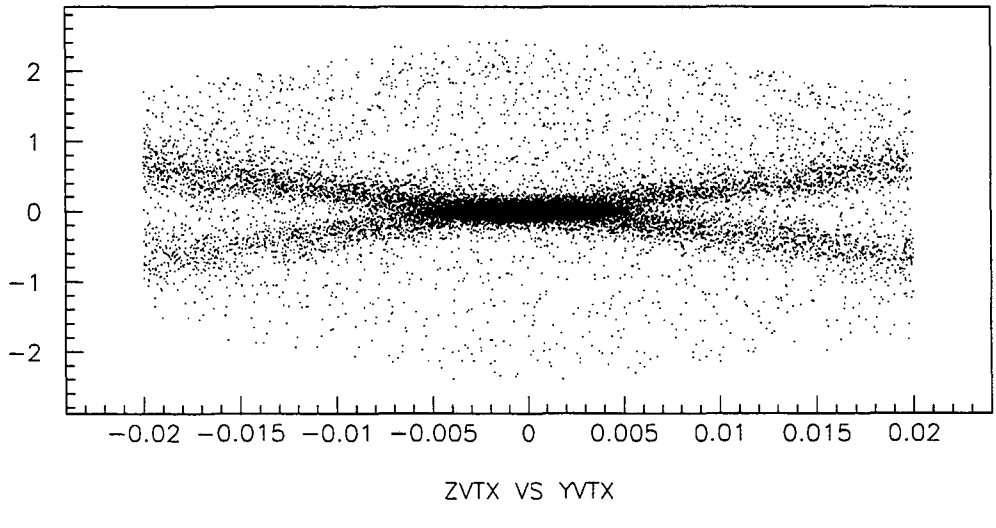

Figure 3.117: A scatter plot of the vertex Z versus Y position for dimuon events where the average silicon hit multiplicity is greater than or equal to 7. (Units are in inches.)

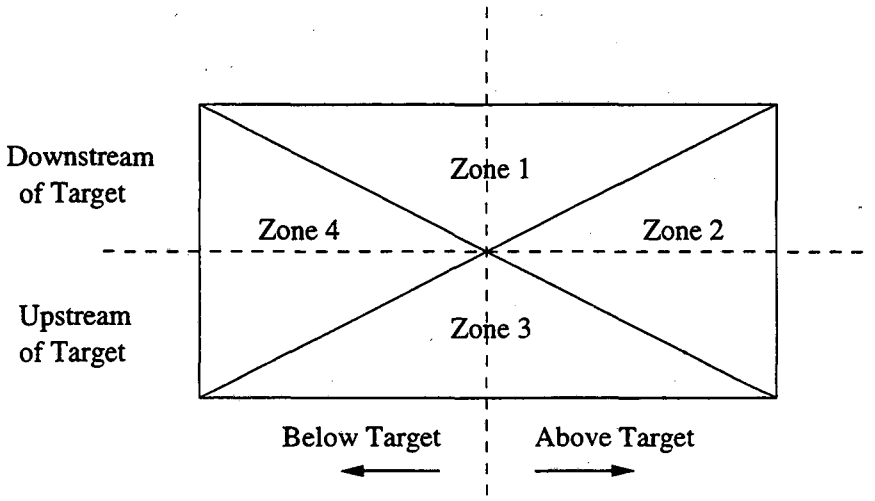

Figure 3.118: The zone map for the scatter plots in Figures 3.116 and 3.117.

The third and fourth cuts applied to the dimuon data set were designed to isolate $b \rightarrow J/\psi \rightarrow \mu^+\mu^-$ events from prompt J/ψ events. The third cut was an impact parameter cut on the muons in the event, where the impact parameter (δ_i, $i = 1, 2$) is defined to be the distance in Y, between the muon track and the target center. This cut was designed to eliminate muons that point back to the target. Figure 3.119 shows the scatter plot of the Z and Y positions of the vertex after the tightest impact parameter cut. The fourth cut was a cut on the Z position of the dimuon vertex. This cut exploits the fact that the b-hadron is long lived relative to the J/ψ and hence will decay downstream of the target whereas the prompt J/ψ's will decay in the target. Figures 3.120 and 3.121 show the invariant mass spectra for cuts with successively tighter requirements on the values of the impact parameter and Z vertex. The downstream plots are for successively larger Z vertex cuts, i.e., further and further downstream of the target. The upstream plots are for successively smaller Z vertex cuts, i.e., further and further upstream of the target. The upstream plots provide an estimate of the background in the downstream plots. The plot in Figure 3.120a (3.120b) contain events where the absolute value of the impact parameters, $\delta_{1,2}$, is greater than 0.04 mm and z_{vertex} is greater than 4 mm (less than -4 mm), corresponding to downstream (upstream) vertices. The plot in Figure 3.120c (3.120d) contain events where $\delta_{1,2} > 0.05$ mm and $z_{vertex} > 5$ mm (< -5 mm). Figure 3.121e (3.121f) contain events where $\delta_{1,2} > 0.06$ mm and $z_{vertex} > 6$ mm (< -6 mm). Finally, Figure 3.121g (3.121h) contain events where $\delta_{1,2} > 0.06$ mm and $z_{vertex} > 7$ mm (< -7 mm), the final cuts used

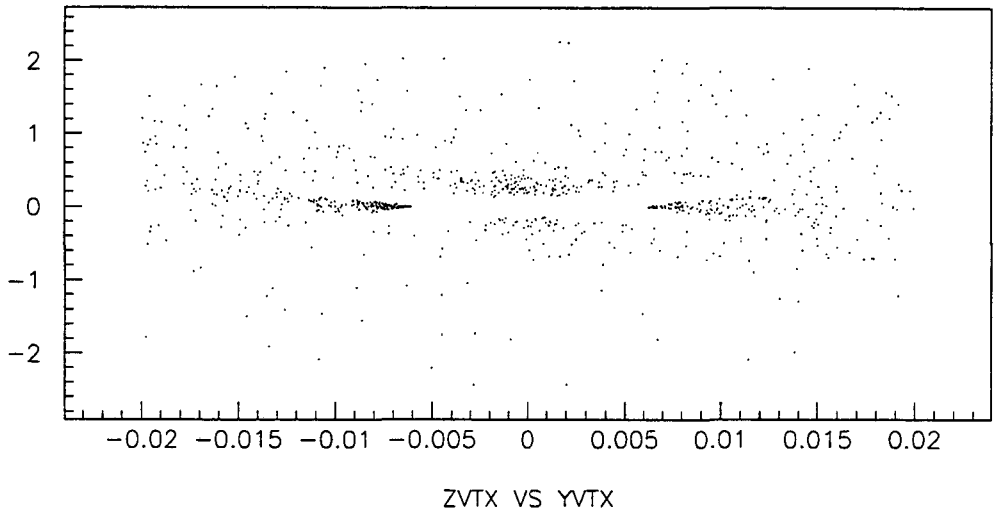

Figure 3.119: A scatter plot of the dimuon vertex Z and Y positions (in.) for the tightest impact parameter cut.

on the dimuon (and dihadron) data set.

3.5.2. Dihadron Analysis

The selection of events in the dihadron data set was essentially identical to the selection of events in the dimuon data set. This was done for two reasons. First, the topology of the dihadron and dimuon b-decay events were not significantly different (2 decay products from a detached vertex). Second, by using the same selection criteria, the uncertainties in determining the effects of the cuts were more likely cancel between the dihadron and dimuon data sets when the ratio was taken. The major difference between the analysis of the dihadron and dimuon events was the addition of a cut on the dihadron events that required that the scalar sum of the momenta of the two hadrons be greater than 95 GeV/c. (Monte Carlo studies show that the acceptance is negligible for events below 100 GeV/c.)

One difficulty with utilizing the dimuon cuts for the dihadron data set was gauging the effects of the NAVSI < 7. For the dimuon events, the effects of the cut could be quantified by calculating the loss of prompt J/ψ to dimuon events from the event sample after the

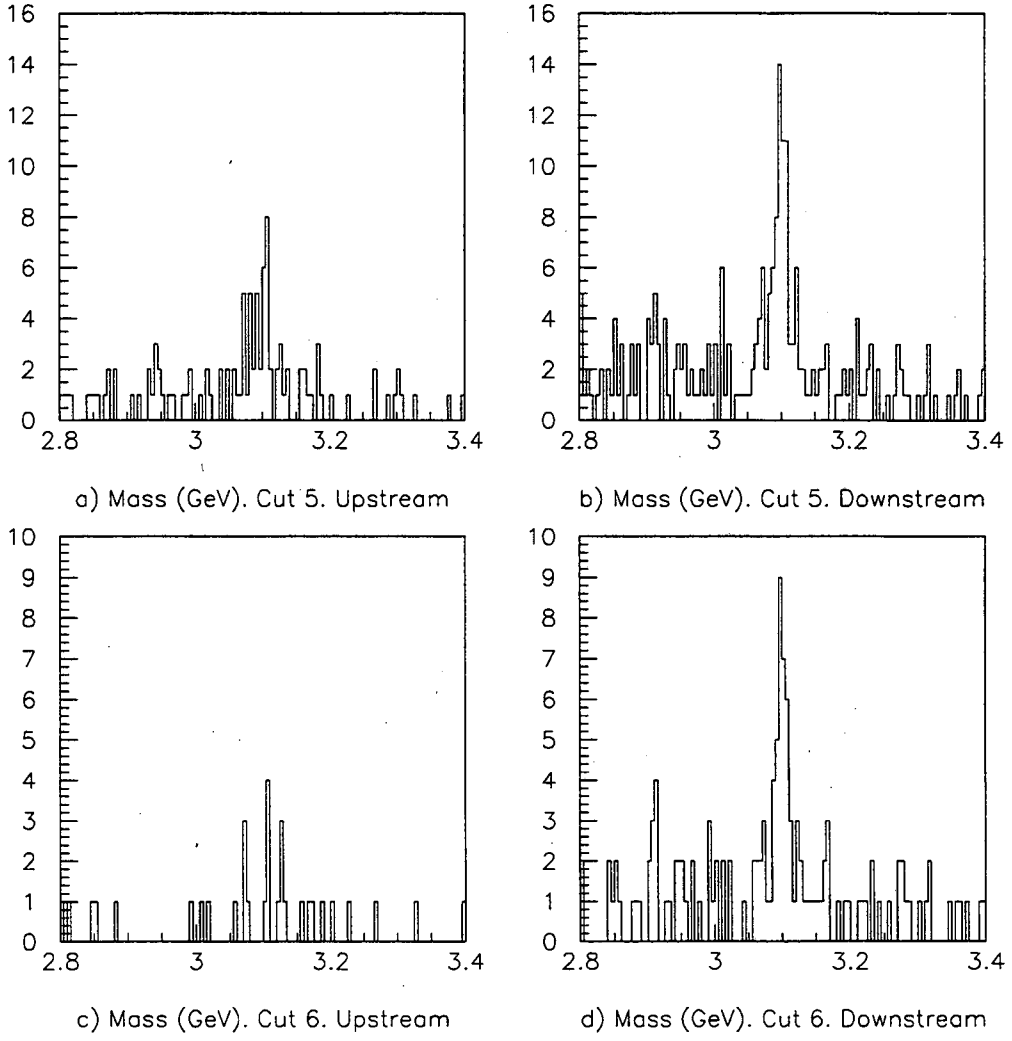

Figure 3.120: Invariant mass plots for successively tighter values of the impact parameter and Z vertex cuts.

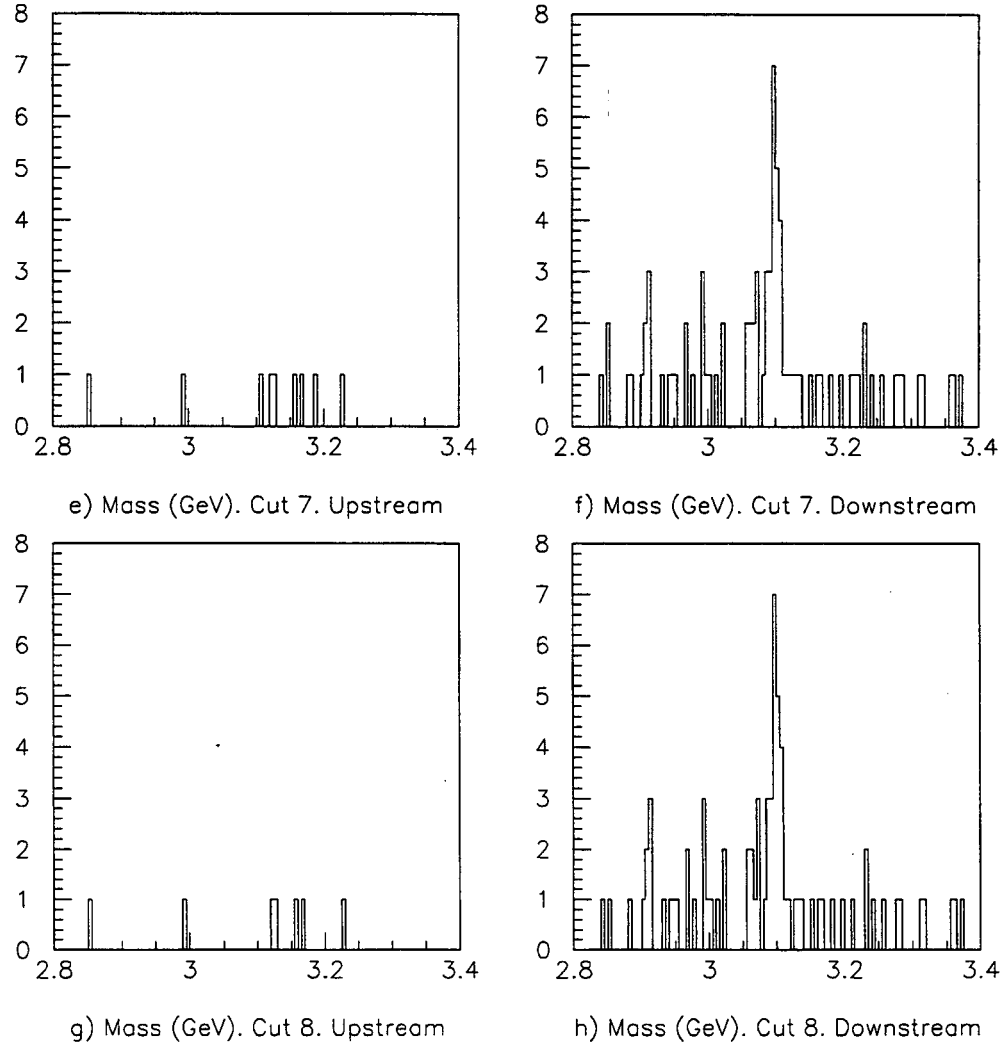

Figure 3.121: Invariant mass plots for successively tighter values of the impact parameter and Z vertex cuts.

application of the cut. In the case of the dihadron data set, no such reference signal was available. As a results, the effects of the cut was estimated by looking at the effects of the cut with the Monte Carlo. The assumption is that the technique of overlaying real silicon detector hits on top of Monte Carlo generated events properly models real signal dihadron events. Using this technique, the efficiency of the NAVSI < 7 was estimated to be $\sim 10\%$. (A weak cross-check of the accuracy of the Monte Carlo estimate was to compare the Monte Carlo predicted effects of the NAVSI cut on J/ψ events with the experimentally observed effects of the cut. For the J/ψ events, the Monte Carlo predicts an event loss of 7.3% which is very close to the experimentally measured value of 8.9%.)

Figure 3.122 shows the mass spectrum between 5 GeV and 6 GeV for the KK, pp and $\pi\pi$ mass assignments after the final set of cuts. Figure 3.123 shows the mass spectrum around the B-mesons. Similarly, Figure 3.124 shows the mass spectrum between 5 GeV and 6 GeV for the $K\pi$, Kp and $p\pi$ mass assignments. Figure 3.125 shows the mass spectrum around the B-mesons for the $K\pi$ mass assignment and around the Λ_b for the Kp and $p\pi$ mass assignments. (Also included are the mass spectra of events upstream of the interaction vertex, made with the same cuts as the downstream events, except that the Z vertex cut are $-$Z vertex cuts.)

3.5.3 Final Efficiency Evaluation

In summary, the acceptance and efficiencies for the full analysis procedure can be separated into three categories, those derived from the Monte Carlo ($\epsilon_{monte\ carlo}$), those determined from the data, and those that cancel in the ratio of the branching ratios. Going through the different efficiencies and acceptances, one by one, for the dimuon and dihadron data set yields the following:

1. ϵ_{live} - Cancels in the ratio.
2. ϵ_{tape} - Cancels in the ratio.
3. $M_U \cdot M_D$ - Contained in $\epsilon_{monte\ carlo}$.
4. $S_U \cdot S_D$ - Cancels in the ratio.
5. $\overline{NX1} \cdot \overline{NX3}$ efficiency - Cancels in the ratio.
6. E_H - Contained in $\epsilon_{monte\ carlo}$.

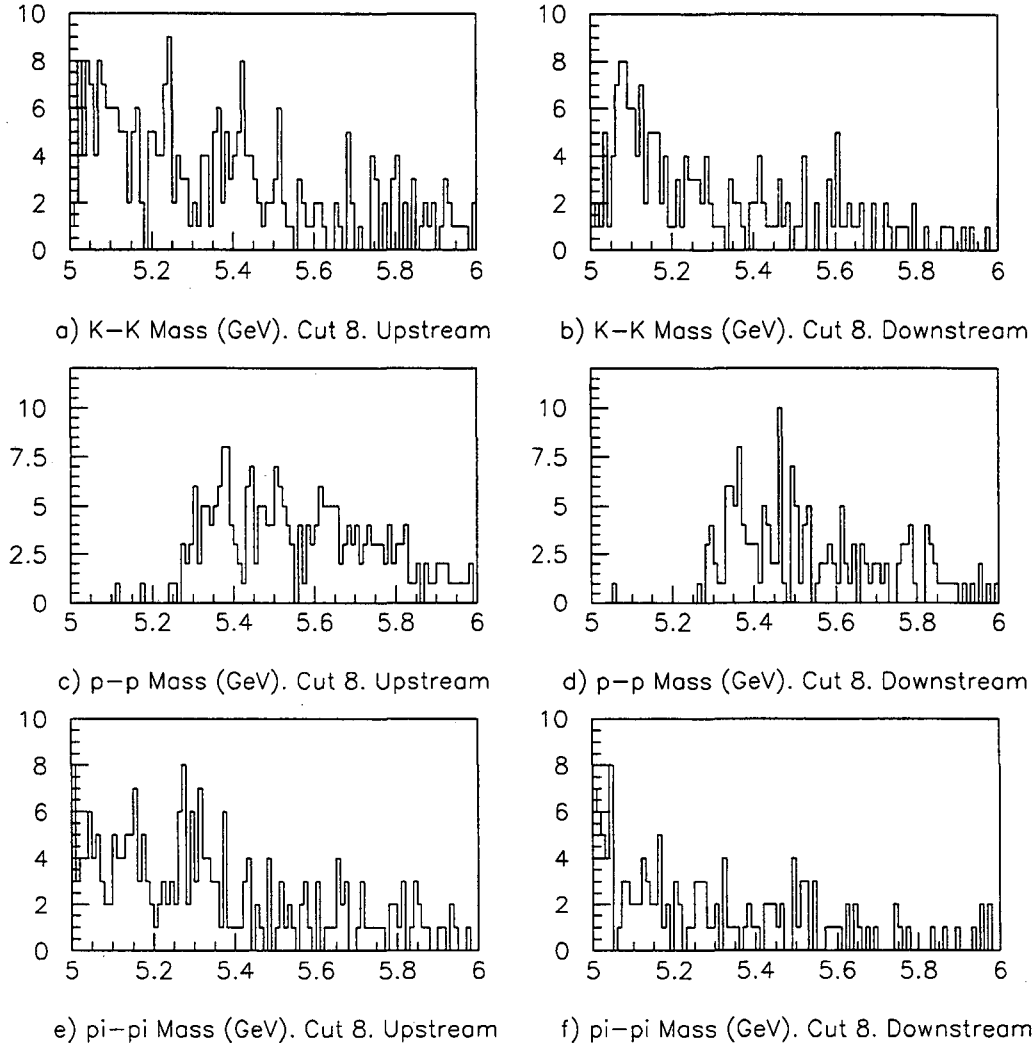

Figure 3.122: Invariant mass plots for the KK, pp, and $\pi\pi$ mass assignments. Plots a, c, and e are for events with vertices upstream of the target. Plots b, d, and f are for events with vertices downstream of the target.

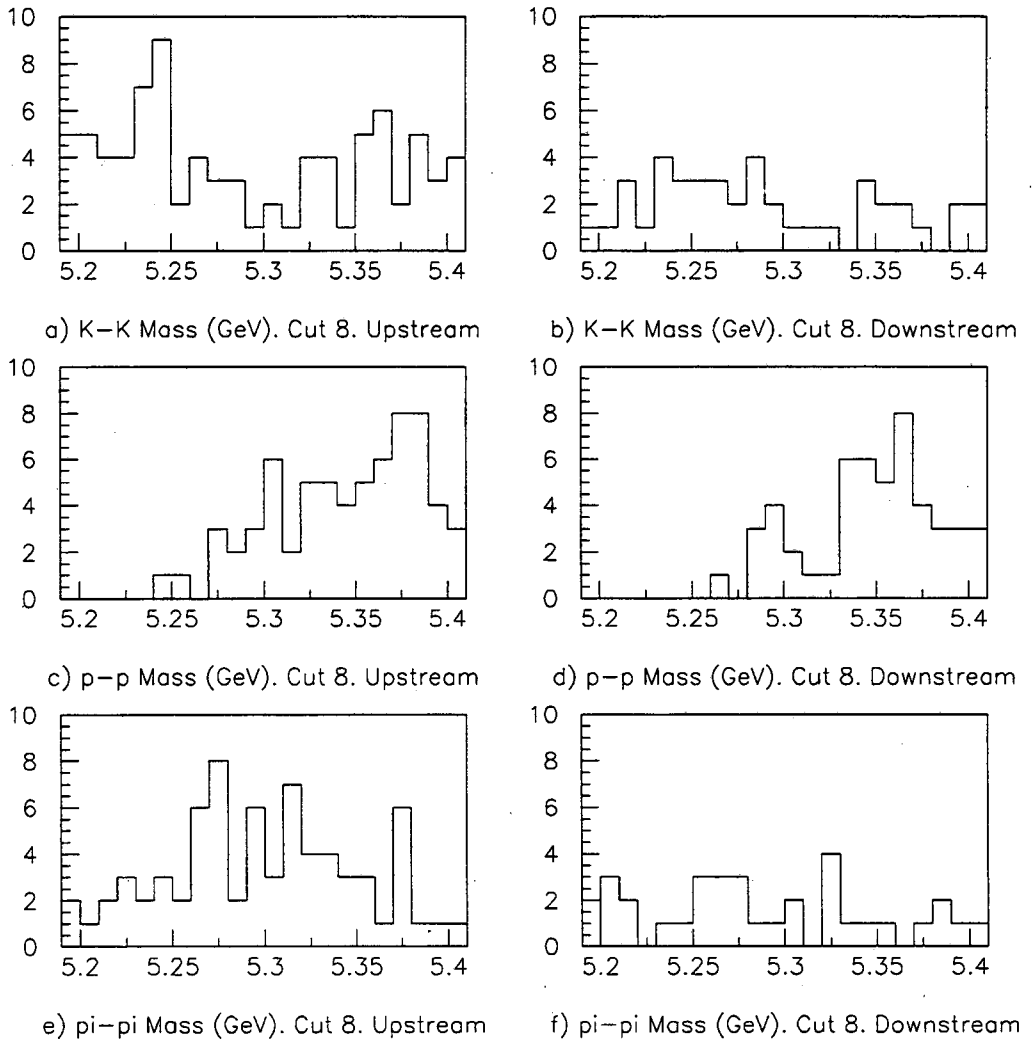

Figure 3.123: Invariant mass plots for the KK, pp, and $\pi\pi$ mass assignments. Plots a, c, and e are for events with vertices upstream of the target. Plots b, d, and f are for events with vertices downstream of the target.

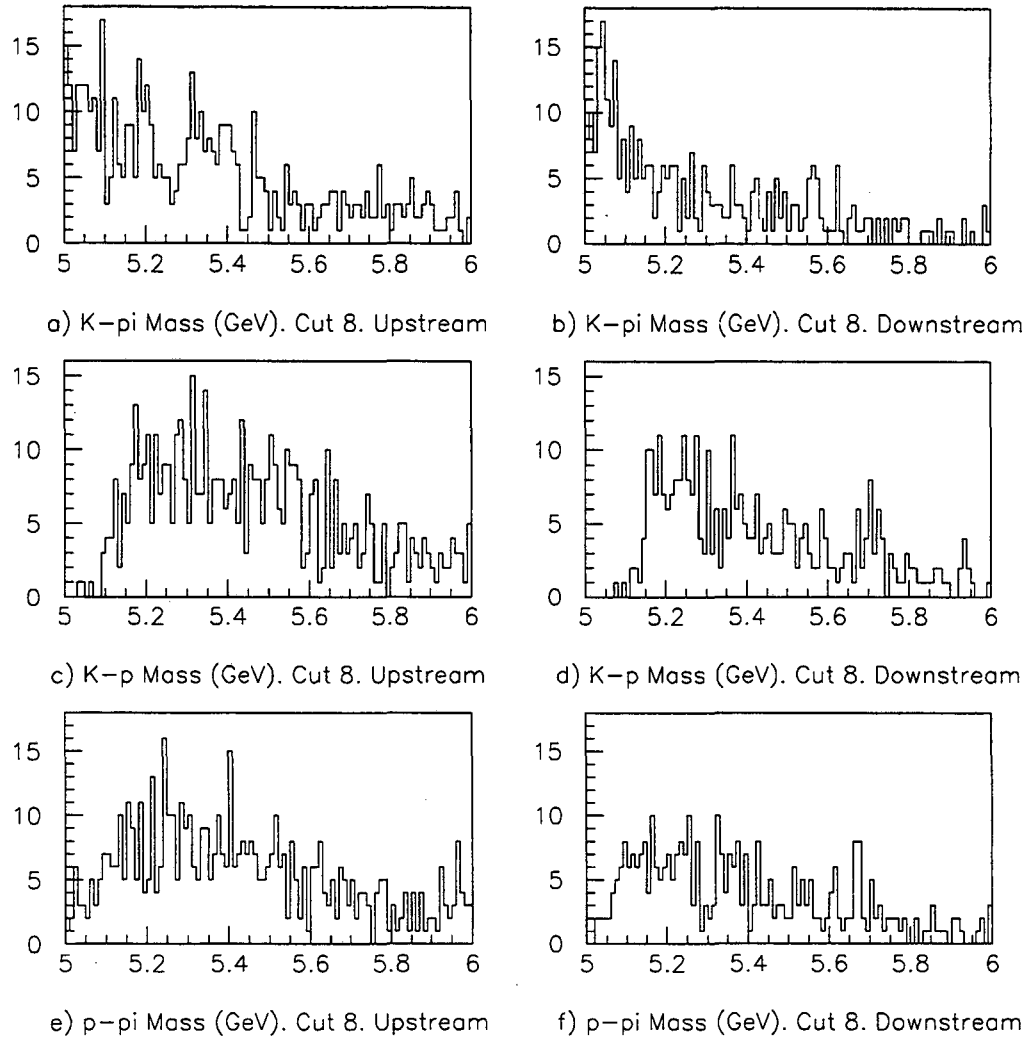

Figure 3.124: Invariant mass plots for the $K\pi$, Kp, and $p\pi$ mass assignments. Plots a, c, and e are for events with vertices upstream of the target. Plots b, d, and f are for events with vertices downstream of the target.

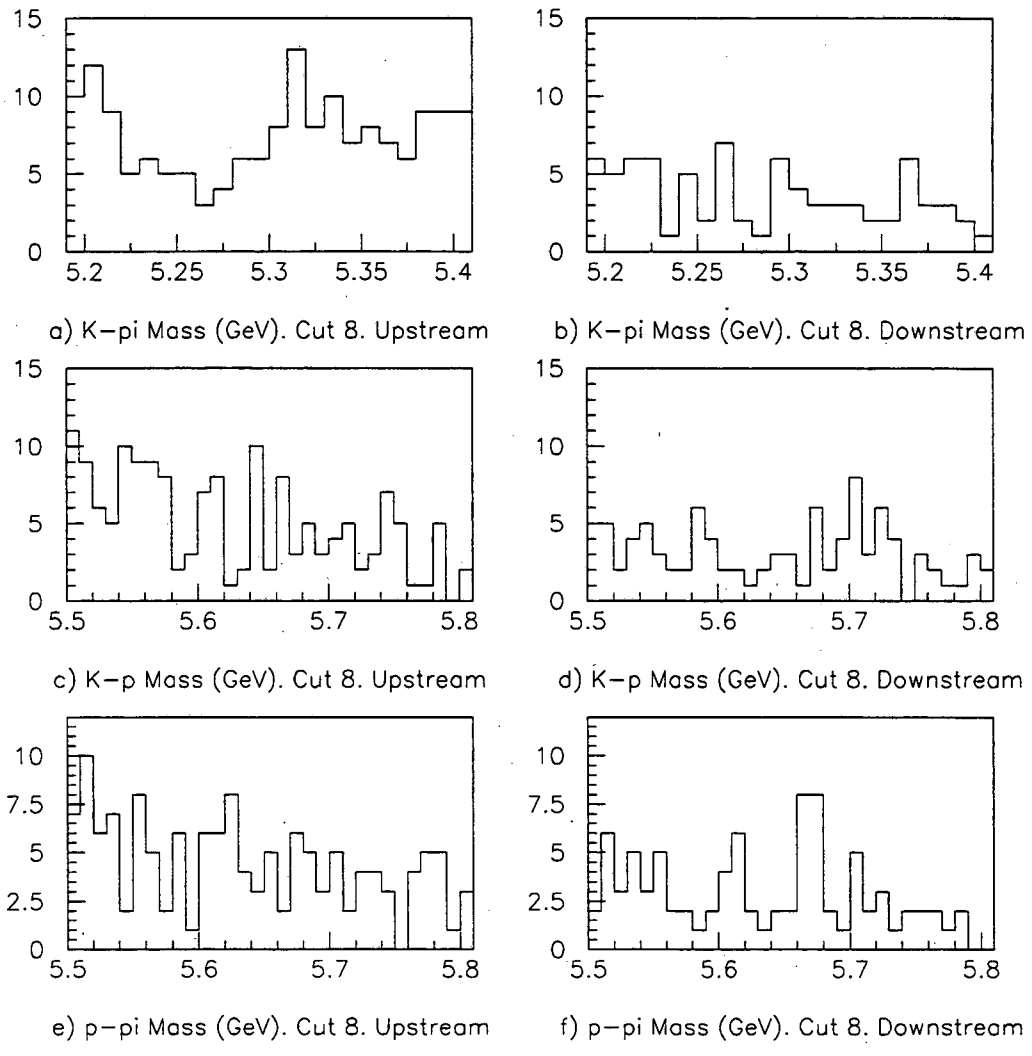

Figure 3.125: Invariant mass plots (GeV) for $K\pi$, Kp, and $p\pi$ mass assignments around the B-meson mass for the $K\pi$ combination and around the Λ_b mass for the Kp and $p\pi$ combinations. Plots a, c, and e are for events with vertices upstream of the target. Plots b, d, and f are for events with vertices downstream of the target.

Efficiency	Value (%)
$\epsilon_{monte\ carlo}$	0.092
Muon Only PID	93.4
NAVSI < 7	91.1
$S_U \cdot S_D$ correction	106
Total	0.0827

Table 3.8: Efficiencies, in percent, for the dimuon events.

7. $(\frac{2}{4}X4 \cdot \frac{2}{4}Y4)$ - Contained in $\epsilon_{monte\ carlo}$.

8. Trigger cross contamination - Obtained from data.

9. Reconstruction - Contained in $\epsilon_{monte\ carlo}$.

10. Particle ID dihadron cuts - Obtained from data.

11. 4+ Hadron cut - Obtained from data.

12. Muon only PID - Obtained from data.

13. NAVSI efficiency - Obtained from data (Monte Carlo) for the dimuons (dihadrons).

14. Impact Parameter cut - Contained in $\epsilon_{monte\ carlo}$.

15. Detached vertex cut - Contained in $\epsilon_{monte\ carlo}$.

Table 3.8 summarizes the values for the different efficiencies for the dimuon events. Table 3.9, 3.10, and 3.11 summarize the values for the different efficiencies for the dihadron events. Note that in the case of the dihadron efficiencies, changes to the $M_U \cdot M_D$ trigger (Matrix 76 and Matrix 77, see section 3.4.4 for more information) and to the E_H trigger during data taking resulted in two distinct running periods with different efficiencies. The efficiencies for the respective run periods for each decay channel are contained in the columns labeled #1 and #2 in the dihadron tables. The entry labeled "Cal. Trig." for the dihadrons corresponds to the enhancements in the calorimeter trigger efficiency due to trigger cross contamination.

Efficiency (%)	B_d Decay Mode							
	$\pi^+\pi^-$		K^+K^-		$p\bar{p}$		$K^+\pi^-$	
	#1	# 2	#1	# 2	#1	# 2	#1	# 2
$\epsilon_{monte\ carlo}$*	0.068	0.037	0.073	0.042	0.052	0.032	0.069	0.038
PID	82	83	82	83	82	83	82	83
Cal. Trig.	114	128	114	128	114	128	114	128
Total	0.064	0.039	0.068	0.045	0.049	0.034	0.065	0.040

Table 3.9: Efficiencies, in percent, during the two run periods for the B_d events. (*Note that $\epsilon_{monte\ carlo}$ includes the NAVSI < 7 cut.)

Efficiency (%)	B_s Decay Mode							
	$\pi^+\pi^-$		K^+K^-		$p\bar{p}$		$K^-\pi^+$	
	#1	# 2	#1	# 2	#1	# 2	#1	# 2
$\epsilon_{monte\ carlo}$*	0.066	0.034	0.071	0.037	0.084	0.049	0.065	0.034
PID	82	83	82	83	82	83	82	83
Cal. Trig.	114	128	114	128	114	128	114	128
Total	0.062	0.036	0.066	0.039	0.079	0.052	0.061	0.036

Table 3.10: Efficiencies, in percent, during the two run periods for the B_s events. (*Note that $\epsilon_{monte\ carlo}$ includes the NAVSI < 7 cut.)

Efficiency (%)	Λ_s Decay Mode			
	$p\pi^-$		pK^-	
	#1	# 2	#1	# 2
$\epsilon_{monte\ carlo}$*	0.058	0.029	0.061	0.031
PID	82	83	82	83
Cal. Trig.	114	128	114	128
Total	0.054	0.031	0.057	0.033

Table 3.11: Efficiencies, in percent, during the two run periods for the Λ_s events. (*Note that $\epsilon_{monte\ carlo}$ includes the NAVSI < 7 cut.)

3.6 Systematic Error

The efficiency calculations outlined in section 3.4 utilized a large number of parameters, extracted from the data, which characterized the performance of the spectrometer. It also utilized a Monte Carlo simulation of the event generation/decay process which contained many parameters, e.g., $\langle {k_t}^2 \rangle$ and $\epsilon_{Peterson}$. The important question that needed to be answered was: How sensitive was the determination of the per channel efficiency, ϵ_i, to the uncertainties in the different spectrometer and Monte Carlo parameters? The goal behind systematic error (or sensitivity) analysis was to get estimates for the uncertainty in the per channel efficiencies caused by the uncertainties in these parameters.

The sensitivities of the per channel efficiency to the various parameters were determined by systematically and independently varying each parameters and observing the changes in the efficiency. Two techniques were used to extract the sensitivities, one technique for each of the two basic classes of parameters. The first technique, used for most of the event generation/decay parameters (referred to as class A parameters for convenience), involved the determination of the "input/output" or "system" function of the spectrometer/reconstruction code combination. The second technique, used mostly for the spectrometer dependent parameters (referred to as class B parameters for convenience), involved running the Monte Carlo and reconstruction code for different values of each parameter.

3.6.1 Class A Parameters

The sensitivity of the per channel efficiencies to the class A parameters was quantified by determining the system function of the spectrometer/analysis code combination. There were two reasons for utilizing this technique; first, the length of time needed to calculate an efficiency by running the complete Monte Carlo/reconstruction code process was long and second, there were a large number of parameters in the event generator. Calculating the sensitivities by individually adjusting the different class A parameters and running through the complete Monte Carlo/analysis process would have taken an intolerable amount of time.

The key to the system function approach to sensitivity analysis was the assumption that the ratio of the number of reconstructed signal events and the number of signal events

generated at the target could be characterized by the following equation:

$$f_i = \frac{\int\int F(X_F, P_t) G_i(X_F, P_t)\, dX_F\, dP_t}{\int\int G_i(X_F, P_t)\, dX_F\, dP_t} \tag{3.36}$$

where $G_i(X_F, P_t)$ is the (X_F, P_t) distribution of produced b-hadrons and $F(X_F, P_t)\, dX_F\, dP_t$ is the fraction of b events in the phase space interval $(P_t, P_t + dP_t)$ and $(X_F, X_F + dX_F)$ that were accepted and fully reconstructed. Thus, $F(X_F, P_t)$ is the system function for the Monte Carlo/analysis process. Variations in the different class A parameters alter $G_i(X_F, P_t)$. If $F(X_F, P_t)$ is known, then the process of determining the sensitivity of the f_i's to uncertainties in these parameters reduces to evaluating the integral in equation 3.36.

$F(X_F, P_t)$ was determined by generating a set of b-hadrons using a flat (X_F, P_t) distribution (i.e., $G_i(X_F, P_t) = 1$) and propagating these b-hadrons through the Monte Carlo/analysis process and recording the number of events that were fully reconstructed. The (X_F, P_t) distribution of the fully reconstructed b-hadrons was equal to (within an overall scale factor) the system function, $F(X_F, P_t)$.

Once the system function was determined, the class A parameters needed to be identified and a suitable range of values needed to be chosen. The "tunable" class A parameters, i.e., those that could affect $G_i(X_F, P_t)$, were the following:

- m_b - b-quark mass.
- μ_f - Factorization scale.
- μ_r - Renormalization scale.
- F_{pdf} - Parton distribution function.
- k_t - Intrinsic k_t.
- P_t - b-hadron P_t.
- $\epsilon_{Peterson}$ - Epsilon of the Peterson fragmentation function.

Table 3.12 shows the high, low, and nominal values for the class A parameters used in the efficiency analysis. The ranges for μ_f and μ_r were the ranges utilized in reference [56]. The different parton distribution functions used in the analysis were MRSD0 [61], MRS-(A) [55] and GRV [62].

Parameter	Low	Nominal	High
m_b	4.5 GeV	4.75 GeV	5.0/5.25 GeV
μ_f	$0.5m_b$	m_b	$2m_b$
μ_r	$0.5m_b$	m_b	$2m_b$
F_{pdf}	MRSD0	MRS-(A)	GRV
k_t	0.4 GeV/c	0.5 GeV/c	0.60 GeV/c
P_t	0.0 GeV/c	0.35 GeV/c	0.70 GeV/c
$\epsilon_{Peterson}$	0.004	0.006	0.008

Table 3.12: A table of the tunable class A parameters in $G_i(X_F, P_t)$.

The ranges for the first four parameters, m_b, μ_f, μ_r and F_{pdf} handle the uncertainties in the "core" b-quark generator that stem from the choice of parton densities, QCD Λ parameter, b-quark mass, renormalization and factorization scales, and higher order corrections. These uncertainties were covered in the theoretical paper by Mangano, et. al. [56] which describes the b-quark generator. The variations in the last three parameters, k_t, P_t and ϵ, handle some of the problems associated with the lack of understanding of the hadronization of the b-quark into a b-hadron. As was stated in section 3.3, an independent fragmentation scheme was chosen for the hadronization of the b-quark. There are numerous problems associated with independent hadronization that are mentioned in the paper by Mangano, et. al. [56] and in the review article by Sjőstrand [63].

Some of the problems with independent fragmentation are outlined here. First, the use of the Peterson fragmentation function results in a non-conservation of energy and momentum, a characteristic that is common to all "pure" independent fragmentation schemes [63]. With the implemented cut of $E_{hadron} < E_{quark}$, which was an attempt to add an energy conservation requirement, the resulting z distribution for the generated b-hadrons, shown in Figure 3.126, was quite different from the Peterson function. In addition, with the definition of z given in equation 3.26, the longitudinal momentum of the b-hadron had a non-zero probability of being opposite to the direction of the b-quark. This is shown in Figure 3.127. In order to determine the effects of these assumptions, the energy conservation requirement was dropped as a test cases, and a $P_{\|} > 0$ requirement was added as a test case.

The results of the studies of the class A parameters are summarized in Tables 3.13, 3.14, 3.15, and 3.16 for $b \to J/\psi \to \mu\mu$, $B_d \to h^+h^-$, $B_s \to h^+h^-$, and $\Lambda \to h^+h^-$,

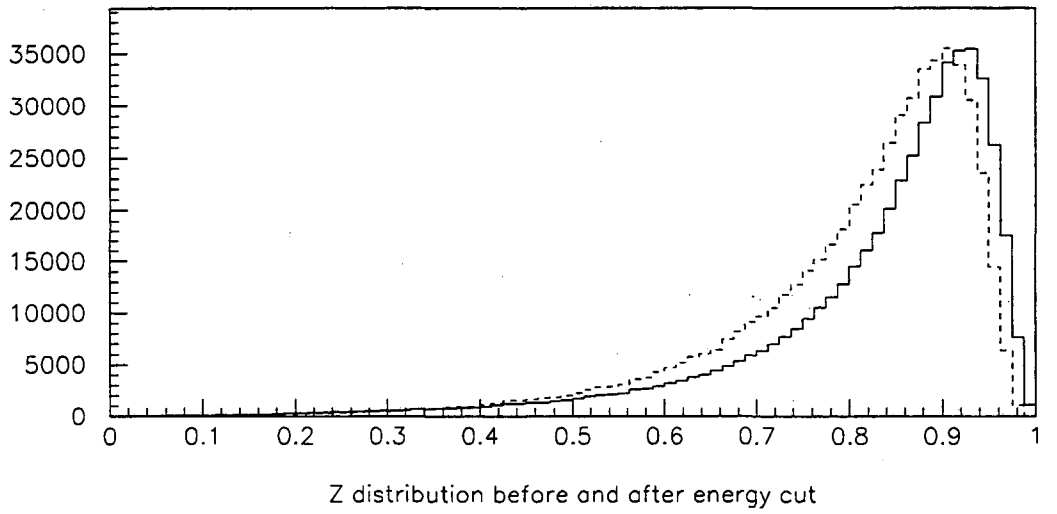

Figure 3.126: z distribution before (solid line) and after (dotted line) the energy conservation cut. The latter distribution had been rescaled to allow for the comparison between the shapes of the two distributions.

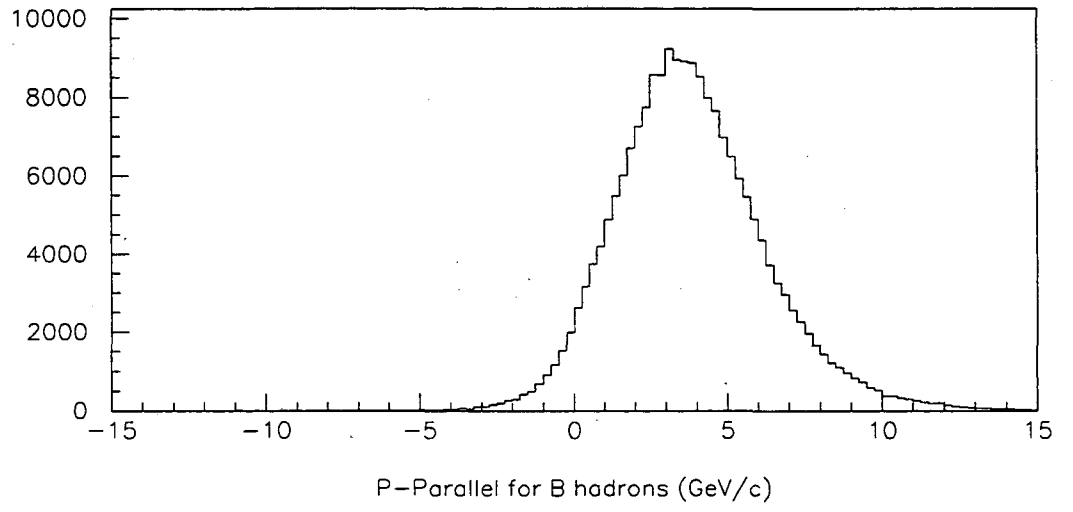

Figure 3.127: Distribution of $P_{\parallel}$ for Monte Carlo generated b-hadrons.

Parameter	$b \to J/\psi \to \mu\mu$ Class A Systematic Errors
m_b	$\pm 7\%$
μ_f	$\pm 2\%$
μ_r	$-0\% + 2\%$
F_{pdf}	-
k_t	$\pm 2\%$
P_t	$-2\% + 0\%$
$\epsilon_{Peterson}$	$\pm 4\%$
$\Delta E \neq 0$	-
$P_{\parallel} > 0$	$-3\% + 0\%$
Total	$\pm 9\%$

Table 3.13: Systematic errors resulting from varying the class A parameters for $b \to J/\psi \to \mu\mu$.

respectively. The - in some of the entries denotes the fact that variations of the parameter for the process resulted in no significant variation in the efficiency within the statistical accuracy of the Monte Carlo simulation. The totals were obtained by "symmetrizing" the asymmetric errors which were then added to the symmetric errors in quadrature. (See section 3.6.2 for a discussion of the symmetrization process.)

3.6.2 Class B Parameters

The class B parameters were those tunable parameters in the efficiency calculation whose effects on efficiency could only be determined by running the complete Monte Carlo/analysis process. Parameters that fell into this category were:

- b-hadron lifetime.
- Detector plane efficiencies.
- Matrix trigger efficiency.
- J/ψ polarization (Dimuon events only).
- J/ψ momentum (Muon events only).
- Muon trigger efficiency (Dimuon events only).

Parameter	B_d Class A Systematic Errors			
	$\pi^+\pi^-$	$K^+\pi^-$	K^+K^-	$p\bar{p}$
m_b	$-3\% + 0\%$	$-3\% + 2\%$	$-4\% + 2\%$	$-7\% + 6\%$
μ_f	$-3\% + 0\%$	$-3\% + 0\%$	$-3\% + 0\%$	$-4\% + 0\%$
μ_r	–	–	–	–
F_{pdf}	$-2\% + 0\%$	$-2\% + 0\%$	–	$-2\% + 0\%$
k_t	–	–	–	$\pm 2\%$
P_t	–	$-2\% + 0\%$	–	–
$\epsilon_{Peterson}$	$-3\% + 0\%$	$-3\% + 2\%$	$-3\% + 2\%$	$-5\% + 3\%$
$\Delta E \neq 0$	–	–	–	–
$P_{\parallel} > 0$	–	–	–	–
Total	$\pm 6\%$	$\pm 6\%$	$\pm 6\%$	$\pm 10\%$

Table 3.14: Systematic errors resulting from the variation of class A parameters for $B_d \to h^+h^-$.

Parameter	B_s Class A Systematic Errors			
	$\pi^+\pi^-$	$K^+\pi^-$	K^+K^-	$p\bar{p}$
m_b	$\pm 3\%$	$\pm 3\%$	$-3\% + 4\%$	$-6\% + 5\%$
μ_f	$-2\% + 0\%$	$-2\% + 0\%$	$-2\% + 0\%$	$-3\% + 0\%$
μ_r	–	–	–	$-0\% + 2\%$
F_{pdf}	$-2\% + 0\%$	$-2\% + 0\%$	$-2\% + 0\%$	$-2\% + 0\%$
k_t	–	$-2\% + 0\%$	$-2\% + 0\%$	$\pm 2\%$
P_t	$-0\% + 2\%$	$-0\% + 2\%$	$-0\% + 2\%$	–
$\epsilon_{Peterson}$	$-3\% + 2\%$	$\pm 2\%$	$-3\% + 2\%$	$\pm 3\%$
$\Delta E \neq 0$	–	–	–	–
$P_{\parallel} > 0$	–	–	–	–
Total	$\pm 6\%$	$\pm 5\%$	$\pm 6\%$	$\pm 8\%$

Table 3.15: Systematic errors resulting from the variation of class A parameters for $B_s \to h^+h^-$.

Parameter	Λ_b Class A Systematic Errors	
	$p\pi^-$	pK^-
m_b	$-2\% + 4\%$	$-2\% + 4\%$
μ_f	-	-
μ_r	-	-
F_{pdf}	-	-
k_t	-	-
P_t	$-0\% + 3\%$	$-0\% + 2\%$
$\epsilon_{Peterson}$	$-0\% + 2\%$	$\pm 2\%$
$\Delta E \neq 0$	-	-
$P_{\|\|} > 0$	$-0\% + 3\%$	$-0\% + 2\%$
Total	$\pm 6\%$	$\pm 5\%$

Table 3.16: Systematic errors resulting from the variation of class A parameters for $\Lambda_b \rightarrow h^+h^-$.

- Calorimeter trigger efficiency (Dihadron events only).

For the b-hadron lifetimes, nominal values of 1.56 ps, 1.61 ps and 1.14 ps for the B_d, B_s, and Λ_b baryons, respectively were used [64]. Systematic effects due to the b-hadron lifetimes were studied by varying the nominal values by plus or minus the uncertainties quoted by the Particle Data Group (PDG) [64]. The strategy for handling the detector and trigger efficiencies was to use efficiencies that were independently determined. Two different sets of hodoscope efficiencies and three different sets of chamber (wire/silicon) efficiencies were used in the systematic analysis.

The trigger matrix parameters correspond to the different lookup tables used in determining what combinations of station 1, 2, and 3 hodoscopes correspond to "interesting" charged particle tracks. (See section 2.5.2 for more details on the $M_U \cdot M_D$ matrix trigger.) During the b-run, 2 different sets of lookup tables were used. For the systematic analysis, both sets were utilized. However, as was mentioned in section 3.4.4, the efficiencies of the two lookup tables were significantly different for the dihadron events, but essentially the same for the dimuon events. For this reason, the matrix trigger was treated as a systematic uncertainty only for the dimuon events, whereas for the dihadrons, separate efficiencies for the two run periods were explicitly determined.

Other parameters unique to the dimuon events were the J/ψ polarization, J/ψ momentum and the muon trigger efficiency. For the J/ψ polarization, the distribution

$(1-\alpha cos^2(\theta))$, where θ is the polar angle of one of the muons in the J/ψ decay measured with respect to the J/ψ momentum vector in the B rest frame, was chosen with a nominal value for α of -0.436 [50]. The variation of α was ± 0.115 from the nominal value, corresponding to the quoted uncertainty of α. For the J/ψ momentum distribution, the CLEO distribution folded at the 1.73 GeV/c momentum limit was the nominal distribution. The original CLEO distribution was used to gauge the uncertainty resulting from the ambiguities in the J/ψ momentum distribution. The final parameter unique to the dimuon events was the muon trigger efficiency. In addition to being dependent on the efficiencies of the muon hodoscopes, the muon trigger efficiency was dependent on the logic used to form the muon trigger. Through the *b*-run, the composition of the muon trigger was changed twice. The effects of the efficiencies of the three different configurations of the muon trigger were also studied. Finally, the effects due to the uncertainty and variation of the calorimeter trigger (unique to the dihadron events) were determined by utilizing the three distinct calorimeter turn-on curves found in the the calorimeter trigger analysis (Section 3.4.4).

The effects of the variation (uncertainty) in all the class B parameters were determined by systematically varying each parameter and running the complete Monte Carlo generation/event analysis process. Approximately 2 million signal events were generated for each individual test case for both dihadron and dimuon events. This resulted in exactly 20,000 dimuon events and 25,000 dihadron events being written into a DST file for each test case. The resulting files were then run through the complete analysis process. Approximately 2500 dimuon events survived and approximately 2000 dihadron events survived the complete analysis process for each test case.

The results of the systematic studies of the class B parameters for the dimuon events are shown in Table 3.17. Some explanation is required about some of the entries in the table and the procedure for determining the total. In the dimuon table, the entries labeled "B_s Parent" and "Λ_b Parent" correspond to the cases where all the $b \rightarrow J/\psi \rightarrow \mu\mu$ events are assumed to originate from B_s and Λ_b decays instead of B_d decays. The "Muon Trigger" entry corresponds to changes to the $(\frac{2}{4}\text{X4}\cdot\frac{2}{4}\text{Y4})$ component of the $\mu^+\mu^-$ trigger. The process for combining the systematic errors was as follows. First, each asymmetric error were converted to a symmetric error by assuming that the magnitude of the symmetric error was equal to the magnitude of the larger (in absolute magnitude) of the two asymmetric errors. Clearly, this is an overestimate of the error. Second, in the case of the "B_s Parent" and "Λ_b Parent" systematics for the dimuon events, approximately 10% of the J/ψ's originate from

Parameter	$b \rightarrow J/\psi \rightarrow \mu\mu$ Class B Systematic Errors
B_s Parent*	+8.7% (1%)
Λ_b Parent*	−3.4% (1%)
b-hadron life time	$+5.4 - 1.3\%$
J/ψ polarization	+3.1%
J/ψ momentum	+1.6%
Chamber Efficiency	±5.5%
Hodoscope Efficiency	±4.4%
Background Noise	±2.5%
Trigger Matrix	–
Muon Trigger*	+14% (2%)
Weighted Total*	±10%

Table 3.17: Systematic errors resulting from the variation of class B parameters for $b \rightarrow J/\psi \rightarrow \mu\mu$. (* See the text for information about the weighting procedure.)

these decays. This implies that the effects of these two systematics on the overall efficiency should each be less than 1%. Hence, a value of 1% was assumed for each systematic when calculating the total class B systematic error. A similar effect occurs for the Muon Trigger entry. Less than 10% of the dimuon events after pass 3 were accepted under the alternate muon trigger. In calculating the effects on the overall efficiency, a 2% error was assigned for this systematic. The weighted total of the systematic errors was obtained by adding the "symmetrized" asymmetric errors and these latter three effective errors in quadrature.

The results for the dihadron events are shown in Tables 3.18, 3.19, and 3.20. The tables contain the systematics for dihadron decays of the B_d, B_s and Λ_b hadrons, respectively. The columns labeled "#1" and "#2" in the dihadron tables correspond to run periods 1 (Matrix 76) and 2 (Matrix 77) for the dihadrons. The row labeled "Cal. Trigger" in the dihadron tables corresponds to uncertainties in the turn-on curve of the calorimeter trigger. Finally, it should be noted that the systematic errors are probably smaller than the totals given above since the systematic errors in the dimuon and dihadron efficiencies resulting from the uncertainties in the chamber and hodoscope efficiencies are correlated.

Parameter	B_d Class B Systematic Error							
	$\pi^+\pi^-$		K^+K^-		$p\bar{p}$		$K^+\pi^-$	
	#1	#2	#1	#2	#1	#2	#1	#2
B_d life time	+6%		+3%		−6%		−	
Chamber Eff.	±7%		±8%		±6%		±5%	
Hodoscope Eff.	±6%		±5%		±7%		±7%	
Background Noise	−		−		−		−	
Cal. Trigger	±5%	±9%	±6%	±10%	±11%	±16%	±5%	±9%
Total	±12%	±14%	±12%	±14%	±16%	±19%	±10%	±12%

Table 3.18: Systematic errors resulting from the variation of class B parameters for $B_d \to h^+h^-$.

Parameter	B_s Class B Systematic Error							
	$\pi^+\pi^-$		K^+K^-		$p\bar{p}$		$K^+\pi^-$	
	#1	#2	#1	#2	#1	#2	#1	#2
B_s life time	+4% − 3%		−5%		+3%		−5%	
Chamber Eff.	±6%		±7%		±8%		±2%	
Hodoscope Eff.	±8%		±8%		±7%		±8%	
Background Noise	±5%		−		±4%		±3%	
Cal. Trigger	±4%	±6%	±5%	±8%	±9%	±14%	±4%	±7%
Total	±13%	±13%	±13%	±14%	±15%	±18%	±11%	±12%

Table 3.19: Systematic errors resulting from the variation of class B parameters for $B_s \to h^+h^-$.

Parameter	Λ_b Class B Systematic Error			
	$p\pi^-$		pK^-	
	#1	#2	#1	#2
Λ_d life time	−4% + 3%		−4% + 3%	
Chamber Eff.	±6%		±5%	
Hodoscope Eff.	±10%		±8%	
Background Noise	−		+3%	
Cal. Trigger	±3%	±6%	±3%	±7%
Total	±13%	±14%	±11%	±13%

Table 3.20: Systematic errors resulting from the variation of class B parameters for $\Lambda_b \to h^+h^-$.

Parameter	Total Systematic Errors
Class A	±9%
Class B	±10%
Total	±13%

Table 3.21: Systematic errors resulting from the uncertainty in all the parameters for $b \to J/\psi \to \mu\mu$.

	B_d Total Systematic Error							
	$\pi^+\pi^-$		K^+K^-		$p\bar{p}$		$K^+\pi^-$	
Parameter	#1	#2	#1	#2	#1	#2	#1	#2
Class A	±6%	±6%	±6%	±6%	±6%	±6%	±10%	±10%
Class B	±12%	±14%	±12%	±14%	±16%	±19%	±10%	±12%
PID	±7%	±4%	±7%	±4%	±7%	±4%	±7%	±4%
Other Triggers	±6%	±9%	±6%	±9%	±6%	±9%	±6%	±9%
Total	±16%	±18%	±16%	±18%	±19%	±22%	±17%	±18%

Table 3.22: Systematic errors resulting from the uncertainty in all the parameters for $B_d \to h^+h^-$.

3.6.3 Systematic Error Summary

The total systematic uncertainty in the determination of the ratio of the branching ratios included not only the class A and class B systematic errors but also the uncertainties in the efficiencies that were determined without the use of the Monte Carlo. These other uncertainties include the uncertainties in determining the trigger cross contamination (see section 3.4.4) and the dihadron particle identification efficiencies.

Parameter	B_s Total Systematic Error							
	$\pi^+\pi^-$		K^+K^-		$p\bar{p}$		$K^+\pi^-$	
	#1	#2	#1	#2	#1	#2	#1	#2
Class A	±6%	±6%	±5%	±5%	±6%	±6%	±8%	±8%
Class B	±13%	±13%	±13%	±14%	±15%	±18%	±11%	±12%
PID	±7%	±4%	±7%	±4%	±7%	±4%	±7%	±4%
Other Triggers	±6%	±9%	±6%	±9%	±6%	±9%	±6%	±9%
Total	±17%	±17%	±17%	±18%	±19%	±21%	±16%	±17%

Table 3.23: Systematic errors resulting from the uncertainty in all the parameters for $B_s \to h^+h^-$.

Parameter	Λ_b Total Systematic Error			
	$p\pi^-$		pK^-	
	#1	#2	#1	#2
Class A	±6%	±6%	±5%	±5%
Class B	±13%	±14%	±11%	±13%
PID	±7%	±4%	±7%	±4%
Other Triggers	±6%	±9%	±6%	±9%
Total	±17%	±18%	±15%	±17%

Table 3.24: Systematic errors resulting from the uncertainty in all the parameters for $\Lambda_b \to h^+h^-$.

Chapter 4

Results

As was stated in the introduction, the goal of the analysis in this thesis was a measurement of the branching ratios of the neutral b-hadrons to two charmless hadrons. The final element in the calculation of these branching ratios was a count of the number of signal events in the invariant mass spectra shown in Figures 3.122 and 3.124. A minor complication in the determination of the branching ratio was the fact that changes in the running conditions of the experiment resulted in two distinct periods of data collection where the overall efficiencies for dihadron b-decays were relatively stable. However, differences in the dihadron efficiencies between these two periods prevented the direct application of the formula given in section 3.1.

The solution to the problem of two distinct running periods was handled by utilizing a weighted sum of the results obtained from the two running periods. The procedure for weighting the results was obtained from the formula for the ratio of branching ratios given in equation 3.4 and which is reproduced below for convenience:

$$\frac{N_i}{N_{ref}} = \left(\frac{\mathrm{BR}_i f_i \epsilon_i}{\mathrm{BR}_{ref} \epsilon_{ref}} \right) \tag{4.1}$$

which can be rewritten, with the substitution $\epsilon_i/\epsilon_{ref} = \alpha_i$, as:

$$N_i = \frac{\mathrm{BR}_i f_i}{\mathrm{BR}_{ref}} \times \alpha_i \times N_{ref} \tag{4.2}$$

Summing the above equation over the two run periods where the measured quantities were $N_i(1)$, $N_i(2)$, $N_{ref}(1)$, $N_{ref}(2)$, $\alpha_i(1)$ and $\alpha_i(2)$ yields:

$$N_i(1) + N_i(2) = \frac{\mathrm{BR}_i f_i}{\mathrm{BR}_{ref}} \times (\alpha_i(1) \times N_{ref}(1) + \alpha_i(2) \times N_{ref}(2)) \tag{4.3}$$

Run Period	Number of events		
	Signal	(statistical)	(systematic)
Run 1 (Matrix 76)	8.1	$(+3.3 - 2.7)$	(± 1)
Run 2 (Matrix 77)	11.4	$(+4.1 - 3.4)$	(± 3)

Table 4.1: Results of the maximum likelihood fit to the dimuon mass spectra.

Minor rearrangement of this equation yields the final formula which was used to determine the ratio of the branching ratios:

$$\frac{\mathrm{BR}_i f_i}{\mathrm{BR}_{ref}} = \frac{N_i(1) + N_i(2)}{(\alpha_i(1) \times N_{ref}(1) + \alpha_i(2) \times N_{ref}(2))} \tag{4.4}$$

From this equation, it is clear that the final step in the analysis of the data is the determination of the total number of signal b-hadron to charmless dihadron events in all the data and a determination of the number of reference cascade b-hadron decays to two muons in each of the two run intervals.

4.1 Event Counting

The methodology used to extract the number of signal events from the various invariant mass spectra was to fit each invariant mass spectrum with a background event distribution and a signal shape that was derived from the Monte Carlo. The fitting procedure chosen for this analysis was a binned maximum likelihood fit.

4.1.1 Dimuon Events

For the dimuon events, a Gaussian line shape was assumed for the signal. A binned maximum likelihood fit to the Monte Carlo invariant mass spectrum, shown in Figure 4.1, yielded a mean of 3.0981 GeV and a sigma of 5.4 MeV. For the background, a linear distribution was assumed. In the process of fitting the linear background distribution and the Gaussian signal to the data, the parameters in the linear distribution were allowed to vary as was the scale of the signal Gaussian. The results of the maximum likelihood fit to the dimuon mass spectrum for the two run periods are shown in Figures 4.2 and 4.3, and tabulated in Table 4.1.

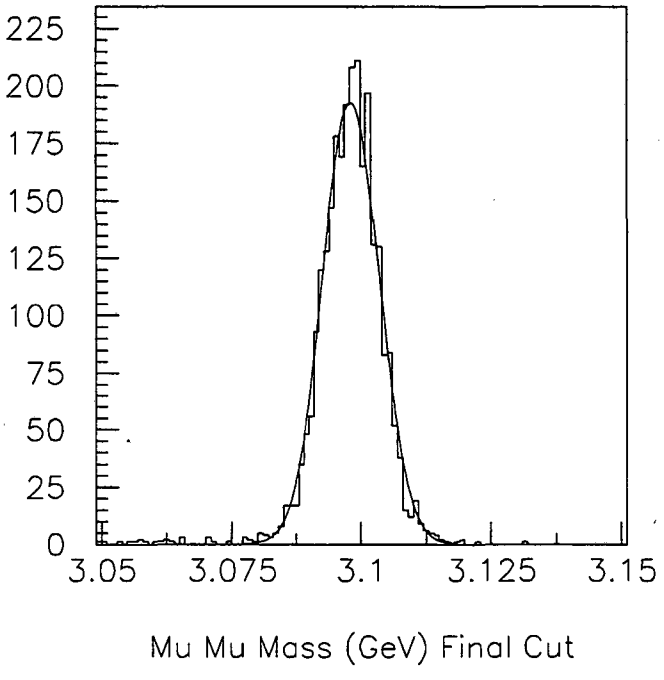

Figure 4.1: Results of the fit of a single Gaussian to the Monte Carlo generated invariant mass spectrum for muons from the cascade decay b–hadron $\rightarrow J/\psi + X \rightarrow \mu^+\mu^- + X$. (Units are in GeV.)

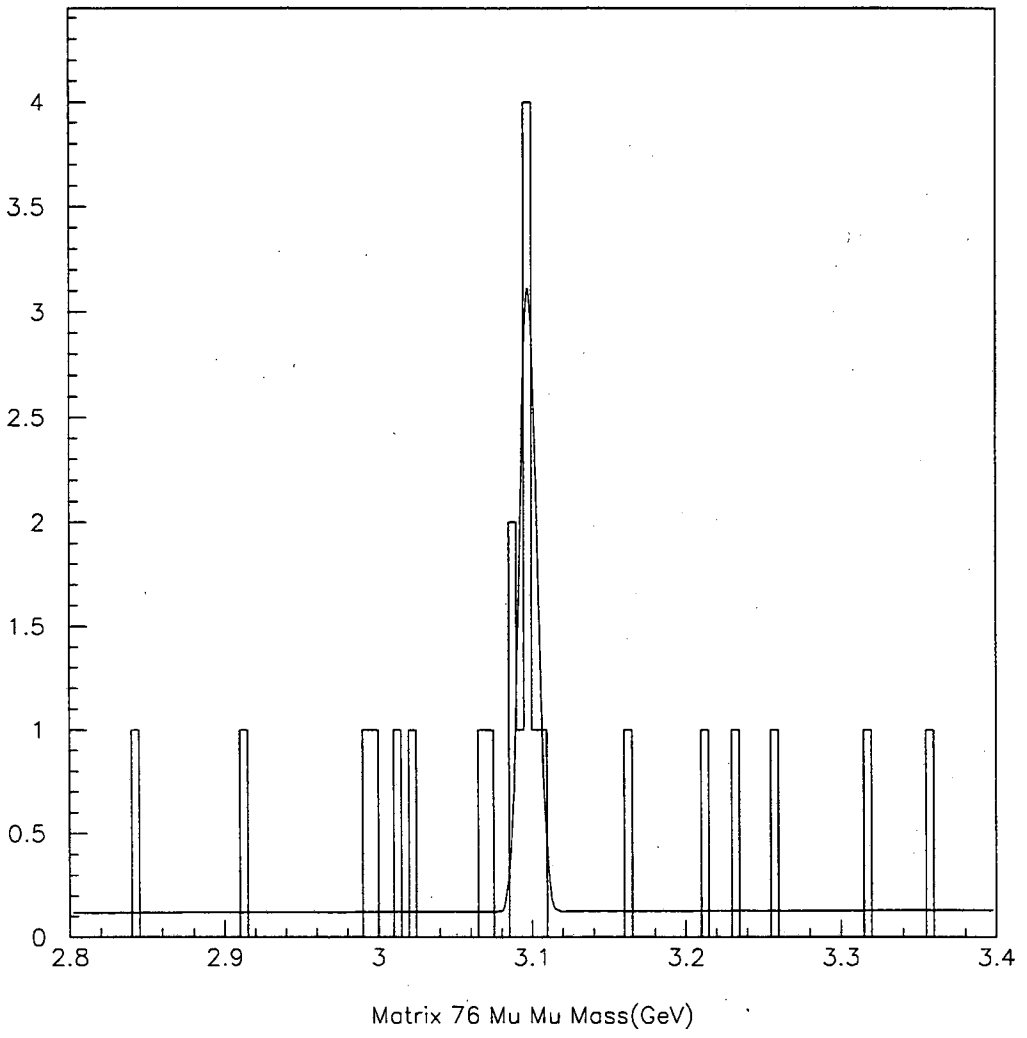

Figure 4.2: Results of the fit of a single fixed width Gaussian and a linear background to the dimuon invariant mass spectrum from run period 1. (Units are in GeV.)

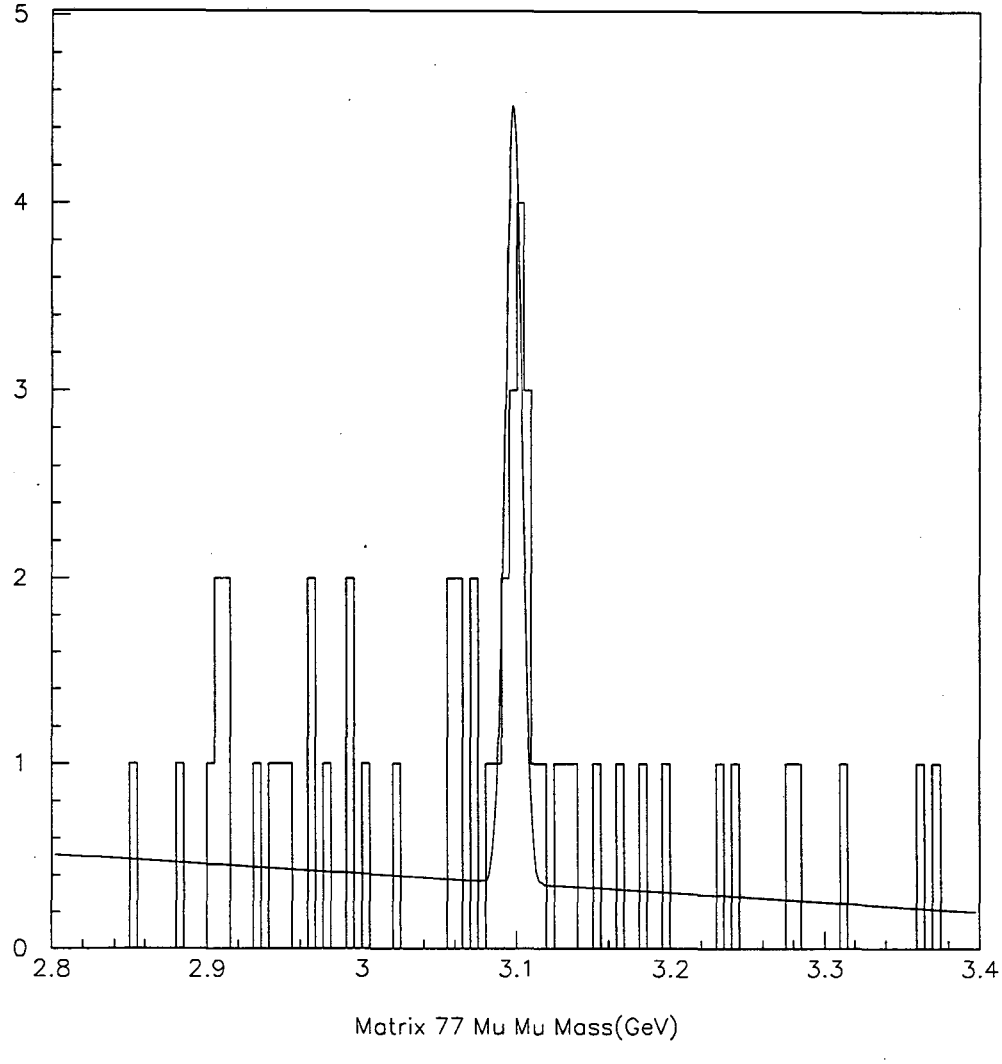

Figure 4.3: Results of the fit of a single fixed width Gaussian and a linear background to the dimuon invariant mass spectrum from run period 2. (Units are in GeV.)

The systematic errors were obtained by varying the mean and sigma of the Gaussian by the errors determined from the fit to the Monte Carlo spectrum. Also included in the systematics were the variations in the event yield obtained by allowing the mean of the Gaussian to float in the maximum likelihood fit.

4.1.2 Dihadron Events

For the dihadron events, either one Gaussian or two Gaussians were used to characterize the predicted line shapes of the signals. One Gaussian was used for the KK, pp, and $\pi\pi$ final states while two Gaussians were used for the $K\pi$, Kp, and $p\pi$ final state. The use of two Gaussians in the latter cases was due to the inability to distinguish among K, π, and p particles, resulting in the need to try both particle assignments (e.g., Kp and pK) for each event. The first Gaussian corresponded to the invariant mass spectrum where the hadrons were correctly identified. The second Gaussian corresponded to the spectrum with the incorrect mass assignments. As with the dimuon case, the Gaussians were obtained from a maximum likelihood fit to the invariant mass spectra generated by the Monte Carlo. Figures 4.4, 4.5, and 4.6 show the results of the fits and Table 4.2 tabulates the parameters of the Gaussians. The column labeled "Relative Scale" gives the relative ratio of the Gaussians in the cases where two Gaussians were required. The small sigma and high mean for the $B_d \to pp$ distributions are the indirect results of cuts on the invariant mass of the accepted events. (For more information see section 3.2.2.) For the B_s events, the invariant mass of the B_s meson was taken to be 5.375 GeV which is 6 MeV higher than the current world average of 5.369 GeV [64]. To accommodate this fact, the means of the Gaussians for the B_s were shifted down by 6 MeV before being fit to the experimental data.

In the process of extracting the signal shapes from the Monte Carlo, an aliasing problem due to particle mis-identification was revealed. This problem was most severe in the $B_d \to \pi\pi$ and $B_s \to KK$ decays. If the kaons in $B_s \to KK$ events were identified as pions, the events would be indistinguishable from $B_d \to \pi\pi$ events. The converse was also true. This aliasing is shown in Figure 4.7. The solid line in the plot shows the invariant mass spectrum of correctly reconstructed, Monte Carlo generated $B_d \to \pi\pi$ events. The dotted line in the plot shows the invariant mass spectrum of Monte Carlo generated $B_s \to KK$ events reconstructed as $B_s \to \pi\pi$ events. Clearly, the spectra are indistinguishable. As a result, only a weighted sum of the branching ratios for $B_d \to \pi^+\pi^-$ and $B_s \to K^+K^-$ could

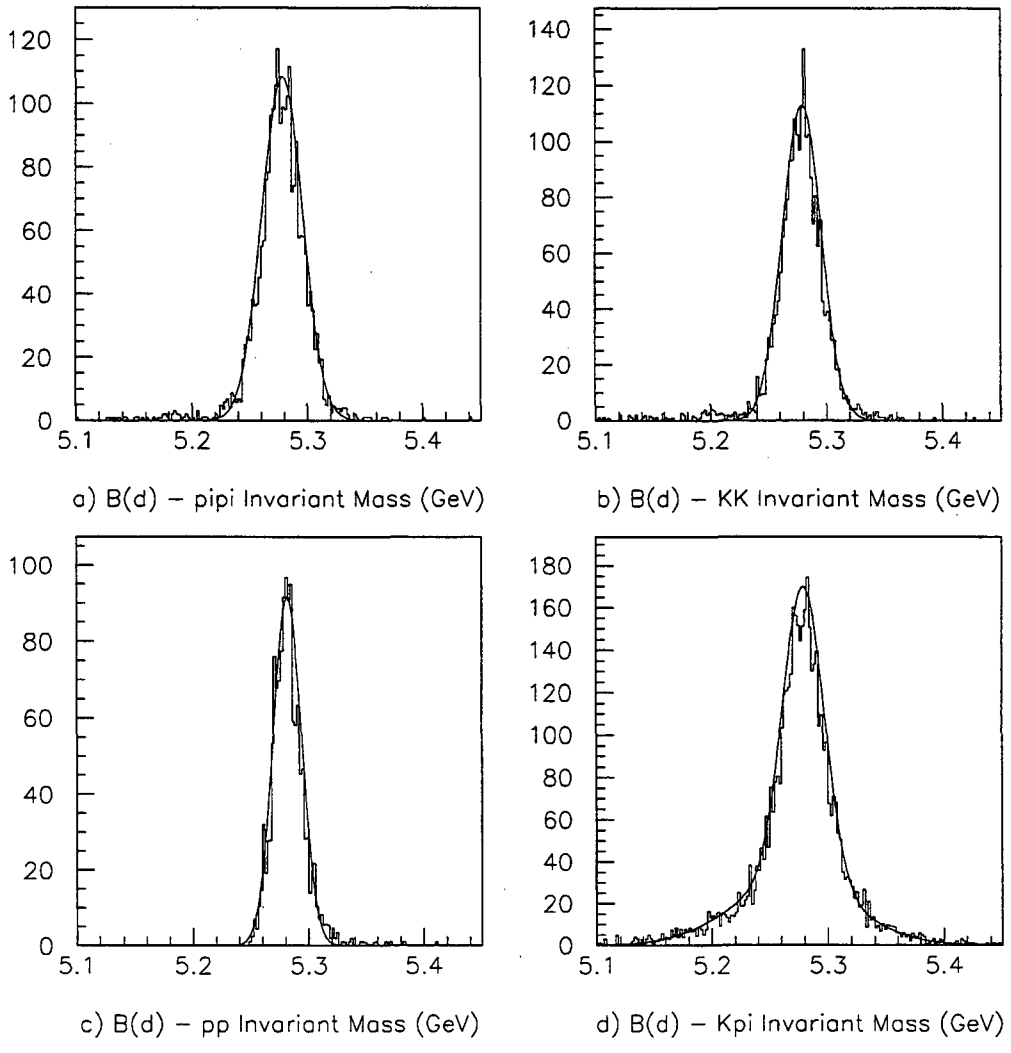

Figure 4.4: Results of the fit to the Monte Carlo generated B_d dihadron invariant mass spectra. (Units are in GeV.)

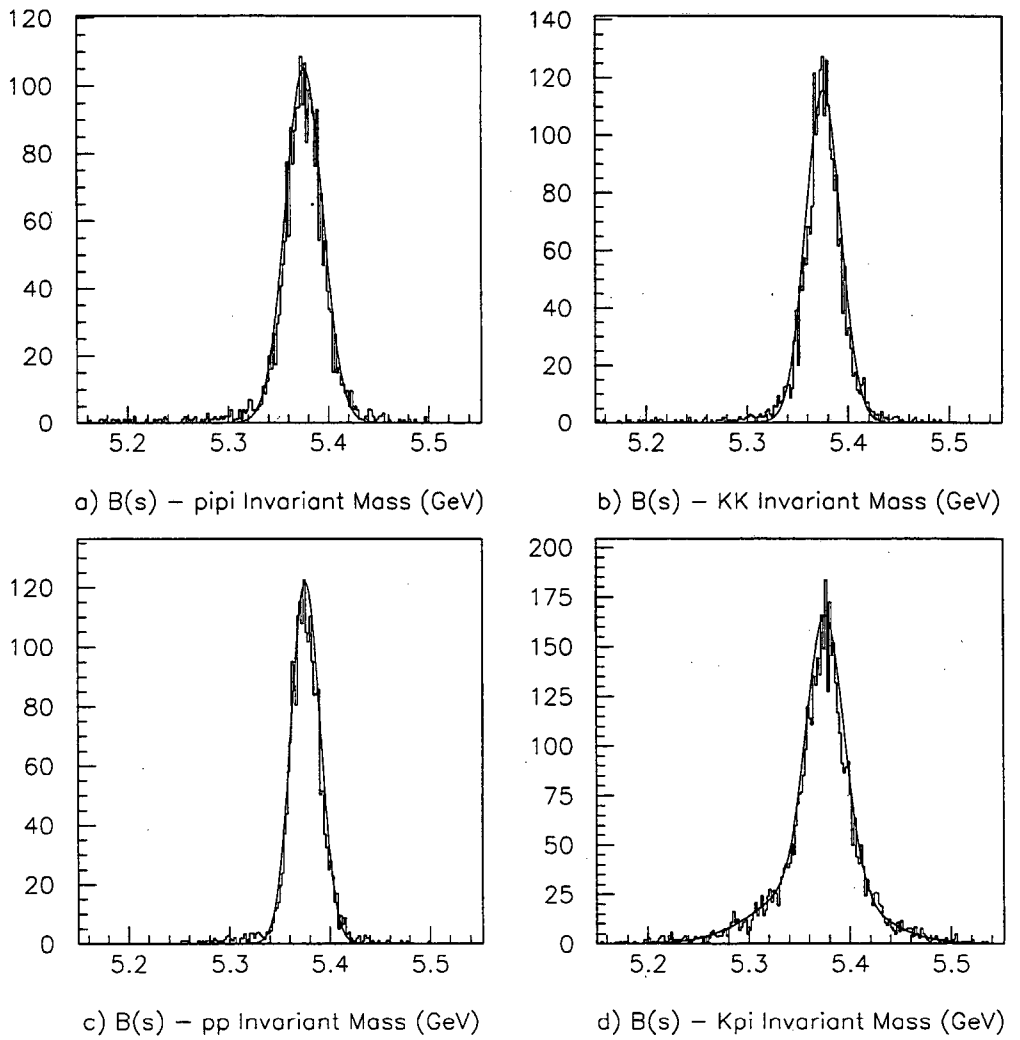

Figure 4.5: Results of the fit to the Monte Carlo generated B_s dihadron invariant mass spectra. (Units are in GeV.)

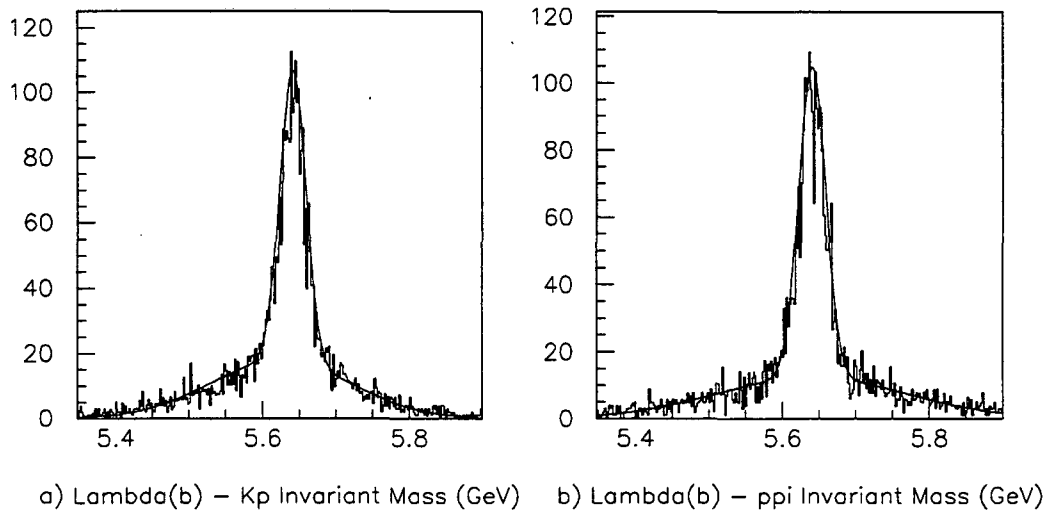

Figure 4.6: Results of the fit to the Monte Carlo generated Λ_b dihadron invariant mass spectra. (Units are in GeV.)

Decay Mode	Mean	Standard Deviation	Relative Scale
$B_d \to \pi^+\pi^-$	5.279	0.0176	–
$B_d \to K^+K^-$	5.279	0.0165	–
$B_d \to p\bar{p}$	5.282	0.0122	–
$B_d \to K^+\pi^-$	5.279	0.0178	1.0
*	5.269	0.0513	0.61
$B_s \to \pi^+\pi^-$	5.376	0.0186	–
$B_s \to K^+K^-$	5.376	0.0172	–
$B_s \to p\bar{p}$	5.376	0.0144	–
$B_s \to K^-\pi^+$	5.377	0.0183	1.0
*	5.365	0.0521	0.63
$\Lambda_b \to pK^-$	5.641	0.0176	1.0
*	5.625	0.095	1.085
$\Lambda_b \to p\pi^-$	5.641	0.0184	1.0
*	5.640	0.128	0.935

Table 4.2: Results of the maximum likelihood fits to the Monte Carlo generated meson-meson, meson-baryon and baryon-anti-baryon invariant mass spectra. The asterisk (*) label the fits to the spectra where the two hadrons were incorrectly identified.

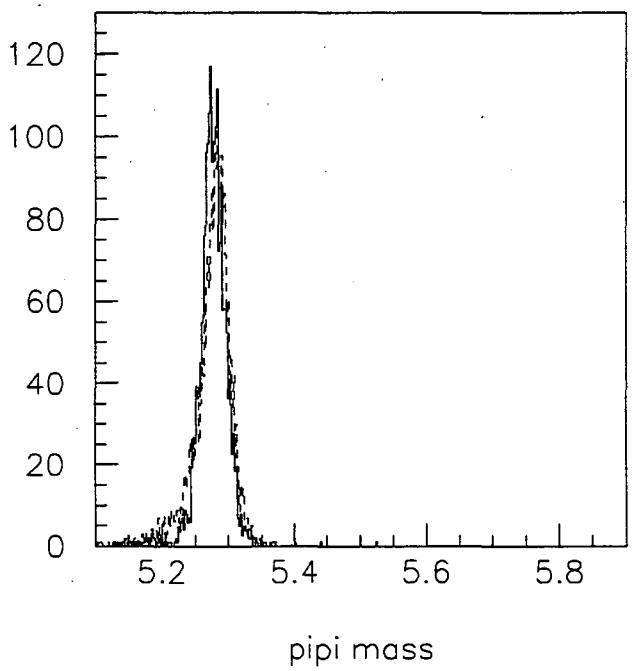

Figure 4.7: Invariant mass plot of Monte Carlo generated $B_d \to \pi\pi$ decays (solid line) that were correctly identified and $B_s \to KK$ decays that were mis-identified as $B_d \to \pi\pi$ decays (dotted line). (Units are in GeV.)

be determined. A slight modification of the procedure used to derive equation 4.4 yielded the following formula for placing a limit on the weighted sum of the ratio of the branching ratios:

$$\frac{\mathrm{BR}_1 f_1}{\mathrm{BR}_{ref}} + r_{sf}\frac{\mathrm{BR}_2 f_2}{\mathrm{BR}_{ref}} = \frac{N_1(1)+N_1(2)+N_2(1)+N_2(2)}{(\alpha_1(1)\times N_{ref}(1)+\alpha_1(2)\times N_{ref}(2))} \tag{4.5}$$

where:

$$r_{sf} = \frac{(\alpha_2(1)\times N_{ref}(1)+\alpha_2(2)\times N_{ref}(2))}{(\alpha_1(1)\times N_{ref}(1)+\alpha_1(2)\times N_{ref}(2))} \tag{4.6}$$

The subscript 1 corresponds to the $B_s \to K^+K^-$ process and the subscript 2 corresponds to the $B_d \to \pi^+\pi^-$ process. Equation 4.5 can be modified further to give the weighted sum of the branching ratios BR_1 and BR_2 as follows:

$$\mathrm{BR}_1 + r_s\mathrm{BR}_2 = \frac{1}{f_1}\times\frac{N_1(1)+N_1(2)+N_2(1)+N_2(2)}{(\alpha_1(1)\times N_{ref}(1)+\alpha_1(2)\times N_{ref}(2))}\times \mathrm{BR}_{ref} \tag{4.7}$$

where:

$$r_s = \frac{f_2}{f_1}\times\frac{(\alpha_2(1)\times N_{ref}(1)+\alpha_2(2)\times N_{ref}(2))}{(\alpha_1(1)\times N_{ref}(1)+\alpha_1(2)\times N_{ref}(2))} \tag{4.8}$$

Looking at the efficiencies that comprise the α's shown in Tables 3.9 and 3.10, it is apparent that r_{sf} should equal one. In addition, the systematic uncertainty in r_{sf} should be extremely small, since the kinematics of $B_d \to \pi\pi$ should be similar to $B_s \to KK$. Therefore, to simplify the analysis, we assume that $r_{sf} = 1$. This in turn leads to the result that $r_s = f_2/f_1$.

For the other decay channels, the mis-identified spectra are sufficiently different in width and mean from correctly identified signal events that there is no aliasing problem. However, most of the mis-identified spectra do fall within the 5.0 GeV – 6.0 GeV mass interval. In order to correctly count events, the net result is that the dihadron invariant mass spectra needed to be fit with the expected signal shape, the background shape and the shapes of the mis-identified spectra. Unfortunately, utilizing this technique resulted in a divergence. Therefore, a much simpler procedure was used which assumed that the different dihadron invariant mass spectra were properly described by the signal shapes and a "generic" background distribution.

For each dihadron invariant mass spectrum, a simultaneous fit was made to the signal(s) and background. However, in contrast to the dimuon case, an exponential distribution of the form given below:

$$\mathrm{backgroundcount}(Mass) = e^{(A+B\times Mass)} \tag{4.9}$$

Mass Spectrum	Lower Limit (GeV)	Upper Limit (GeV)
$\pi\pi/KK/K\pi$	5.06	6.0
pp	5.245	5.5
$p\pi/Kp$	5.4	6.0

Table 4.3: A table of the mass range over which the maximum likelihood fit was made for the dihadron events.

where A and B are parameters, was used for all the background in each spectrum except the pp mass spectrum. The latter case required special consideration because of the indirect effects of the mass cuts that were applied to the dihadron data sample. The presence of these mass cuts also resulted in a need to restrict the mass region over which the maximum likelihood fit was made. As can be seen from the invariant mass spectra shown in Figure 4.8, the low end of some of the spectra show a "turn-on" effect. In the case of the pp spectrum, the turn-on region overlaps the signal region for the $B_d \to pp$ decay channel. For the cases where the mass cuts did not directly affect the signal region, there was still a need to remove the regions near the cuts from the fits in order to minimize their effects on the fit to the background. Table 4.3 gives the range over which the maximum likelihood fit was made for each invariant mass spectrum.

For the pp mass spectrum, three different background shapes were used in the extraction of the events. The first method utilized a curve obtained from a smoothed version of a pp mass spectrum obtained with loose cuts. A multiquadratic algorithm [65] was used to smooth the pp mass spectrum. A cubic spline interpolation algorithm [66] was then used to obtain values for the background from a histogram of the smoothed mass spectrum. Figures 4.9 and 4.10 show the fit of this fixed shape background distribution to the pp invariant mass spectra with successively tighter vertex cuts. The other two background distributions were polynomial fits to pp invariant mass plot generated with loose vertex cuts. With these looser cuts, the majority of the events should be background events. The polynomials that were used were 5^{th} degree polynomials.

The results of the maximum likelihood fit for each invariant mass spectrum extracted from the collected data are shown in Figures 4.11, 4.12, 4.13, 4.14, 4.15, 4.16, and 4.17. The number of events determined by these fits are tabulated in Tables 4.4 and 4.5. For the Kp, $K\pi$, and $p\pi$ final states, the fit results in a double counting of the actual

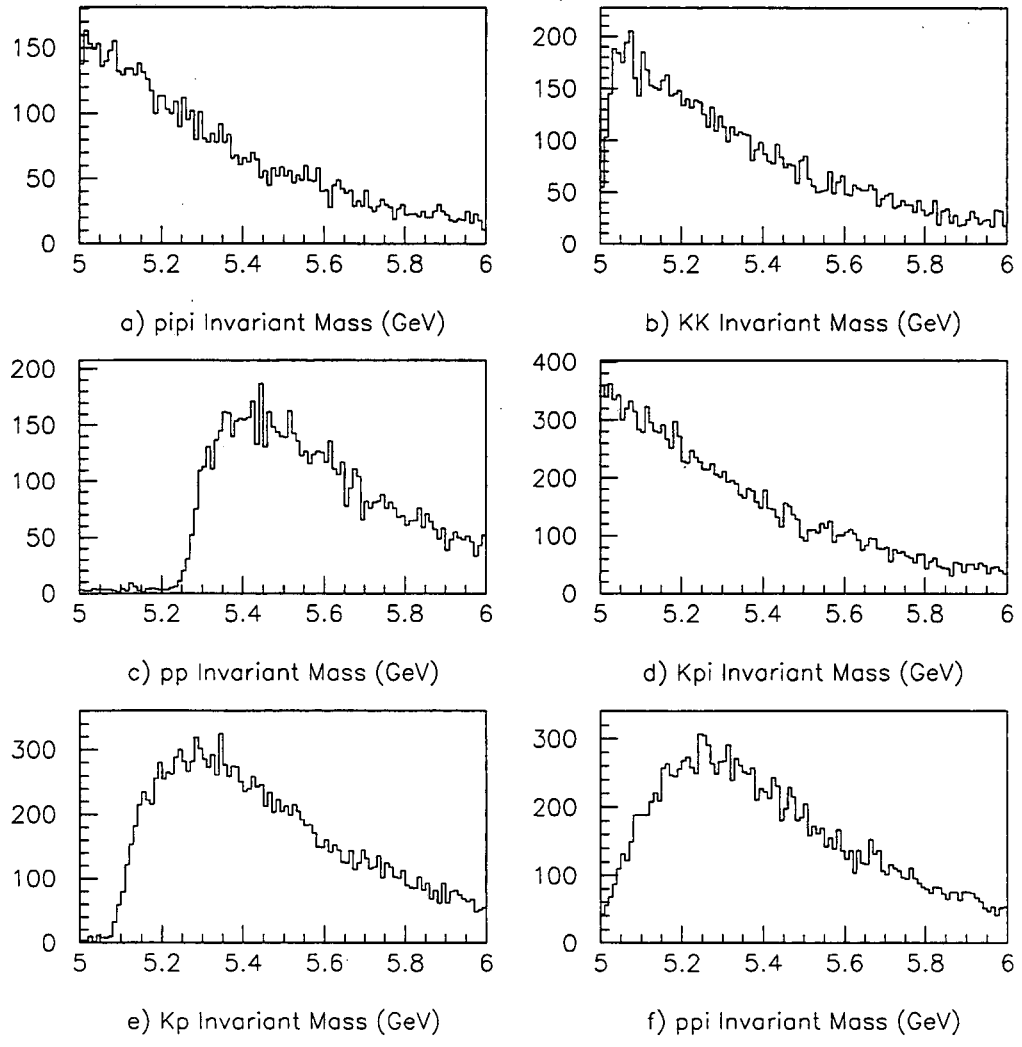

Figure 4.8: Plots of the different dihadron invariant mass spectra with loose cuts. (Units are in GeV.)

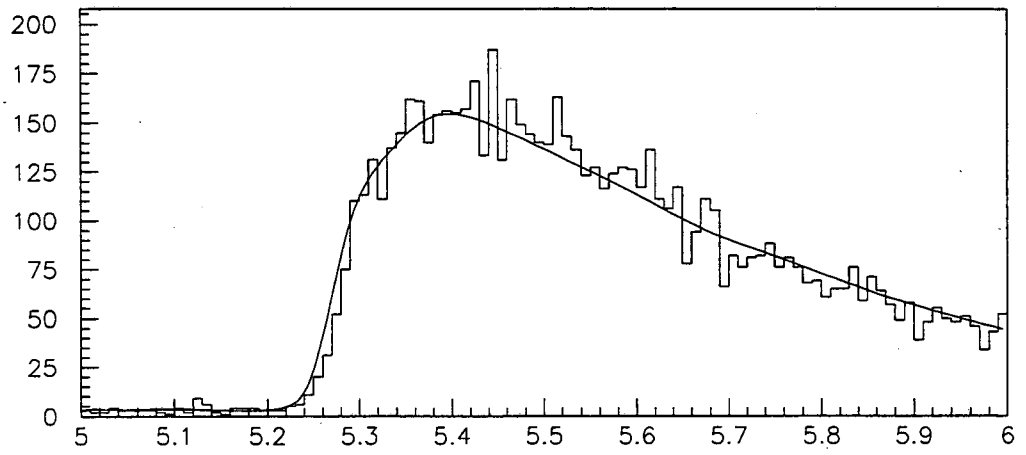

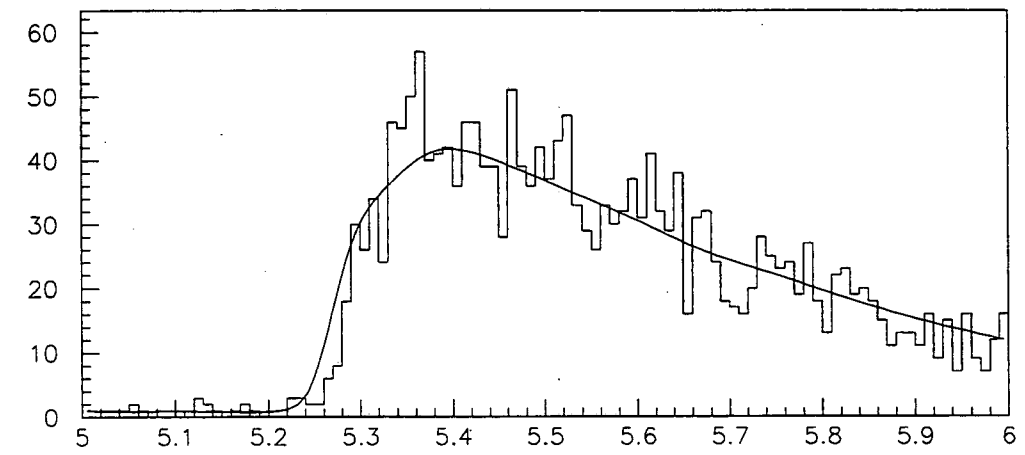

Figure 4.9: Results of the fits of the background shape obtained from the smoothed pp invariant mass spectrum to pp invariant mass spectra obtained after successively tighter vertex cuts. (Units are in GeV.)

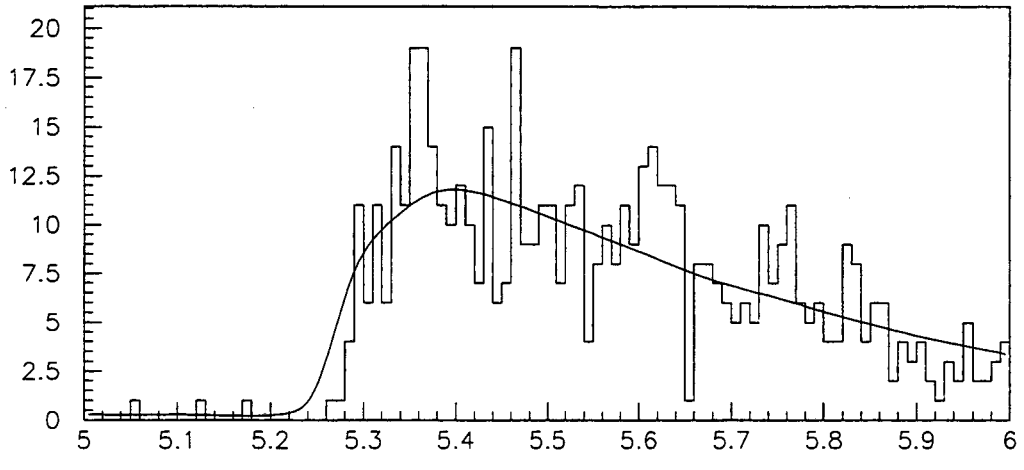

Figure 4.10: Results of the fits of the background shape obtained from the smoothed pp invariant mass spectrum to pp invariant mass spectra obtained after successively tighter vertex cuts. (Units are in GeV.)

Mode	Number of Events			
	B_d		B_s	
	Signal	(statistical)	Signal	(statistical)
$\pi^+\pi^-$	2.6	$(+4.1\ -3.4)$	-2.5	$(+3.0\ -2.3)$
K^+K^-	-1.0	$(+4.4\ -3.7)$	-3.8	$(+3.4\ -2.7)$
$p\bar{p}$	2.0	$(+4.2\ -3.2)$	13.0	$(+7.2\ -6.2)$
$K^+\pi^-$ (real)*	-4.4	$(+3.4\ -3.0)$	-1.4	$(+3.1\ -2.7)$

Table 4.4: Results of the maximum likelihood fits to the various meson–meson and baryon–anti-baryon invariant mass spectra. (* See the text for more information on these entries.)

Mode	Λ_b Number of Events	
	Signal	(statistical)
pK (real)*	1.0	$(+4.5\ -4.0)$
$p\pi$ (real)*	6.0	$(+5.0\ -5.0)$

Table 4.5: Results of the maximum likelihood fits to the various meson–baryon invariant mass spectra. (* See the text for more information on these entries.)

number of events. Table 4.6 contains the scale factors used to convert the fit results to the number of events shown in Tables 4.4 and 4.5. The major systematic error in the number of events is the result of possible variations in the actual mean of the signal distribution. This was handled by varying the position (mean) of each of the signal Gaussians by one standard deviation in the b-hadron masses given in the 1996 Review of Particle Physics [64] and in a recent paper by the ALEPH collaboration [67]. This corresponded to a variation of 1.8 MeV for the B_d meson, 2.0 MeV for the B_s meson and 21 MeV for the Λ_b baryon. Instead of quoting a systematic error, the fits with the largest event counts are shown in Tables 4.4 and 4.5.

4.2 Consolidation of Results

With the efficiencies and event counts along with their errors given in Tables 3.8, 3.9, 3.10, 3.11, Tables 3.21, 3.22, 3.23, 3.24, and Tables 4.2, 4.3, 4.4, and 4.5, the ratio of the branching ratios can finally be determined. For convenience, the relevant numbers are summarized in Tables 4.7, 4.8, 4.9, and 4.10. In the process of consolidating the results,

Decay	Conversion Factor
$B_d \to K\pi$	0.49
$B_s \to K\pi$	0.49
$\Lambda_b \to Kp$	0.50
$\Lambda_b \to p\pi$	0.51

Table 4.6: A table of the factors used to convert from the effective number of events obtained from the fits to the "double counted" spectra to the actual number of events.

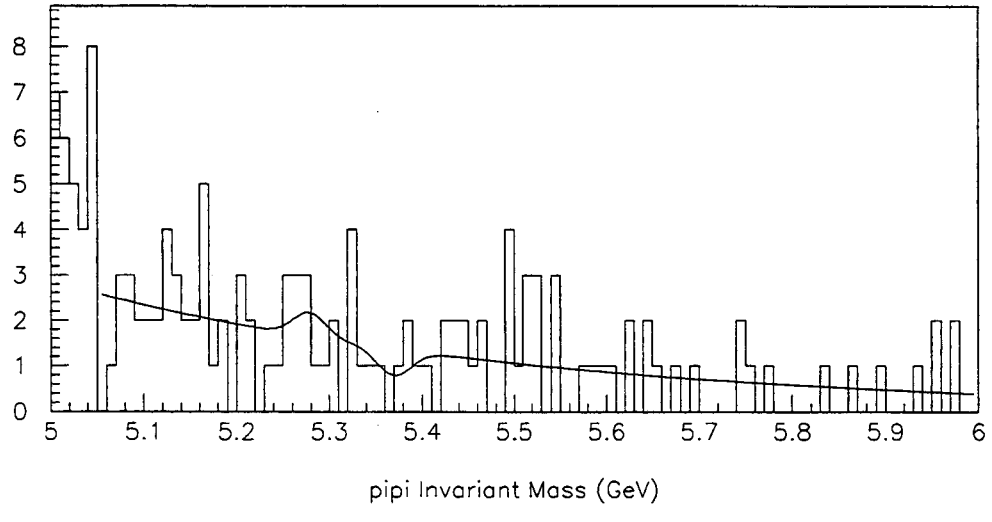

Figure 4.11: Results of the maximum likelihood fit to the invariant mass spectrum of the dihadron events assuming two pions. (Units are in GeV.)

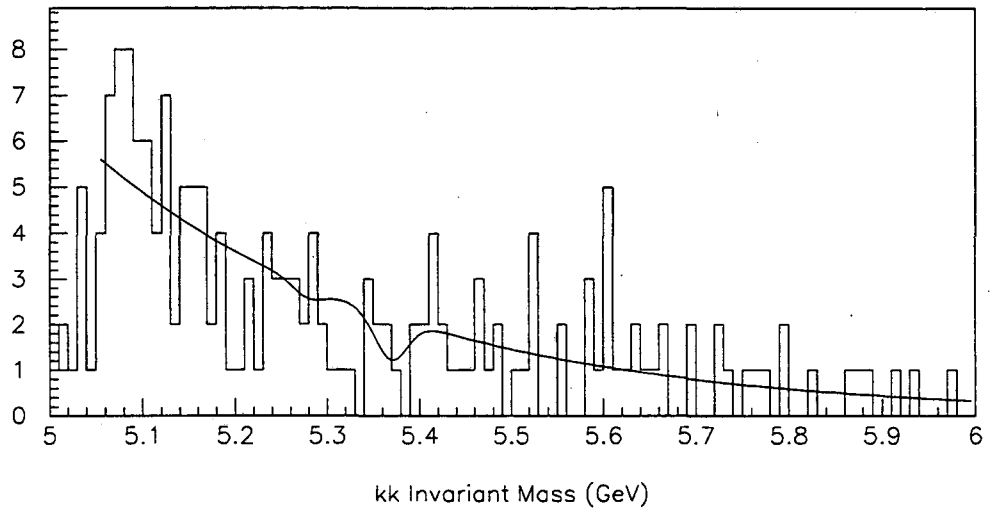

Figure 4.12: Results of the maximum likelihood fit to the invariant mass spectrum of the dihadron events assuming two kaons. (Units are in GeV.)

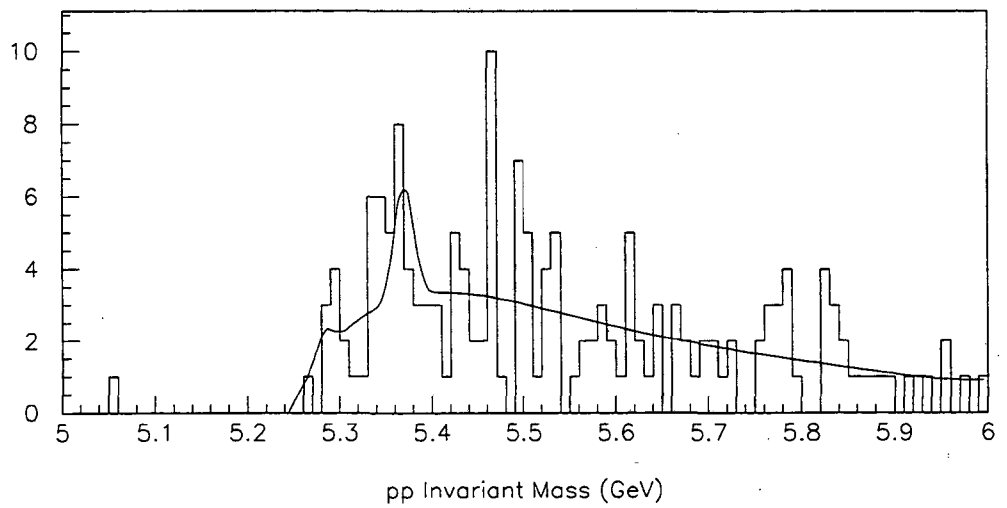

Figure 4.13: Results of the maximum likelihood fit to the invariant mass spectrum of the dihadron events assuming two protons for the B_d decay. (Units are in GeV.)

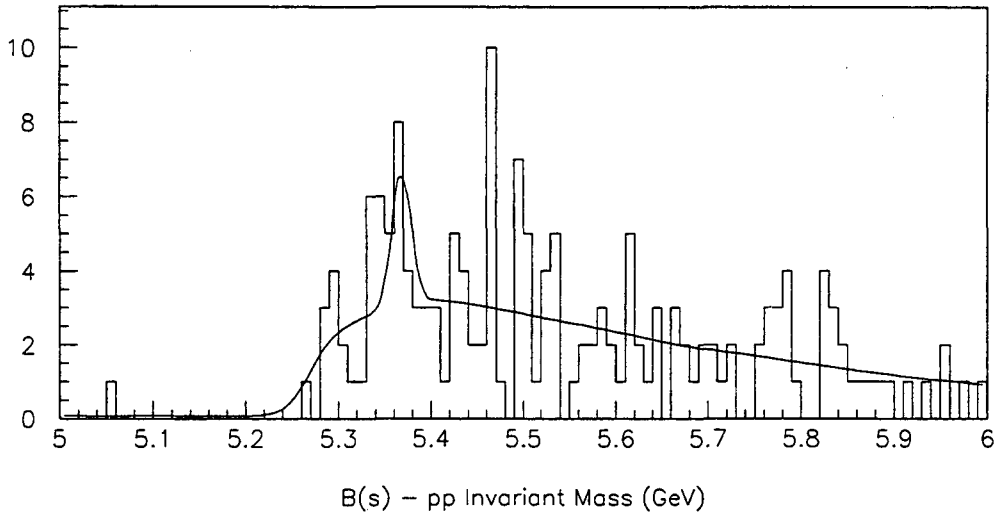

Figure 4.14: Results of the maximum likelihood fit to the invariant mass spectrum of the dihadron events assuming two protons for the B_s decay. (Units are in GeV.)

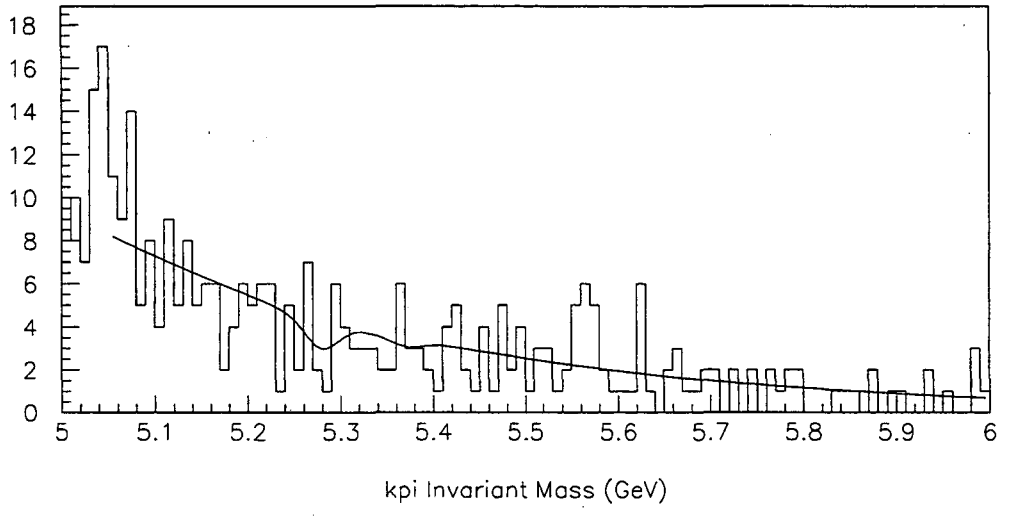

Figure 4.15: Results of the maximum likelihood fit to the invariant mass spectrum of the dihadron events assuming one pion and one kaon in the event. (Units are in GeV.)

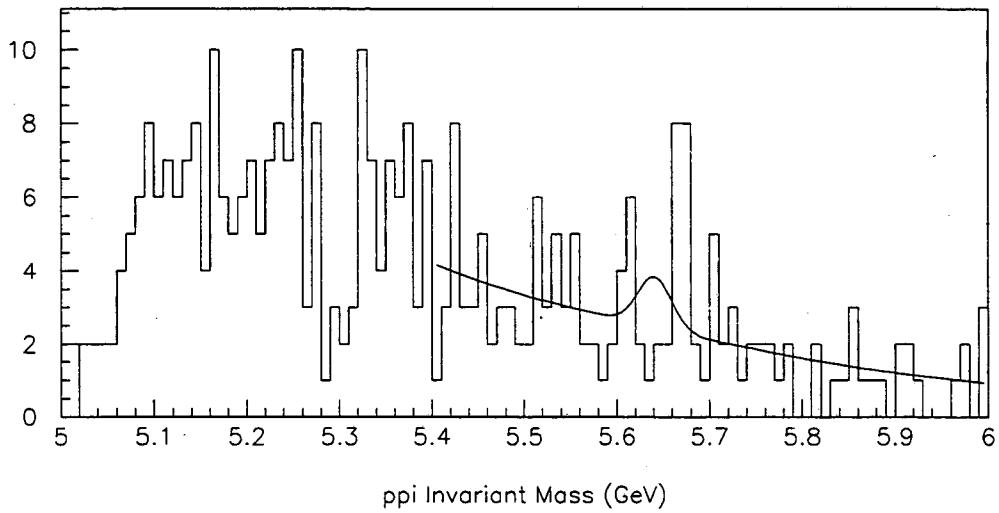

Figure 4.16: Results of the maximum likelihood fit to the invariant mass spectrum of the dihadron events assuming one pion and one proton. (Units are in GeV.)

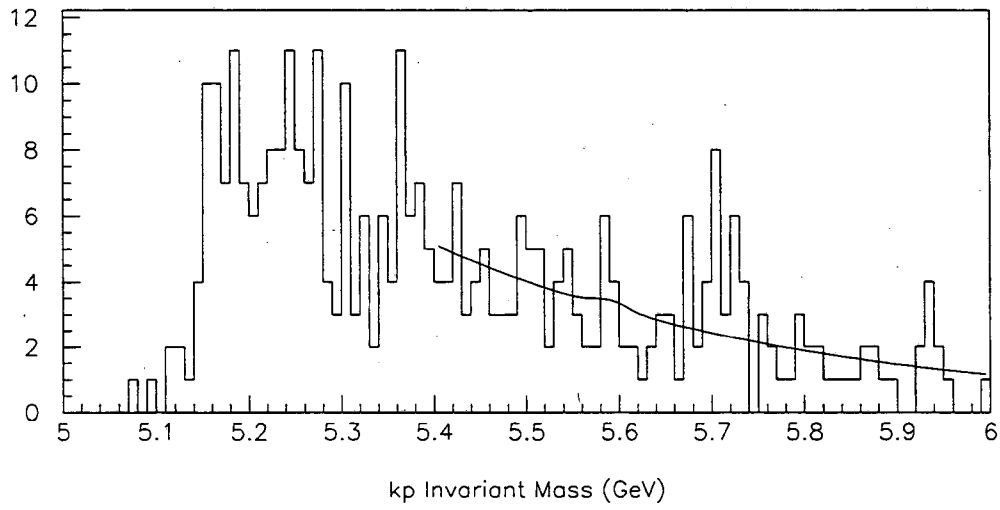

Figure 4.17: Results of the maximum likelihood fit to the invariant mass spectrum of the dihadron events assuming one kaon and one proton. (Units are in GeV.)

$b \to J/\psi + X \to \mu\mu + X$		
Event Count		
Run #1	Run #2	Efficiency
8.1 ± 3.3	11.4 ± 4.1	$(0.0827 \pm 0.011)\%$

Table 4.7: Consolidation of results for $b \to J/\psi + X \to \mu\mu + X$.

	$B_d \to h^+h^-$		
		Efficiency	
Mode	Event Count	Run #1	Run #2
$\pi^+\pi^-$	2.6 ± 4.1	$(0.064 \pm 0.010)\%$	$(0.039 \pm 0.007)\%$
K^+K^-	-1.0 ± 4.4	$(0.068 \pm 0.011)\%$	$(0.045 \pm 0.008)\%$
$p\bar{p}$	2.0 ± 4.2	$(0.049 \pm 0.009)\%$	$(0.034 \pm 0.007)\%$
$K^+\pi^-$	-4.4 ± 3.4	$(0.065 \pm 0.011)\%$	$(0.040 \pm 0.007)\%$

Table 4.8: Consolidation of results for B_d.

asymmetric errors were "symmetrized" by taking the larger of the two errors.

4.3 Calculation of Upper Limits

To reiterate, the primary goal of the analysis was a measurement of the branching ratios of neutral b-hadrons to two charmless hadrons. The results can be presented in different forms, each with different degrees of model dependence and each with different degrees of usefulness to different individuals. For this reason, the results of the analysis are presented in two ways.

	$B_s \to h^+h^-$		
		Efficiency	
Mode	Event Count	Run #1	Run #2
$\pi^+\pi^-$	-2.5 ± 3.0	$(0.062 \pm 0.011)\%$	$(0.036 \pm 0.006)\%$
K^+K^-	-3.8 ± 3.4	$(0.066 \pm 0.011)\%$	$(0.039 \pm 0.007)\%$
$p\bar{p}$	13.0 ± 7.2	$(0.079 \pm 0.015)\%$	$(0.052 \pm 0.011)\%$
$K^+\pi^-$	-1.4 ± 3.1	$(0.061 \pm 0.010)\%$	$(0.036 \pm 0.006)\%$

Table 4.9: Consolidation of results for B_s.

	$\Lambda_b \to h^+h^-$		
		Efficiency	
Mode	Event Count	Run #1	Run #2
Kp	1.0 ± 4.5	$(0.054 \pm 0.009)\%$	$(0.031 \pm 0.006)\%$
$p\pi$	6.0 ± 5.0	$(0.057 \pm 0.009)\%$	$(0.033 \pm 0.006)\%$

Table 4.10: Consolidation of results for Λ_b.

The form of the result with the least model dependence gives the branching ratio of the neutral b-hadron ($\mathrm{BR}_i(b)$) to two charmless hadrons as a function of BR_{ref}, the branching ratio of the cascade decay $B \to J/\psi + X \to \mu^+\mu^- + X$, where B is any b-hadron, and f_i, the fraction of neutral b-hadrons of type i produced in proton on nucleon interactions. To calculate these upper limits at the 90% confidence limit, the following procedure was used:

1. As was stated before, all asymmetric errors were symmetrized by taking the larger of the two errors.

2. The efficiencies and the event counts in Tables 4.7, 4.8, 4.9, and 4.10 were then inserted into equation 4.4.

3. Each ratio of the branching ratios was assumed to be a random variable with a Gaussian distribution where the mean was equal to the value obtained from step 2.

4. The standard deviation of each Gaussian distribution was determined by combining the errors in the efficiencies and event counts with the assumption that the errors were uncorrelated.

5. The 90% confidence limit was obtained for each ratio of branching ratios by utilizing the "Bayesian approach" of renormalizing the probability distribution within the physical region as outlined in the Particle Data Group Review of Particle Properties [64]. In this case, the physical region is assumed to be the region where the ratio of the branching ratios is positive.

Table 4.11 gives the upper limits on the ratios at the 90% confidence level for the decay modes studied in this thesis that do not have the aliasing problem. Table 4.12 shows the

$BR_i f_i/BR_{ref}$	Upper Limit (90% CL)
$B_d^0 \to K^+K^-$	0.52
$B_d^0 \to p\bar{p}$	0.88
$B_d^0 \to K^+\pi^-$	0.34
$B_s^0 \to \pi^+\pi^-$	0.35
$B_s^0 \to p\bar{p}$	1.62
$B_s^0 \to \pi^+K^-$	0.40
$\Lambda_b \to p\pi^-$	1.32
$\Lambda_b \to pK^-$	0.84

Table 4.11: A table of the 90% confidence limits on the ratio of the branching ratios that were obtained for the unaliased modes.

	Probability Distribution	
$BR_i f_i/BR_{ref}$	Mean	Standard Deviation
$B_d^0 \to K^+K^-$	-0.078	± 0.34
$B_d^0 \to p\bar{p}$	$+0.21$	± 0.45
$B_d^0 \to K^+\pi^-$	-0.37	± 0.31
$B_s^0 \to \pi^+\pi^-$	-0.23	± 0.28
$B_s^0 \to p\bar{p}$	$+0.87$	± 0.57
$B_s^0 \to \pi^+K^-$	-0.13	± 0.29
$\Lambda_b \to p\pi^-$	$+0.59$	± 0.53
$\Lambda_b \to pK^-$	$+0.11$	± 0.47

Table 4.12: A table of the means and sigmas of the Gaussian distributions used in the calculation of the 90% confidence limits in Table 4.11.

means and standard deviations for the Gaussian distributions that served as the basis for the 90% confidence limits shown in Table 4.11.

The more model dependent form of the results utilizes the measured branching ratio (BR_{ref}) of the reference decay and the measured value of the production fractions (f_i) of the various b-hadrons. The cascade branching ratio BR_{ref} is determined from the branching ratio for the decay b-hadron $\to J/\psi + X$ and the branching ratio for the decay $J/\psi \to \mu\mu$. The current value for the b-hadron decay, obtained from the $B^{\pm}/B^0/B_s^0/b-$ baryon admixture entry in the Particle Data Group Review of Particle Physics, is $(1.16 \pm 0.10)\%$ [64]. The current value for the branching ratio of J/ψ to two muons is $(6.01 \pm 0.19)\%$. A recent result from CDF [68] gives the b-hadron production fractions shown in

Fraction	Value
f_u	$0.39 \pm 0.04 \pm 0.04$
f_d	$0.38 \pm 0.04 \pm 0.04$
f_s	$0.13 \pm 0.03 \pm 0.01$
f_{Λ_b}	0.096 ± 0.017

Table 4.13: A table of the production fractions of b-hadrons measured by the CDF collaboration.

BR_i	Upper Limit (90% CL)
$B_d^0 \to K^+K^-$	0.00095
$B_d^0 \to p\bar{p}$	0.0016
$B_d^0 \to K^+\pi^-$	0.0019
$B_s^0 \to \pi^+\pi^-$	0.0020
$B_s^0 \to p\bar{p}$	0.0090
$B_s^0 \to \pi^+K^-$	0.0022
$\Lambda_b \to p\pi^-$	0.0097
$\Lambda_b \to pK^-$	0.0061

Table 4.14: Experimental limits on the branching ratios that were obtained in this analysis for the unaliased modes.

Table 4.13. Combining these results with the values in Table 4.12 yields the upper limits for the branching ratios at the 90% confidence level, shown in Table 4.14, for the dihadron decays of the neutral b-hadrons

For the decay modes with aliasing problems, i.e., $B_d \to \pi^+\pi^-$ and $B_s \to K^+K^-$, the two weighted sums of branching ratios, corresponding to the two types of results for the unaliased modes, are shown in Table 4.15. Note that we have assumed that the coefficient r_{sf} given in equation 4.6 is equal to one with negligible uncertainty and therefore, the uncertainty in the coefficient r_s is determined by the uncertainty in the ratio of the f_i's. (See Equation 4.8.) Given this assumption, r_s is determined equal to 2.92 ± 0.83.

$B_d \to \pi^+\pi^- + B_s \to K^+K^-$	Upper Limit (90% CL)
$\frac{\mathrm{BR}_1 f_1}{\mathrm{BR}_{ref}} + \frac{\mathrm{BR}_2 f_2}{\mathrm{BR}_{ref}}$	0.35
$\mathrm{BR}_1 + r_s \mathrm{BR}_2$	0.0020

Table 4.15: Experimental limits on the branching ratios for aliased modes, where $r_s = 2.9 \pm 0.8$ and BR_1 is the branching ratio of B_s to KK and BR_2 is the branching ratio of B_d to $\pi\pi$.

Chapter 5

Conclusions

In the analysis of b-hadrons produced in proton on gold interactions, the upper limits at the 90% confidence level, shown in Table 5.1, on the branching ratios for b-hadrons into two charmless hadrons were found. These limits assume that the $B_d/B_s/\Lambda_b$ hadrons are produced in proton on nucleon interactions in the ratio $(38\pm5.7) : (13\pm3.2) : (9.6\pm1.7)$ [68] and that the branching ratio for the cascade decay b-hadron $\rightarrow J/\psi + X \rightarrow \mu^+\mu^- + X$ is $(6.97 \pm .64) \times 10^{-4}$ [64]. The limits found in this analysis are significantly higher than the upper limits obtained from b-hadrons produced in other environments, e.g. e^+e^- colliders at the $\Upsilon(4s)$-resonance and Z-resonance. As was stated in the introduction, the environment at fixed-target b-experiments, although promising because of the relatively high b-quark production rates, suffers from a low signal to noise ratio which makes the extraction of a b-decay signal extremely difficult. In contrast, at e^+e^- colliders, the signal to noise ratio is high, and hence the detection of small branching ratio decays is reduced to obtaining sufficient statistics.

As can be seen from the extraction of the b-hadron $\rightarrow J/\psi + X \rightarrow \mu^+\mu^- + X$ cascade decay from the E789 data, given a distinctive signature, in this case, the $J/\psi \rightarrow \mu^+\mu^-$ decay and a detached vertex, b-physics is possible in a fixed target environment. However, the results of the charmless dihadron b-decay search suggest that the techniques employed in this thesis are not sufficient for conducting searches for rare processes. The results of the charmless dihadron decay search indicate that the primary limitation in the extraction of an upper limit was the presence of dihadron background at the b-hadron mass. Additional statistics would have reduced the uncertainty in the branching ratio of the reference $b-$ hadron $\rightarrow J/\psi + X \rightarrow \mu^+\mu^- + X$ decay. However, without a means of

Branching Ratio	Upper Limit (90% CL)
$\mathrm{BR}(B_s \to K^+K^-) + r_s\mathrm{BR}(B_d \to \pi^+\pi^-)$	0.0020
$\mathrm{BR}(B_d^0 \to K^+K^-)$	0.00095
$\mathrm{BR}(B_d^0 \to p\bar{p})$	0.0016
$\mathrm{BR}(B_d^0 \to K^+\pi^-)$	0.0019
$\mathrm{BR}(B_s^0 \to \pi^+\pi^-)$	0.0020
$\mathrm{BR}(B_s^0 \to p\bar{p})$	0.0090
$\mathrm{BR}(B_s^0 \to \pi^+K^-)$	0.0022
$\mathrm{BR}(\Lambda_b \to p\pi^-)$	0.0097
$\mathrm{BR}(\Lambda_b \to pK^-)$	0.0061

Table 5.1: A table of the experimental limits on the branching ratios. $r_s = 2.9 \pm 0.8$ and is equal to the ratio of the production fractions for B_s and B_d mesons.

reducing the dihadron background, the additional statistics will not significantly reduce the 90% confidence limits that are achievable with the techniques used in this analysis.

Bibliography

[1] O. W. Greenberg, Physical Review Letters **13**, 598 (1964).

[2] S. L. Glashow, Nuclear Physics **22**, 579 (1961).

[3] S. Weinberg, Physical Review Letters **19**, 1264 (1967).

[4] A. Salam, (Almquist and Wiksell, Stockholm, 1968).

[5] Kobayashi and Maskawa, Progress in Theoretical Physics **49**, 652 (1973).

[6] N. Cabibbo, Physical Review Letters **10**, 531 (1963).

[7] J. H. Christenson *et al.*, Physical Review Letters **13**, 138 (1964).

[8] L. Wolfenstein, Physical Review Letters **51**, 1945 (1983).

[9] L. Montanet *et al.*, Physical Review D **50**, 1315 (1994).

[10] J. L. Rosner, in *B Decays*, 2nd ed., edited by S. Stone (World Scientific, River Edge, New Jersy, 1994).

[11] F. Abe *et al.*, Physical Review Letters **74**, 2626 (1995).

[12] A. Abachi *et al.*, Physical Review Letters **74**, 2632 (1995).

[13] A. Ali, in *B Decays*, 2nd ed., edited by S. Stone (World Scientific, River Edge, New Jersy, 1994).

[14] T. Browder *et al.*, in *B Decays*, 2nd ed., edited by S. Stone (World Scientific, River Edge, New Jersy, 1994).

[15] T. Browder *et al.*, Progress in Particle Physics **35**, 81 (1995).

[16] W. B. Atwood *et al.*, in *B Decays*, 2nd ed., edited by S. Stone (World Scientific, River Edge, New Jersy, 1994).

[17] S. Stone, in *B Decays*, 2nd ed., edited by S. Stone (World Scientific, River Edge, New Jersy, 1994).

[18] H. Schroder, in *B Decays*, 2nd ed., edited by S. Stone (World Scientific, River Edge, New Jersy, 1994).

[19] A. Deandrea *et al.*, Physics Letter B **320**, 170 (1994).

[20] N. G. Desphande *et al.*, Physical Review Letters **74**, 26 (1995).

[21] A. Buras, Preprint TUM-T31-85/95, Technische Universität Müchen, Garching, Germany (unpublished).

[22] Z. Xing, Nuovo Cimento **108A**, 1143 (1995).

[23] L. Chau, Physical Review D **43**, 2176 (1991).

[24] M. Gronau *et al.*, Physical Review D **50**, 4529 (1994).

[25] M. Bauer *et al.*, Zeitschrift für Physik C **34**, 103 (1987).

[26] A. Deandrea *et al.*, Physics Letter B **318**, 549 (1993).

[27] J. G. Körner, Zeitschrift für Physik C **43**, 165 (1989).

[28] M. Jarfi, Physical Review D **43**, 1599 (1991).

[29] G. Kaur, Physical Review D **46**, 466 (1992).

[30] H. Albrecht *et al.*, Physics Letters B **241**, 278 (1990).

[31] D. M. Asner *et al.*, Physical Review D **53**, 1039 (1996).

[32] D. Bortoletto *et al.*, Physical Review Letters **62**, 2436 (1989).

[33] R. Akers *et al.*, Physics Letters B **337**, 393 (1994).

[34] P. Abreu *et al.*, Physics Letters B **357**, 255 (1995).

[35] M. Artuso, in *B Decays*, 2nd ed., edited by S. Stone (World Scientific, River Edge, New Jersy, 1994).

[36] P. Nason *et al.*, Nuclear Physical B **303**, 607 (1988).

[37] L. Montanet *et al.*, Physical Review D **50**, (1994), 1995 off-year partial update for the 1996 edition available on the PDG WWW pages (URL: http://pdg.lbl.gov/).

[38] Y. Chen, Ph.D. thesis, National Cheng Kung University, Tainan, Taiwan, 1993.

[39] G. Moreno *et al.*, Physical Review D **43**, 2815 (1991).

[40] M. S. Kowitt, Ph.D. thesis, University of California, Berkeley, CA, 1992.

[41] T. Yoshida, Ph.D. thesis, Kyoto University, 1986.

[42] G. M. López, Ph.D. thesis, Centro De Investigacion Y de Estudios Avanzados DEL I.P.N., Mexico, 1989.

[43] M. J. Leitch *et al.*, Physical Review Letters **72**, 2542 (1994).

[44] A. Peisert, Ph.D. thesis, University of Geneve, 1982.

[45] H. Glass *et al.*, IEEE Trans. Nucl. Sci. **NS-30**, 30 (1983).

[46] M. Adams *et al.*, Nucl. Instr. and Methods **217**, 237 (1983).

[47] J. A. Crittendon *et al.*, Physical Review D **34**, 2586 (1986).

[48] L. Montanet *et al.*, Physical Review D **50**, 1336 (1994).

[49] L. Montanet *et al.*, Physical Review D **50**, 1242 (1994).

[50] D. M. Jansen *et al.*, Physical Review Letters **74**, 3118 (1995).

[51] H. Glass, Ph.D. thesis, State University of New York, Stony Brook, New York, 1985.

[52] D. M. Alde *et al.*, Physical Review Letters **66**, 133 (1991).

[53] D. M. Alde *et al.*, Physical Review Letters **66**, 2285 (1991).

[54] P. B. Straub, Ph.D. thesis, University of Washington, 1990.

[55] A. D. Martin *et al.*, Physical Review D **50**, 6734 (1994).

[56] L. Mangano *et al.*, Nuclear Physical B **405**, 507 (1993).

[57] P. Nason *et al.*, Nuclear Physical B **327**, 49 (1989).

[58] C. Peterson *et al.*, Physical Review D **27**, 105 (1983).

[59] J. Chrin, Zeitschrift für Physik C **36**, 165 (1987).

[60] D. Decamp *et al.*, Physics Letters B **244**, 551 (1990).

[61] A. D. Martin *et al.*, Physics Letters B **306**, 145 (1993).

[62] M. Glück *et al.*, Zeitschrift für Physik C **67**, 433 (1995).

[63] T. Sjöstrand, International Journal of Modern Physics A **3**, 751 (1988).

[64] R. Barnett *et al.*, Physical Review D **54**, 1 (1996).

[65] M. Goossens *et al.*, Technical Report No. Q121, CERN (unpublished).

[66] W. H. Press *et al.*, 2nd ed. (Cambridge University Press, Cambridge, UK, 1992).

[67] D. Buskulic *et al.*, Preprint CERN-PPE/96-28, CERN, Genèva (unpublished).

[68] F. Abe *et al.*, Preprint FERMILAB-Pub-96/119-E, Fermilab, Batavia, Illinois (unpublished).

Appendix A

Calorimeter Calibration

In order to determine the efficiency of the hadronic trigger (E_H) the calorimeter needed to be calibrated. In order to understand the calibration process, a more detailed understanding of the components of the calorimeter and its readout is required.

Figure A.1 is a schematic overview of the calorimeter and its readout system. As was stated in section 2.4.8, the energy of a shower produced by a particle incident on the calorimeter was "sampled", or measured at discrete points along the Z axis by planes of scintillators. The output signal from each scintillator (of which there are 148 in total) was a flux of photons that was roughly proportional to the number of particles passing through the scintillator. This photon flux was then amplified by a photomultiplier tube. The output from the photomultiplier tube was passed through an integrator (charge integration). The output of the integrator was then digitized by an analog to digital converter (ADC). The output of the ADC was then passed through a digital zero suppression filter before being sent to the data acquisition system (DAQ) for storage onto magnetic tape. Finally, an analog sum of the photomultiplier tube outputs was made to form the E_H trigger. The output of the analog sum was also sent through an integrator and an ADC and sent to the DAQ for storage onto tape.

One peculiar aspect of the ADC's used in the calorimeter readout was that they were non-linear. More specifically, the output of the i^{th} ADC, D_i, was related to the input, S_i of the ADC via the quadratic equation given in equation A.1.

$$S_i = a_i * D_i^2 + b_i * D_i + c_i \tag{A.1}$$

As should be evident from the above equation and the design of the calorimeter, a measure-

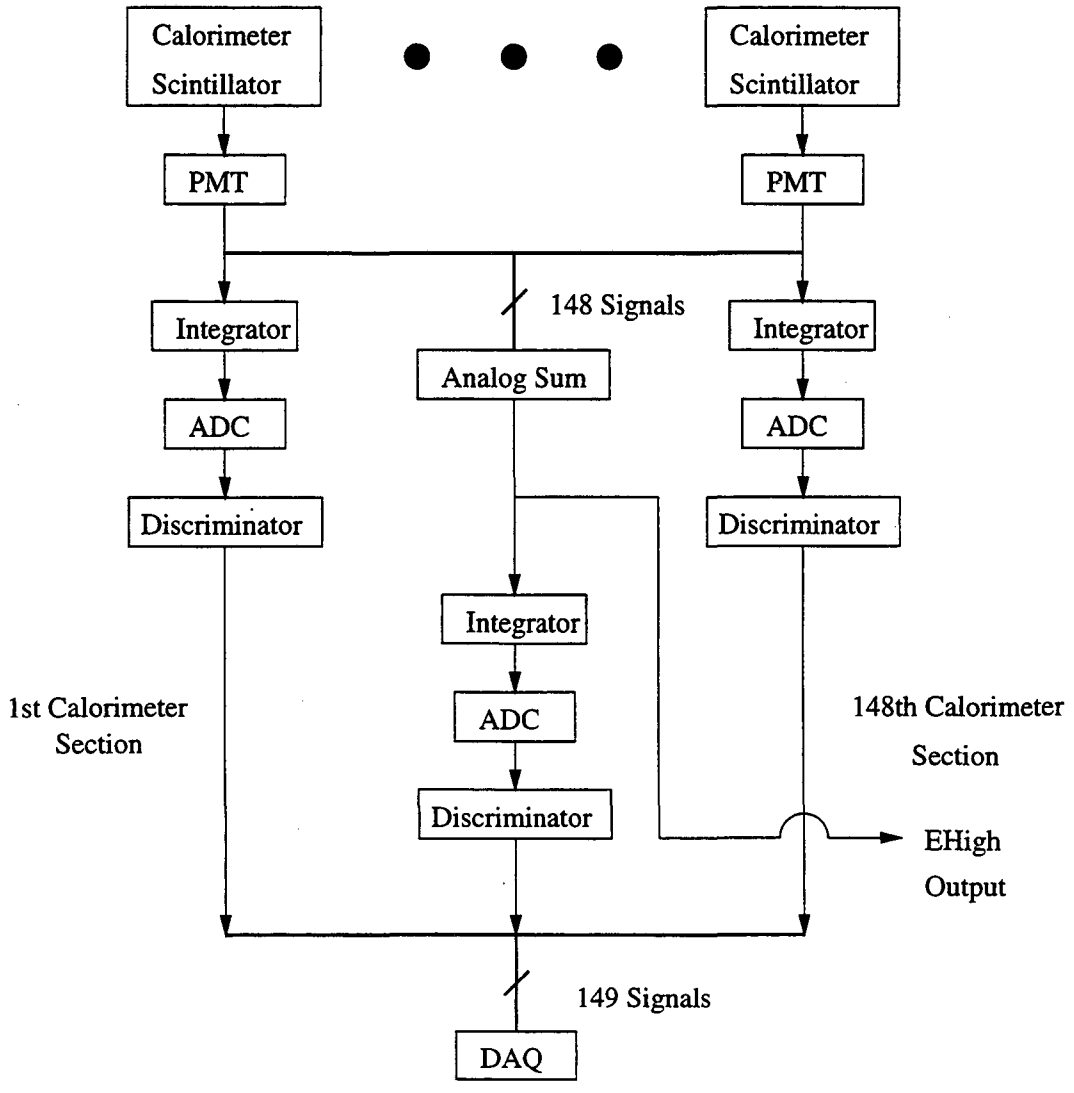

Figure A.1: A schematic of the signal flow from the calorimeter to the data acquisition equipment.

ment of the energy of an incident particle with the calorimeter was dependent on a large number of parameters. In previous experiments that utilized the E789 calorimeter, techniques were used to determine the value of a large number of these parameters. The most important of these techniques was the use of an electronic pulsers to get an absolute determination of the coefficients for the ADC's (a_i,b_i,c_i). Another was the use of optical fibers and nitrogen lasers to monitor the response of the PMT/ADC chain. Unfortunately, these techniques were not used in E789. As a result of this decision, the process of calibrating the calorimeter was made much more difficult.

The procedure for determining the values of all the parameters in the calorimeter calibration was to compare the response of the calorimeter to particles of known momentum (measured with the analysis magnet). Parameter values were chosen to minimize the difference between the measured momentum of the particle and the output of the calorimeter. In order to make this statement more exact, an exposition of the parameters needs to be made.

The list of available tuning parameters can be determined by finding the exact equation that governs the input/output relationship of the calorimeter. This equation can be found by looking at the input/output relationship between the components of the calorimeter. The starting point is the input/output relationship of the ADC's given in equation A.1. The input to the ADC was connected to the output of the PMT via an integrator, therefore the relationship between the PMT output, I_i, and the ADC input, S_i, should be linear with a constant offset $L0_i$. This relationship is shown in equation A.2.

$$S_i = \alpha_i * I_i + L0_i \tag{A.2}$$

The constant offset term can be attributed to such factors as a non-zero output from the integrator.

It should be immediately apparent that the scale factor can be absorbed into a_i, b_i and c_i. This leads to equation A.3 relating the PMT output to the ADC output.

$$I_i = a_i * D_i^2 + b_i * D_i + c_i - L0_i \tag{A.3}$$

Next, the PMT output, I_i, was assumed to be linearly related to the photon flux, Φ_i, incident at the input to the PMT. Note that in the linear relationship shown in equation A.4, provisions have been made for a constant DC signal, $I0_i$.

$$I_i = \beta_i * \Phi_i + I0_i \tag{A.4}$$

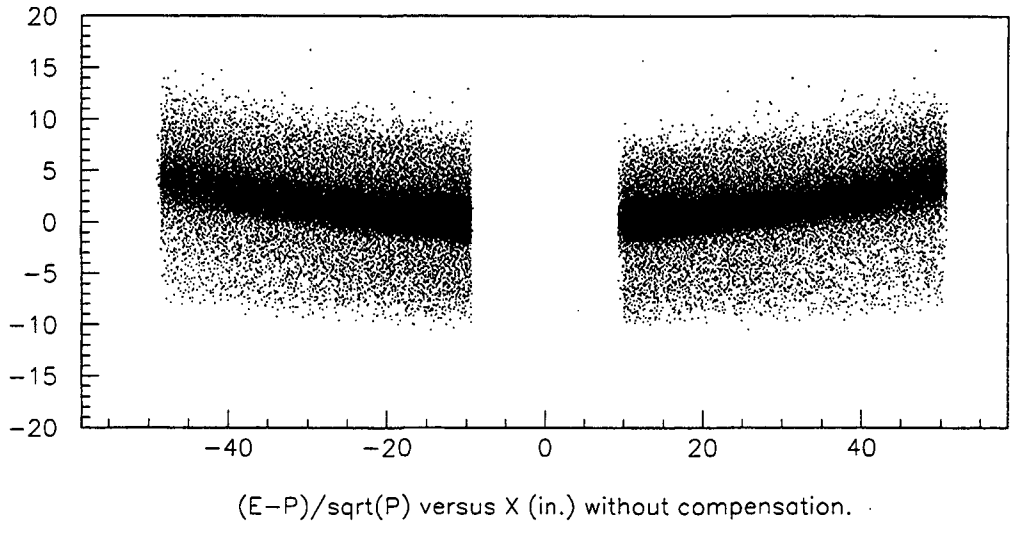

Figure A.2: A plot of $(E-P)/\sqrt{P}$ versus X (in.) with no compensation.

As before, the multiplicative term can be absorbed into the other coefficients, leading to equation A.5

$$\Phi_i = a_i * D_i^2 + b_i * D_i + c_i - L0_i - I0_i \tag{A.5}$$

Note that Φ_i is the photon flux associated with an "event", which means that it was zero when no shower particles were passing through scintillator i. (In making this statement, any random fluctuations in the constants terms are ignored.)

The next effect that needed to be handled was the variation in the photon collection efficiency of the scintillator/PMT combination as a function of the X-position of the shower (the photon generation point). The effects of the collection efficiency can be seen in the plot of the $(E-P)/\sqrt{P}$ versus X shown in Figure A.2. The PMT's are located at the outer edges of the scintillators, at about $\pm$ 50 in. The fraction of the photons collected by the PMT's is greater for showers that are located closer to the PMT's, hence, the greater measured energy. To handle this effect, the photon flux at the PMT (Φ_i) due to the particle shower was assumed to be related to the photon flux created by the shower (Q_i) by a multiplicative factor, $f_i(x)$. This relationship is shown in equation A.6.

$$\Phi_i = f_i(x) * Q_i \tag{A.6}$$

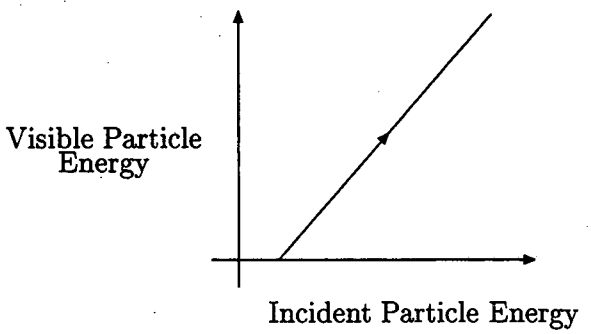

Figure A.3: A plot of the hypothetical "visible" energy vs. energy relationship

To be more general, an offset term, $Q0_i$, can be added to equation A.6. This offset term models a threshold effect in the photon flux vs. shower energy relationship. This can be understood by considering an "ideal" calorimeter where all the incident particle's "visible" energy is related to the energy of the particle by the relationship shown in Figure A.3. The visible energy is defined as the energy that can be detected by the calorimeter. Experimentally, the minimum detectable energy threshold was extremely small, i.e., offset term was approximately zero, $Q0_i = 0$.

The relationship that results when equation A.5 and A.6 are combined is given in equation A.7.

$$Q_i = \frac{1}{f_i(x)} * \left(a_i * D_i^2 + b_i * D_i + c_i - L0_i - I0_i\right) \tag{A.7}$$

It should be noted that there are serious problems with the interpretation of this equation and that care must be taken in using it.

As was stated in the beginning, the final goal was the calibration of the calorimeter. The above analysis has identified the following parameters that must be determined.

1. $f_i(x)$ – Photon collection efficiency.
2. a_i, b_i, c_i – ADC "conversion coefficients".
3. $I0_i$ – Integration offset.
4. $L0_i$ – PMT offset.

The next step in the calibration process was finding a procedure for determining the value of these parameters. Given the excellent momentum resolution of the E789 spectrometer, the method chosen for determining the calorimeter parameters was a least squares fit of

the calorimeter output for an isolated incident particle to the momentum of the particle as measured by the spectrometer. More specifically, the quantity that was to be minimized is shown in equation A.8.

$$\sum_{k=1}^{N} \left(\frac{P_k - \sum_i (Q_i)_k}{\sigma_k} \right)^2 \tag{A.8}$$

The sum over k is a sum over events and the sum over i is a sum over the individual ADC's in the calorimeter. Note that there may be an overall scale factor that multiplies the $\sum(Q_i)_k$ term. However, it has been absorbed into the other constants.

In order to simplify the calibration procedure, some modifications were made to equation A.7. The first simplification was the consolidation of the individual scintillator section $f_i(x)$'s into two "global" photon collection efficiency functions, one for the left half of the calorimeter and one for the right half of the calorimeter, $f_L(x)$ and $f_R(x)$. By making these global function replacements, the x position of the shower was assumed to be the same in a given scintillator and the photon collection efficiency was assumed to be approximately the same for all scintillators in each half of the calorimeter. The position assumption was a fairly good assumption, i.e., the x position of a shower was approximately the same at the different scintillator planes in the calorimeter. However, the similarities in photon collection efficiencies between different scintillators is not known, hence the absolute validity of the second simplification is open to question.

Equation A.9 shows the form of the collection efficiency function that was assumed in this analysis.

$$f(x) = \left(\frac{e^{-(L-|x|)/\lambda} + R * e^{-(L+|x|)/\lambda}}{e^{-L/\lambda} * (1+R)} \right) \tag{A.9}$$

The λ parameter is an attenuation length, R is a reflection coefficient and L is the length, in x, of the scintillator. Both λ and R are determined from the minimization procedure. The choice of this function is based on the assumption that the scintillator acted as a short piece of waveguide with energy loss. The fact that this function appears to captures the form of the collection efficiency was the only justification for its use.

Although the $f(x)$ given in equation A.9 completely characterizes the photon collection efficiency, an additional linear x factor was added to the photon collection efficiency relationship. This factor was added to correct for a residual linear x dependency that remained in the data after compensation for the waveguide effect. The complete photon

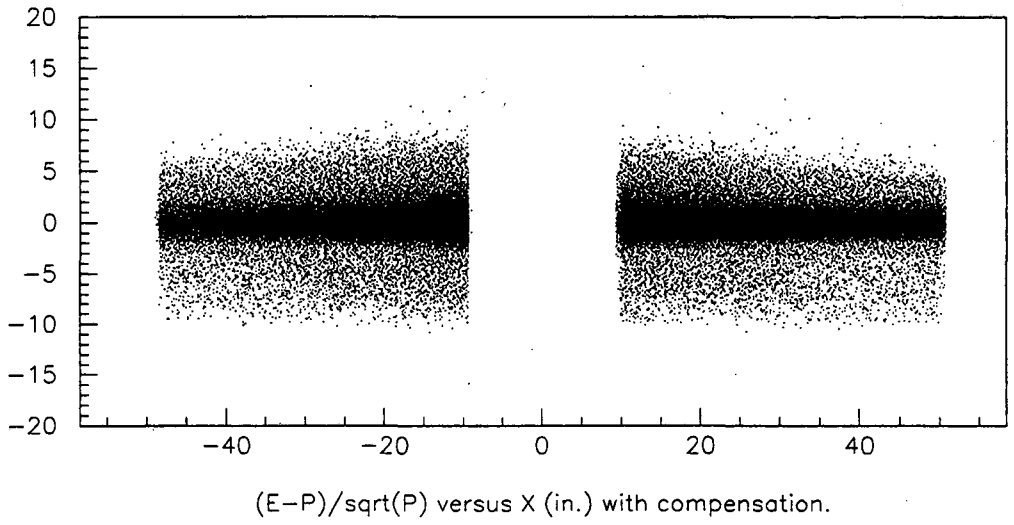

Figure A.4: A plot of $(E-P)/\sqrt{P}$ versus X (in.) after compensation.

efficiency relationship that was used is shown in equation A.10.

$$f(x) = \left(\frac{e^{-(L-|x|)/\lambda} + R * e^{-(L+|x|)/\lambda}}{e^{-L/\lambda} * (1+R)} \right) * (A * x + B) \tag{A.10}$$

In the end, the residual x dependency turned out to be caused by a bug in the calibration routine which was subsequently fixed. The linear compensation factor was kept after the bug was fixed. The resulting slope corrections were negligible. Figure A.4 shows $(E-P)/\sqrt{P}$ versus X after compensation was added.

The procedure for determining the optimal λ and R values turns out to be a problem in nonlinear least squares fitting. For this reason, the determination of these parameters (along with the coefficients in the linear x dependency) was separated from the procedure for finding the ADC parameters. This turned the calibration procedure into an iterative process.

The next simplification that was made in equation A.8 was in σ_k. It can be argued that σ_k is proportional to the square root of the energy that is measured by the calorimeter. However, setting σ_k to $\sqrt{\sum (Q_i)_k}$ would complicate the minimization procedure. For this reason, σ_k was assumed to be independent of the Q_i's for the purpose of deriving the minimization equations. In addition, since the Q_i's were initially unknown, σ_k was estimated

by $\sqrt{P_k}$ in the initial stages of the calibration procedure. In the later stages, where the Q_i's had been determined, the σ_k were set to $\sqrt{\sum(Q_i)_k}$.

The procedure for deriving the set of linear equations that determine the remaining free parameters in the least squares minimization of equation A.8 was a straight forward process of taking the partial derivatives of the equation with respect to each free parameter and setting the resulting equation to zero. However, in the process of deriving the minimization equations a problem is encountered with the constant terms in equation A.7, c_i, $L0_i$, and $I0_i$. First, it should be readily apparent that c_i, $L0_i$, and $I0_i$ cannot be individually determined for a given i, only the sum $c_i - L0_i - I0_i$. Second, it turns out that even this sum cannot be determined. This can be seen as follows. First, define the constant Z_i to be equal to $c_i - L0_i - I0_i$. Assuming that $f(x)$ is a known function, the calibration procedure then proceeds by minimizing A.15 with respect to a_i, b_i, and Z_i. This means taking the partial derivative of A.15 with respect to the parameters and setting the derivatives to zero. The difficulty arises in the partial derivative with respect to the Z_i's. The equation of interest is the partial derivative of A.11 with respect to Z_i.

$$(Q_i)_k = \frac{1}{f(x_k)} * \left(a_i * (D_i)_k^2 + b_i * (D_i)_k + Z_i\right) \tag{A.11}$$

This gives equation A.12.

$$\frac{\partial}{\partial a_j}(Q_m)_k = \frac{1}{f(x_k)}\delta_{jm} \tag{A.12}$$

The full minimization equation for this parameter is therefore

$$0 = \sum_{k=1}^{N}\left(\frac{E_k - \sum_i (Q_i)_k}{\sigma_k^2}\right)\sum_m \delta_{jm}\frac{1}{f(x_k)} \tag{A.13}$$

Which then reduces to :

$$0 = \sum_{k=1}^{N}\left(\frac{E_k - \sum_i (Q_i)_k}{\sigma_k^2}\right)\frac{1}{f(x_k)} \tag{A.14}$$

Hence, the M partial derivatives, where M is the number of ADC's, has resulted in ONE equation. Clearly, without more information, progress cannot be made. Without complicating the calibration procedure, the only recourse was to lump the parameters into one global constant. (Actually, two, one for each half of the calorimeter.)

At this point, the full set of equations from the least squares minimization procedure can be derived. These equations are obtained by taking the partial derivatives of equation A.15 with respect to the free parameters, a_i, b_i, and $C0$, where $(Q_i)_k$ is defined

in equation A.16. Note that $C0$ is the sum over all the individually indeterminate constant terms. (See equation A.17.)

$$\sum_{k=1}^{N}\left(\frac{E_k-\sum_i(Q_i)_k-C0/f(x_k)}{\sigma_k}\right)^2 \tag{A.15}$$

$$(Q_i)_k=\frac{1}{f(x_k)}*\left(a_i*(D_i)_k^2+b_i*(D_i)_k\right) \tag{A.16}$$

$$C0=\sum_i(c_i-L0_i-I0_i) \tag{A.17}$$

Defining the "generic" free parameter α, the partial derivative of equation A.15 with respect to α is given in equation A.18.

$$0=\sum_k\left(\frac{E_k}{\sigma_k^2}-\frac{\sum_i(Q_i)_k}{\sigma_k^2}-\frac{C0}{f(x_k)E_k}\right)\frac{\partial}{\partial\alpha}\left(\sum_h(Q_h)_k+\frac{C0}{f(x_k)}\right) \tag{A.18}$$

For $\alpha = a_i$, b_i, and $C0$, the partial derivatives of $\sum_h Q_{ih}(k) + C0/f(x_k)$ are given in equations A.20, A.21, and A.21.

$$\frac{\partial}{\partial a_j}\left(\sum_h(Q_h)_k+\frac{C0}{f(x_k)}\right)=\frac{1}{f(x_k)}(D_j)_k^2 \tag{A.19}$$

$$\frac{\partial}{\partial b_j}\left(\sum_h(Q_h)_k+\frac{C0}{f(x_k)}\right)=\frac{1}{f(x_k)}(D_j)_k \tag{A.20}$$

$$\frac{\partial}{\partial C0}\left(\sum_h(Q_h)_k+\frac{C0}{f(x_k)}\right)=\frac{1}{f(x_k)} \tag{A.21}$$

Expanding the $(Q_h)_k$'s and re-arranging terms, the following three sets of equations can be derived.

$$\begin{aligned}\sum_k\frac{E_k}{\sigma_k^2}\frac{1}{f(x_k)}(D_j)_k^2 &= \sum_i\left(\sum_k(D_j)_k^2\frac{1}{f(x_k)}\frac{1}{\sigma_k^2}\frac{1}{f(x_k)}(D_i)_k^2\right)a_i\\ &+\sum_i\left(\sum_k(D_j)_k^2\frac{1}{f(x_k)}\frac{1}{\sigma_k^2}\frac{1}{f(x_k)}(D_i)_k\right)b_i\\ &+\sum_k(D_j)_k^2\frac{1}{f(x_k)}\frac{1}{\sigma_k^2}\frac{1}{f(x_k)}C0\end{aligned} \tag{A.22}$$

$$\begin{aligned}\sum_k\frac{E_k}{\sigma_k^2}\frac{1}{f(x_k)}(D_j)_k &= \sum_i\left(\sum_k(D_j)_k\frac{1}{f(x_k)}\frac{1}{\sigma_k^2}\frac{1}{f(x_k)}(D_i)_k^2\right)a_i\\ &+\sum_i\left(\sum_k(D_j)_k\frac{1}{f(x_k)}\frac{1}{\sigma_k^2}\frac{1}{f(x_k)}(D_i)_k\right)b_i\\ &+\sum_k(D_j)_k\frac{1}{f(x_k)}\frac{1}{\sigma_k^2}\frac{1}{f(x_k)}C0\end{aligned} \tag{A.23}$$

$$\sum_k \frac{E_k}{\sigma_k^2}\frac{1}{f(x_k)} = \sum_i \left(\sum_k \frac{1}{f(x_k)}\frac{1}{\sigma_k^2}\frac{1}{f(x_k)}(D_i)_k^2\right) a_i + \sum_i \left(\sum_k \frac{1}{f(x_k)}\frac{1}{\sigma_k^2}\frac{1}{f(x_k)}(D_i)_k\right) b_i + \sum_k \frac{1}{f(x_k)}\frac{1}{\sigma_k^2}\frac{1}{f(x_k)} C0 \tag{A.24}$$

By defining the two vectors in equations A.25 and A.26 the minimization equations are reduced to the simple form shown in equations A.27.

$$\vec{B}_k = \begin{pmatrix} \frac{1}{f(x_k)}(D_j)_k^2 \\ \frac{1}{f(x_k)}(D_j)_k \\ \frac{1}{f(x_k)} \end{pmatrix} \tag{A.25}$$

$$\vec{X} = \begin{pmatrix} a_i \\ b_i \\ C0 \end{pmatrix} \tag{A.26}$$

$$\sum_k \frac{E_k}{\sigma_k^2}\vec{B}_k = \sum_k \left(\vec{B}_k \frac{1}{\sigma_k^2}\vec{B}_k^T\right)\vec{X} = \mathbf{A}\vec{X} \tag{A.27}$$

The calorimeter calibration process has seemingly been reduced to solving the set of linear equations shown in equation A.27. However, things are not quite as they appear as the following paragraphs will show. The problem is in how the vector $\vec{B}_k$ and matrix $\mathbf{A}$ are constructed.

The difficulties in constructing $\vec{B}_k$ and matrix $\mathbf{A}$ can be seen by looking at an idealized calorimeter and an idealized set of "tuning" events. The idealized calorimeter is designed to have no noise. This means that the constant terms, $L0_i$ and $I0_i$, that comprise $C0$ are truly constant. In addition, in the idealized calorimeter, there is no variation in the photon collection efficiency each scintillator, i.e, $f(x) = 1$. Finally, the ADC's in this idealized calorimeter are assumed to true "square law" encoders, that is the ADC output/input relationship is as shown in equation A.28.

$$S_i = a_i * D_i^2 + b_i * D_i \tag{A.28}$$

Where S_i is the input to the i_{th} ADC and D_i is its output. The idealized set of tuning events consists of only single hadron events with no contamination from neutrals particles. That is the energy that is deposited in the calorimeter is due solely to the incident hadron.

Now consider the response of a scintillator cell to an event. In this idealized situation, the scintillator response is shown in equation A.29.

$$Q_i = a_i * D_i^2 + b_i * D_i - L0_i - I0_i \tag{A.29}$$

For scintillators that are not "hit", Q_i will be zero. This means that the "quiescent" output of the ideal ADC will a value $D_i = D0_i$ such that the relationship in equation A.30 holds.

$$a_i * D0_i^2 + b_i * D0_i = L0_i + I0_i \tag{A.30}$$

Now consider the addition of this idealized event to the construction of $\vec{B}_k$ and $\mathbf{A}$. The ADC outputs of ALL the scintillators MUST be used in the construction of $\vec{B}_k$ and $\mathbf{A}$. If they are not, then the energy measured by the calorimeter will be calculated incorrectly. Recall that the individual constants $L0_i$ and $I0_i$ cannot be individually determined. This resulted in the following equation relating the energy measured in the calorimeter $\sigma Q_i'$ and the actual energy deposited in the calorimeter Q_{total}:

$$Q_{Total} = \sum_i Q_i' + C0 \tag{A.31}$$

where

$$Q_i' = a_i * D_i^2 + b_i * D_i \tag{A.32}$$

Since the $L0_i$ and $I0_i$ terms for "quiescent" cells are included in $C0$, they must be cancelled by the Q_i' terms for the quiescent cells. This means that the quiescent output for the ADC's that are connected to quiescent cells MUST be included in the creation of $\vec{B}$ and $\mathbf{A}$. (Note that the same would be true even if the $L0_i$ and $I0_i$ terms were not lumped into a single constant.)

Getting back to the "real" calorimeter, the same statement holds true for the real calorimeter also. For scintillators that are not "hit", the quiescent output of the ADC's need to be used. Note that "quiescent" means the value when there is no energy deposited in the scintillator. That means that care must be taken to ensure that the quiescent value is not contaminated by energy deposited by neutral particles. This suggests that the quiescent outputs of all the ADC's in the calorimeter need to be determined. Unfortunately, these ADC levels are not available. The calorimeter readout system sets all ADC levels that are below a certain threshold to zero as a result of the digital discriminator in the readout chain. The quiescent ADC levels have effectively been thrown out.

Without the quiescent ADC levels, it would appear that progress cannot be made. However, this is not completely true. In the non-ideal case, the constant coefficient $C0$ contains contributions from the tunable c_i parameter from each ADC (See equation A.17.) If one assumes that non zero quiescent ADC outputs are all due to the constant offsets $L0_i$ and $I0_i$, one might naively think that one has the freedom to adjust (i.e., tune) the c_i's to cancel out the $L0_i$ and $I0_i$ contribution. This would then allow us to assume that the quiescent ADC outputs (D_i) are equal to zero. However, this is patently WRONG, what has happened is that we have made a subtle change in what $C0$ represents. In reality, if the quiescent ADC outputs are set equal to zero ($D_i = 0$), the new $C0$, call it $C0'$ to distinguish it from the original $C0$, that gets determined in the minimization process is related to the original $C0$ by the equation shown in equation A.33.

$$C0' = C0 + \sum_i \left(a_i * D0_i^2 + b_i * D0_i \right) \tag{A.33}$$

where $D0_i$ is the real quiescent output of the ADC's.

Another piece of evidence that suggests that the $C0'$ that is determined is not the same as the original $C0$ is that $C0$ may be non-zero whereas $C0'$ must zero. Again, this is best seen by looking at the "idealized" calorimeter scenario in the configuration where there is no deposited energy in the calorimeter. In this case, the ADC outputs should be zero, since there is no signal. However, the Q_i's are also zero since there is no energy deposition in the calorimeter. This means that $C0'$ MUST be zero.

At this point, it would appear that the way to continue is to proceed with the minimization procedure, assuming $D0_i$ and $C0'$ are both zero. This would mean that the tunable parameters are actually only a_i and b_i. However, this procedure is not correct. The best way to see this is to look at the calorimeter output equation, i.e., the equation for Q_{Total} (See A.34.) Note that for simplicity, the photon collection efficiency is assumed to be equal to one.

$$Q_{Total} = \sum_i \left(a_i * D_i^2 + b_i * D_i + c_i - L0_i - I0_i \right) \tag{A.34}$$

This can be separated into a sum over only those ADC's where energy has been deposited and a sum over ADC's where energy has not been deposited as shown in equation A.35.

$$\begin{aligned} Q_{Total} \;=\; & \sum_i \left(a_i * D_i^2 + b_i * D_i + c_i - L0_i - I0_i \right) \\ & + \sum_j \left(a_j * D0_j^2 + b_j * D0_j + c_j - L0_j - I0_j \right) \end{aligned} \tag{A.35}$$

Where i is a sum over ADC's from scintillators that were hit and j is a sum over quiescent ADC's. This can be rewritten with $C0'$ as a sum over hit scintillators as shown in equation A.36:

$$\begin{aligned} Q_{Total} &= \sum_i \left(a_i * D_i^2 + b_i * D_i + c_i - L0_i - I0_i\right) \\ &\quad - \sum_i \left(a_i * D0_i^2 + b_i * D0_i + c_i - L0_i - I0_i\right) \\ &\quad + C0' \end{aligned} \tag{A.36}$$

Where again, i is a sum over only hit scintillator ADC's.

Further algebraic manipulation yields equation A.37.

$$Q_{Total} = \sum_i \left(a_i * D_i^2 + b_i * D_i - a_i * D0_i^2 - b_i * D0_i\right) \tag{A.37}$$

Where i is again the sum over only those ADC's from scintillators where energy was deposited. Note that $C0'$ has disappeared because it is supposed to be zero. At this point, it appears that nothing has been accomplished at the expenditure of a considerable amount of effort since the quiescent ADC outputs, $D0_i$, are still required. However, things are not that bleak. Assume for the moment that the number of hit scintillators in an idealized single hadron event is the same for all events. Next, assume that the $D0_i$'s are approximately the same. If these two assumptions are made then equation A.37 can be reduced to equation A.38.

$$Q_{Total} = \sum_i \left(a_i * D_i^2 + b_i * D_i\right) + CC0 \tag{A.38}$$

Where the constant term $CC0$ term is a global constant that attempts to approximate the effects of the non zero quiescent ADC outputs. More precisely, as shown in equation A.39, CC0 is conceptually an average over events of the quiescent ADC outputs. Note that the sum is over "hit" scintillators.

$$CC0 = - < \sum_i \left(a_i * D0_i^2 + b_i * D0_i\right) > \tag{A.39}$$

At this point, a viable calibration procedure becomes evident. Equations A.25, A.26, and A.27 are the basis for the calibration procedure. However, the interpretation of the pieces of each component of these equations is dramatically different. In constructing matrix **A**, only ADC values are used in regions where energy deposition is expected. (This is a result of the fact that the quiescent ADC values have been assumed to be zero). The

coefficients a_i and b_i still retain their interpretation while the $C0$ becomes the $CC0$ of equation A.39. The events that are used in the construction of the matrix **A** then obtained as follows:

1. Select events from tape that contain isolated, non muon tracks.
2. Determine the spectrometer determined energy of the track.
3. Determine the scintillators in the calorimeter that contain the shower created by the track (particle).
4. Create the vector $\vec{B_k}$ for this event by using only ADC outputs from the scintillators that contain the shower.
5. Create the addition to matrix **A** from $\vec{B_k}$.
6. Repeat the above steps for a "sufficient" number of events.
7. Solve the linear equation A.27.

When the above calibration prescription is followed, an interesting result that pops up is that the constant term $CC0$ turn out to be positive. In contrast, equation A.39 seems to suggest that the constant term should be negative. In addition, a plot of calorimeter determined energy vs. particle momentum that is generated from the "optimal" calibration coefficients is slightly smaller than the expected value of unity. The root cause of these "problem" can be traced to the problem of identifying "hit" scintillator.

The calibration procedure is critically dependent on using ADC values from those scintillators that contain energy that is deposited by the track of interest. If the sum over ADC's is missing some terms, then the equation for the total energy as measured by the calorimeter, equation A.38 can be rewritten as equation A.40. In this equation, the sum over i is the sum over ADC's that have been determined, by the calibration program, to contain track energy; the sum over j is the sum over ADC's that also contain energy but were not selected by the calibration program; $CC0$ is the constant term specified by equation A.39. If the calibration program misses some of the scintillators that contain track energy, then the constant term that gets determined in the optimization procedure is not $CC0$, but rather $CC0'$, specified in equation A.41. In this case, $CC0'$ can clearly be positive. Finally, if the calibration program is not summing over enough of the scintillator ADC's, one would expect

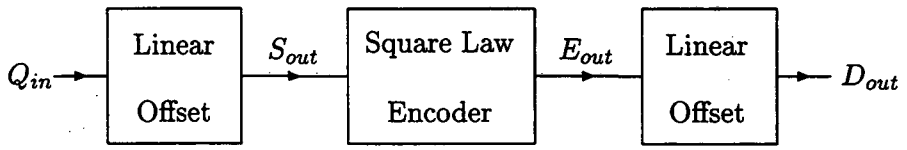

Figure A.5: A functional diagram of the ADC.

that the "missing" energy would be more pronounced at higher energy than at lower energy, hence the less than unity slope of the calorimeter energy vs. momentum distribution.

$$Q_{Total} = \sum_i \left(a_i * D_i^2 + b_i * D_i\right) + \sum_j \left(a_j * D_j^2 + b_j * D_j\right) + CC0 \tag{A.40}$$

$$CC0' = < \sum_j \left(a_j * D_j^2 + b_j * D_j\right) > + CC0 \tag{A.41}$$

Up to this point, the quiescent ADC levels were assumed to be caused by non zero inputs to the ADC's. One can conceive of another source of a non zero quiescent ADC level. This second source can be seen by looking at a functional diagram of the ADC. Figure A.5 is just such a diagram, showing the input output relationship of the ADC's. Q_{in}, S_{out}, E_{out}, and D_{out} may be related by the relationship given in equations A.42, A.43, and A.44.

$$S_{out} = Q_{in} + Q0 \tag{A.42}$$

$$S_{out} = a * E_{out}^2 + b * E_{out} \tag{A.43}$$

$$D_{out} = E_{out} + E0 \tag{A.44}$$

The analysis in the previous paragraphs handles the situation where $Q0$ in equation A.42 is non-zero. However, it does not handle the situation where the quiescent ADC output is due to an offset that is generated at the output of the square law encoder, i.e, $Q0 = 0$ and $E0 \neq 0$. This is because in this situation, the effects of $E0$ cannot be modeled as a constant offset at the input of the ADC. However, it is expected that this offset is negligible, i.e., $E0 = 0$ is a good approximation.

One final point that needs to be mentioned before the complete calibration procedure is described is that the calorimeter must be tuned for different event types. That is, there are separate tuning constants for electrons, hadrons and muons. This separation is required because the energy deposition mechanism is different for the two types of interactions.

Finally, the complete calibration process can be outlined. Recall that the calibration procedure is an iterative process because of the photon collection efficiency function. Complete calibration process consists of the following steps :

1. Select events from tape that contain isolated, non-muon tracks that are within the fiducial region of the calorimeter.

2. Filter the selected events to provide equal statistics in equal sized momentum intervals.

3. Make a first pass attempt at determining a_i, b_i, and $C0$ assuming a constant (vs. x) photon collection efficiency function. Only events in a narrow x range are used to minimize the effects of the photon collection efficiency function. Use the momentum of the incident particle to determine the uncertainty, σ_k.

4. Histogram the distribution of ratio of the energy as measured by the calorimeter and the energy as measured by the analysis magnet vs. the x position of the incident track.

5. Fit the waveguide function to the distribution.

6. Make a second pass at determining the a_i, b_i, and $C0$ parameters, this time assuming the waveguide photon collection efficiency function. As before, only events in a narrow x range are used.

7. Histogram the distribution of ratio of the energy as measured by the calorimeter and the energy as measured by the analysis magnet vs. the x position of the incident track. As before, a FLAT photon collection efficiency function is used.

8. Fit the waveguide function to the distribution.

9. Make a third pass at determining the a_i, b_i, and $C0$ parameters, again assuming the waveguide photon collection efficiency function. As before, only events in a narrow x

range are used. However, in this iteration, the sigma in the least squares fit function is determined from the calorimeter energy instead of the track momentum.

10. Histogram the distribution of ratio of the energy as measured by the calorimeter and the energy as measured by the analysis magnet vs. the x position of the incident track. As before, a FLAT photon collection efficiency function is used.

11. Fit the waveguide function to the distribution.

12. Make a fourth pass at determining the a_i, b_i, and $C0$ parameters, again assuming the waveguide photon collection efficiency function. As before, only events in a narrow x range are used. However, in this iteration, the sigma in the least squares fit function is determined from the calorimeter energy instead of the track momentum.

13. Histogram the distribution of ratio of the energy as measured by the calorimeter and the energy as measured by the analysis magnet vs. the x position of the incident track. Unlike before, the waveguide collection efficiency function is used.

14. Fit the the residual x dependence with a straight line.

15. Make a final pass at determining the a_i, b_i, and $C0$ parameters, assuming the waveguide photon collection efficiency function and the residual linear x dependence. As before, only events in a narrow x range are used. Also, as before, the sigma in the least squares fit function is determined from the calorimeter energy instead of the track momentum.

The effectiveness of the calibration procedure can be seen in Figures A.6 and A.7 which plot $(E-P)/\sqrt{P}$ and $(E-P)/\sqrt{P}$ versus P for isolated hadrons.

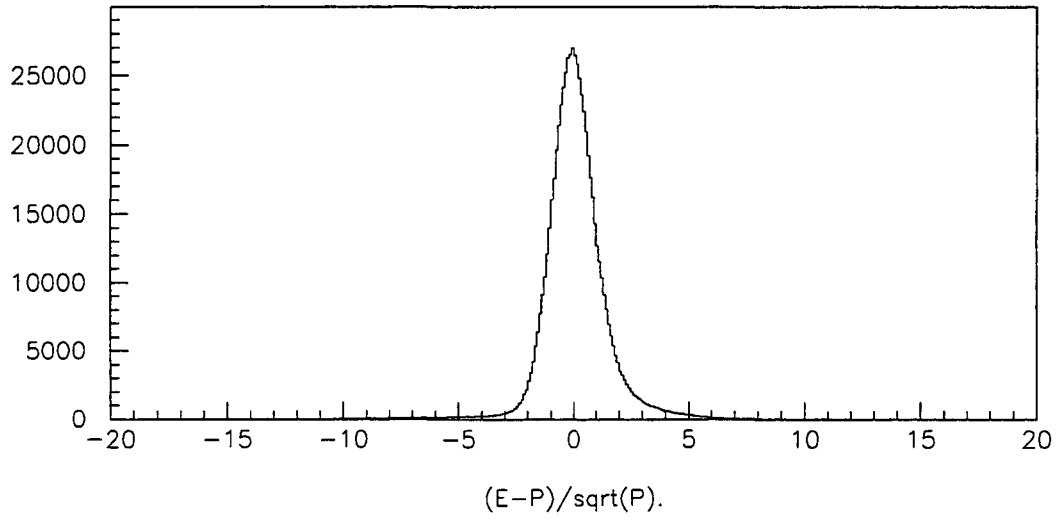

Figure A.6: The final $(E-P)/\sqrt{P}$ distribution.

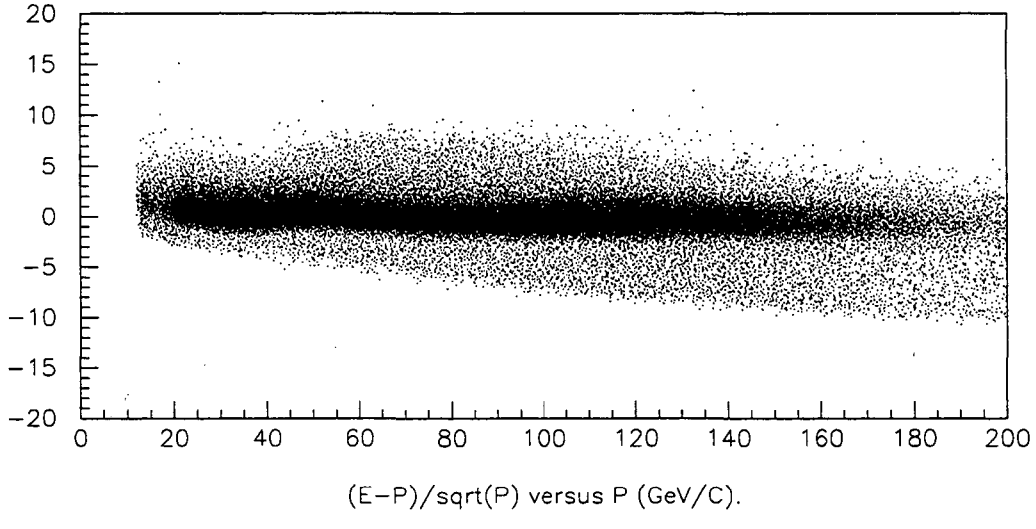

Figure A.7: The final $(E-P)/\sqrt{P}$ versus P distribution.

Ernest Orlando Lawrence Berkeley National Laboratory
One Cyclotron Road | Berkeley, California 94720

Prepared for the U.S. Department of Energy under Contract No. DE-AC03-76SF00098